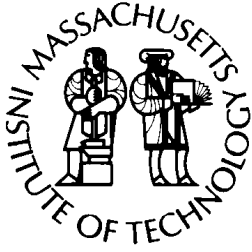
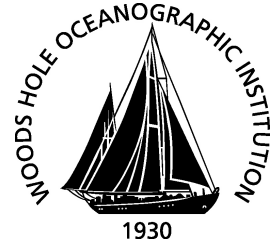


MIT/WHOI

**Massachusetts Institute of Technology
Woods Hole Oceanographic Institution**



**Joint Program
in Oceanography/
Applied Ocean Science
and Engineering**



DOCTORAL DISSERTATION

A Modeling Study of the Marine Biogeochemistry,
Plankton Dynamics, and Carbon Cycle on the
Continental Shelf Off the West Antarctic Peninsula

by

Cristina Schultz

June 2019

A MODELING STUDY OF THE MARINE
BIOGEOCHEMISTRY, PLANKTON DYNAMICS, AND
CARBON CYCLE ON THE CONTINENTAL SHELF OFF
THE WEST ANTARCTIC PENINSULA

by

Cristina Schultz

B.S., University of São Paulo, Brazil (2009)

Submitted in partial fulfillment of the requirements for the degree of
Doctor of Philosophy
at the

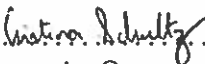
MASSACHUSETTS INSTITUTE OF TECHNOLOGY
and the

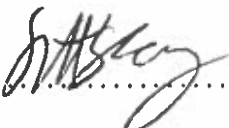
WOODS HOLE OCEANOGRAPHIC INSTITUTION


June 2019


© 2019. Cristina Schultz. All rights reserved.

The author hereby grants to MIT and WHOI permission to reproduce
and to distribute publicly paper and electronic copies of this thesis
document in whole or in part in any medium now known or hereafter
created.

Author 
Joint Program in Oceanography/Applied Ocean Science and Engineering
Massachusetts Institute of Technology
and Woods Hole Oceanographic Institution
February 25, 2019

Certified by 
Scott C. Doney
Joe D. and Helen J. Kington Professor in Environmental Change
University of Virginia
Thesis Supervisor

Certified by 
Weifeng Zhang
Associate Scientist
Woods Hole Oceanographic Institution
Thesis Supervisor

Accepted by 
Shuhei Ono
Chair, Joint Committee for Chemical Oceanography
Massachusetts Institute of Technology
Woods Hole Oceanographic Institution

**A MODELING STUDY OF THE MARINE BIOGEOCHEMISTRY,
PLANKTON DYNAMICS, AND CARBON CYCLE ON THE
CONTINENTAL SHELF OFF THE WEST ANTARCTIC PENINSULA**

by

Cristina Schultz

Submitted to the Joint Program in Oceanography/Applied Ocean Science and
Engineering

Massachusetts Institute of Technology
and Woods Hole Oceanographic Institution

on February 25, 2019, in partial fulfillment of the
requirements for the degree of
Doctor of Philosophy

Abstract

Over the past several decades, the West Antarctic Peninsula (WAP) has undergone physical and ecological changes at a rapid pace, with warming surface ocean and a sharp decrease in the duration of the sea ice season. The impact of these changes in the ocean chemistry and ecosystem are not fully understood and have been investigated by the Palmer-LTER since 1991. Given the data acquisition constraints imposed by weather conditions in this region, an ocean circulation, sea ice and biogeochemistry model was implemented to help fill the gaps in the dataset. The results with the present best case from the suite of sensitivity experiments indicate that the model is able to represent the seasonal and interannual variations observed in the circulation, water mass distribution and sea ice observed in the WAP, and has identified gaps in the observations that could guide improvement of the simulation of the regional biogeochemistry. Comparison of model results with data from the Palmer-LTER project suggests that the large spatial and temporal variability observed in the phytoplankton bloom in the WAP is influenced by variability in the glacial sources of dissolved iron. Seasonal progression of the phytoplankton bloom is well represented in the model, and values of vertically integrated net primary production (NPP) are largely consistent with observations. Although a bias towards lower surface dissolved inorganic carbon (DIC) and alkalinity was identified in the model results, interannual variability was similar to the observed in the Palmer-LTER cruise data.

Thesis Supervisor: Scott C. Doney

Title: Joe D. and Helen J. Kington Professor in Environmental Change
University of Virginia

Thesis Supervisor: Weifeng Zhang

Title: Associate Scientist
Woods Hole Oceanographic Institution

Acknowledgments

To the National Science Foundation (NSF) for the financial support.

To everyone involved with the Palmer Long Term Ecological Research (LTER) project, for the great input, encouragement and fun times.

To my advisors. More than offering support and help, you have been great examples on balancing life, getting your priorities straight, and as collaborative, ethical scientists.

To my wonderful husband Alex, I love you and I cannot imagine having someone more supportive by my side. In the moments when I felt discouraged to keep doing climate research you have offered me very wise words: "do it because you love it, and do it because it's important. Even if some people do not pay attention today. It will be needed, and it will be there".

To my family. This work would not be possible without your constant support throughout the years.

To my labmates (humans and dogs), who have made going to work so much fun. To my friends, old and new. The world is definitely better with you.

Contents

1	Introduction	25
2	Implementation of a circulation and sea ice model for the West Antarctic Peninsula	29
2.1	Introduction	29
2.2	Literature Review	31
2.2.1	Teleconnections - ENSO and SAM	31
2.2.2	Circulation and water masses	33
2.3	Methods	35
2.3.1	Model Description	35
2.3.2	Data used for skill assessment	38
2.3.3	Experiments	40
2.4	Results	50
2.4.1	Drivers of MLD	50
2.4.2	Sea Ice Extent	52
2.4.3	General Surface Circulation	56
2.4.4	Water Masses	59
2.4.5	Influence of Modes of Climate Variability	62
2.4.6	Influence of Seasonal Runoff	67
2.4.7	Influence of Langmuir Circulation Parameterization on MLD	69
2.5	Discussion and Conclusions	74

3	Implementation of biogeochemical model and analysis of chlorophyll patterns	83
3.1	Introduction	83
3.2	Literature Review	85
3.3	Methods	88
3.3.1	Model Description - Regulated Ecosystem Model with two Phytoplankton Classes(REcoMv2)	89
3.3.2	Experiment Setup	94
3.4	Results	101
3.4.1	Non-linearity in photosynthesis-irradiance (P-I) in the presence of subgrid-scale sea-ice variations	101
3.4.2	Assessing the timing of the bloom and possible limitations to phytoplankton growth for PAR_NONL experiment	105
3.4.3	Sensitivity analysis of the biogeochemical model	109
3.5	Discussion and Conclusions	115
4	Simulation of net primary production (NPP) and air-sea CO₂ fluxes	133
4.1	Introduction	133
4.2	Literature Review	135
4.2.1	Quantifying Primary Production and Export – concepts and methods	135
4.2.2	Primary Production and Export in the WAP	137
4.2.3	Inorganic carbon in the surface ocean and air-sea fluxes	139
4.3	Methods	140
4.3.1	Changes in initial and boundary conditions	140
4.3.2	WAP_BGC Experiment	141
4.3.3	Diagnostics Files	141
4.4	Results	144
4.4.1	Comparing exp19 and WAP_BGC	144
4.4.2	General patterns of NPP, GPP, Export and e-ratios	146

4.4.3	Inorganic carbon cycle and air-sea CO ₂ fluxes	152
4.5	Discussion and Conclusions	157
5	Conclusions	173
A	Tables	179
B	Including effects of different sea ice categories in PAR transmittance	
	- Implementation	185

List of Figures

2-1	WAP map with locations of interest.	34
2-2	Model grid.	36
2-3	Map of the WAP showing the location of the Palmer-LTER stations.	39
2-4	Mean temperature during the Palmer-LTER cruises (top left) and January average calculated for the MITgcm output (bottom left), mean salinity during the Palmer-LTER cruises (top right) and January means for the MITgcm output (bottom right) for Line 400 of the Palmer-LTER grid.	41
2-5	Scaling coefficients for the freshwater input flux.	44
2-6	Relationship between wind-ice drag coefficient and SIC proposed by Andreas et al (2010, left) and relationship between wind enhancement coefficient and SIC developed for this study (right).	49
2-7	Time series of salinity for the MITgcm grid point closes to Station 200.000 (closest to the coast, left) and 200.200 (right) of the Palmer-LTER cruise grid for experiments ICEdrag, Ricr, BELLS and RUNOFF05.	51
2-8	Time series of salinity difference between experiment BELLS and experiments ICEdrag, Ricr and RUNOFF05 for the MITgcm grid point closest to Palmer-LTER station 200.00.	52
2-9	Monthly mean sea ice concentration calculated between 1991 and 2003 for experiment ICEdrag (left), BELLS (center) and for the SSM/I satellite data (right), for January, April, August and December.	53
2-10	Temporal correlation between the SSM/I satellite data and ICEdrag (left) and BELLS (right) experiments, calculated between 1991 and 2003.	54

2-11	Correlation coefficient between SSM/I data and the MITgcm experiments (ICEdrag and BELLS) for the points closest to the PALMER-TER stations on line 200 (left) and 500 (right).	55
2-12	Sea ice thickness simulated by BELLS (left) and ICEdrag (right) on Line 200.	56
2-13	Monthly mean surface salinity and surface current velocity for experiments BELLS (left) and ICEdrag (right), for January (top) and July (bottom).	57
2-14	Monthly mean surface salinity and surface current velocity for experiments BELLS (left) and ICEdrag (right), for July (top) and January (bottom).	58
2-15	Location of the station points for lines 200 (left) and 500 (right), with bathymetry on the background. The continental shelf stations (depth < 750 m) are represented in blue, and the shelf break/offshore stations are represented in red.	59
2-16	Θ -S diagrams for monthly mean January values of experiments BELLS (top) and ICEdrag (bottom), for onshore (left) and shelf break/offshore (right) stations of line 200. The x axis shows salinity values and the y axis shows temperature for each point, and the boxes show the limits of each water mass analyzed.	61
2-17	Θ -S diagrams for monthly mean July values of experiments BELLS (top) and ICEdrag (bottom), for onshore (left) and shelf break/offshore (right) stations of line 200. The x axis shows salinity values and the y axis shows temperature for each point, and the boxes show the limits of each water mass analyzed.	62
2-18	Θ -S diagrams for monthly mean January values of experiments BELLS (top) and ICEdrag (bottom), for onshore (left) and shelf break/offshore (right) stations of line 500. The x axis shows salinity values and the y axis shows temperature for each point, and the boxes show the limits of each water mass analyzed.	63

2-19	Time series of sea ice concentration anomalies (calculated as the difference between the monthly average and the monthly climatology) for the points closes to Line 200 for MITgcm experiments ICEdrag (left), BELLS (center) and for the SSM/I satellite data.	65
2-20	Time series of sea ice concentration anomalies (calculated as the difference between the monthly average and the monthly climatology) for the points closest to Line 600 for MITgcm experiments ICEdrag (left), BELLS (center) and for the SSM/I satellite data.	66
2-21	Comparison of temperature (left) and salinity (right) for Line 200 from the Palmer-LTER 1998 cruise data (top) and the MITgcm ICEdrag (center) and BELLS (bottom) January/February 1998 mean.	67
2-22	Comparison of temperature (left) and salinity (right) for Line 600 from the Palmer-LTER 1998 cruise data (top) and the MITgcm ICEdrag (center) and BELLS (bottom) January/February 1998 mean.	68
2-23	Comparison of temperature (left) and salinity (right) for Line 600 from the Palmer-LTER 1999 cruise data (top) and the MITgcm ICEdrag (center) and BELLS (bottom) January/February 1999 mean.	69
2-24	Comparison of temperature (left) and salinity (right) for Line 600 from the Palmer-LTER 2002 cruise data (top) and the MITgcm ICEdrag (center) and BELLS (bottom) January/February 2002 mean.	70
2-25	Surface temperature and salinity difference between tests ICEdrag and SRunoff for Line 200 of the Palmer-LTER grid.	71
2-26	Correlation between monthly mean sea ice concentration on MITgcm simulations and SSM/I satellite data for lines 200 and 600 of the Palmer-LTER grid.	72
2-27	Surface current velocity difference between tests ICEdrag and SRunoff in January (top left) and July (top right); and SRunoff simulated surface current velocity in January (bottom left) and July (bottom right).	73

2-28	Calculated mean MLD difference between KPP_LC (top), KPP_epsI (middle) and KPP_Ut (bottom) and the Srunoff experiment for January (left) and July (right). Dashed contours indicate differences in sea ice concentration (SIC).	77
2-29	Mixed layer depth (MLD, in color) and sea ice concentration (SIC, contours) for experiment KPP_Ut (left and middle) and difference between KPP_Ut and ICEDrag (right) for April (top), June (middle) and August (bottom) of 1999.	78
2-30	Correlation between experiments (legend) and SSM/I satellite data sea ice concentration (SIC) for the period 1991-2003 for lines 200 (top left), 400 (top right) and 600 (bottom).	79
2-31	Mean calculated MLD for the Palmer-LTER data (black dashed line) and mean January MLD for each experiment (legend), for lines 300-600 of the Palmer-LTER grid.	79
2-32	Climatological MLD calculated from the Palmer-LTER cruises (blue) and average MLD calculated from daily outputs for Januaries of 2013 and 2014 (orange) plotted for lines 300 to 600. The dotted lines represent a deviation of $1.96 \times$ the standard deviation for each dataset.	80
2-33	Difference between Palmer-LTER MLD and KPP_Ut MLD and bathymetry (grey scale) for the month of January of 1994 (top left), 1995 (top right), 1997 (bottom left) and 1999 (bottom right).	80
2-34	Time-series of MLD (left), SIC (middle) and wind speed (right) of experiment KPP_Ut for the points of line 300 of the Palmer-LTER grid.	81
3-1	Climatological monthly mean surface chlorophyll for experiments PAR_NONL (top) and CTRL (bottom), for the months of November (left), December (middle) and January (right). Note the log-scale used in the color bar.	102

3-2	Year-distance plot of water-column maximum chlorophyll concentration (bottom row) at each location along the line 200 during the Palmer-LTER cruises for CTRL run (left), PAR_NONL (center) and Palmer data, and the anomaly relative to the geometric mean model or observed station data (top row). X-axis shows the station number, and Y-axis shows the cruise name (cruise period described in Appendix A). Note that a log-scale color bar is used for the chlorophyll concentrations (bottom row) while a linear-scale color bar is used for anomalies (top row).	119
3-3	Year-distance plot of water-column maximum chlorophyll concentration (bottom row) at each location along the line 600 during the Palmer-LTER cruises for CTRL run (left), PAR_NONL (center) and Palmer data, and the anomaly relative to the geometric mean model or observed station data (top row). X-axis shows the station number, and Y-axis shows the cruise name (cruise period described in Appendix A). Note that a log-scale color bar is used for the chlorophyll concentrations (bottom row) while a linear-scale color bar is used for anomalies (top row).	120
3-4	Spatial correlation between model experiments CTRL and PAR_NONL and the Palmer-LTER cruise chlorophyll data, calculated for the water-column maximum chlorophyll concentration at each cruise station and for the corresponding monthly mean in the model data. Cruises marked by a star indicate cruises where correlation was statistically significant at the 0.05 level.	121
3-5	Spatial variance between model experiments CTRL and PAR_NONL and the Palmer-LTER cruise chlorophyll data, calculated for the water-column maximum chlorophyll concentration at each cruise station and for the corresponding monthly mean in the model data.	121

3-6	Monthly mean surface chlorophyll at the grid station closest to Palmer Station E from October through April each season versus year, for CTRL (top) and PAR_NONL (bottom) runs. Note the log-scale color bar.	122
3-7	Fraction of monthly geometric mean surface chlorophyll composed of small phytoplankton chlorophyll at the grid point closest to Palmer Station E, from October through April every season versus year, for CTRL (top) and PAR_NONL (bottom).	122
3-8	Spatial correlation between model experiment PAR_NONL and the Palmer-LTER cruise chlorophyll data, calculated for the maximum chlorophyll concentration at each cruise station and for the corresponding monthly mean for December, January and February in the model data, for lines 400-600 (top) and lines 200-300 (bottom). Cruises marked by a star indicate cruises where correlation was statistically significant at the 0.05 level. Period of each cruise is described in Appendix A.	123
3-9	Deviation from the geometric mean station water-column maximum chlorophyll concentration for January 1994 (top) and January 2006 (bottom), for the PAR_NONL experiment (left) and Palmer-LTER cruise (right).	124
3-10	Deviation from the geometric mean station water-column maximum chlorophyll concentration for January 2004 (top) and 2011 (bottom), for the PAR_NONL experiment (left) and Palmer-LTER cruise (right).	125
3-11	PAR_NONL climatological monthly mean surface dissolved iron concentration dFe (left) for the months of December (top) and January (bottom), and surface dFe anomalies from the climatological monthly mean, for December 2005 (top middle), December 2010 (top right), January 2006 (bottom middle) and January 2011 (bottom right).	126

3-12	PAR_NONL surface chlorophyll concentration versus time for grid point near Palmer Station E (top) and Rothera Station (bottom), in grey, and observed surface chlorophyll collected at these stations (green). Note the log-scale used on the y-axis.	127
3-13	Spatial correlation versus year between model experiments PAR_NONL, exp1, exp19 and the Palmer-LTER cruise chlorophyll data, calculated for the water-column maximum chlorophyll concentration at each cruise station and for the corresponding monthly mean in the model data, for lines 200-600 (top), lines 400-600 (middle) and lines 200-300 (bottom). Cruises marked by a star indicate cruises where correlation was statistically significant at the 0.05 level.	128
3-14	Spatial correlation versus year between model experiments and the Palmer-LTER cruise chlorophyll data, calculated for the water-column maximum chlorophyll concentration at each cruise station and for the corresponding monthly mean in the model data, for lines 200-600. Data is shown for exp1 (top) and exp19 (bottom). Cruises marked by a star indicate cruises where correlation was statistically significant at the 0.05 level.	128
3-15	Climatological January monthly mean dissolved inorganic nitrogen (DIN) contoured as a function of depth and longitude for PAR_NONL experiment (bottom) and average DIN concentration during the January Palmer-LTER cruises (top), for lines 200 (left) and 600 (right) of the Palmer-LTER grid.	129
3-16	Climatological January monthly mean dissolved inorganic silicate (DSi) contoured as a function of depth and longitude for PAR_NONL experiment (bottom) and average DSi concentration during the January Palmer-LTER cruises (top), for lines 200 (left) and 600 (right) of the Palmer-LTER grid.	129

3-17	Taylor diagram comparing maximum chlorophyll at each station sampled during cruise LMG11-01 and the corresponding MITgcm grid points during January 2011 of experiments PAR_NONL exp1 and exp19 for Palmer-LTER grid lines 400-600 (left) and 200-300 (right).	130
3-18	Maximum water-column chlorophyll, climatological maximum water-column chlorophyll, surface diatom iron limitation (FeLimDia), surface small phytoplankton iron limitation (FeLimPhy), surface diatom light limitation (LLimDia) and surface small phytoplankton light limitation (LLimPhy) versus time for stations 600.040 (left) and 600.160 (right) for the exp19 experiment (top) and PAR_NONL (bottom), for the period between October 2010 and April 2011. Note that the log-scale y-axis on the left applies to the chlorophyll concentrations while the y-axis on the right applies to the limitation factors.	130
3-19	Taylor diagram comparing maximum chlorophyll at each station sampled during cruise LMG12-01 and the corresponding MITgcm grid points during January 2012 of experiments PAR_NONL, exp1 and exp19 for Palmer-LTER grid lines 200-300.	131
3-20	PAR_NONL simulated sea ice fraction versus time for the period between October 2011 and April 2012 and simulated climatological sea ice fraction between October and April, for MITgcm grid points corresponding to the location of Palmer-LTER grid points 200.040 (left) and 200.160 (right).	131

3-21	Maximum water-column chlorophyll, climatological maximum water-column chlorophyll, surface diatom iron limitation (FeLimDia), surface small phytoplankton iron limitation (FeLimPhy), surface diatom light limitation (LLimDia) and surface small phytoplankton light limitation (LLimPhy) versus time for stations 200.040 (left) and 200.160 (right) for the exp19 experiment (top) and PAR_NONL (bottom), for the period between October 2011 and April 2012. Note that the log-scale y-axis on the left applies to the chlorophyll concentrations while the y-axis on the right applies to the limitation factors.	132
4-1	Spatial correlation between model experiments WAP_BGC and exp19 and the Palmer-LTER cruise chlorophyll data, calculated for the water-column maximum chlorophyll concentration at each cruise station and the corresponding monthly mean in the model data (top), for the stations sampled in lines 400-600 (middle) and lines 200-300 (bottom). Points marked with a star indicate where correlation was significant at a 0.05 level.	145
4-2	Distribution of anomaly of water-column maximum chlorophyll concentration at each station, where the anomaly is computed as the difference from the geometric mean calculated individually for model and observation, for model exp19 (left), model WAP_BGC (middle) and for observed Palmer-LTER cruise data (right).	146
4-3	Monthly climatology of surface chlorophyll concentration for WAP_BGC experiment, calculated using model output from 1991 to 2014.	160
4-4	Model WAP_BGC climatological (from 1991-2014) showing monthly means for NPP (left), carbon export below 100 m (middle) and e-ratio (right) for November (top), December (middle) and January (bottom). Dashed line represents sea ice concentration and dots plotted in November represent the location of the Palmer-LTER grid stations.	161

4-5	Climatological monthly mean C export (top) and NPP (bottom) calculated for 1991 to 2014 for WAP_BGC results, for December (left) and January (right), for stations of Line 600 of the Palmer-LTER grid.	162
4-6	Climatological monthly mean C export (top) and NPP (bottom) calculated for 1991 to 2014 for WAP_BGC results, for December (left) and January (right), for stations of Line 200 of the Palmer-LTER grid.	162
4-7	Vertically integrated NPP (top) and deviations from the mean integrated NPP calculated for all the stations (bottom) for WAP_BGC monthly means of January 2002 (high chlorophyll year, left) and Palmer-LTER cruise LMG02-01.	163
4-8	Vertically integrated NPP (top) and deviations from the mean integrated NPP calculated for all the stations (bottom) for WAP_BGC monthly means of January 2003 (left) and Palmer-LTER cruise LMG03-01.	164
4-9	WAP_BGC yearly and vertically integrated simulated NPP (top), carbon export (middle) and e-ratio (bottom) for Palmer-LTER grid North (Lines400-600, orange) and South (Lines 200 and 300, blue) areas (left), and onshore (stations 0-60, blue) and shelf break/offshore (stations 160-220, orange) areas (right).	164
4-10	WAP_BGC yearly (August to July) simulated NPP (top) and carbon export (bottom) for the model climatology (left), and anomalies for August 2005-July 2006 (middle) and August 2007-July 2008 (right).	165
4-11	Vertical profile of experiment WAP_BGC simulated NPP anomaly from the climatology, MLD and particle export across line 200 of the Palmer-LTER grid for the monthly mean of December 2007 (left) and January 2008 (right).	165
4-12	Vertical profile of experiment WAP_BGC simulated NPP anomaly from the climatology, MLD and particle export across line 600 of the Palmer-LTER grid for the monthly mean of December 2007 (left) and January 2008 (right).	166

4-13	Vertical profile of experiment WAP_BGC simulated NPP anomaly from the climatology, MLD and particle export across line 600 of the Palmer-LTER grid for the monthly mean of November 2005 (left) and December 2005 (right).	166
4-14	Climatological surface DIC (left), Alkalinity (middle) and air-sea CO ₂ flux (right) calculated for WAP_BGC results from 1991 to 2014 for November (top), December (middle) and January (bottom).	167
4-15	Correlation coefficient (left) and bias (right) between experiment WAP_BGC results and Palmer-LTER cruise data for surface DIC and surface alkalinity, for all stations of the Palmer-LTER grid (top), Lines 400-600 (middle) and Lines 200 and 300 (bottom). Points marked with a star indicate where correlation was significant at a 0.05 level.	168
4-16	Data for Line 200 of the LTER grid; A – Surface DIC from experiment WAP_BGC at the points sampled during Palmer-LTER cruises; B – Surface DIC from Palmer-LTER cruises; C – Anomalies from the average surface DIC during the months of Palmer-LTER cruises, calculated for each station from experiment WAP_BGC output; D – Anomalies from the average surface DIC during Palmer-LTER cruises, calculated for each station from Palmer-LTER cruise data.	168
4-17	Data for Line 600 of the LTER grid; A – Surface DIC from experiment WAP_BGC at the points sampled during Palmer-LTER cruises; B – Surface DIC from Palmer-LTER cruises; C – Anomalies from the average surface DIC during the months of Palmer-LTER cruises, calculated for each station from experiment WAP_BGC output; D – Anomalies from the average surface DIC during Palmer-LTER cruises, calculated for each station from Palmer-LTER cruise data.	169

4-18	Data for Line 200 of the LTER grid; A – Surface Alkalinity from experiment WAP_BGC at the points sampled during Palmer-LTER cruises; B – Surface Alkalinity from Palmer-LTER cruises; C – Anomalies from the average surface Alkalinity during the months of Palmer-LTER cruises, calculated for each station from experiment WAP_BGC output; D – Anomalies from the average surface Alkalinity during Palmer-LTER cruises, calculated for each station from Palmer-LTER cruise data.	170
4-19	Data for Line 600 of the LTER grid; A – Surface Alkalinity from experiment WAP_BGC at the points sampled during Palmer-LTER cruises; B – Surface Alkalinity from Palmer-LTER cruises; C – Anomalies from the average surface Alkalinity during the months of Palmer-LTER cruises, calculated for each station from experiment WAP_BGC output; D – Anomalies from the average surface Alkalinity during Palmer-LTER cruises, calculated for each station from Palmer-LTER cruise data.	171
4-20	Vertical profile of DIC sampled at Palmer-LTER cruise LMG-0101 (top) and experiment WAP_BGC monthly mean for January 2001 (bottom), for line 600 (left) and line 200 (right) of the Palmer-LTER cruise.	171
4-21	Climatological monthly mean air-sea CO ₂ flux from WAP_BGC experiment output, for January (left) and August (right).	172
4-22	All data from WAP_BGC results. On black box: total annual air-sea flux of CO ₂ from 1991 to 2014. Anomaly from the climatological yearly air-sea CO ₂ flux calculated for the period between August 2001 and July 2002 (A) and August 2005 to July 2006 (D); anomaly from climatological yearly NPP (calculated from 1991 to 2014) for the 2001-2002 period (B) and the 2005-2006 period (E); Anomaly from yearly mean surface salinity (calculated between 1991-2014) for the 2001-2002 period (C) and for the 2005-2006 period (F).	172

List of Tables

2.1	Temperature and salinity limits used to define the water masses analyzed.	59
A.1	Tracers included in the biogeochemical model REcoMv2	180
A.2	Parameters changed during sensitivity analysis experiments	181
A.3	Parameters changed during sensitivity analysis experiments	182
A.4	Cruises sampled by the Palmer-LTER Project	183

Chapter 1

Introduction

The coastal ocean along the western side of the West Antarctic Peninsula (WAP) has experienced substantial physical changes over the past several decades. During the second half of the 20th century, this region showed the highest atmospheric warming rates of the Southern Hemisphere [92], accompanied by a shorter sea ice season [77], and retreat of 80% of the glaciers in the region [11]. In the ocean, the WAP presented a summer near surface warming of more than 1°C during the same period [56]. The increased surface ocean temperature is believed to be caused by the atmospheric warming and early sea ice retreat, and could lead to a positive feedback that would further increase the atmospheric temperature. Over the past two decades, however, the atmospheric warming trend has leveled out or even reversed direction [90], indicating that the changes in the WAP are influenced by climate variability as well and cannot be fully explained by global warming.

Among the phenomena that are thought to influence the physics in the WAP are the stratospheric ozone hole and modes of climate variability like the Southern Annular Mode (SAM) and the El Niño Southern Oscillation (ENSO). During positive SAM phases, there is an increase in warm, northerly winds in the WAP, leading to decreased sea ice. Warmer conditions and less sea ice in the WAP are also observed during La Niña events, along with more intrusions of Upper Circumpolar Deep Water (UCDW), a relatively warm and nutrient-rich water mass derived from the Antarctic Circumpolar Current (ACC). The variability of the physical environment will in turn

affect the ecosystem in the WAP up to higher trophic levels, with a documented poleward shift of ice-dependent species and their replacement by ice avoiding species [17][72]. Much of the current understanding about WAP ecosystem responses to climate change and variability is based on the Palmer Long Term Ecological Research (LTER) program. The Palmer LTER program started in 1991 and has been collecting a range of physical, biological and chemical data along the WAP since. The project includes semi-weekly sampling from Palmer Station from October to March and a cruise that happens every year during the austral summer.

Primary production (PP) in the WAP is strongly influenced by sea ice, which controls the stability of the surface water column through changes in the meltwater, brine rejection, wind mixing and access of phytoplankton to photosynthetically available radiation (PAR). Other sources of freshwater are also thought to influence PP, particularly glacial meltwater. Glacial sources are thought to be the main source of dissolved iron to the WAP [2][3] and to drive the observed onshore-offshore gradient in the phytoplankton bloom, characterized by much higher production rates in the coastal areas. PP in the WAP, however, has decreased by about 12% over the past decades [65], although this decrease is not constant throughout the region. In the northern WAP strong winds and less sea ice lead to a deeper surface mixed layer, which combined with an increase in the number of cloudy days has led to a decrease in PAR and therefore in PP as well. In the south, however, areas that were previously covered by sea ice are more exposed and primary production is thought to be increasing.

Besides influencing the composition and abundance of upper trophic levels, changes in PP can also affect the potential of the region to act as a sink of atmospheric carbon. The Antarctic coastal shelves are thought to be an important sink of carbon [4], and surface inorganic carbon in the WAP is strongly influenced by PP [21]. Other factors that control surface inorganic carbon at the WAP include respiration, freshwater inputs, brine rejection and mixing with dissolved inorganic carbon (DIC)-rich subsurface waters [21][9]. All these factors contribute to the highly variable distribution of DIC and partial pressure of CO_2 (p_{CO_2}) throughout the WAP.

The fate of the carbon incorporated by PP, however, is not completely understood in the WAP. The composition of the WAP ecosystem, with important contribution of mesozooplankton grazers such as krill and salps, would suggest it is an efficient carbon pump. However, data collected at Palmer station during the phytoplankton growth season and from LTER cruises during the austral summer suggest a persistent and large imbalance between net community production (NCP) and particle sinking to the deep ocean [79][19]. Although an imbalance between NCP and particle export is not unexpected given that assimilated organic matter can be remineralized or transported to a different region, the magnitude of this imbalance at the WAP suggests other mechanisms are at play. It is currently thought that mixing can have a large role in transporting suspended particles downward [80], which could affect the depth at which organic matter is remineralized and therefore how much carbon will be exported to the deep ocean.

Understanding the mechanisms behind the changes in the biogeochemistry of the WAP is a substantial challenge. The physics in the region is influenced by a complex interplay between modes of climate variability and by global warming, and is further complicated by the fact that the ocean, the atmosphere and sea ice respond to these forcings at different time scales. The changes in the chemistry and ecosystem of the WAP, however, depend on the sum of all of these responses. Monitoring the changes in the WAP and deciphering the causes behind them could help predicting the ways in which the WAP ecosystem is expected to change and the ways in which the WAP could influence the global carbon cycle.

Although the WAP has been sampled more frequently than other Antarctic regions, there are still important spatial and temporal gaps in the datasets. In addition to being geographically remote, data collection in the WAP is made difficult by the harsh climate, so that most of the data available have been collected during the summer. Modeling studies, therefore, are important to test hypotheses that have been generated by analyzing the available datasets, to inform future data collection and to generate new hypotheses on the mechanisms at play at the WAP during the cold months.

The goal of this thesis, therefore, is to implement an ocean circulation, sea ice and biogeochemistry model for the WAP to study the mechanisms that influence primary production and the carbon cycle in the region. In order to properly simulate the biogeochemistry of the WAP, it is important to properly represent the regional ocean circulation, sea ice and surface ocean mixed layer. For that reason, chapter 2 is focused on the implementation of a regional version of the MITgcm (MIT General Circulation Model) that properly represents the variability of the circulation and sea ice in the WAP. The grid and forcing files are similar to those used in [69], and modifications were made to improve the depth of the surface mixed layer and the representation of the sea ice interannual variability in the model relative to available field and remote sensing observations.

Chapter 3 of this thesis is aimed at implementing a biogeochemistry model on top of the physical circulation model, and at performing sensitivity analyses to properly simulate the phytoplankton seasonal cycles and interannual variability. For that purpose, initial and boundary conditions were built for the biogeochemical tracers, and a suite of about two dozen sensitivity experiments was conducted to find an appropriate set of parameters for the biogeochemical model, as well to understand the mechanisms that improve the model performance. In chapter 4 the experiment that best represented the observed chlorophyll seasonality and variability was investigated further to address the potential of the model to simulate air-sea CO₂ fluxes, net primary production, and particle export at the WAP. In all of the chapters, model output was compared to physical, biological and chemical data collected during the Palmer-LTER cruises, as well as data from Palmer Station and from the Rothera Time Series (RaTS).

Chapter 2

Implementation of a circulation and sea ice model for the West Antarctic Peninsula

2.1 Introduction

During the second half of the 20th century, west Antarctic Peninsula (WAP) winter air temperatures have shown a warming of $3.7 \pm 1.6^\circ\text{C}/\text{century}$, the highest warming rate in the Southern Hemisphere and up to 4.8 times the global average rate [92]. Also, on a study conducted with satellite data from the period between 1979 and 2004, [77] concluded that during this period sea ice retreated 31 ± 10 days earlier and advanced 54 ± 9 days later in the Antarctic Peninsula. It was also noted by [11] that 80% of the glaciers on the Antarctic Peninsula retreated during the 20th century at accelerating rates, and that deglaciation in the WAP contributes as much to sea level rise as all Alaskan glaciers combined. In the ocean around the WAP, summer near surface temperatures rose more than 1°C in the same period, with a strong salinification of the surface ocean due to changes in the sea ice [56]. The authors argue that atmospheric warming and early sea ice retreat lead to increased ocean surface temperature, which in turn could enhance the trend towards higher temperatures in the atmosphere.

Since the late 1990s, however, the atmospheric temperature trend in the Antarctic Peninsula has reversed and a statistically significant cooling has been observed [90], with the decrease in temperature being more marked during the summer.

This reversal in the atmospheric trend is a signal that the changes in the WAP are affected by a suite of phenomena of different time scales, like the stratospheric ozone hole and the strength, temporal trends and spatial patterns of climate variability modes like the Southern Annular Mode (SAM) and the El Niño Southern Oscillation (ENSO).

The plethora of phenomena influencing the WAP makes the understanding of the variability in climate and biogeochemistry in the area a challenge, since not only the forcings of climate variability span a wide range of temporal and spatial time scales, but the response of the atmosphere, the ice and the ocean also work at different scales. The ocean circulation has a slow response to atmospheric temperature changes (although the mixed layer responds faster), while sea ice has a faster response to the atmosphere due to the influence of wind in sea-ice transport, which has seasonal and sometimes even synoptic time scales. The response of the physics in this area has substantial consequences also for the chemistry and ecosystem of the region through changes on the circulation and stability of the ocean mixed layer.

To better understand the ways in which the region responds to the different drivers of variability the use of hindcast modeling studies is very useful given that although the area is well sampled by Antarctic standards, there are still constraints in data collection due to the harsh climate. Also, it has been suggested by different studies [28][31] that an assessment of the fate of carbon and future predictions for ocean acidification and ecosystem changes in the WAP should include modeling studies that can properly simulate the seasonal and interannual variability currently observed.

In this chapter, I will describe the implementation of a sea ice and circulation numerical model used to simulate the physics of the WAP. The model as implemented is coupled to a biogeochemistry model aimed at studying the timing of the phytoplankton bloom and the carbon cycle in the region (Chapters 3 and 4), and therefore adjustments are required to properly simulate the physical variables that are impor-

tant to the biogeochemistry. More specifically, the adjustments to the model were made so that the simulated sea ice variability was consistent with satellite data and the simulated mixed layer depth (MLD) was comparable to the data collected during the Palmer-LTER cruises. This chapter, therefore, includes a description of the model as well as of the adjustments made, and the results of a detailed skill assessment of the model results, performed using satellite data, Palmer-LTER data and data from the Rothera Time-Series (RaTS) collected in Marguerite Bay.

2.2 Literature Review

2.2.1 Teleconnections - ENSO and SAM

The Southern Annular Mode (SAM) is characterized by latitudinal differences in atmospheric pressure between Antarctica and mid latitudes. During the positive phase of SAM, the sea level pressure anomaly is positive in the southern hemisphere mid latitudes and negative in Antarctica, with the opposite happening during the negative phase [86]. Also, during positive SAM years, there is a negative atmospheric pressure anomaly in the high latitudes of the Southeast Pacific Ocean that creates a cyclonic flow and intensifies the action of warm, northerly winds in the WAP, decreasing sea ice [77].

El Niño Southern Oscillation (ENSO) is defined by the switching of sea level pressure anomaly between the Indian Ocean/ Australian region and the Southeastern Tropical Pacific Ocean. Although ENSO is a tropical climate oscillation, it impacts the whole globe through atmospheric teleconnections. In the high southern latitudes, its most significant impacts are found in the South Pacific off the coast of the Antarctic Peninsula [88]. During La Niña events, the polar front jet is strengthened, which leads to more storms and warmer conditions and less sea ice in the Southern Bellingshausen and western Weddell Sea [77], therefore affecting the WAP, which is located between them. It was also noted by [52] that during La Niña years there is more intrusion of Circumpolar Deep Water (CDW) onto the WAP continental shelf, a water mass

derived from the Antarctic Circumpolar Current (ACC), that brings nutrient-rich, warmer waters.

[22] have found that the association of negative SAM and El Niño and positive SAM and La Niña occur more often than expected by chance, and they tend to have similar and intensified effects when they occur together. The result is that during negative SAM and El Niño years there is an increase in sea ice in the WAP due to the influence of southerly winds, and during positive SAM and La Niña years, there is a decrease in sea ice due to the action of warm northerly winds [77]. The combination of positive SAM and El Niño or negative SAM and La Niña, however, tends to dampen the effect of these modes on the WAP.

The increase in atmospheric temperature in the WAP during the second half of the twentieth century has been associated with a trend towards positive SAM since the 1980s [77]. The atmospheric cooling in the WAP since the late 1990s, on the other hand, has been associated with more cyclonic conditions in the north Weddell Sea (which in turn is associated with a strengthening of the mid-latitude jet), which leads to easterly to southeasterly cold winds blowing over the WAP.

The biogeochemistry of the WAP is linked to climate variability because the extent, thickness and seasonality of sea ice has a direct impact on the ecosystem and on the supply of nutrients to the region. During colder years with higher sea ice concentrations, a shorter and simpler food web is observed, with prevalence diatoms representing the dominant phytoplankton group and a high concentration of krill [71]. In warmer years with less sea ice, however, the food chain is more complex, with increased concentration of salps and a longer food web based on microbial food webs [24]. [85] argues that the marginal ice zones (MIZs) can be productive areas, given that the sea ice can act as a buffer for wind mixing, while sea ice melt increases the vertical stability of the water column, increasing light availability to phytoplankton. Indeed, [20] find that in the WAP the net community production (NCP) is low when the mixed layer depth (MLD) exceeds 40 meters.

2.2.2 Circulation and water masses

The WAP continental shelf is relatively wide (around 130 km), deep (400 m) and is characterized by a complex bathymetry that includes plateaus and deep depressions, which influence the circulation and mixing of water masses [63]. A map with key locations described during this thesis is shown on Figure 2-1. On a large scale, a northward flow along the shelf break that represents the southern boundary of the Antarctic Circumpolar Current (ACC), and a southward flowing branch along the inner shelf characterize the circulation in the WAP [32][52]. [63] describe a southward flowing geostrophic current along the coast, named Antarctic Peninsula Coastal Current (APCC) that is formed during the ice-free season, when the water is fresher near the coast, and extends from Adelaide Island to Alexander Island. It is characterized by a strong cross-shelf gradient with vertical scale of 100 to 150 m and horizontal cross-shelf scale of 20 km, and along-shore velocities of about 0.3 m/s [64]. The APCC is a possible mechanism to transport nutrients and plankton to the southernmost parts of the WAP, and its dependence on the freshwater fluxes to form during the warmer months indicate that its strength and duration could be altered with changing freshwater fluxes and sea ice cycles.

[63] could not trace the path of the APCC inside of Marguerite Bay, where different sources of freshwater could alter its path. [52], analyzing dynamic topography data, describe a double gyre structure on the shelf, with a southern cyclone on the outer shelf and an anticyclone present near or over Marguerite Bay. This structure is accompanied by an offshore anticyclone, more developed in years of moderate to strong El Niño while the Southern cyclone is more apparent in years of positive SAM and La Niña. Other studies, however, suggest that the circulation in Marguerite Bay is composed of a cyclonic circulation cell [5][40].

The Circumpolar Deep Water (CDW), which is a subsurface water mass derived from the ACC, intrudes onto the shelf sporadically, bringing warm and nutrient rich water that plays an important role in phytoplankton growth. The CDW is present at the edge of the WAP at depths around 200 to 600 m [40] and the intrusions are

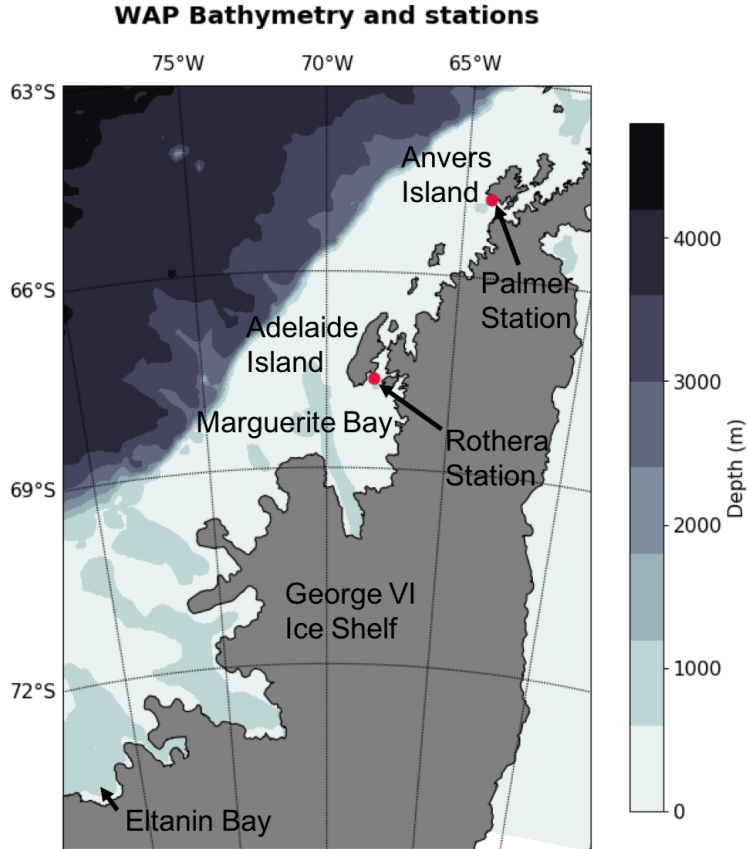


Figure 2-1: WAP map with locations of interest.

seen as a bulge of warmer water moving towards the coast, usually seen around line 300 of the Palmer LTER grid (around Adelaide Island, figure 2-1) but also common further north around line 500 [52]. Bathymetric features such as troughs that cut across the shelf (such as the Marguerite Trough) are important pathways for CDW to move towards the coast, but recent studies also reveal the importance of small eddies, with horizontal scales of around 5 km, to deliver CDW to the coastal areas [64].

The CDW is modified as the intrusions progress across the shelf, cooling linearly with distance towards the coast, and being characterized by temperatures above 1°C and salinities higher than 34.64 [40]. Above the CDW or its modified version (mCDW), there is the Antarctic Surface Water (AASW), which is formed by a relatively deep mixed layer during the winter, but is stratified during the summer. The stratification during the warmer months happens because of increasing heat input through solar insolation during the sea ice-free period, and dilution during the melt

of sea ice, which leads to fresher waters. AASW is characterized by temperatures ranging from -1.8°C to 1°C and salinities between 33 and 33.7 [63], the large spread being due to temporal changes in the surface waters.

As the near surface waters stratify, remnants of the winter mixed layer are trapped between the AASW and the mCDW, represented by a cold layer of water (temperature below -1°C) located between 80-100 meters deep called Winter Water (WW; [63]). The presence of the WW is attenuated near the coast, where the temperature minima are higher and surface salinity tends to be lower (typically below 33.25).

2.3 Methods

2.3.1 Model Description

The model used to study the WAP is the Massachusetts Institute of Technology General Circulation Model (MITgcm). The MITgcm resolves Boussinesq Navier-Stokes equations on an Arakawa-C grid and z-level (fixed depth) vertical layers with higher resolution for the near-surface levels [51]. The ice component is described in [49] and uses elastic-viscous-plastic (EVP) rheology. Although the MITgcm has successfully been used by multiple studies to reproduce the circulation, ice dynamics and biogeochemistry of the Southern Ocean [34][85][28], these studies have used horizontal resolutions on the order of a degree of latitude and longitude in circumpolar studies, and much can be learned by using a higher resolution regional model adapted to the WAP.

Grid

The grid used for this study is the same that was implemented in [69], ranging from a southwestern most point located at 74.7°S , -95°W and a northeastern most point at -55°S , -55.6°W and including the Bellingshausen Sea, the full extension of the WAP and the Drake Passage (Figure 2-2). The model domain was chosen to include the ice shelves at the South of the Bellingshausen Sea and the tip of Chile, so that the

general circulation would be well represented and the ACC would be able to influence shelf break processes.

The grid is curvilinear with 0.2 degrees of resolution for latitude and resolution varying between 0.0538 and 0.1147 degrees for longitude, which represents cells ranging from 5.98 km in the south of the domain to 12.75 km in the north of the domain. Vertically, a depth-based coordinate is used (z-levels; [49]), with partial cells used to resolve sub-grid cell steps. In the first 100 meters, the vertical levels are 10 meters apart, and the vertical resolution gets coarser with depth.

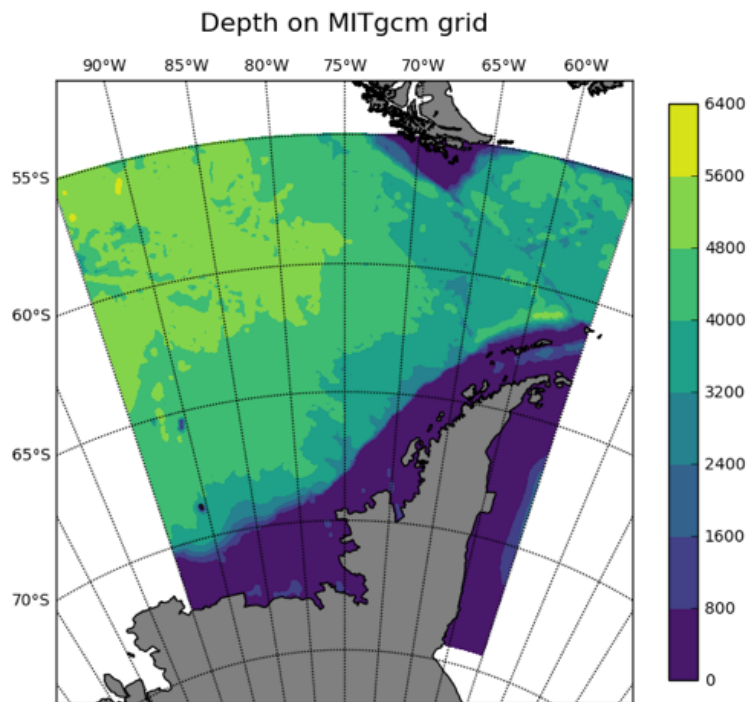


Figure 2-2: Model grid.

Initial and Boundary Conditions and Surface Forcing

The Initial conditions for temperature and salinity were obtained from the World Ocean Atlas (WOA) reanalysis [7]. Since data collection in the area is scarce, parts of the data had to be interpolated, generating spurious values under George VI Ice Shelf that are, however, quickly lost during model spin-up. The boundary conditions are composed of model monthly means for the period between 1990-1999, derived from

the results of [34]. Sea ice velocities are not prescribed at the boundaries to avoid spurious ice convergence if sea ice is exiting the domain.

The atmospheric variables that need to be prescribed for surface forcing include atmospheric temperature at 2 meters, precipitation, zonal and meridional wind velocity at 20 meters, specific humidity at 2 meters and short and long wave radiation. These were obtained from the ERA-Interim reanalysis [13], provided by the European Center for Medium-Range Weather Forecasts (ECMWF), and force the upper layer of the model with a horizontal resolution of 1.5° and at 6-hour intervals.

The bathymetry used comes from the BEDMAP2 dataset [23], but is complemented with data from the General Bathymetric Chart of the Oceans (GEBCO) north of 60°S , which is the northern most latitude on BEDMAP2.

The model domain has three open boundaries (north, east and west), which need to be prescribed for temperature, salinity, current velocity, and sea ice concentration, thickness and velocity. The data for the boundaries were obtained from a circumpolar version of the MITgcm, with 0.25° horizontal resolution that extends from Antarctica to 30°S and is described in [34]. To interpolate between the two grids, the nearest point between each grid cell was found and the data were interpolated linearly using monthly means calculated for the lower-resolution circumpolar grid between 1990 and 1999. Some adjustments were needed at the boundaries to avoid convergence and further thickening of sea ice, and fluctuations of sea level height due to imbalances caused by sea-level height fluctuations.

The setup of the MITgcm used for this study was originally used to study freshwater distribution in the Bellingshausen Sea, therefore the freshwater inputs were carefully chosen to be as realistic as possible, given the constraints imposed by lack of data. A general surface runoff input was built that represents surface melt of land-based ice, oceanic melting of ice cliffs and iceberg calving and melting. Also, since the data on iceberg melt is scarce, assumptions were made to provide values for this source. The values chosen represent the amount calculated by [91], distributed uniformly around the coast and linearly decreasing with distance from land until 100 km. Including appropriate freshwater forcing is important given that density at this

region is mainly controlled by salinity. In the study of [69] using this model grid, it was observed that sea ice dominates the seasonal changes in the freshwater, but that the annual-mean contribution of the different sources was comparable.

Although the freshwater input to the model was setup to be as realistic as possible, it is important to note that ideally freshwater input would have a vertical component and be distributed with depth, while in the model the runoff is added to the surface. Adding a vertical distribution to the freshwater runoff would require adapting the model code and making extra assumptions regarding the amount of freshwater to be added to each depth, therefore the runoff was kept at the surface. However, it is important to keep in mind that adding the freshwater to the surface could lead to a more stable mixed layer, given that water with lower density is added to the surface. The depth at which freshwater is added could also impact the distribution of nutrients, particularly iron, and change the depth at which chlorophyll maxima occur.

2.3.2 Data used for skill assessment

Considering that the WAP is inadequately sampled during much of the year due to limited ship accessibility, information on the circulation and freshwater content found in the literature was used as comparison. Data collected from the Palmer-LTER project, Rothera Time Series (RaTS) and sea ice satellite data were also used.

The Palmer-LTER project started in 1991 and has been collecting a range of physical, biological and chemical data along the WAP since. The data collected by the Palmer project include semiweekly small-boat water-column sampling from Palmer Station (64.77°S, 64.05°W) from October through March each year and an annual cruise each January-February since 1993. The cruise sampling grid spans 500 km along the coast and 250 km across the shelf. Along shelf transects are spaced every 100 km, and the stations are separated by 20 km as shown in figure 2-3. All the data collected are available through the project web page (<http://pal.lter.edu/data/>).

Rothera Time-Series (RaTS) is a data set maintained by the British Antarctic Survey (BAS) of quasi-weekly data collected close to the Rothera Research Station,

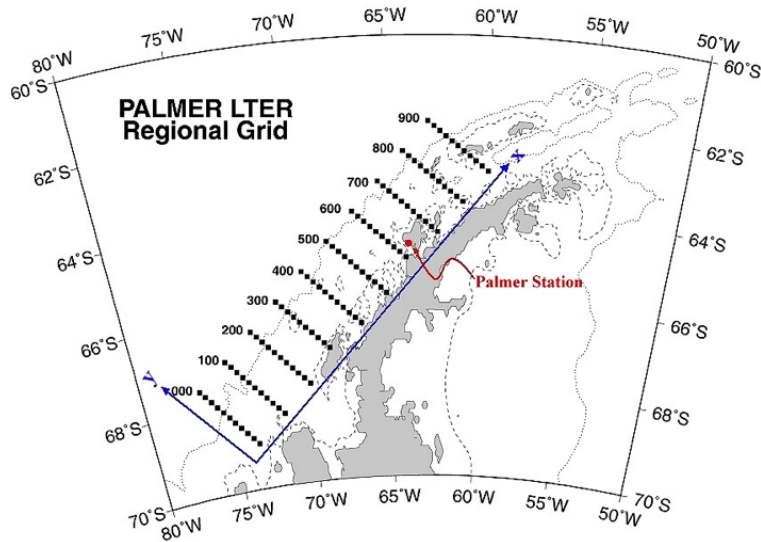


Figure 2-3: Map of the WAP showing the location of the Palmer-LTER stations.

located on the eastern side of Adelaide Island to the north of Marguerite Bay. The data collection started in 1997 and includes valuable winter data. The measurements are made from a rigid inflatable boat or through a hole cut in the ice, and include full depth (500 m) Conductivity-Temperature-Depth (CTD) profiles, fluorescence, photosynthetically available radiation (PAR) and discrete depth bottle data (at 15 m depth) for measuring chlorophyll concentrations, nutrients, dissolved organic carbon (DOC) and oxygen isotopes.

The satellite sea-ice data used were previously generated from brightness temperature data derived from the Special Sensor Microwave/Imagers (SSM/Is), provided as either monthly means or 8-day means, with horizontal resolution of 0.2 degrees of latitude and longitude. Although the technology to retrieve ice thickness information from radar altimeters exists, the data available for Antarctica are limited in temporal coverage; therefore, the assessment of the ice thickness relied on using the same ice configuration as [34], which was validated within the constraints of the limited data available.

2.3.3 Experiments

Drivers of Mixed Layer Depth (MLD)

To test the skill of the model in reproducing the water-column characteristics and the variability necessary to properly study the biogeochemical phenomena at the WAP, the physical setup described above (and described with more detail in [69]) was integrated for 20 years, from 1984 until 2003, and data were analyzed from 1991 (beginning of data collection for the Palmer-LTER project) onwards. The years between 1984 and 1990 were considered spin-up and therefore not used in any of the analyses. The final experiments in this chapter are run for 31 years, ending in 2014. The initial tests, however, were run for only 20 years, given this is enough to evaluate the skill of the model in reproducing seasonal and interannual variations with less cost in computer time.

Monthly mean output were saved for a set of physical and biogeochemical diagnostics, and compared to data from the Palmer-LTER project. The first test performed consisted of comparing the mean temperature and salinity of the model output for the month of January (from 1991-2003), in which most of the Palmer-LTER data was collected, to the mean temperature and salinity from the Palmer-LTER cruises, collected between January and February each year. The LTER dataset was compared to the MITgcm output by finding, in the model grid, the points closest to the station data, and comparing the vertical profile for each Palmer-LTER grid lines between 200 and 600.

An initial analysis shows that, throughout the whole grid, MLD is shallower in the model than in the Palmer-LTER data, with simulated data also exhibiting lower salinity close to the surface as exemplified in figure 2-4 for Line 400. Properly simulating the MLD is important for the scope of this project, since the variations in the surface layer mixing is essential for the onset and intensity of phytoplankton bloom, and therefore to the simulation of the ecosystem and export of organic matter to the deep. Also, a shallower ML can curb air-sea CO₂ exchange, since shallower mixing can mean less access of dissolved inorganic carbon (DIC)-rich deeper waters to the

surface.

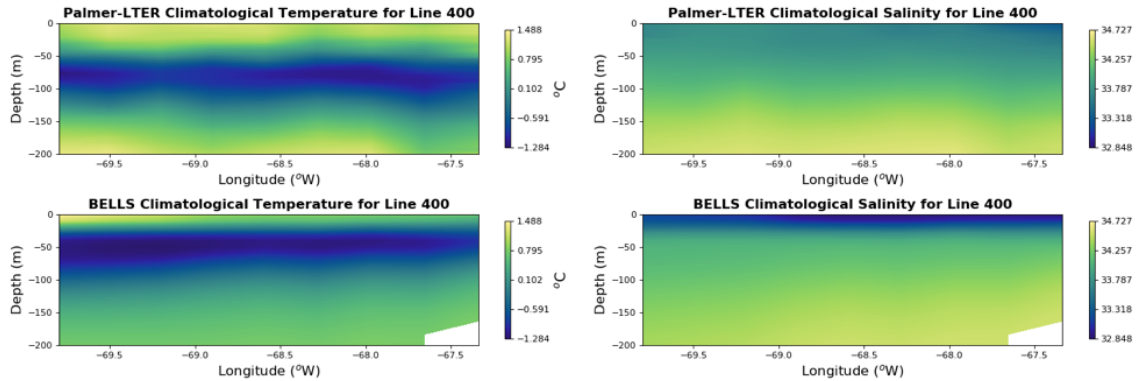


Figure 2-4: Mean temperature during the Palmer-LTER cruises (top left) and January average calculated for the MITgcm output (bottom left), mean salinity during the Palmer-LTER cruises (top right) and January means for the MITgcm output (bottom right) for Line 400 of the Palmer-LTER grid.

In this study, a few hypotheses were suggested as the cause for the shallow simulated MLD: there could be 1) adjustments needed to the parameterization of the vertical mixing in the model; 2) adjustments to the amount of freshwater discharge in the model; or 3) inaccuracies in the sea ice formation and melt that could lead to more ice being melted in certain areas. Since at this temperature range salinity is the main driver of density changes, a higher discharge of freshwater at a certain location would cause stronger stratification.

Two of the possible reasons for the shallow ML involve the freshwater input into the region. Identifying the source of this freshwater, whether it consists of meteoric water or sea ice melt, is important given that different sources have different concentrations of biogeochemical variables, such as micronutrients, that can influence the biogeochemistry and ecology in the WAP [60]. [59], using oxygen isotopes, identified a high concentration of meteoric water close to the coast in the WAP, due to orographic precipitation and glacial discharge. The low salinity close to the coast is responsible for an onshore-offshore density gradient that highly influences the southward flowing geostrophic currents observed by [63]. Sea ice melt water, on the other hand, was observed in lower concentrations, with patchier distribution and net sea-ice formation in the north of the domain and net sea-ice melt towards the south [57]. In [69], how-

ever, model results suggest that in the Bellingshausen Sea sea ice melting dominates the freshwater cycle.

Both meteoric and sea ice melt water respond to climate variability, with their concentrations being highly influenced by wind patterns [60]. The standard simulation for the Bellingshausen Sea was called BELLS, and the next paragraphs describe the initial tests performed to assess the main drivers of the shallow ML, as well as the reasoning behind them.

RUNOFF05 To test the influence of the prescribed freshwater flux on the model mixed layer, a sensitivity test was integrated with the surface runoff being multiplied by 0.5. Although [69] presented sensitivity analyses with different freshwater concentrations and distributions, the authors were focused in understanding the large-scale budget of freshwater, for which summer variations in MLD are less of a concern. This test, therefore, is aimed at investigating the effects of local changes in the runoff flux in the summer MLD.

ICEdrag To adjust the formation of polynyas around Eltanin Bay (south of the Palmer-LTER grid) and the freshwater fluxes around GeorgeVI Ice Shelf, [69] decreased the air-sea-ice drag coefficient in the model from its default value of 2×10^{-3} . The movement of sea ice is mostly controlled by winds instead of ocean currents, and lowering the drag coefficient would also lower the impact of the winds on transporting sea ice to different regions, hence curbing the formation of polynyas. For the Palmer-LTER grid region, it could also mean that sea ice could be melting locally instead of being transported, decreasing the surface salinity in melt areas. For this test, then, the air-sea ice drag coefficient was increased from 5×10^{-4} , which was the value used during the BELLS integration, to 2×10^{-3} , which is the standard value proposed for the MITgcm. A drag coefficient of 2×10^{-3} , although being the standard value used for MITgcm simulations, is higher than the optimal found by [61] during sensitivity analyses performed for the Arctic region.

Ricr A third test aimed at investigating whether the cause for a shallow ML is the parameterization of vertical mixing in the ocean. The vertical mixing scheme chosen is the K-profile parameterization, or KPP, which unifies the treatment of a variety of unresolved processes involved in vertical mixing (Large et al, 1994). In this scheme, mixing in the ocean interior below the surface layer is governed by shear instability, which is a function of the gradient Richardson number, and internal wave activity. Double diffusion processes are not implemented in the MITgcm version of KPP. The depth of the surface boundary layer is based on a critical value for turbulent processes, parameterized by a bulk Richardson number, and calculated for each grid point.

The Richardson number is a dimensionless number that measures the relative importance of mechanical and buoyancy effects in the water column. The bulk Richardson number is defined as:

$$Ri_B = \frac{gh\Delta\rho}{\rho_0(|\Delta u|)^2} \quad (2.1)$$

where $\Delta\rho$ is the density contrast over depth interval h , Δu is the velocity contrast between vertical layers, ρ_0 is the reference density, g is the gravity acceleration and h is depth. In the model, Ri_B is calculated by computing the velocity and buoyancy differences between a given depth and the surface reference. Mixing occurs in the boundary layer, which extends to the depth at which Ri_B exceeds a critical number, called critical Richardson number or Ri_{cr} . Therefore, increasing Ri_{cr} could mean increasing the depth in which mixing occurs. For the Ricr test, Ri_{cr} was increased from the default value of 0.3 (value used for the BELLS run) to 0.9. Although the value of 0.9 was chosen arbitrarily, it should provide an indication of the influence of the KPP parameterization on the MLD. Further tests were conducted with changes to the Richardson number based on recent parameterization schemes to include the effect of Langmuir circulation to the vertical mixing.

Adding Seasonal Runoff (SRunoff)

Given that the goals of [69] were focused on the overall yearly freshwater budget on the WAP, initially no seasonality was added to the freshwater input, which was provided as a single value in m/s (per grid cell point). In this experiment, in order to simulate the increased freshwater flux during the summer, the freshwater input was adjusted to have elevated values in the summer. Initially, the runoff was given in m/s, and the first step in making the seasonal runoff file was to multiply the input by the number of seconds per year to get the total runoff in one year. The total yearly value was then multiplied by a cosine scaling function, different for each month. The sum of the scaling coefficients at every month equals one, so that the total amount of runoff in one year is maintained. The scaling coefficients are shown on figure 2-5, and this experiment was named SRunoff. This test was integrated for 22 years, with the first 7 being considered spin-up (1984-1990), so that final 15 years were analyzed.

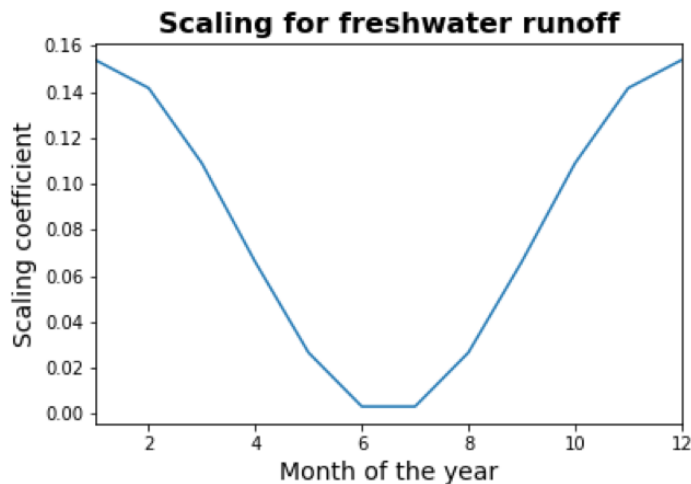


Figure 2-5: Scaling coefficients for the freshwater input flux.

Adding Langmuir Circulation

The previous tests determined that changes in the sea ice drag coefficient had a larger impact on the MLD than changes in the freshwater flux and in the Richardson number. However, a shallow bias still persisted (see below in the simulation). Recent research

suggests that the neglect of Langmuir circulation in most climate models could be partially responsible for the shallow mixed layer bias, especially in the Southern Ocean [6][12]. Langmuir circulation can be observed as a series of shallow, counter-rotating vortices in the surface ocean when wind reaches a certain speed. It is more closely aligned with the wind than Ekman’s theory of wind drift due to its shorter time scale, since it is generated within minutes and stops as soon as the wind does [83].

Langmuir turbulence also provides a mechanism for converting wave energy into turbulent energy, causing the mixed layer to deepen. Langmuir turbulence can be implemented in ocean circulation models by coupling wave models to predict an enhancement factor to be added to the turbulent velocity scale in the KPP parameterization, but coupling wave models is a time consuming and computationally expensive endeavor. Also, there are limited data available for validation of a wave model in the Southern Ocean, with no guarantee that the wave model would reproduce the dynamics of the region. To include Langmuir circulation to this model, therefore, two approaches were tested, based on the parameterizations proposed by [46](L17 from now on) and [45](LF17 from now on).

KPP_εsl The approach suggested by L17 represents Langmuir turbulence as an enhancement factor applied to the turbulent velocity scale used in KPP. The idea of an enhancement factor had already been presented by [54] by using:

$$\varepsilon = \sqrt{1 + 0.08 \times La_t^{-4}} \quad (2.2)$$

in which La_t is the turbulent Langmuir number, given by:

$$La_t = \sqrt{\frac{u^*}{u_0^s}} \quad (2.3)$$

where u^* is the friction velocity and u_0^s is the magnitude of the Stokes drift velocity. This formulation, however, introduced too much mixing in extra-tropical regions on simulations conducted with the CESM (Community Earth System Model). The excessive mixing could be a result of not including wind-wave misalignment. The

parameterization proposed by L17 uses a theoretical wave model developed by the authors, and approximates by using the Stokes drift profile, the boundary layer depth and the surface friction velocity. The two latter terms are available in the ocean model, and the Stokes drift profile depends on the high-frequency part of the wave spectrum, which is reasonably well described by empirical wave spectra. Then, by using the Phillips spectrum [67] and the directional spreading of wind waves of [96], an enhancement factor is proposed so that:

$$\varepsilon = f(u_{10}, u^*, h_{BL}) \quad (2.4)$$

where u_{10} is the wind velocity at 10 meters and h_{BL} is the boundary layer depth. This approach, however, does not take swell into consideration given that swell is remotely generated and dependent on the history of wind wave propagation, requiring the use of a prognostic wave model. This parameterization was tested in a simulation named `kpp_eps1`.

KPP_Ut The parameterization described by LF17 is based on the entrainment of dense water from below the surface ocean boundary layer directly, which controls the deepening properties of this layer and affects the exchange of heat and momentum between the atmosphere, surface ocean and deep ocean. Several large-scale eddy simulation studies indicate that the rate of entrainment (entrainment buoyancy flux, $\overline{w'b'_e}$) is enhanced in the presence of Langmuir turbulence. This would be possible because in the presence of Langmuir circulation more turbulent kinetic energy (TKE) is expected to be available near the base of the boundary layer for entraining denser water from below the mixed layer. Langmuir turbulence could also contribute to the erosion of the thermocline due to enhanced shear instability beneath downwelling regions of the Langmuir cells. Quantifying the Langmuir enhanced $\overline{w'b'_e}$ is challenging, however, due to its small magnitude in the TKE budget as a whole.

From the many factors that affect $\overline{w'b'_e}$, two are dominant: the destabilizing surface buoyancy flux, which controls $\overline{w'b'_e}$ in convective turbulent regimes, and the shear instability localized at the base of the boundary layer, usually associated with inertial

oscillations of the surface current. When both are present, a proportionality is usually assumed by introducing a new velocity scale. In LF17 a new velocity scale (U_t), based on the surface layer turbulent Langmuir number, is introduced to account for the effects of Langmuir turbulence:

$$U_t(z) = \frac{C_\nu N(z) w_s(z) |z| \left[\frac{-\overline{w'b'_e} h_b}{w_s(z)^3} \right]^{-1/2}}{Ri_c} = \frac{C_\nu N(z) w_s(z) |z| \left[\frac{0.15 w^{*3} + 0.17 u^{*3} (1 + 0.49 La_{SL}^{-2})}{w_s(z)^3} \right]^{-1/2}}{Ri_c} \quad (2.5)$$

where N is the local buoyancy frequency, w_s is the turbulent velocity scale, C_ν is a defined parameter based on buoyancy and La_{SL} is the surface layer turbulent Langmuir number. The Langmuir number is assumed to be reasonably estimated by the theoretical wave model proposed by L17.

KPP_LC Another experiment to test the influence of Langmuir circulation, named LC, combines the approaches of LF17 and L17, parameterizing therefore the effects of Langmuir turbulence on both the mixing within the boundary layer and the entrainment at the base.

Implementation of Langmuir Turbulence in the code

To implement the changes proposed in experiments KPP_epsl, KPP_Ut and KPP_LC, two scripts contained in the KPP package had to be modified: kpp_calc.F and kpp_routines.F. The script kpp_calc.F serves as an interface between MITgcm and the routine kppmix, where boundary layer depth, vertical viscosity, vertical diffusivity and counter gradient term are computed. Kpp_routines.F contains the subroutines associated with the KPP package that are necessary to compute the vertical mixing. Among these subroutines is BLDEPTH, which determines the oceanic planetary boundary layer depth, and was modified and renamed as BLDEPTHLF17 to include the modifications proposed by LF17.

The modifications on kpp_calc.F are the inclusion of EXF_FIELDS, which allows the KPP package to read the external forcings so that wind speed can be used, and

defining the variables `hbl_old` and `wspd10`. `Hbl_old` is a variable created to store the oceanic boundary layer (`hbl`) from the previous time-step, which will be used in the calculations involving Langmuir circulation. 10-meter wind speed is read from the external forcing package (`EXF`), and calculated as:

$$wspd10 = \sqrt{uwind^2 + vwind^2} \quad (2.6)$$

where `uwind` is the zonal component of the wind and `vwind` is the meridional component. Given the wind is taken directly from the external forcing package, however, a correction needs to be made to account for the influence of sea ice concentration in the Stokes drift. Therefore, a relationship between sea ice concentration and wind velocity was developed based on the study of [1], which uses data collected at several locations in the Arctic region during a year-long experiment to develop a bulk flux algorithm for prediction of surface fluxes of momentum and heat. [1] propose the following relationship between sea ice concentration (`SIC`) and drag coefficient of the friction between atmosphere and ocean at 10 m height (`Cd`):

$$10^3 Cd = 1.5 + 2.233 \times SIC - 2.333 \times SIC^2 \quad (2.7)$$

This equation, however, does not take into consideration the wind speed, and to develop an equation that could be used for the purposes of this study we assume that the quadratic dependence of the drag coefficient on `SIC` can be translated linearly to the dependence of Stokes drift on `SIC`. A quadratic coefficient of sea ice called `sicoef`, therefore, is introduced to modify the wind speed at 10 m. When plotting the equation from [1] (Figure 2-6), it is seen that the drag coefficient is enhanced when `SIC` is at intermediate concentrations. The theoretical explanation for this effect derives from the fact that every ice floe will have high pressure in the upwind face and low pressure on the downwind face. Essentially, these sea ice floes behave as sails to enhance the momentum transfer from winds to the ocean. Thus, as the number of floes increases, the momentum transfer will increase as well due to the larger frontal area coverage. However, if the floes become too packed they shelter

each other, decreasing the momentum transfer.

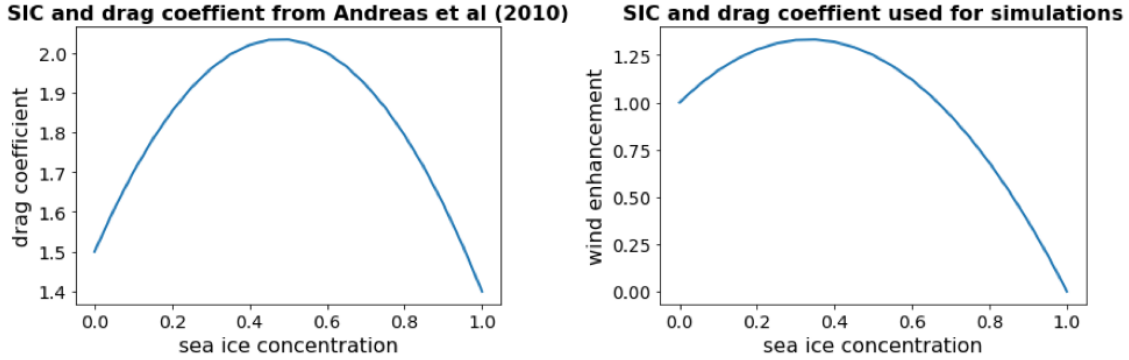


Figure 2-6: Relationship between wind-ice drag coefficient and SIC proposed by Andreas et al (2010, left) and relationship between wind enhancement coefficient and SIC developed for this study (right).

The coefficient to be multiplied by the wind speed in this study is of the form:

$$sicoef = 1 + 2 \times SIC - 3 \times SIC^2 \quad (2.8)$$

This relationship is plotted on Figure 2-6 and was developed so that *sicoef* is one in the absence of sea ice (no effect of SIC), zero when SIC=1 (no effect of wind speed and Langmuir circulation) and so that the peak is 1.35 at intermediate SIC, consistent with the maximum enhancement on the wind-ice drag coefficient proposed by [1].

The enhancement factor is calculated in `kpp_routines` using the wind speed and boundary layer from the previous time-step according to equation 25 of L17. The new velocity scale (U_t) is calculated according to equation 26 of LF17, also using the wind speed read by `kpp_calc.F`. For `KPP_eps1`, the velocity scale is multiplied by the calculated enhancement factor. For `KPP_Ut`, `vtsq`, which is the turbulent shear contribution to the bulk Richardson number, is multiplied by U_t (calculated by equation 26 of LF17), and for `Kpp_LC` both modifications are implemented.

2.4 Results

2.4.1 Drivers of MLD

The ICEdrag, RUNOFF05 and Ricr tests were integrated from 1984 until 1993. The decadal length of the simulation is enough to get past the spin-up period, have 3 years of run to be analyzed and at least one year (1993) that can be compared to Palmer-LTER CTD data. Therefore, the tests were not run for the whole period analyzed in the interest of time and to avoid spending computer time unnecessarily.

Salinity is used as the primary metric to assess the impact of the changes made to the model on the BELLS run, given that at the temperature range in this region salinity is the main driver of changes in density. For this analysis, some of the spin-up years were included to assess whether the changes found were cyclical or whether any trend would propagate and amplify with time. Therefore, the years between 1987 and 1993 were included in the analyses. The nearest points to the stations sampled during the Palmer-LTER cruises for lines 200, 300 and 500 were identified on the MITgcm grid, and the time-series of salinity at these points was plotted from the surface to 100 meters, which should include the ML.

The trends found between the runs were similar for all points analyzed, and the results shown in figure 2-7 for stations zero (onshore) and 200 (offshore) of Line 200. All the tests successfully simulated the shoaling and freshening of the ML during the summer months and presented similar interannual variability. The only visible change in salinity was found on the ICEdrag test, in which the surface salinity was higher and the freshwater less accentuated. The differences in salinity between the ICEdrag test and the BELLS run are more accentuated offshore, where the impact of freshwater discharge is attenuated.

The salinity difference between the BELLS run and the tests performed was also plotted for the same stations. The results are shown in figure 2-8 for station 200.000, but the same pattern was observed in all the stations analyzed. It is seen that the salinity difference between the BELLS run and RUNOFF05 was very small, indicating that even for the onshore stations changes in the freshwater input do not have a large

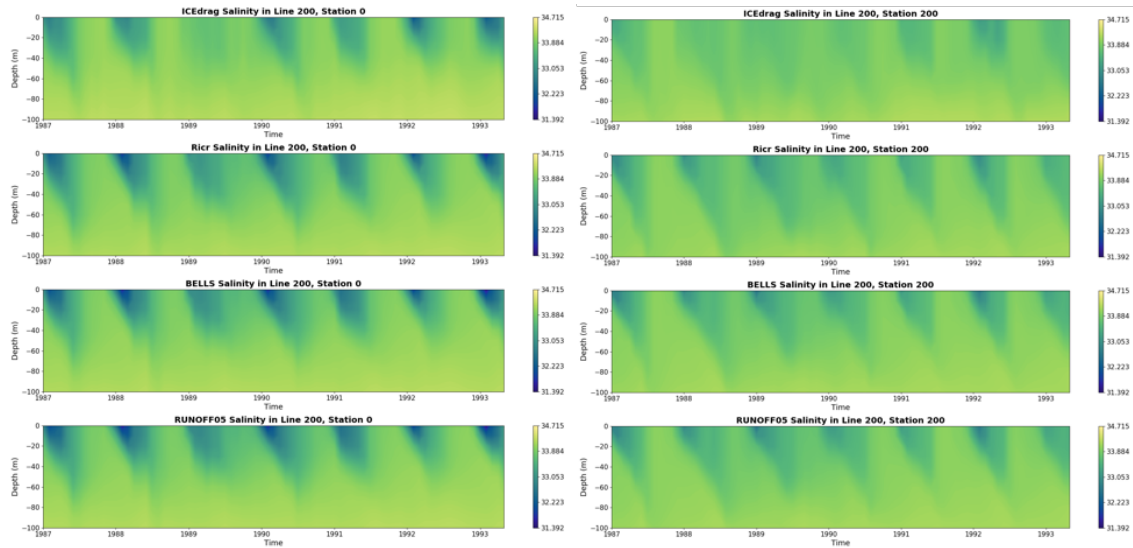


Figure 2-7: Time series of salinity for the MITgcm grid point closes to Station 200.000 (closest to the coast, left) and 200.200 (right) of the Palmer-LTER cruise grid for experiments ICEdrag, Ricr, BELLS and RUNOFF05.

influence on the MLD. The ICEdrag test, however, had salinity differences larger than 1.0 on the surface layer, suggesting that excessive sea ice melt in the Palmer region is a plausible explanation for the shallow ML. In the subsurface waters, between 60-80 m depth, the salinity difference is positive (higher in the BELLS run), indicating that more mixing happened due to decreased buoyancy of the surface layer, and the less saline surface waters were mixed deeper. Ricr had a similar profile to ICEdrag, but with smaller salinity differences when compared to BELLS, indicating increased mixing but with no change in the salt budget as expected. While the salinity difference on the surface layer surpassed 1.0 for the ICEdrag test, it was around 0.1 for Ricr. The subsurface differences for both ICEdrag and Ricr experiments, however, were around 0.2, indicating that both experiments deepened the ML.

The ICEdrag test, therefore, had the most success in increasing the surface salinity values and deepening the ML, with these effects being attributed to changes in the sea ice dynamics. The next step, then, was to assess whether increasing the air-ice drag coefficient had any negative effect in the extension and variability of sea ice. To properly assess the skill of the ICEdrag experiment in simulating sea ice interannual variability, it was integrated for the whole 20-year period.

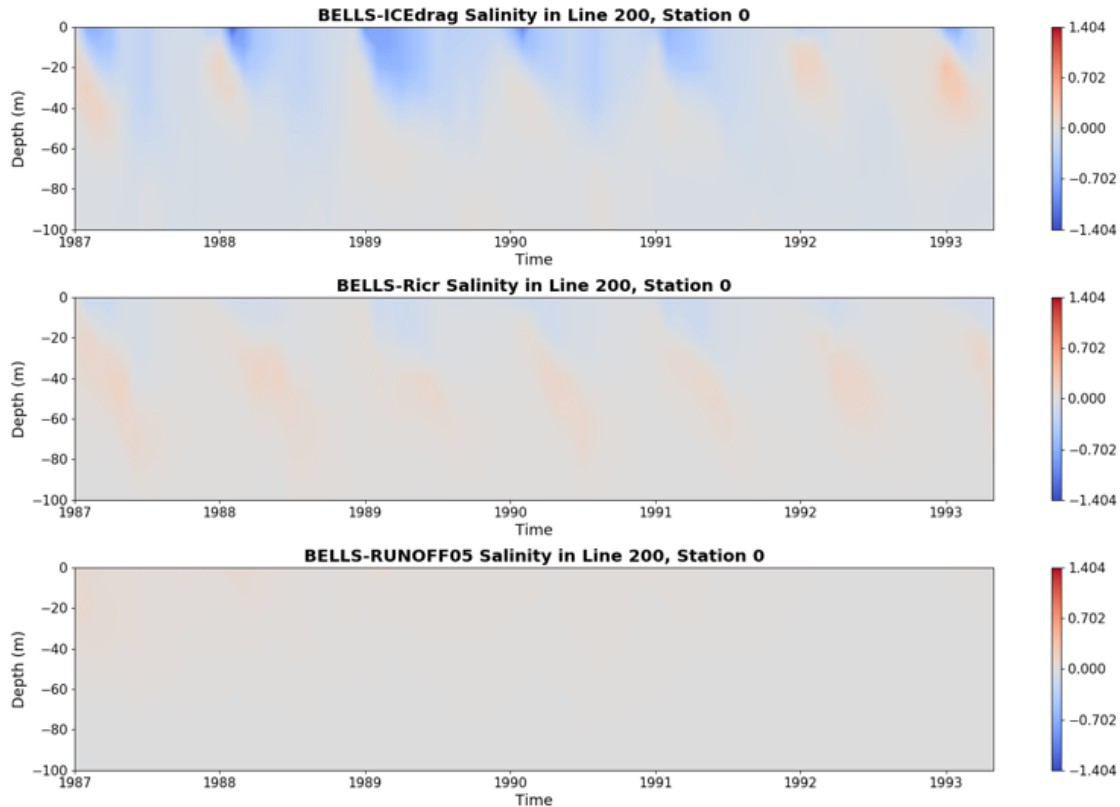


Figure 2-8: Time series of salinity difference between experiment BELLS and experiments ICEdrag, Ricr and RUNOFF05 for the MITgcm grid point closest to Palmer-LTER station 200.00.

2.4.2 Sea Ice Extent

To evaluate the overall skill of both BELLS and ICEdrag runs in simulating the sea ice extent and variability, the first step was to calculate the monthly means between the years 1991-2003 to analyze the general patterns of sea ice extension and concentration. The monthly means for the SSM/I data were calculated for the same period for comparison. The model and SSM/I sea ice concentration ranges are presented as the fraction of each cell covered by sea ice, ranging from 0-1.

The calculated monthly means do not show large differences between the sea ice concentration of runs BELLS and ICEdrag (figure 2-9). The concentrations in the first few months of the year (January until April) are lower in the simulations compared to the SSM/I data, with concentrations above 0.5 being restricted to a few coastal regions in the south of the grid. The maximum extension of sea ice is reached in

August, and both tests accurately simulate the location of the line that separates the ice-free area, defined by sea ice concentrations lower than 0.15. Although the location of the 0.15 sea ice concentration line is similar in both simulations year-round, the 0.5 sea ice concentration line retreats faster in the ICEdrag test.

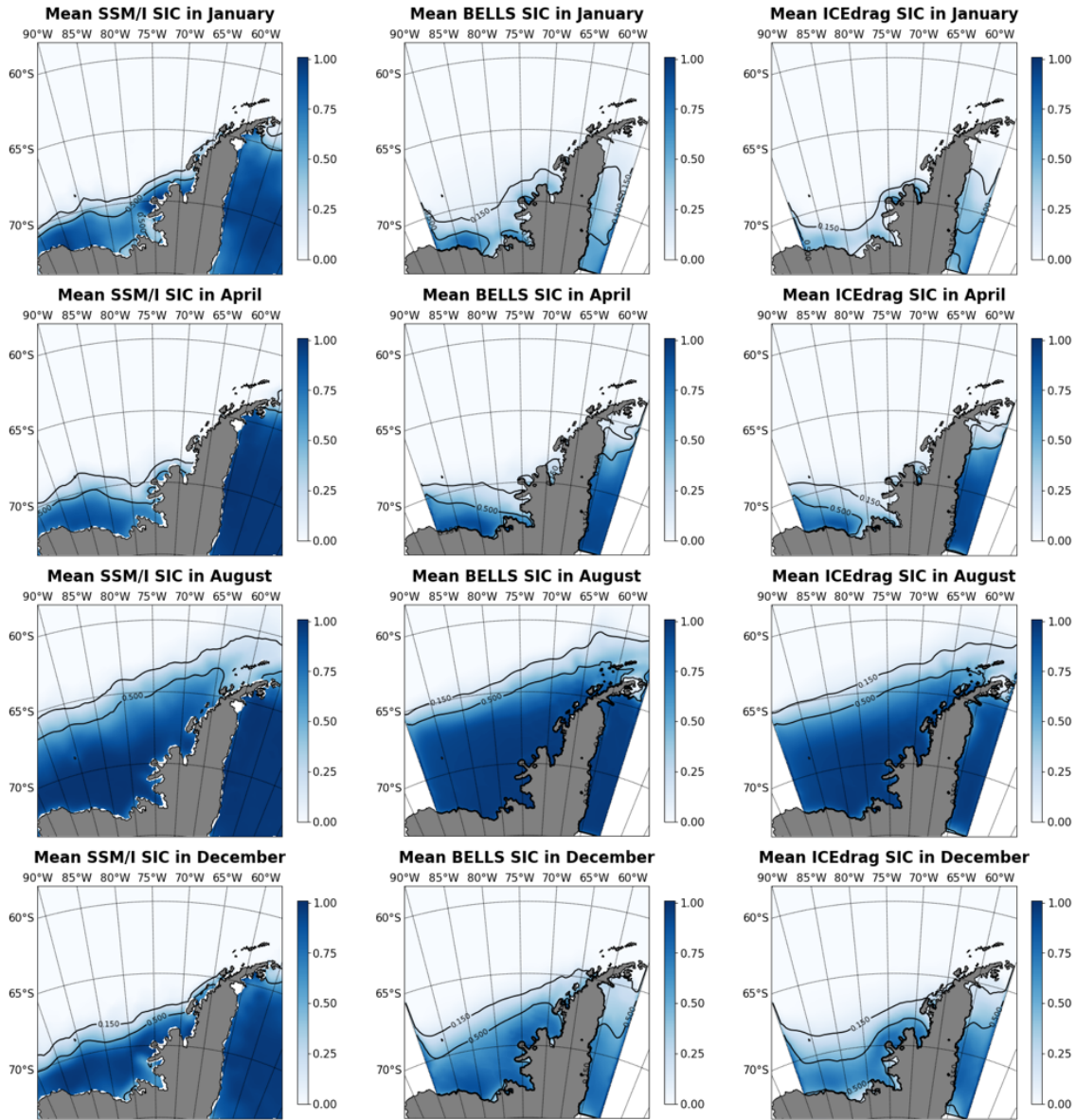


Figure 2-9: Monthly mean sea ice concentration calculated between 1991 and 2003 for experiment ICEdrag (left), BELLS (center) and for the SSM/I satellite data (right), for January, April, August and December.

In order to have a more quantitative measure of the differences in the sea ice cycle between runs BELLS and ICEdrag, and their skill in reproducing the observed

sea ice concentration, the spatial distribution of temporal correlation was calculated between the experiments and the SSM/I data (figure 2-10). For this calculation, the model outputs were interpolated to the satellite grid, which has a coarser horizontal resolution of 25 km, and the temporal correlation coefficient was calculated for each grid point, using the monthly means for each year between 1991 and 2003 as the time-series. The results show that the area of correlation higher than or equal to 0.9 significantly increased with the increase of the air-ice drag coefficient. Although the areas south of 70°S and the northern most areas impacted by sea ice still present lower correlations, meaning the model is less effective at properly simulating the variability of the minima and maxima during sea ice advance and retreat, the area around the Palmer grid is well represented. Like most of the domain, the shelf break area of the Palmer-LTER grid exhibits correlation coefficients higher than 0.9, but the points closest to shore still present lower values.

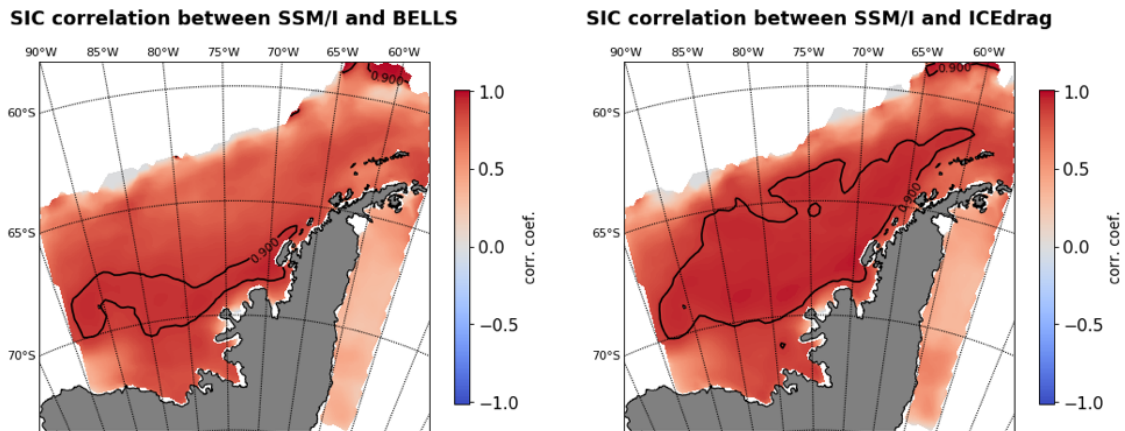


Figure 2-10: Temporal correlation between the SSM/I satellite data and ICEdrag (left) and BELLS (right) experiments, calculated between 1991 and 2003.

To better visualize the effect of the changes made to the air-ice drag coefficient in the area of interest, which includes the Palmer-LTER grid and Marguerite Bay, the correlation coefficient between experiments BELLS and ICEdrag and the SSM/I data was plotted for each station in the Palmer-LTER grid lines 200 (part south of the grid) and 500 (part north of the grid), shown in figure 2-11. On Line 200, the correlation between the experiments and SSM/I is always above 0.8, indicating that

both represent well the variability of sea ice in the southern part of the grid. The lowest correlation between ICEdrag and satellite data on line 200, however, was 0.89, indicating an improvement from BELLS. For Line 500, the model-data correlation was weaker, but the ICEdrag experiment still performed better, with correlation consistently above 0.85 offshore of station 40.

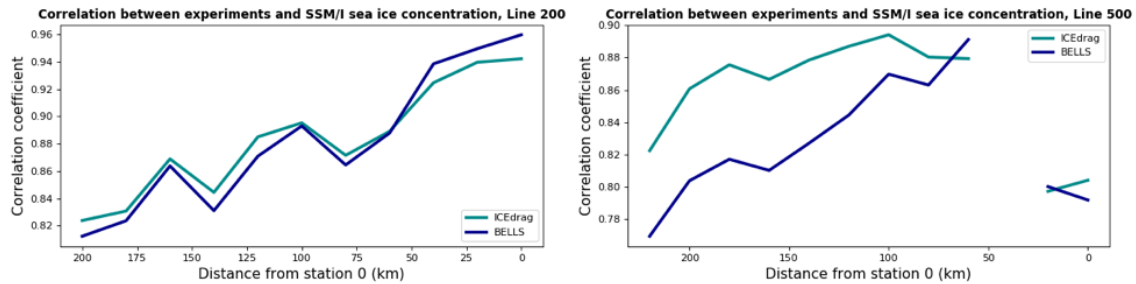


Figure 2-11: Correlation coefficient between SSM/I data and the MITgcm experiments (ICEdrag and BELLS) for the points closest to the Palmer-LTER stations on line 200 (left) and 500 (right).

Although sea ice thickness data is not available for comparison, an analysis of its behavior in the model is helpful to understand the mechanisms that lead to improved performance in simulating the sea ice variability in the ICEdrag experiment. Oxygen isotope data collected during the Palmer-LTER cruises reveals that although the freshwater influence in the WAP is patchy and highly variable, in some years sea ice is formed towards the northern part of the Palmer-LTER grid and subsequently melted in the southern part, indicating southward motion of sea ice [64]. The sea ice thickness in ICEdrag reaches higher values compared to the BELLS experiment as exemplified in figure 2-12, plotted for Line 200. The periods of sustained thickness higher than 0.5 m, however, are longer in the BELLS results. Particularly in Line 200, where sea ice would be supplied by lateral advection in some years, the peak sea ice thickness is higher in the ICEdrag experiment, reaching 2 m in years of El Niño and negative SAM, such as 1991-1992, 1994-1995, 2001-2002 and 2002-2003. In years of La Niña and SAM, however, such as 1996, 1998 and 2000, the sea ice thickness is lower in the ICEdrag experiment. Although increasing the wind-ice drag increases maxima of sea ice thickness (possibly due to ridging) in the ICEdrag experiment, the

thickness in this experiment is more variable, leading to more dynamic and easily melted sea ice. The performance of the model in simulating sea ice concentration was improved in general with ICEdrag, but even more so in the northern part of the model grid by facilitating sea ice movement.

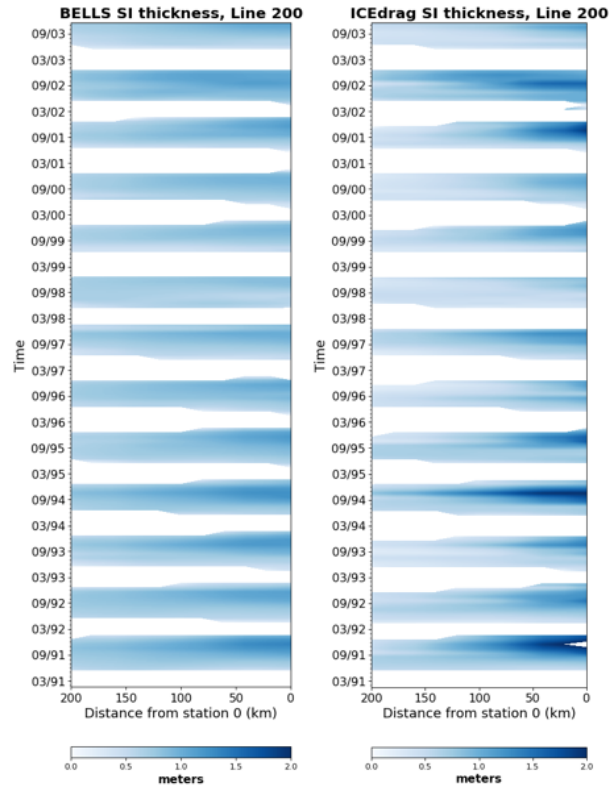


Figure 2-12: Sea ice thickness simulated by BELLS (left) and ICEdrag (right) on Line 200.

Given that the ICEdrag test had the most impact in deepening the ML and also performed well in simulating sea ice extension and variability, both BELLS and ICEdrag tests will be used for the next steps of the skill assessment in order to assess whether the changes made for experiment ICEdrag impacted the circulation in the model outputs.

2.4.3 General Surface Circulation

A next step is to analyze the surface currents and compare them to the information available in the literature. Monthly mean salinity and currents were calculated be-

tween the years 1991 and 2003 for the BELLS and ICEdrag runs. When looking at the whole grid domain (figure 2-13), given the offshore currents are stronger than the shelf circulation, the only visible characteristic of the circulation is the presence of the ACC flowing northward along the shelf break. The ACC is seen year-round and with similar velocity in both experiments. During the summer months, the surface salinity close to the shore is significantly lower in the BELLS simulation due to local sea ice melt, especially around Marguerite Bay and Charcot Island, where salinity reaches values below 32, while remaining above 32.2 in the ICEdrag experiment.

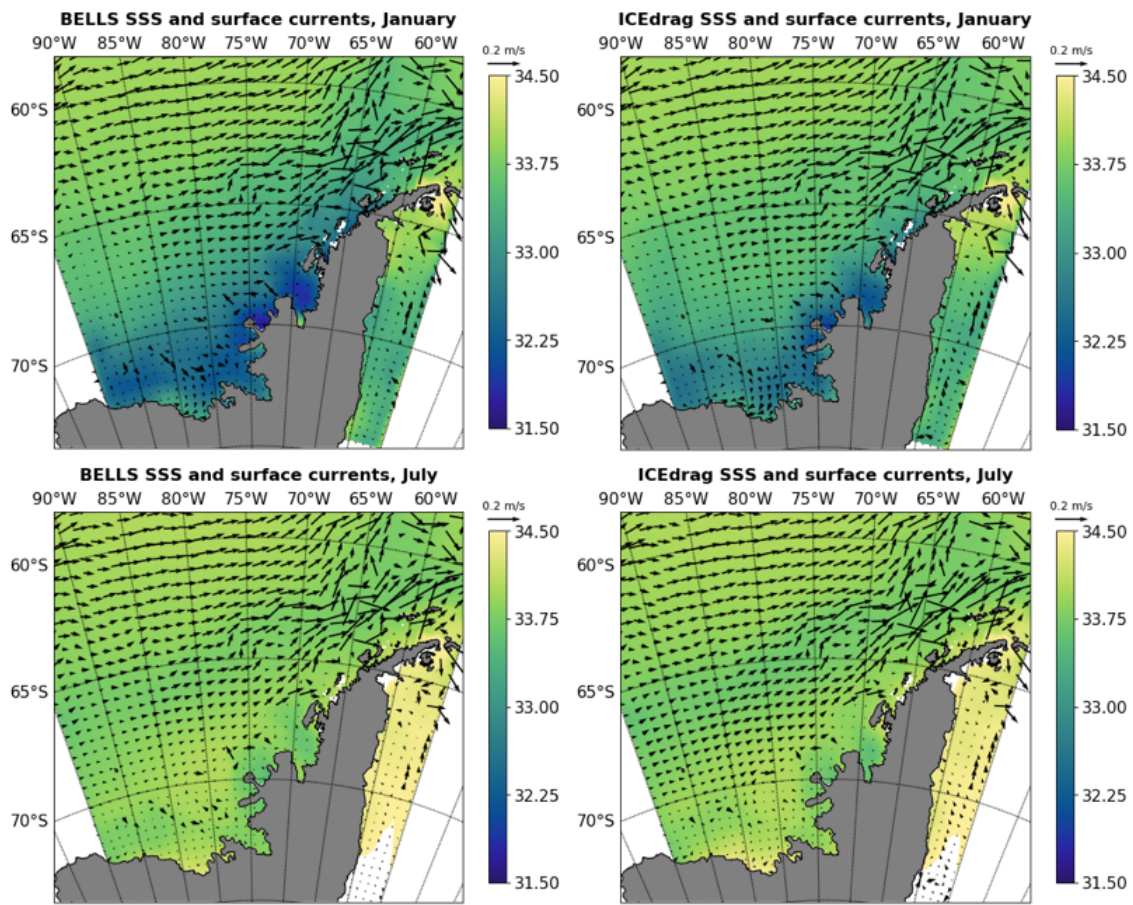


Figure 2-13: Monthly mean surface salinity and surface current velocity for experiments BELLS (left) and ICEdrag (right), for January (top) and July (bottom).

When zooming into the Marguerite Bay area, it becomes clear that both experiments show an anticyclonic circulation pattern during the winter. In ICEdrag, the circulation reverses to a cyclonic pattern (southward flowing close to the shore inside

the bay) during the summer months (figure 2-14). In January, when both runs indicate a cyclonic circulation, the meridional component is stronger in the ICEdrag run, with a southward flowing current, while in the BELLS run the zonal component dominates, with an onshore current. By March, the points closer to the coast show a northward component in the BELLS test, while in ICEdrag the circulation is still predominantly southward. During the winter months, the surface circulation in Marguerite Bay is very similar on both tests, and the return to a southward flowing cyclonic circulation is complete in the ICEdrag test by December, while in BELLS there is still a prevalence of a northward flow during this month.

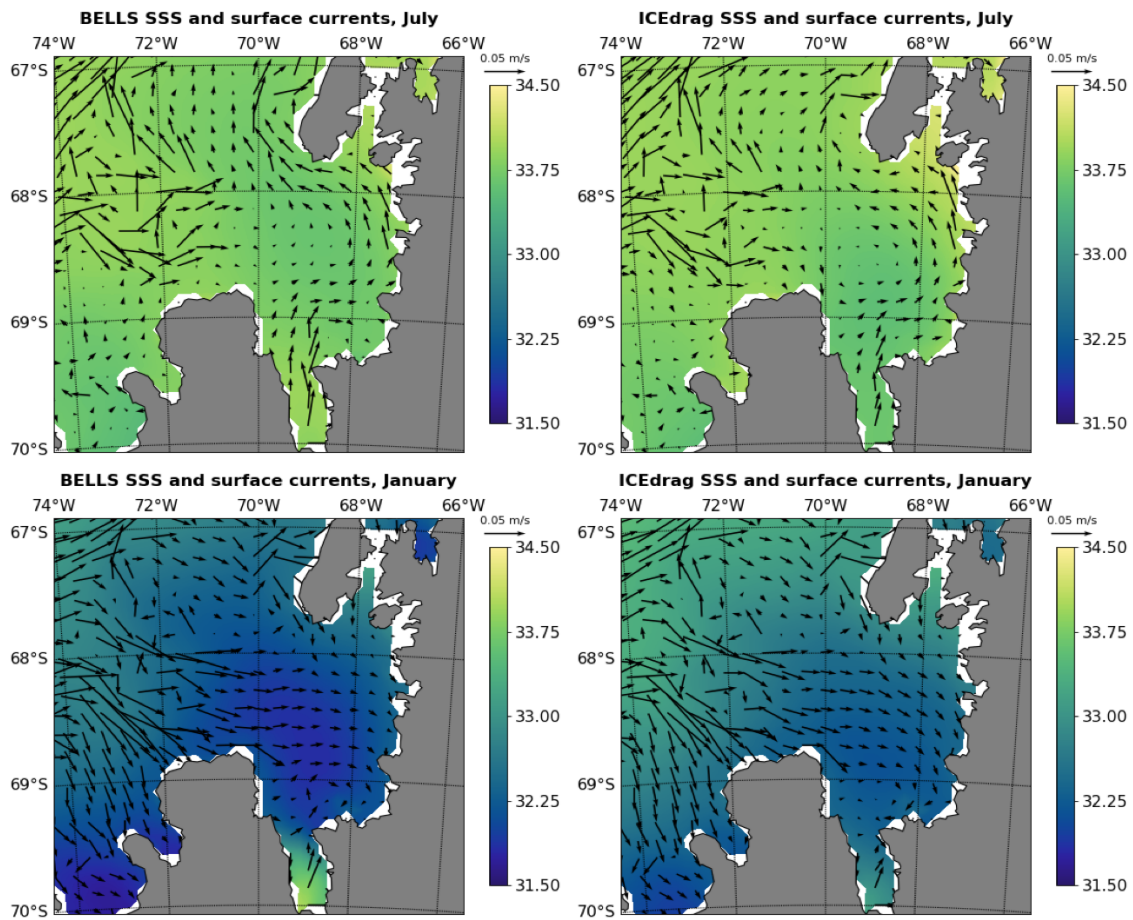


Figure 2-14: Monthly mean surface salinity and surface current velocity for experiments BELLS (left) and ICEdrag (right), for July (top) and January (bottom).

Table 2.1: Temperature and salinity limits used to define the water masses analyzed.

Water Mass	Temperature Limit	Salinity Limit
Antarctic Surface Water (AASW)	$-1.8^{\circ}\text{C} \leq T \leq 1^{\circ}\text{C}$	$33 \leq S \leq 33.7$
Winter Water (WW)	$-1^{\circ}\text{C} \geq T$	$34 \leq S \leq 34.2$
Circumpolar Deep Water (CDW)	$1^{\circ}\text{C} \leq T \leq 2^{\circ}\text{C}$	$34.6 \leq S \leq 34.74$

2.4.4 Water Masses

For each point on the Palmer-LTER grid, a T-S diagram was built using the calculated monthly means for both simulations (ICEdrag and BELLS). On the background of each diagram, density lines were plotted using the 48-term expression of the equation of state described in [53] for surface pressure (sea pressure of zero). Different diagrams were built for shelf and shelf break/offshore stations, with shelf stations being defined by grid points with depth of less than 750 m, following the definition of [17]. The shelf stations for lines 200 and 500 are marked in blue on figure 2-15, while the shelf break stations are represented by the red points. The limits of CDW, AASW and WW as described in [63] and [40] were drawn to each diagram (table 2.1). The diagrams were plotted for lines 200, 300 and 500. Lines 300 and 500 were cited as the locations where CDW intrusion is more frequent [52].

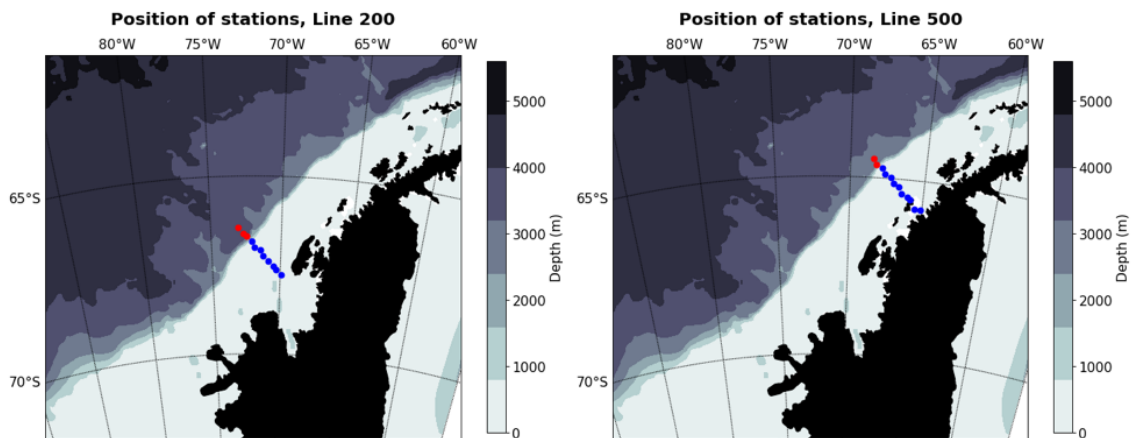


Figure 2-15: Location of the station points for lines 200 (left) and 500 (right), with bathymetry on the background. The continental shelf stations (depth < 750 m) are represented in blue, and the shelf break/offshore stations are represented in red.

On Line 200 (figures 2-16 and 2-17), BELLS exhibits lower salinities and temperatures in the surface layer compared to ICEdrag, due to the influence of sea ice melt. Another consequence is that in the ICEdrag run the subsurface and mid-depth values have a slightly higher range of salinities due to increased mixing. Although both have points within the range of WW during the summer (figure 2-16), fewer points fall within this range on the ICEdrag run, possibly because warmer surface water gets mixed deeper in the ICEdrag run, causing the remaining winter temperature to increase for some points. The deeper waters on the shelf points in the BELLS simulation are close to the CDW limits, while on the ICEdrag run the deeper shelf points have colder water with fewer locations reaching temperatures of at least 1°C . [69] also found in the model a bias towards lower temperatures compared to core-CDW waters. This bias, however, is consistent with the WOA fields used to initialize the model.

Throughout the winter (figure 2-17), the surface waters in both runs transition to values close to the WW limits, although some points remain with salinities below WW range, with the lower salinity limit of ICEdrag being 33.88 in August, while BELLS reaches values of 33.73, compared to the lower limit of 34 for WW. In December, the surface layer is within the AASW limits in the ICEdrag, with WW values being reached around 80 m depth. For the BELLS, WW values are reached around the same depth, but the surface waters have lower salinity than the AASW limit, around 32.6 at the lowest value.

The same differences and ranges were found for both runs at Line 300, but with a more marked presence of CDW in the offshore stations in the ICEdrag experiment. According to [52], CDW intrusions are often found in this line, and occasionally also on Line 500. On Line 500 (figure 2-18), the difference between the two runs analyzed is smaller, with both having surface values slightly warmer than 2°C at onshore and offshore stations by the end of the summer. In ICEdrag, subsurface waters are always warmer than WW, and both experiments show the lowest temperatures around 60 meters depth. The lower sea ice concentration could be responsible for the warmer surface temperatures in ICEdrag, since it exposes the surface ocean to the atmosphere.

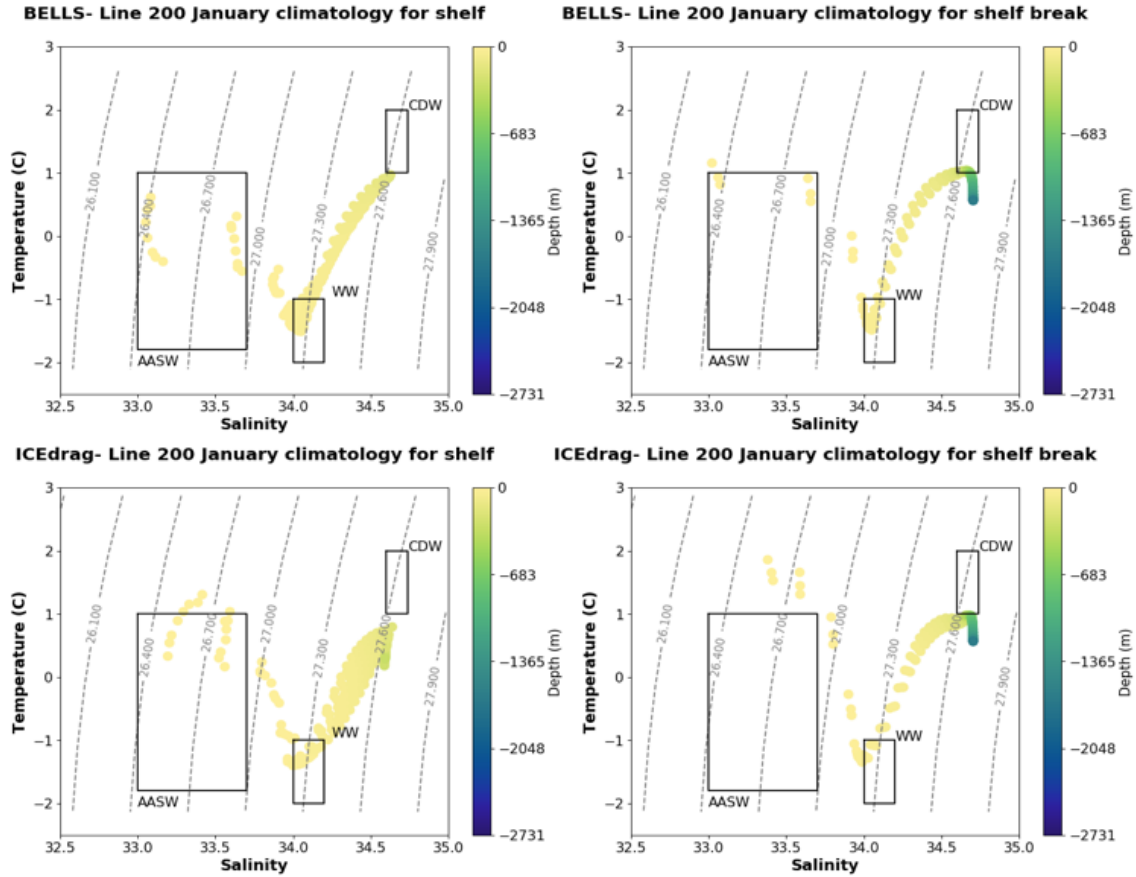


Figure 2-16: Θ - S diagrams for monthly mean January values of experiments BELLS (top) and ICEdrag (bottom), for onshore (left) and shelf break/offshore (right) stations of line 200. The x axis shows salinity values and the y axis shows temperature for each point, and the boxes show the limits of each water mass analyzed.

At the end of the winter, in August and September, the surface values are close to the WW limits.

In general, both runs properly simulate the entrainment of WW below warmer, fresher water during the summer months, and the deeper MLD during the winter. The remaining WW in the summer is found between 80-100 m, consistent with the literature. The analysis indicates less mixing in the BELLS run during the summer, with more points exhibiting temperature and salinity values within the range of WW. At depth, in the shelf stations, the ICEdrag run has slightly colder temperature than the other simulations, indicating less influence from CDW.

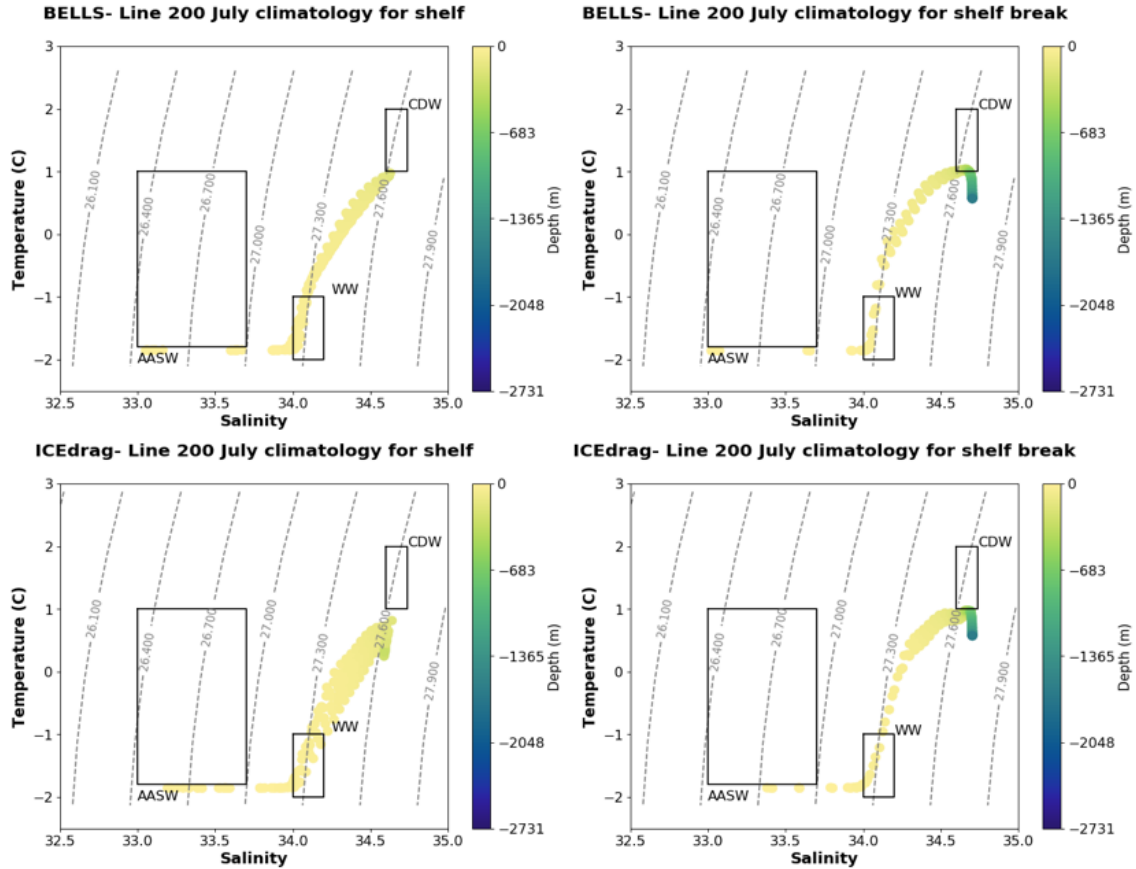


Figure 2-17: Θ -S diagrams for monthly mean July values of experiments BELLS (top) and ICEdrag (bottom), for onshore (left) and shelf break/offshore (right) stations of line 200. The x axis shows salinity values and the y axis shows temperature for each point, and the boxes show the limits of each water mass analyzed.

2.4.5 Influence of Modes of Climate Variability

To assess the drivers of the variability in the experiments and the impact of teleconnections on the model, individual years were also analyzed. The years with the clearest association between negative SAM and El Niño during the time series analyzed were 1991/1992 according to [77], but since there were no summer cruises during these years, 2002 was also included to represent this association. To represent the association of strong positive SAM and La Niña, the authors point to the years of 1998 and 1999, so these were analyzed separately as well. Also 1997 was an El Niño year with weak SAM signal, while 2000 was a La Niña year with weak SAM, so these years were analyzed to compare the difference to the strong SAM years. Model

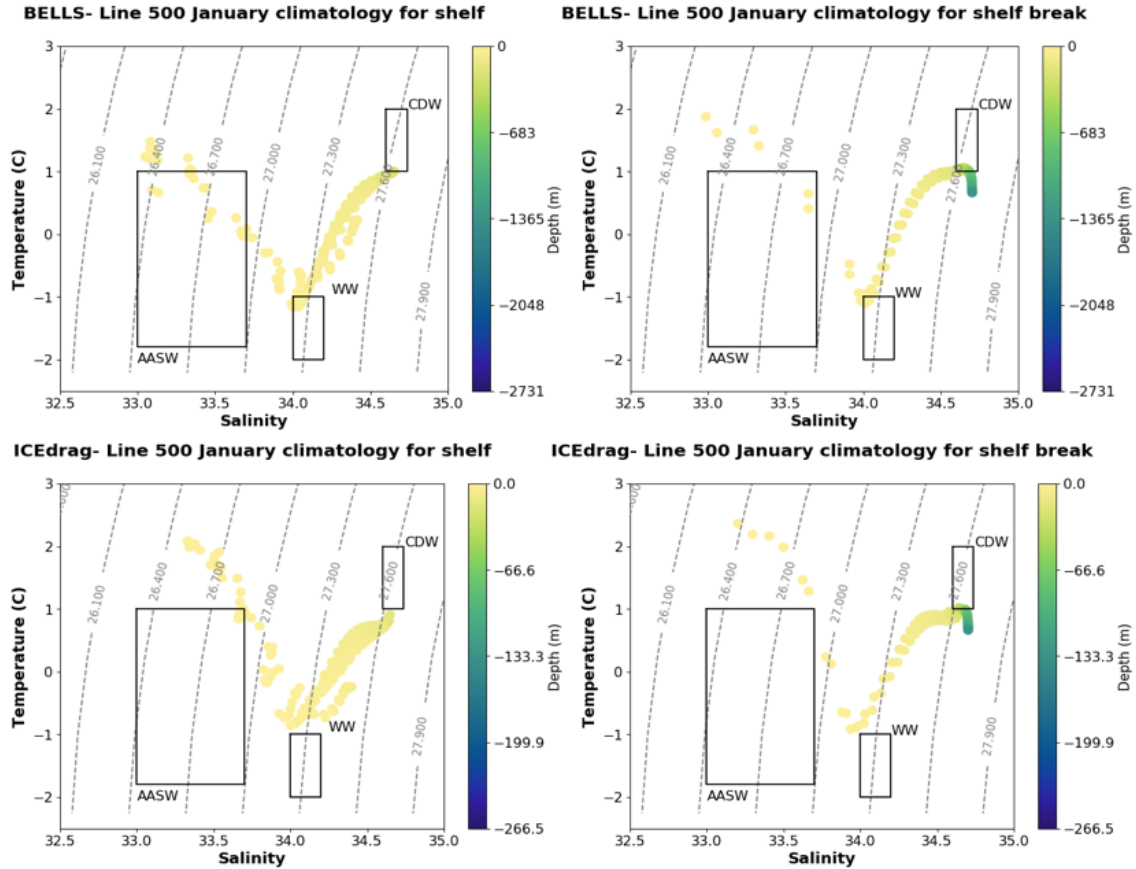


Figure 2-18: Θ - S diagrams for monthly mean January values of experiments BELLS (top) and ICEdrag (bottom), for onshore (left) and shelf break/offshore (right) stations of line 500. The x axis shows salinity values and the y axis shows temperature for each point, and the boxes show the limits of each water mass analyzed.

output was plotted for the years to be analyzed, as well as the deviations from their calculated climatologies. For that, the monthly climatology for the whole period was subtracted from the monthly mean outputs of each year so that we can evaluate, relative to the whole period, whether the model simulated the observed sea ice anomalies during different phases of SAM and El Niño.

When negative SAM and El Niño co-occur there is a prevalence of southerly winds in the WAP, and a tendency towards increased sea ice concentrations. On the other hand, when positive SAM occurs with La Niña the opposite is expected, with warm northerly winds and less sea ice. It is expected that changes in sea ice concentration will also change the surface layer of the ocean due to changes in brine rejection during sea ice formation and increased freshwater input during sea ice melt. Given there is

an improvement in the sea ice correlation between the model experiments and SSM/I data, it is also worth exploring how well each run (ICEdrag and BELLS) simulated the different years.

Sea Ice Concentration and Extent

The monthly mean sea ice concentration was plotted for each experiment analyzed (ICEdrag and BELLS) and for the SSM/I data, for the whole LTER grid. Also, in order to summarize the analyses in fewer figures, the points closest to the stations in lines 200 and 600 of the Palmer-LTER grid were identified in the MITgcm grid and in the SSM/I coordinates, and the monthly anomaly of the sea ice concentration (from the monthly climatology) for each line and each station was plotted for the duration of the simulation. The lines were chosen to represent the southernmost and northernmost extension of the grid lines analyzed.

The decrease in sea ice concentrations during positive SAM and La Niña years is better captured by the ICEdrag experiment on Line 200 (figure 2-19), with the year 1998 presenting especially low concentrations and a short sea-ice season that is not well represented in the BELLS experiment. Also in line 600 (figure 2-20) the anomalies are better matched between ICEdrag and the satellite data, with negative anomalies more visible in ICEdrag during 1992-1993 and positive anomalies during 1997-1998. Close to the coast, however, both experiments underestimate the presence of sea ice observed in the satellite data.

Comparison with Palmer-LTER vertical profiles

For each year analyzed, the Palmer-LTER cruise data were compared to the model. To do so, for each LTER grid line between 200 and 600, the stations where CTD data were collected were identified and the closest point on the MITgcm grid was found. After that, the CTD data were interpolated to the MITgcm vertical resolution and the MLD was calculated. As was mentioned before, salinity is the main driver of density changes at this temperature range, so the criteria used to calculate MLD was the same used in [62], which calculates the density and uses $\Delta\sigma \geq 0.05 \text{ kg/m}^3$ over

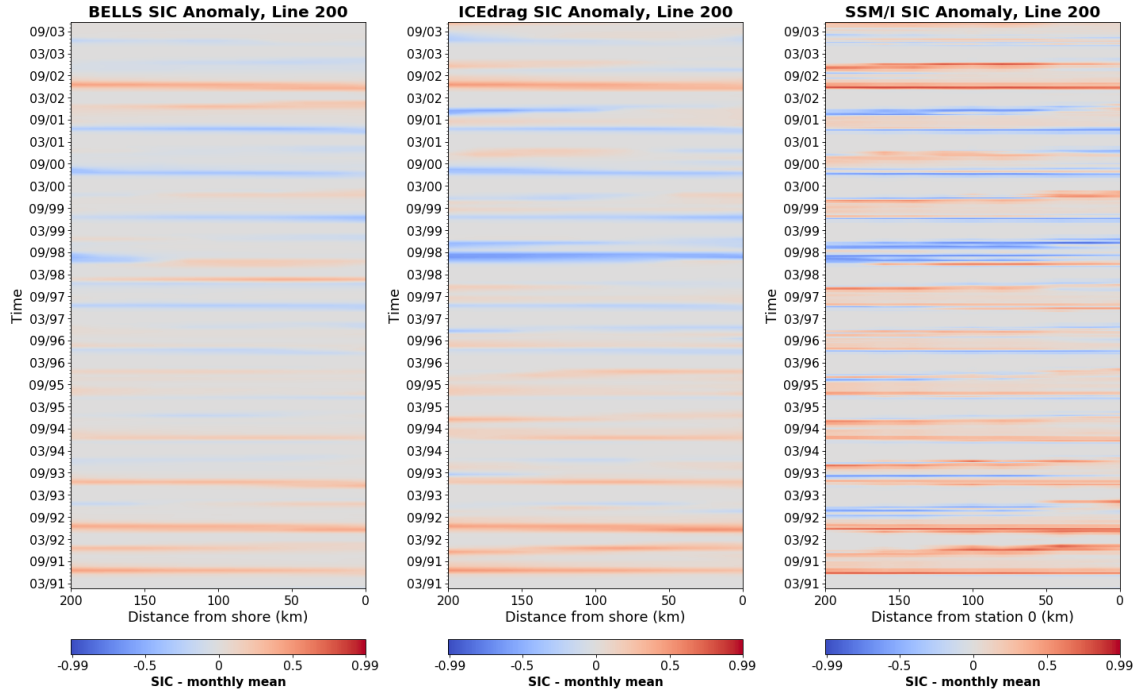


Figure 2-19: Time series of sea ice concentration anomalies (calculated as the difference between the monthly average and the monthly climatology) for the points close to Line 200 for MITgcm experiments ICEdrag (left), BELLS (center) and for the SSM/I satellite data.

a 5-meter interval as the threshold. Since the Palmer-LTER cruises happen between January and February each year and the model output is provided as monthly mean, the output used to represent each year was based on whether the cruise happened mostly during January or mostly during February. For most of the cruises, data were compared to the model January mean, but in 1998, for example, the cruise happened mostly during February and that month was used as comparison. The vertical profiles of temperature and salinity were compared for years 1998 and 1999, which are positive SAM and La Niña years (with 1998 being identified as a low ice year), and for 2002, which is a negative SAM and El Niño year with high sea ice concentration.

Overall, in 1998 (figures 2-21 and 2-22), the WW presence is attenuated in the ICEdrag experiment and is less visible compared to the Palmer-LTER data, especially towards the north of the grid (Lines 500, 600). On the BELLS run, WW is more visible but closer to the surface, with lower temperatures in the surface layer compared to the observed data. Surface salinity is lower in both experiments, more evident towards

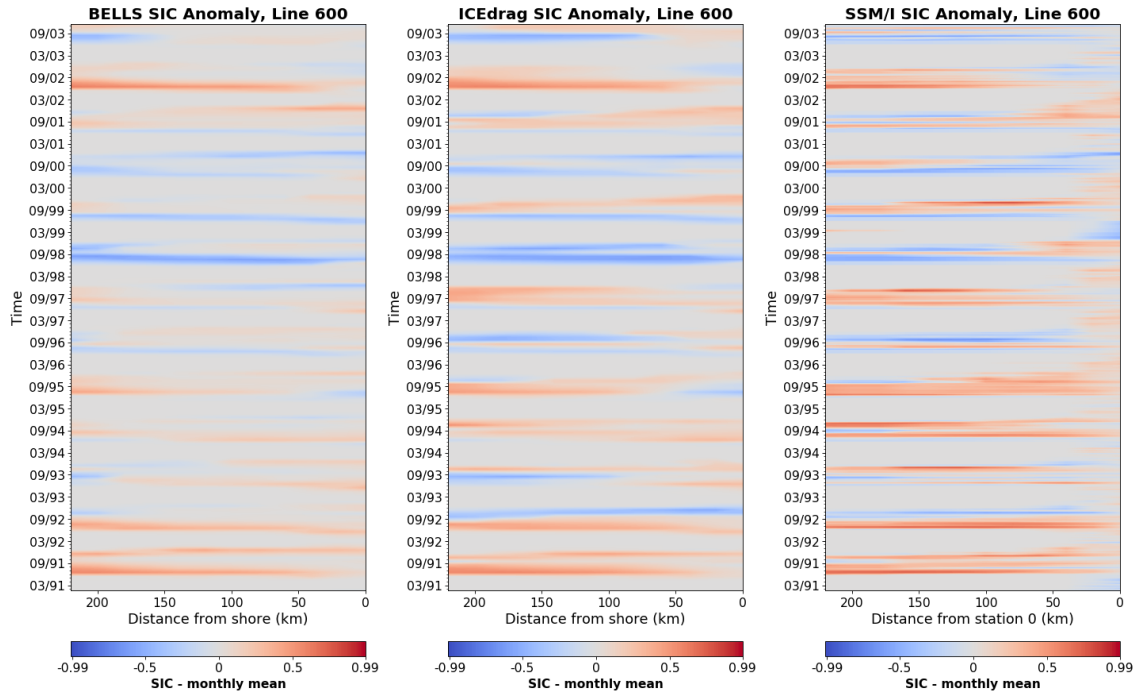


Figure 2-20: Time series of sea ice concentration anomalies (calculated as the difference between the monthly average and the monthly climatology) for the points closest to Line 600 for MITgcm experiments ICEdrag (left), BELLS (center) and for the SSM/I satellite data.

the south of the grid, but this difference is accentuated in the BELLS run. During 1999 (figure 2-23), both models presented lower salinity and higher temperature close to the surface, with the difference in temperature (when compared to the Palmer-LTER data) being higher in the ICEdrag experiment while the difference in salinity is higher in the BELLS run. In 2002 (figure 2-24), which is a high sea ice year, the trends were similar, but the salinity in the surface layer is lower on the model in both experiments, possibly due to increased sea ice melt.

Although both experiments exhibited problems in simulating the vertical profile of salinity and temperature observed in the Palmer-LTER cruises, ICEdrag had a closer representation of the profiles and deeper mixed layer than BELLS. It should also be noted that accurate representation of the conditions observed in the cruises is not to be expected, given we are comparing single CTD casts with monthly mean model results. Given ICEdrag was the experiment with the best performance so far, however, it will be the only run to be compared to other experiments performed from

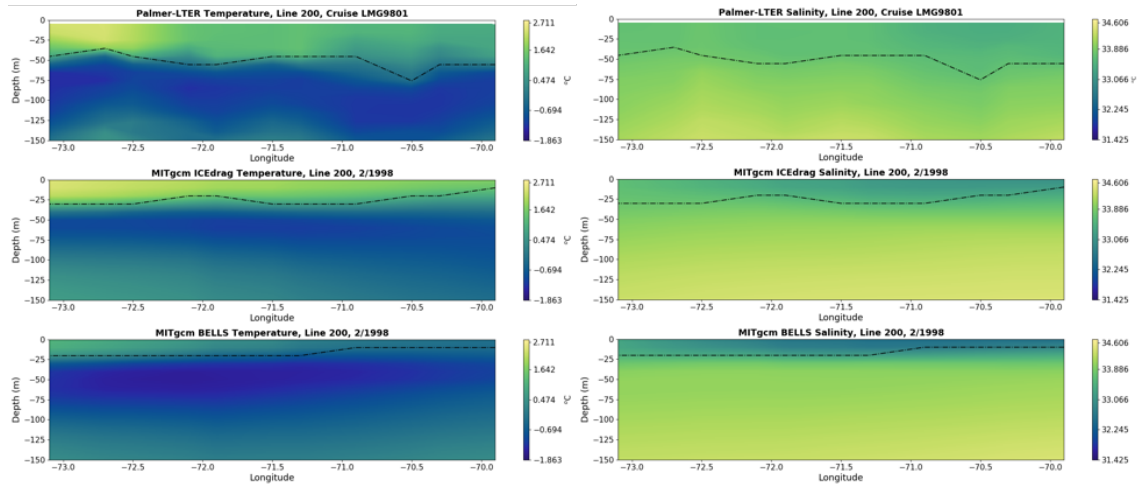


Figure 2-21: Comparison of temperature (left) and salinity (right) for Line 200 from the Palmer-LTER 1998 cruise data (top) and the MITgcm ICEdrag (center) and BELLS (bottom) January/February 1998 mean.

this point on.

2.4.6 Influence of Seasonal Runoff

Although glacial input is not thought of as the main driver of freshwater cycle in the WAP [57][59] and test RUNOFF05 showed no significant changes in salinity, adding a seasonal cycle to the meteoric water is important for the nutrient cycle due to its role as an iron source [2][3]. In RUNOFF05 the amount of freshwater input was changed, but no seasonal cycle between the summer and winter months was introduced, and therefore it is important to check what the effects of adding such a seasonal cycle are on the model results. For that purpose, test SRunoff was compared with ICEdrag to analyze the effects of introducing seasonal cycle in meteoric water input in the seasonal and interannual variability of sea ice, circulation and MLD.

SRunoff introduced both a seasonal and a spatial signal, as can be seen in figure 2-25, which shows the difference between the surface temperature and salinity of tests SRunoff and ICEdrag, so that positive values indicate lower salinity in the SRunoff test. As expected, salinity in SRunoff was lower near the coast compared to ICEdrag, with differences reaching 0.3 at the end of the summer. There is no indication that the introduced salinity variability led to significant changes in the simulated sea ice

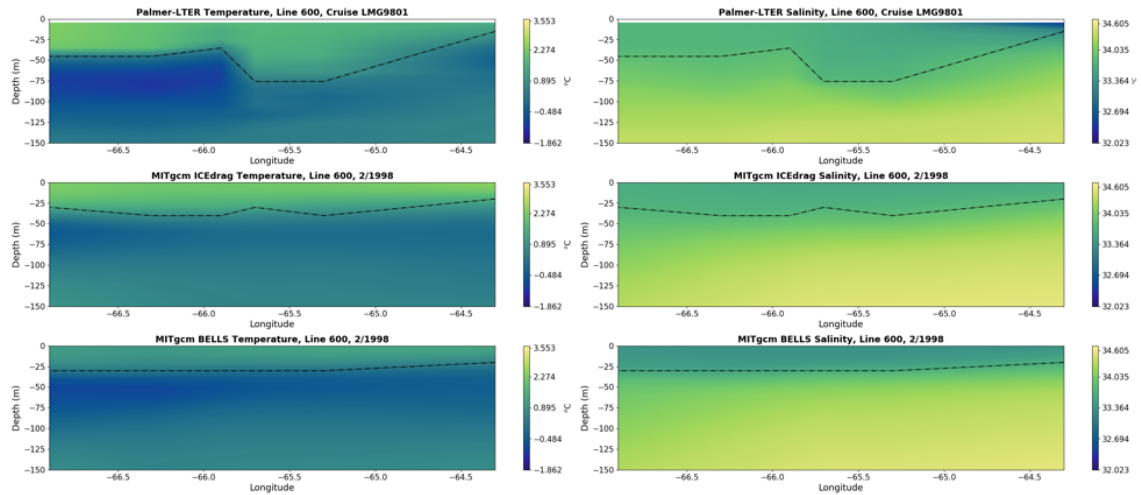


Figure 2-22: Comparison of temperature (left) and salinity (right) for Line 600 from the Palmer-LTER 1998 cruise data (top) and the MITgcm ICEdrag (center) and BELLS (bottom) January/February 1998 mean.

concentration between tests ICEdrag and SRunoff. Both tests presented similar sea ice extension and variability, as can be seen in figure 2-26, which shows the correlation between monthly mean sea ice concentration from SSM/I data and the tests conducted for the period between 1991 and 2005.

Although the low salinity signal introduced is similar for every year, interannual differences in the outputs are observed. It is noticed that in years of low sea ice concentration, such as 1998,1999 and 2000, the salinity differences between the experiments extend farther offshore, while years of higher sea ice concentration such as 1991,1992 and 1997, the salinity differences are more pronounced closer to the coast.

The next step is to analyze the changes in the circulation between the tests. For that purpose, the difference in the surface current velocity was calculated. The surface salinity and current velocity for test SRunoff is shown on figure 2-27, as well as the salinity and current difference between ICEdrag and SRunoff. As can be seen from the figure, the circulation patterns are similar between the two tests, but SRunoff shows a weakening of the cyclonic circulation inside of Marguerite Bay during the summer and a strengthening of the anticyclonic circulation observed during the winter. Throughout the year, a strengthening of the southward flowing near shore circulation south of Marguerite Bay is seen in the SRunoff test. The changes in the

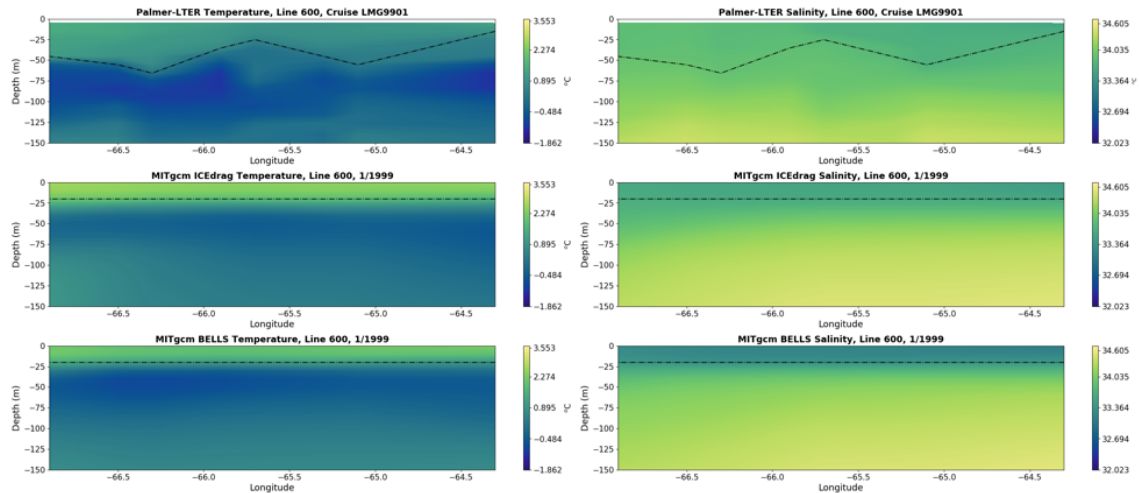


Figure 2-23: Comparison of temperature (left) and salinity (right) for Line 600 from the Palmer-LTER 1999 cruise data (top) and the MITgcm ICEdrag (center) and BELLS (bottom) January/February 1999 mean.

circulation, however, are of the order of 10^{-3} m/s relative to mean velocity fields of the order of 10^{-1} m/s.

Although small changes were observed between SRunoff and ICEdrag, the representation of the sea ice variability and MLD, which are of primary importance for the biogeochemistry of the region, were not compromised. However, the shallow MLD problem persists and subsequent new tests were done to address this problem using the seasonal runoff forcing.

2.4.7 Influence of Langmuir Circulation Parameterization on MLD

The first step in assessing the effects of the Langmuir circulation parameterizations introduced was to look at the changes in calculated MLD throughout the whole LTER grid. As a first step, the monthly average MLD (calculated using the same method as previous tests) and sea ice concentration for the 13 years for which the tests were analyzed (1991-2003) were calculated and compared to the SRunoff test to assess which regions showed an increase in MLD and by how much. As can be seen in figures 2-28, introducing both approaches at the same time (KPP_LC) led to similar

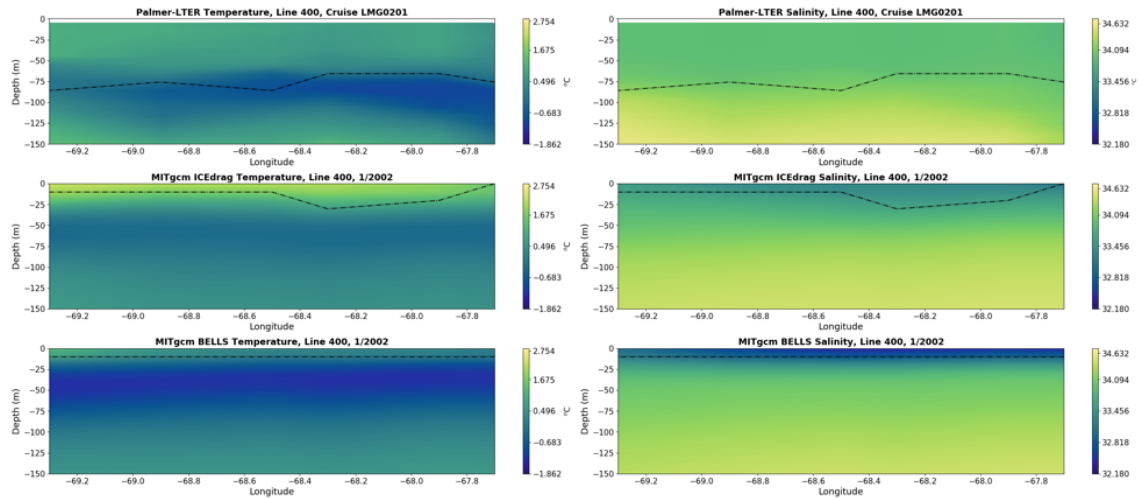


Figure 2-24: Comparison of temperature (left) and salinity (right) for Line 600 from the Palmer-LTER 2002 cruise data (top) and the MITgcm ICEdrag (center) and BELLS (bottom) January/February 2002 mean.

values of increase in MLD in the summer and winter, around 8 meters. During the summer, no deepening was observed around the continental shelf break, while during the winter there was less deepening in the open ocean region. Given that the MLD is shallower during the summer season, the proportional increase was higher during this season. To test the individual contribution of each approach, KPP_epsI and KPP_Ut were also compared to SRunoff. The changes in MLD observed in the KPP_Ut run were even more pronounced than the ones observed in the KPP_LC run throughout the year, especially during the winter period. KPP_Ut also presented more change in the SIC, with a small decrease around the ice edge in both seasons.

Since the sea ice concentration presented changes in the KPP_Ut test, individual years of observed positive and negative sea ice anomalies were analyzed for this test in order to assess the extent of this difference and whether it would be detrimental to the performance of the model in simulating the variability of sea ice concentration. For this purpose, 1994 and 1995 were chosen as years of increased sea ice concentration, and 1997 and 1999 were chosen as years of decreased sea ice. The comparison of MLD and SIC between SRunoff and KPP_Ut showed a similar pattern for all years analyzed (results for 1999 are shown in figure 2-29), with less sea ice around the ice edge in KPP_Ut. Although the sea ice concentration is lower around the ice edge,

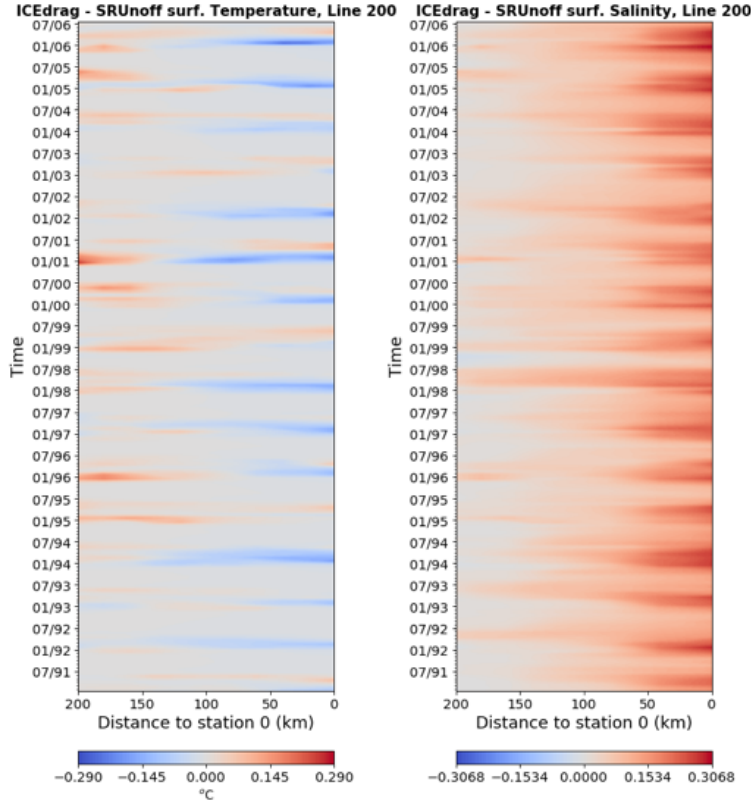


Figure 2-25: Surface temperature and salinity difference between tests ICEdrag and SRUnoff for Line 200 of the Palmer-LTER grid.

the line of 10% sea ice concentration didn't change significantly. The largest increases in MLD in KPP_Ut during the winter is observed at the marginal ice zone where the concentration of sea ice is decreased.

Before assessing the performance of the new parameterizations in simulating the MLD at the Palmer-LTER grid, the correlation coefficients between the simulated and observed SIC for each station of the Palmer LTER grid were calculated again to assess whether the sea ice variability during the whole period was compromised (figure 2-30). Although the correlation with KPP_Ut sea ice was slightly lower in some of the stations, the correlation coefficients are still close enough to justify the use of the parameterizations implemented on this experiment.

After confirming that all parameterizations presented increased MLD, with KPP_Ut presenting more pronounced deepening than KPP_epsI and KPP_LC, the tests were conducted to assess how well they are able to simulate the MLD in the Palmer-LTER

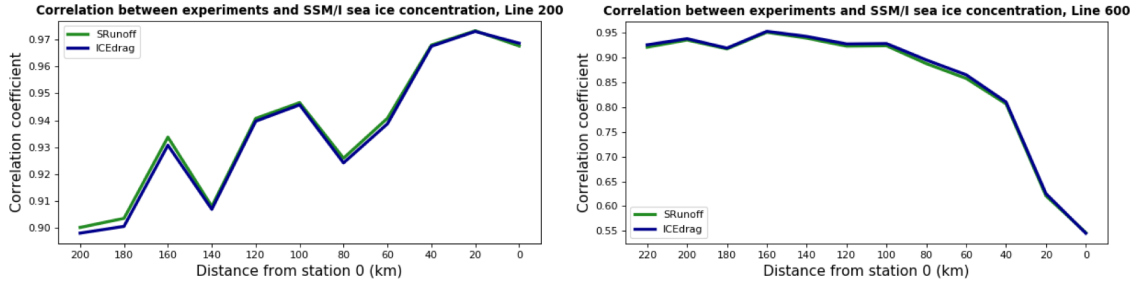


Figure 2-26: Correlation between monthly mean sea ice concentration on MITgcm simulations and SSM/I satellite data for lines 200 and 600 of the Palmer-LTER grid.

grid. An initial analysis was done by comparing the average MLD at every LTER cruise station from line 200 until 600 for all the Palmer-LTER summer cruises with the average for all the Januaries in each test (figure 2-31). Overall, KPP_Ut presented the most pronounced deepening of the MLD, although the calculated MLD for the Palmer-LTER data remains deeper. The biases between the simulated and observed data are higher in the northern part of the grid, however, with differences as high as 50 meters in line 600.

A comparison between simulated monthly means and MLD calculated from a single observation should be analyzed carefully since the MLD can vary at a much faster time scale than monthly, and the observed data may not represent the average condition for the whole month. To assess the range of values to be expected from the Palmer-LTER data and from the model output, the climatological MLD for the Palmer-LTER data was compared to the average MLD calculated from daily outputs for the month of January from a simulation conducted using the same setup as KPP_Ut during the years 2013 and 2014. The average MLD from the data and from the simulation is shown in figure 2-32 for lines 300 to 600 along with an error bar defined as the standard deviation of each dataset multiplied by 1.96. This dashed lines, therefore, represent a deviation from the mean that should include 95% of the MLD values. For this analysis, only the stations that were sampled more than 5 different cruises were considered, unlike the general Palmer-LTER climatology for which all data collected during January and February is used. What can be observed from figure 2-32 is that the model outputs have lower variability than the Palmer-LTER

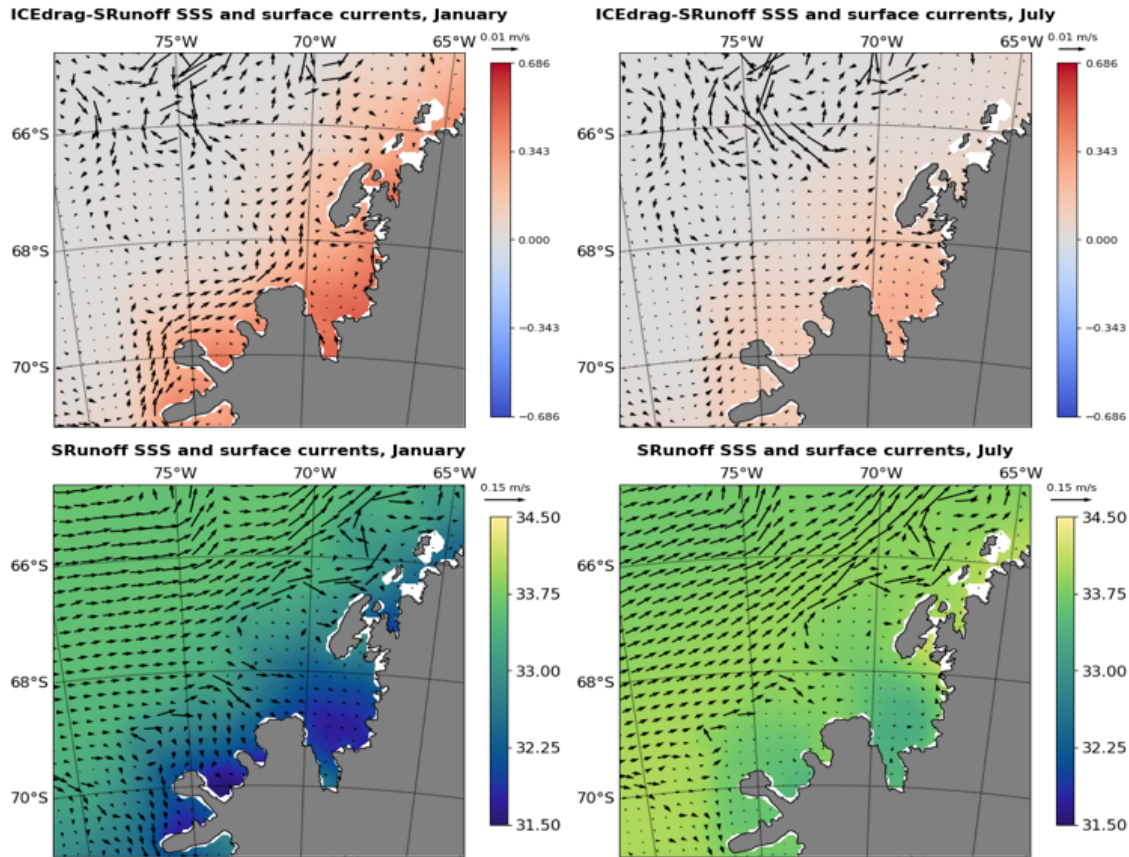


Figure 2-27: Surface current velocity difference between tests ICEDrag and SRunoff in January (top left) and July (top right); and SRunoff simulated surface current velocity in January (bottom left) and July (bottom right).

data, and that the average MLD from the model output is shallower than the Palmer-LTER data for all points. For most stations, however, the model output falls within the error bar from the Palmer-LTER data.

Given that KPP_Ut presented the lowest biases compared to the Palmer-LTER data, this experiment was analyzed further to investigate its performance at different years and analyze the skill of the model at predicting interannual variability of the MLD. The analysis was done by comparing the years chosen to represent high (1994, 1995) and low (1997, 1999) sea ice condition, and the difference between the observed and the simulated MLD was plotted on top of the model grid bathymetry (figure 2-33), which could also help with the understanding how bathymetry influences the performance of the model.

The low sea ice years analyzed presented deeper MLD in the model in the station closest to shore of line 300. Although the sea ice is well represented by the model at this point, which was verified by calculating the correlation between observed and simulated sea ice, the MLD does not correlate well with either total wind speed (correlation 0.25) or sea ice (correlation <0.4) at this point. Coastal areas are highly influenced by local phenomena that the model is unable to reproduce, such as the passage of icebergs or ice calving, which could help explain the disparities between observed and modeled data at these points. Also, an analysis of the time series of monthly mean MLD, sea ice and wind speed (used by the model as a forcing) shows that even when comparing monthly means the time scale of wind speed variation is much faster than either MLD or sea ice, which could explain the low correlation coefficients calculated. However, a visual analysis of the time series confirms that years of increased wind speed present lower sea ice concentrations and deeper MLDs (figure 2-34).

Other areas where the model presents high biases in MLD are the stations closest to shore on line 200 and shelf stations on line 500, which are areas of sharp increases in depth. This raises the possibility that the errors found are due to misrepresented circulation around the canyon. The deepening of MLD in experiment KPP_Ut when compared to SRunoff remained around 10 meters for all years and throughout the grid. This difference in MLD is observed even when comparing line 500 of year 1995, in which MLD was fairly well represented, and year 1999, in which the differences from the Palmer-LTER data surpassed 80 meters.

2.5 Discussion and Conclusions

An ocean circulation and sea ice version of the MITgcm was run in the WAP and tested for its skill to reproduce the sea ice cycle and MLD around the area of the Palmer-LTER grid, which includes the coastal, shelf and shelf-break region of the WAP. Although the model has been previously implemented and tested in [69], the questions addressed in that study were focused on larger scale distribution of freshwater sources

and did not evaluate in detail some aspects of the circulation and water mass features necessary to properly implement a biogeochemical model in the region. This study, therefore, focused on the distribution and variability of MLD, SIC and on whether the model properly simulated the water mass distribution on the shelf.

One of the modifications made to the initial setup of the model included an increase in the wind-sea ice drag coefficient, which had been previously decreased so that the freshwater fluxes in the GeorgeVI Ice Shelf would match observations. Since the areas that were improved by using a lower drag coefficient are outside of the Palmer-LTER grid, a new assessment of the impact of using a higher drag coefficient was not performed. Using a smaller drag coefficient, however, lowered the transport of sea ice and delayed its retreat during the spring, which lead to more sea ice melt in the Palmer grid and consequently shoaled the surface mixed layer. Increasing this coefficient improved the simulated sea ice by increasing the interannual variability of sea ice concentration and helped deepen the ML, although maintaining shallower values than observed in the Palmer-LTER dataset.

Shallow MLD in the Southern Ocean is a bias that has been previously observed in other modeling studies, and one of the possible causes is that models do not include the effects of Langmuir circulation. Ideally, including Langmuir circulation would include coupling the circulation model to a wave model. However, including a wave model is extremely time consuming and computationally expensive. Therefore, two different approaches were tested, based on the studies of L17 and LF17. The approach described in L17 represents Langmuir circulation as an enhancement factor applied to the turbulent velocity scale in the vertical mixing, while LF17 introduces a new formulation for the velocity scale. Since both approaches depend on wind speed, which is taken directly from the external forcing package, a correction term is applied to the wind speed to take into account the influence of sea ice. The term applied was adapted from the relationship between SIC and drag coefficient proposed by [1] assuming that the quadratic dependence of the drag coefficient on SIC linearly translates to the dependence of Stokes drift on SIC.

The approach that showed the best results were obtained using the lower wind-sea-

ice drag coefficient associated with the new formulation of the velocity scale, which deepened the ML and brought the results closer to the Palmer-LTER data. A bias towards shallower MLD persists, though, specially towards the northern part of the LTER grid. The model results were compared to the Palmer-LTER cruise data, which provides a valuable time series that is still limited in temporal and spatial resolution. Each cruise station was compared to model monthly means, therefore an exact match between observed and simulated data is not to be expected.

Overall, the model has a good representation of sea ice coverage and interannual variability, and successfully reproduced the seasonal distribution of the water masses present at the WAP in the shelf. Although there is a bias towards lower temperatures in the model in the water mass corresponding to CDW, warmer and more saline waters are found in the canyons that occur through the shelf, and this water mass is mixed and modified. This is important for the implementation of a biogeochemical model due to the higher nutrient content of the CDW in the WAP. Some of the errors found, especially close to the coast, can be attributed to the relatively coarse spatial resolution of the model and to the influence of local phenomena that is not represented in the model. Introducing a parameterization of Langmuir circulation increased the MLD, as expected, although the ML remains shallower in some of the comparisons with the LTER data, it is important to keep in mind that the data collected during the cruises might not accurately represent the monthly mean of the region.

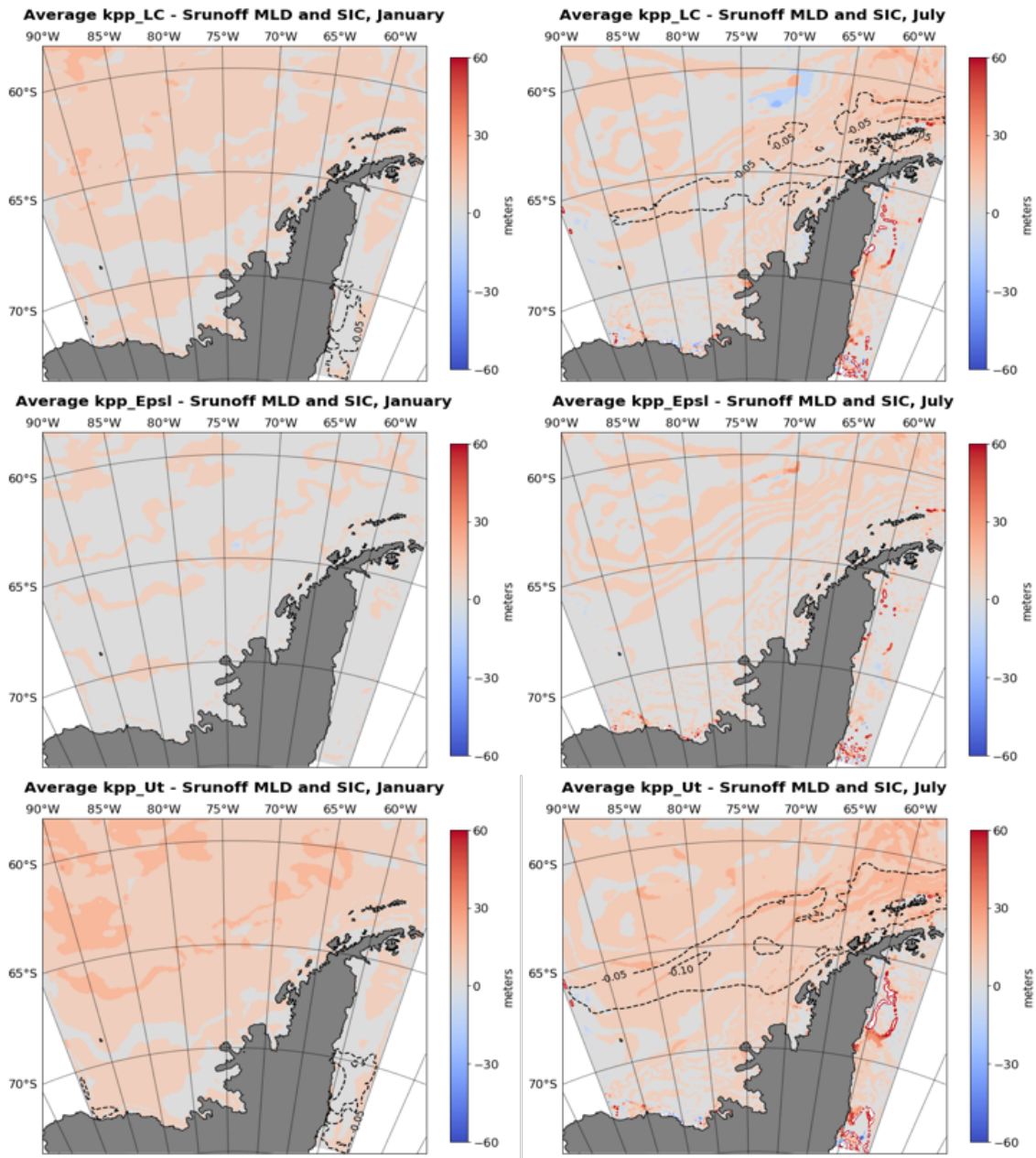


Figure 2-28: Calculated mean MLD difference between KPP_LC (top), KPP_epsI (middle) and KPP_Ut (bottom) and the Srunoff experiment for January (left) and July (right). Dashed contours indicate differences in sea ice concentration (SIC).

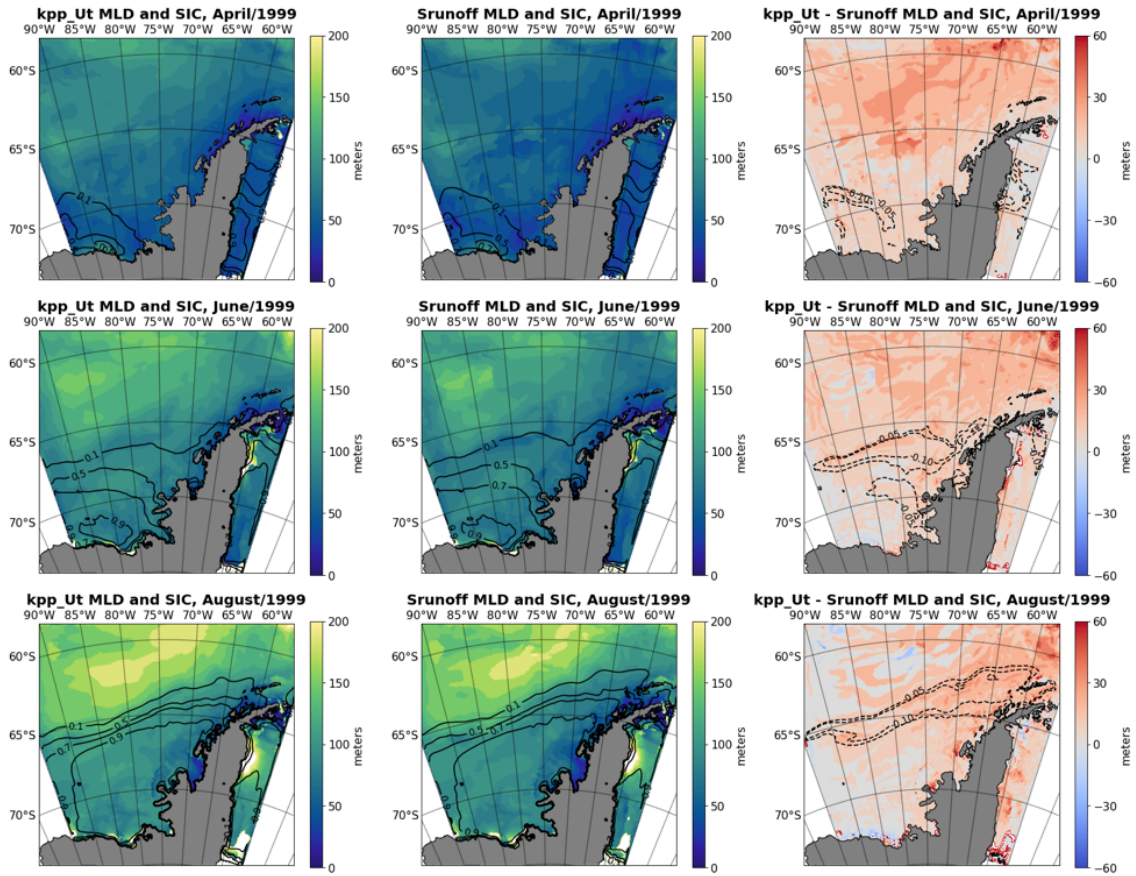


Figure 2-29: Mixed layer depth (MLD, in color) and sea ice concentration (SIC, contours) for experiment KPP_Ut (left and middle) and difference between KPP_Ut and ICEdrag (right) for April (top), June (middle) and August (bottom) of 1999.

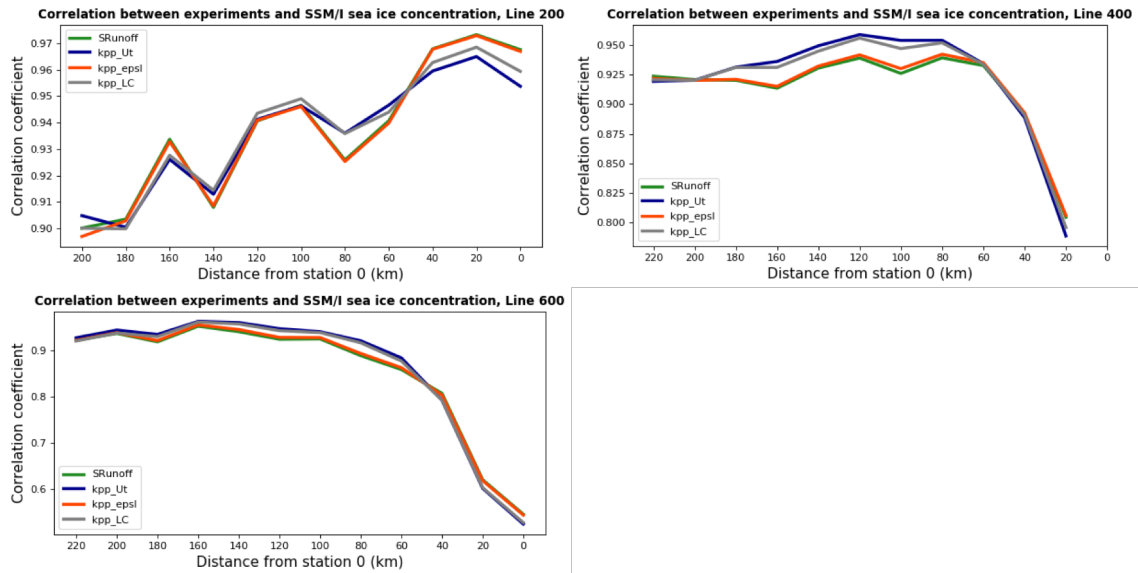


Figure 2-30: Correlation between experiments (legend) and SSM/I satellite data sea ice concentration (SIC) for the period 1991-2003 for lines 200 (top left), 400 (top right) and 600 (bottom).

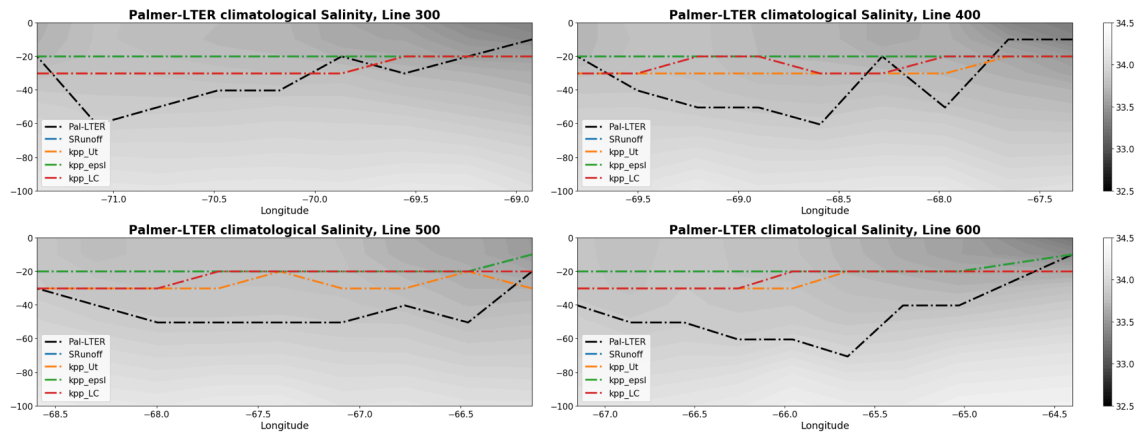


Figure 2-31: Mean calculated MLD for the Palmer-LTER data (black dashed line) and mean January MLD for each experiment (legend), for lines 300-600 of the Palmer-LTER grid.

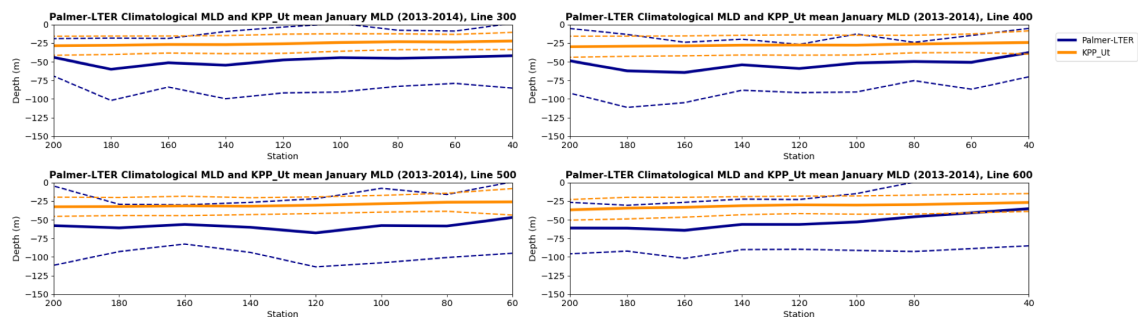


Figure 2-32: Climatological MLD calculated from the Palmer-LTER cruises (blue) and average MLD calculated from daily outputs for Januaries of 2013 and 2014 (orange) plotted for lines 300 to 600. The dotted lines represent a deviation of $1.96 \times$ the standard deviation for each dataset.

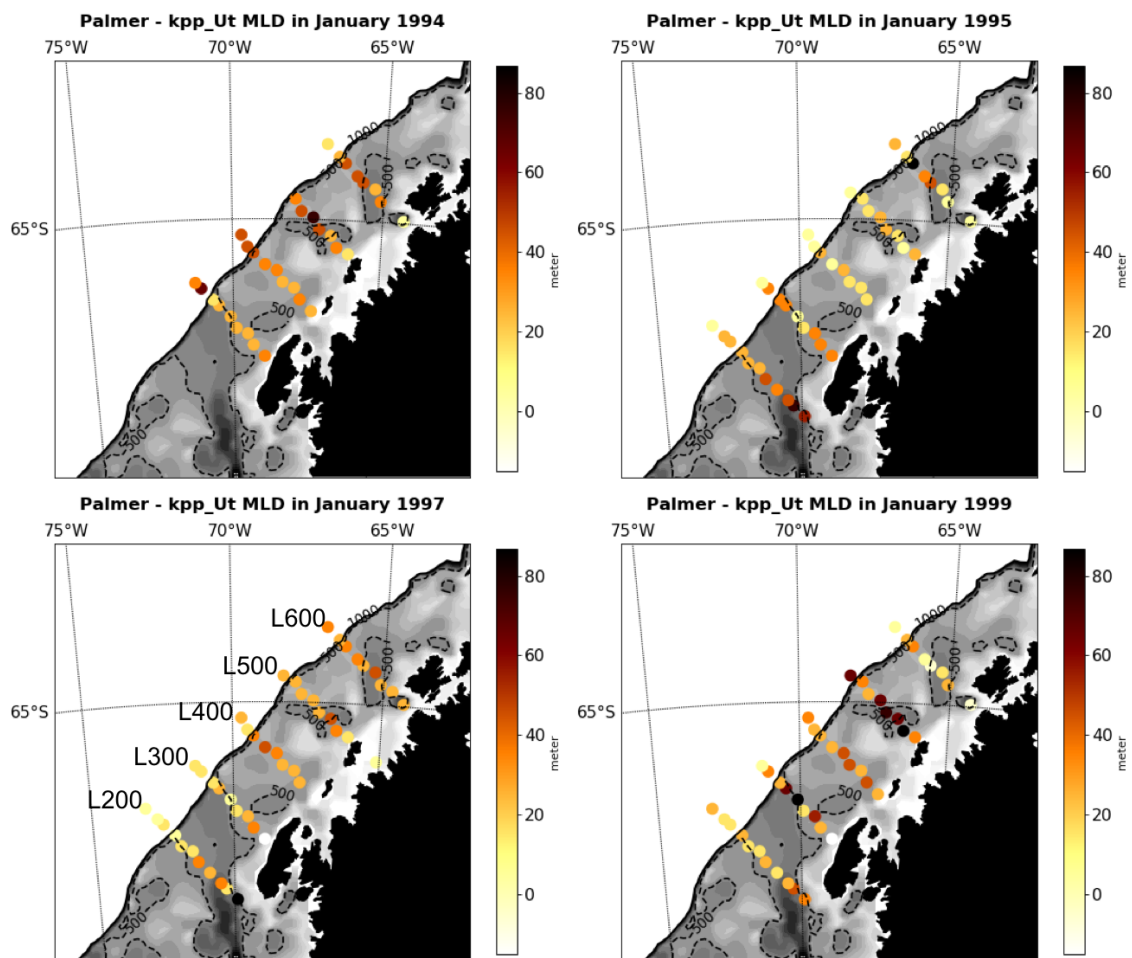


Figure 2-33: Difference between Palmer-LTER MLD and KPP_Ut MLD and bathymetry (grey scale) for the month of January of 1994 (top left), 1995 (top right), 1997 (bottom left) and 1999 (bottom right).

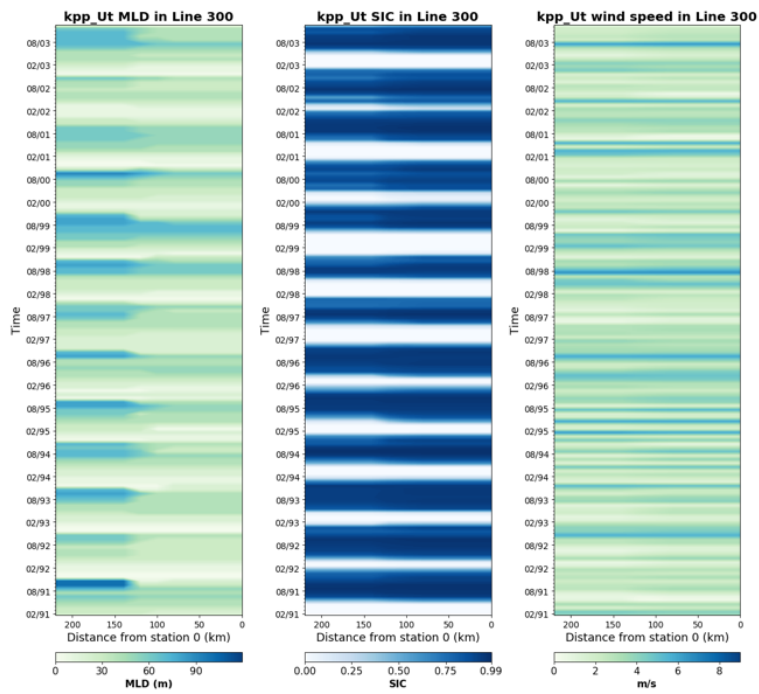


Figure 2-34: Time-series of MLD (left), SIC (middle) and wind speed (right) of experiment KPP_Ut for the points of line 300 of the Palmer-LTER grid.

Chapter 3

Implementation of biogeochemical model and analysis of chlorophyll patterns

3.1 Introduction

The substantial physical changes the west Antarctic Peninsula (WAP) has undergone in the past decades, including atmospheric and ocean temperature variations and substantial reduction in the sea ice season, have affected the ecosystem in this region up to higher trophic levels, with poleward shifts of ice dependent species and their replacement by ice avoiding species [17][72]. Understanding the mechanisms behind these changes could help us predict not only the future of the Antarctic Peninsula ecosystem, but also help us understand changes that could come to other places in the world where environmental changes have not yet been as significant as they have in the WAP. Also, the Antarctic continental shelves are thought to be an important sink of atmospheric CO₂ [4], and a mechanistic understanding of the effects of climate variability and climate change in the ecosystem of the WAP could also help quantify the response of the system to increased atmospheric carbon and its consequence for the global carbon budget.

The ecosystem in the WAP is characterized by bottom-up control [74], and the strong dependence of phytoplankton blooms on sea ice dynamics, ocean and atmospheric circulation mean that biological and physical factors need to be analyzed in conjunction in order to understand the changes observed. El Niño Southern Oscillation (ENSO) and the Southern Annular Mode (SAM) influence the sea ice concentration in the WAP [77], which in turn influences the timing and intensity of the phytoplankton bloom by controlling the stability of the water column through changes in the addition of meltwater and wind mixing, and the amount of photosynthetically available radiation (PAR) available for phytoplankton.

Macronutrients are not thought to be a major factor controlling phytoplankton blooms in the WAP given that their concentrations are usually high enough to sustain the bloom, only reaching depletion extremely rarely during particularly intense blooms [39]. Dissolved iron, on the other hand, is thought to be the limiting factor for the low chlorophyll concentrations observed in the open ocean and near the shelf break. Closer to the coast, iron is not thought to be a limiting factor for phytoplankton growth where concentrations can surpass 4 nM [3]. The understanding of the iron cycle in the region, however, is limited due to the lack of data. Although evidence suggests that glacial melt is the main source of dissolved iron to the region [3], the concentration of this micronutrient in the glacial end-member is still poorly constrained.

Combining the rich datasets collected through the Palmer-LTER program and the Rothera Time-Series (RaTS) with a circulation, sea ice and biogeochemistry model presents the opportunity to explore questions that cannot currently be answered with in situ data alone due to the gaps in temporal and spatial coverage. Also, using such a model allows us to test the hypotheses formulated thus far by analyzing the datasets. In this study, therefore, some questions will be addressed:

- Is the model able to reproduce the observed spatial and temporal distributions of chlorophyll in the WAP?
- What is the effect of the sea ice seasonal cycle, interannual variability and

thickness in transmitting PAR to the surface ocean, and how do non-linearities in the photosynthesis-irradiance (P-I) curve affect the phytoplankton blooms in sea-ice covered areas?

- What is the role of dissolved iron in controlling phytoplankton growth in the WAP?

3.2 Literature Review

The biology of the WAP is characterized by high interannual variability due to the influence of Southern Annular Mode (SAM) and El Niño Southern Oscillation (ENSO). Around Palmer station, for example, [74] found that the vertically integrated peak summer chlorophyll varied by a factor of five between years. Although the magnitude of biological variables differs from year to year some features are persistent, such as an observed onshore-offshore gradient with higher onshore levels of chlorophyll concentration, net primary production (NPP, [24]) and net community production (NCP, [20]).

The variability in primary production does not seem to be driven by macronutrients. In an analysis of 20 years of data, [39] found that macronutrients were only depleted under very intense blooms and that, overall, only 30% of the available nutrients in the mixed layer were used by phytoplankton. The abundance of macronutrients, therefore, indicates that blooms could be primarily controlled by a combination of physical factors, micronutrients and grazers.

Quantifying the influence of micronutrients is hard due to the lack of data in the region and the complexity of the iron cycle. Recent studies based on particulate and dissolved iron collected during the summers of 2010 through 2012 ([3]) suggest that the concentration of dissolved iron in the coastal areas of the WAP is patchy but can reach up to 4 nM, while offshore they are much lower (<0.1 nM) and suggest iron limitation. The study also suggested that glacial melt is the primary source of dissolved iron to the coastal regions, although the concentration of the glacial end-member has not been determined and estimates varied by a factor of 30 in the

LTER sampling grid. Previously published data on dissolved iron concentration (dFe) in glacial ice showed concentrations between 5-50 nM ([68]), however [3], using the difference in dFe concentration and contribution of meteoric water between 2011 and 2012 in the WAP, calculated a meteoric dFe concentration of 102 nmol/kg.

The magnitude and timing of the phytoplankton bloom in the WAP is also impacted by the presence of sea ice. Sea ice can influence PP by promoting stratification of the surface mixed layer upon melting (due to the input of low density freshwater), by protecting the surface layer from wind mixing, and by blocking radiation from reaching the surface ocean. Among all of these effects, the effect sea ice has on mixed layer depth (MLD) seems to play a larger role in influencing PP than the effect it has in directly blocking PAR. [85], in a modelling study in the Southern Ocean, observes that the contribution of PAR to PP is largely uniform after a minimum threshold is reached, which happens when sea ice starts breaking in the spring, while [93], analyzing data from Ryder Bay, finds that phytoplankton bloom starts early in the spring when light levels are still low, below 1 mol photon/m²d. Light limitation, therefore, does not seem to be an issue during the growing season, even when sea ice is still present.

The link between the presence of sea ice and lower MLD in the coastal and mid-shelf areas of the WAP has been established [94], and several authors argue that shallow MLD leads to higher values of PP, NCP and chlorophyll concentrations [20][15][39][94]. More important than the overall sea ice concentration during the winter, shallow MLD seems to be related to a later sea ice retreat, which would protect the surface ocean from strong wind mixing in late winter and early spring [94][71].

The effect of the Southern Annular Mode (SAM) on the seasonal cycle of sea ice and chlorophyll at Palmer Stations is detailed in [39]. In a principal component analysis of the chlorophyll time series, the authors find that the first component, which explains 26% of the variability, is related to a long bloom starting early December and lasting until March, with the largest peak in March and an earlier secondary peak in December or January. This bloom likely represents succession of different

phytoplankton assemblages and the interannual variability of the first component can be explained by the influence of SAM. When SAM is negative during the winter preceding the bloom, increased sea ice conditions promote stability in the surface layer upon melting, facilitating the phytoplankton bloom by creating a shallow ML. When SAM is positive in the spring, however, more mixing occurs due to increased wind. The increased mixing will inhibit diatom growth but promote blooms by different phytoplankton types throughout the summer. The second principal component for chlorophyll described in [39] explains 20% of the variance and describes blooms starting late spring and peaking in December. This pattern can be explained by low sea ice extension in October, linked to La Niña conditions. The second principal component of dissolved silica drawdown shows a similar pattern, indicating a predominance of diatoms.

Although shallow ML is known to increase photosynthesis by keeping phytoplankton close to the surface, where PAR is higher, [93] also point to the possibility of higher mixing leading to lower concentrations of dissolved iron, since the inputs of this micronutrient happen close to the surface and deeper waters are expected to have lower concentrations. The authors also found that in years of low chlorophyll concentrations both the short-term net growth rate and net loss rate were higher, indicating a strong role of ecosystem dynamics in controlling the phytoplankton population. At bloom termination light and macronutrients are still available in the WAP, and better understanding the effects of grazing in the phytoplankton population is important to identify the mechanisms that determine the end of the bloom.

Besides changes in total PP, different years also present different phytoplankton community composition, and given that the WAP is a bottom-up system [74], different phytoplankton assemblages may lead to different ecosystem composition at higher trophic levels as well. [24] find that the first stage of the phytoplankton bloom in the WAP is composed primarily by diatoms, which are replaced by smaller phytoplankton (mostly cryptophytes) during a second stage. In years when the blooms are smaller there is a higher concentration of cryptophytes and other small phytoplankton and higher abundance of salps in the zooplankton assemblage. In contrast, years of large

PP exhibit diatom dominated blooms and predominance of krill in the zooplankton.

Cryptophytes are generally spatially and temporally segregated from diatoms, and are associated, near Palmer Stations, with mid-shelf fronts and low salinity plumes [74]. At Rothera Station the same segregation between phytoplankton types is observed, and cryptophytes are associated with glacial meltwater, low nutrient stocks found after the bloom and low PAR during the winter [70]. The Rothera Station time series (RaTS), which contains invaluable winter data, data also shows that in years when summer is preceded by winter with strong mixing, the phytoplankton composition of the bloom tends to be similar to the winter composition, with high percentage of small phytoplankton. The RaTS dataset also shows that in both low and high PP years the timing of the bloom is similar, starting in mid-August [93] and contributing to the hypothesis of grazing control in the early stages of the bloom.

If the trend of decreasing sea ice persists, it is expected that phytoplankton concentrations will be lower in the future and that there will be a change towards smaller species [70]. A change towards smaller phytoplankton could also lead to less biological export of CO₂ to the deep ocean, limiting the capacity of the coastal regions to act as a carbon sink. This study, therefore, is aimed at improving the understanding of the drivers of phytoplankton bloom and succession in the WAP. Given the lack of iron data, models become a powerful tool to test the hypotheses currently formulated on the influence of this micronutrient in the phytoplankton bloom, as well as provide an insight on the extent of the influence of glacial discharge as a source of micronutrients.

3.3 Methods

For this study, an ocean circulation, sea ice and biogeochemistry model was implemented and compared to in situ data collected in the WAP. The physical part of the model, as well as its skill assessment, is described in chapter 2 of this thesis. The biogeochemical model, as well as the changes and setup details, are described below.

3.3.1 Model Description - Regulated Ecosystem Model with two Phytoplankton Classes(REcoMv2)

REcoMv2 is a relatively simple marine biogeochemical model containing two different phytoplankton groups, one zooplankton group, one detritus compartment and organic and inorganic forms of the main nutrients (iron, nitrogen, silica and carbon). The emphasis of the model is on phytoplankton physiology, and cellular stoichiometry is variable. In total, the model solves a mass balance equation for 21 tracers of the form:

$$\frac{\partial A}{\partial t} = -(U + w) \cdot \nabla A + \nabla \cdot (\kappa \nabla A) + S(A) \quad (3.1)$$

where A is the concentration of a tracer, U is the three-dimensional advection velocity, κ is the turbulent diffusivity and S represents the biogeochemical sources and sinks of the tracer. Both the velocity and the diffusivity are given by the physical model, and the sinking velocities (w) increase linearly with depth for detritus and is constant for phytoplankton. The biogeochemical sources and sinks are described below. The phytoplankton equations are calculated separately for diatoms and small phytoplankton, using different parameters that are adjusted to represent their physiology. Although bacteria are not added as a compartment in the model and therefore not explicitly modeled, the functionality is added via the remineralization terms.

The Antarctic ecosystem is relatively simple in terms of food-web complexity if compared to lower latitude ecosystems, and macronutrients are not thought to be limiting in this region. The choice of a model with a single heterotrophic compartment and that does not differentiate between new and regenerated nitrogen, therefore, seems appropriate to represent the phenomena of interest for this study without the addition of extra compartments. Adding unnecessary complexity to the model would result in a more computationally expensive model and complicate the skill assessment process by introducing more variables that could need sensitivity analysis tests.

Inorganic Carbon

The sources of dissolved inorganic carbon (DIC) are respiration, remineralization of detritus and dissolution of calcium carbonate detritus, while the sinks are fixation by primary production and formation of calcium carbonate. Alkalinity is increased by nitrogen assimilation and dissolution of calcium carbonate, while it is decreased by remineralization of organic matter and calcification.

Ocean-atmosphere CO₂ fluxes are calculated using atmospheric partial pressure of CO₂ (p_{CO_2} , which needs to be provided), DIC, total alkalinity (TA), temperature, salinity and wind at 10 m altitude. The code to calculate the CO₂ flux (F_{CO_2}) is based on the Ocean Carbon-Cycle Model Intercomparison Project (OCMIP), which uses a quadratic relationship with wind based on the [95] calculation for piston velocity. Chemical enhancement is also taken into consideration. The surface CO₂ concentration is calculated at every time-step following the DOE Methods Handbook ([14]) using DIC and TA, and the gas exchange is treated as a boundary condition for DIC. The calculated flux, therefore, can be either a source or a sink of DIC.

Inorganic Nutrients

All the inorganic nutrients have photosynthesis as a sink, being taken up by phytoplankton (small and diatoms). The biological uptake and release of dissolved inorganic nitrogen (DIN) and dissolved silica (DSi) are linked to variable nutrient to carbon ratios, but the proportion relative to carbon is fixed for dissolved iron (dFe). The source of DIN is remineralization of DON, while DSi is replenished by remineralization of detrital silica. The total dFe is assumed to be the sum of the inorganic bound or “free” iron (Fe’) and the organic complexed form (FeL, where L is a ligand). These two forms are assumed to be in chemical equilibrium according to

$$K_{FeL} = \frac{Fe' \times L}{FeL} \quad (3.2)$$

where K_{FeL} is the equilibrium constant. The sources of iron are respiration (by phytoplankton and heterotrophic), remineralization of dissolved organic carbon

(DOC) and zooplankton excretion. The sinks of dFe are photosynthesis and scavenging, which is proportional to detritus concentration.

Phytoplankton

The phytoplankton equations are based on a modified version of the physiological model of [25]. The model used here also includes grazing and aggregation of [75] and the formation and loss of silica of [33]. All the physiological rates depend on the intracellular ratios of N:C, Chl:C and Si:C. Chlorophyll (Chl) is calculated as a function of irradiance (I) and nitrogen assimilation. It is remineralized at a constant rate and lost by aggregation and grazing.

Nitrogen Pool The phytoplankton N pool is assumed to be proportional to the carbon biomass and is built up by the assimilation of DIN. Excretion enriches the DON pool and is downregulated at high intracellular N:C ratios. Phytoplankton aggregation and grazing transfer N to the detritus and zooplankton pools. The uptake of N depends on a maximum photosynthesis rate, which is calculated for carbon and converted using a C:N ratio (q). The uptake is affected by intracellular N status and extracellular N through Michaelis-Menten kinetics. The uptake equation, then, is represented by:

$$\alpha_{phy}^N = p_{phy}^{max} \times \sigma_{phy}^N \times f_{phy}^{lim} \times \left(\frac{DIN}{DIN + K_{phy}^N} \right) \quad (3.3)$$

where α_{phy}^N is the assimilation rate, p_{phy}^{max} the maximum photosynthesis rate, σ_{phy}^N is the optimal N:C uptake ratio, f_{phy}^{lim} is the N limitation term resulting from the internal N quota, and K_{phy}^N is the half-saturation constant.

The model uses a uniform general limitation function for all types of quota (q) regulations, given by:

$$f(q_1, q_2, \Theta) = \left\{ 1 - \exp(-4\Theta \times (q_1 - q_2)^2) \right\} \quad (3.4)$$

if $q_1 < q_2$ and 0 if $q_1 > q_2$. This equation gives a limitation term close to one if q_1

$\ll q_2$ but tends to zero if $q_1 \rightarrow q_2$. Θ is a dimensionless constant that determines how close q_1 and q_2 have to be to significantly decrease f . For N, the limitation is calculated as:

$$f_{phy}^{lim} = f(q_{phy}, q_{phy,max}, \Theta_{max}) \quad (3.5)$$

where q_{phy} is the nitrogen to carbon ratio, and $q_{phy,max}$ is a determined maximum for this ratio.

Carbon Pool The source of carbon to phytoplankton is assimilation during photosynthesis, while the loss terms are excretion of DOC, respiration, aggregation and grazing. The photosynthesis rate is a saturating function of the photosynthetically available radiation (PAR), with saturating light level being determined by the internal chlorophyll status. The initial slope of the photosynthesis-irradiance (P-I) curve is obtained by multiplying light harvesting efficiency per chlorophyll (α) with intracellular Chl:C ratio (q_{phy}^{Chl}). The photosynthesis equation, then, is given by:

$$P_{phy} = P_{phy}^{max} \times (1 - \exp(-\alpha_{phy} \times q_{phy}^{Chl} \times \frac{PAR}{P_{phy}^{max}})) \quad (3.6)$$

where the apparent maximum photosynthetic rate (P_{phy}^{max}) is based on the true constant maximum photosynthetic rate but varies with external dFe, temperature and the metabolic state of the cell. Growth is faster at higher temperatures, and this is parameterized using a maximum growth rate with an Arrhenius function, while growth limitation by iron is represented by a Michaelis-Menten term. For diatoms, photosynthesis is also regulated by a silica limitation term calculated using an equation similar to equation 3.4, where q is the silica to nitrogen ratio.

Chlorophyll Chlorophyll is degraded at a constant rate and lost via aggregation and grazing, with synthesis being proportional to nitrogen assimilation.

Zooplankton

The growth term for zooplankton in the model is based on grazing on phytoplankton, while the sinks are excretion and a quadratic mortality term. Sloppy feeding and feces transfer part of the grazing directly into the detritus pool, and a term is added to include preference for diatoms during grazing.

Detritus and Dissolved Organic Matter (DOM)

The detritus compartment, also described in terms of N and C pools, grows due to phytoplankton aggregation, sloppy feeding and zooplankton mortality, while the loss terms are degradation to DON and DOC. The remineralization is done at a constant rate that is modified by temperature.

Excretion and degradation of detritus are the sources for the DOM compartment, which is separated into DON and DOC. The sink of DOM is remineralization into DIC and DIN, which occurs at a fixed rate that is altered by Arrhenius function to account for temperature effects.

Nutrient and Light Limitation

While DIN and DSi limitations are calculated following the general limitation term previously described, the iron limitation is calculated using a Michaelis-Menten kinetics:

$$l_{lim}^{Fe} = \frac{dFe}{dFe + K_{Fe}} \quad (3.7)$$

Where l_{lim}^{Fe} is the limitation and K_{Fe} is the half-saturation constant. The most limiting nutrient determines the maximum production (P^{max}), which is then multiplied by the light limitation factor:

$$l_{lim} = 1 - \exp\left(\frac{-\alpha_{phy} \times q_{phy}^{Chl} \times PAR}{P^{max}}\right) \quad (3.8)$$

Light limitation, therefore, depends on the nutrient limitation and both limitations

vary from zero to one, with primary production being lower the closer the limitation terms are to zero.

3.3.2 Experiment Setup

The physical setting of the model, including the grid, physical forcing files and setup is the same as experiment KPP_Ut described in chapter 2 of this document. An initial control run (CTRL) was run without any changes to the original biogeochemical model and using GLODAPv2 data (described below) to build the initial condition and boundary files for DIN, DSi and DIC. The experiments were run for 31 years starting in 1984. The first 7 years (1984-1990) were considered spin-up, and data were analyzed from 1991 until 2014. The outputs are saved every 10 days.

Including non-linearities in PAR due to sea ice influence (PAR_NONL)

[48] argue that sub-grid scale variability in sea ice thickness influence NPP and should be taken into account when calculating the light influence on phytoplankton growth. Instead of using the grid cell mean irradiance to compute NPP, the authors account for the sub-grid scale effects by calculating the light limitation under each sea ice category and averaging the result. This approach, for the study conducted with the 1 degree of latitude/longitude simulation using CESM (Community Earth System Model), delayed the onset of the phytoplankton bloom and increased interannual variability of NPP in the Southern Ocean seasonal ice zone.

The theoretical explanation that justifies this approach is that, for the irradiance levels typical of surface oceans, the rate of photosynthetic carbon fixation (P) will be higher if calculated for the average of different irradiance levels (I) than the average P calculated for each individual I due to the non-linearities of the P-I relationship due to the concave shape of the P-I curve. In short:

$$P\left(\frac{I_1 + I_2}{2}\right) \geq \frac{P(I_1) + P(I_2)}{2} \quad (3.9)$$

In order to implement the non-linearities in the light limitation, a different equa-

tion should be implemented, of the form:

$$\overline{Limphy(I)} = \sum_{i=0}^n Limphy(I_i) \times A_i \quad (3.10)$$

where I_i is the irradiance at the surface of the ocean for open water and for each sea ice category, and A_i , ranging from zero to one, is the fraction of the grid cell covered by open ocean or the sea ice category. Changes had to be done to the code on the SEAICE package of the model, therefore, to create a variable that could store the short-wave reaching the surface of the ocean under each sea ice category and pass them to the biogeochemical model prior to averaging them. The details of for the implementation of these changes in the model are provided in Appendix B.

Description of forcing files

The biogeochemical parameters defined by REcoMv2 need initialization and boundary files, so that the fluxes at the boundaries of the grid can be properly calculated. To make these files, existing datasets need to be interpolated to the MITgcm-WAP grid. Large scale reanalysis datasets were used when available, and a lower resolution Southern Ocean basin REcoMv2 simulation was used for the biogeochemical tracers for which there are no datasets available.

DIN and DSi (dissolved inorganic nitrogen and silicate) For DIN and DSi, the dataset used to build the initial condition and boundary files was the World Ocean Atlas 2013, version 2 (WOA13v2, [7]), which is gridded from in situ data from several different sources. The data have 1° latitude/longitude horizontal resolution and 102 vertical levels for the annual climatology, with data also being available for seasonal and monthly averages. The monthly averages, however, only present data down to 500 meters depth. To build the input files for this study, the monthly climatologies were used from the surface to 500 m, and below this depth the annual climatological value was used.

DIC For DIC, the data used were from the Global Ocean Data Analysis Project version 2 (GLODAPv2), which is an international data synthesis project for interior ocean inorganic carbon data and related variables for the global ocean, described in more detail in [38]. It includes data from approximately one million individual seawater samples collected from over 700 cruises between 1972 and 2013. The variables encompassed by GLODAPv2 include salinity oxygen, nutrients, carbon dioxide, total alkalinity, pH and chlorofluorocarbons (CFCs). All the data collected are calibrated and used to produce global climatological maps. The maps created have a horizontal resolution of 1° of latitude and longitude and 33 vertical levels.

Total Alkalinity (TA) In this study GLODAPv2 data were used, and seasonal amplitude calculated from the dataset described by [82] was applied to the top 100 meters, assumed to represent the surface mixed layer. The Takahashi dataset contains surface data for a series of carbonate cycle variables and also for nitrate, phosphate and silicate. This dataset was built using the GLODAP, CARINA (Carbon Dioxide in the Atlantic Ocean) and LDEO (Lamont-Doherty Earth Observatory) datasets, and presents monthly averages for the surface ocean (data used in the calculation ranged from zero to 50 meters) with a horizontal resolution of 4° of latitude and 5° of longitude.

dFe (dissolved iron) Measurements of dissolved iron are relatively scarce and are not included in reanalyses such as World Ocean Atlas (WOA) or the Global Ocean Data Analysis Project for Carbon (GLODAP). Given this limitation, using an interpolation from a biogeochemical model is a reasonable alternative approach, and the forcing files were interpolated from the REcoMv2 grid described in [30]. The model results used for the interpolation are also from a version of MITgcm with REcoMv2 biogeochemistry, configured globally without the Arctic region. The model grid has horizontal resolution of 2° for longitude and a $1/3$ to 2° for latitude, with higher resolution around the equator and in the Southern Hemisphere, where latitude is scaled to the cosine of the latitude. It also has 30 vertical layers, ranging in

resolution from 10 m at the surface to 500 m in the deep ocean. The model was forced with the normal year atmospheric forcing fields from the coordinated ocean research experiments [42].

In the WAP, as well, dissolved iron data are scarce and information about dissolved iron (DFe) distribution and variability was only recently published by [2] and [3], using data collected during the Palmer-LTER cruises and at Rothera station as part of RaTS. The authors describe that dFe exhibits very high spatial and interannual variability, with concentrations reaching up to 8 nmol/kg in coastal waters with values lower than 0.1 nmol/kg in the mid to outer shelf, especially in the northern half of the Palmer-LTER grid. The dFe concentration was more closely correlated with meteoric sources (glacial melt and precipitation), implying that these are the major sources of the nutrient to this region. Although sea ice and dust sources appear to be minor, their relative importance is higher in the offshore areas due to the distance from the coast. The initial condition obtained from the global REcoMv2 grid had concentrations peaking around $0.4 \mu\text{mol}/\text{m}^3$ at the surface at Marguerite Bay and lower concentrations towards the northern part of the Palmer-LTER grid. Although these concentrations are lower than reported in the literature, the dFe gradients are consistent with observations. The dFe sources are also supplemented by input of dust and glacial sources.

Dust deposition is derived from the Model of Atmospheric Transport and Chemistry (MATCH) model detailed in [50]. MATCH is run globally, with a horizontal resolution of 1.9 degrees of latitude and longitude (T62 grid), 28 vertical levels from surface to 10 mb, and is driven by winds from the National Center for Environmental Prediction/National Center for Atmospheric Research (NCEP/NCAR) Reanalysis data set. The iron parameterizations in the model are from the Dust Entrainment and Deposition Model [98] and include wet and dry deposition and sources from combustion. The model diagnostic used was soluble iron deposition (sFEd_{dep}), provided in units of kg/m²d. The data were converted to $\mu\text{mol}/\text{m}^2\text{d}$ using standard atomic weight of iron of 55.845 g/mol.

Although glacial inputs are believed to be a significant source of dissolved iron to

the region, again the lack of data on the variability of iron concentration in glacial sources presents a challenge to properly simulate this input. The concentration of both particulate and dissolved iron in the WAP is thought to be highly variable, since the estimated concentration of the pure meteoric glacial melt water end-member varied by a factor of 30 in the LTER sampling grid [3]. These authors, however, estimated a meteoric dFe concentration of 102 nM based on the difference of meteoric water (obtained from oxygen isotopes) and dFe measured between the years 2011 and 2012. The high concentrations are due to source mechanisms involving dFe-enriching subglacial processes and glacial meltwater streams. Previously published literature, however, indicates glacial ice to contain between 5 and 50 nM of dFe in the Southern Ocean [68].

Considering that the glacial concentrations observed in the WAP are highly variables, the concentration chosen for this study was 50 nM, which corresponds to the higher end of the glacial concentrations observed. To avoid modifying the code, and taking advantage of the fact that the input of freshwater is at the surface, the glacial input of dFe was calculated to scale to the general surface runoff described in chapter 2, but was added to the file containing the atmospheric source of iron. Therefore, both atmospheric and glacial sources are forced at the surface of the grid by the same file and at a daily frequency. The glacial iron input, therefore, is higher during the summer months following the freshwater input, but lacks interannual variability which is difficult to predict in this region due to the lack of data and the influence of local phenomena in the coastal areas.

Initial and boundary conditions for the remaining biogeochemical tracers were also obtained from the REcomv2 grid described in [30].

Description of experiments

The control experiment for this study (CTRL) uses the same setting for the physics described in chapter 2, and the same parameters for the biogeochemical model used in [28]. Experiment PAR_NONL is similar to the CTRL run, but with the modifications in the PAR and sea ice packages described in Appendix B. For the skill assessment

of the biogeochemical model, parameters related to phytoplankton growth and dFe controls were modified and the skill of every simulation to reproduce data from the Palmer-LTER project was assessed. The parameters modified included pzdia, which is a measure of the preference of zooplankton grazing on small zooplankton, maximum photosynthesis rate for small phytoplankton and diatoms, Fe:N intracellular ratio for phytoplankton, half-saturation constant for iron uptake, initial slope of the P-I curve for both phytoplankton types, Fe scavenging rate and grazing rate. The range of values used for these experiments, names exp1 to exp20, is provided in Appendix A.

CTRL and PAR_NONL experiments were integrated over 31 years (1984 to 2014), with the first 7 years considered spin-up. The sensitivity analysis experiments (exp1 to exp20) were initially integrated for 7 years, and years of integration 3 to 7 were analyzed. For the skill assessment of experiments exp1 to exp20, monthly mean surface chlorophyll outputs for each test were compared to the same outputs from experiment PAR_NONL. Some experiments were discontinued after the initial 7 year integration, based on whether they showed higher chlorophyll concentrations offshore, higher concentration of small phytoplankton relative to diatoms, or if phytoplankton growth was suppressed. These criteria were based on the assessment that both CTRL and PAR_NONL overestimated chlorophyll in the shelf break and offshore areas, but that both presented a smaller bloom of small phytoplankton following the diatom bloom as described in the literature. The choice to run the skill assessment experiments for a shorter amount of time was done in order to avoid spending computer time unnecessarily.

Data used for skill assessment

Rothera Oceanographic and Biological time-series (RaTS) The RaTS time-series [10] is a component of the Long-Term Monitoring and Survey core programme of the British Antarctic Survey (BAS). The RaTS main station is located at Ryder Bay around 4 km from the coast, at 68.156°W , 67.581°S , and at a depth of about 520 meters, but a second station nearby can be sampled instead depending on whether the conditions allow for researchers to reach the primary location. Ideally,

observations would happen every 5 days during the summer and weekly during the winter, but sampling is weather and sea ice dependent. The station can be reached by a small boat or by snow mobile if the ice is thick enough.

The data collection includes a conductivity-temperature-depth (CTD) cast to 500 meters and water samples at a depth of 15 meters, which is a depth representative of the chlorophyll maximum in most years. The water samples are analyzed for chlorophyll and macronutrients. RaTS started in January 1997 and is ongoing, but there are two periods when no data were collected. These are June to December of 2000, when the station could not be reached due to the sea ice conditions, and September to December 2001, because of a fire in the laboratory.

Palmer-LTER data The range of the Palmer-LTER cruise data has been described in chapter 2. For the analysis of the biogeochemistry, data from the Palmer Station E were also used. Station E is at the edge of the Palmer Station boating range, at approximately 200 m depth, and shows a signature of the Palmer Deep Canyon, thought to have increased presence of warm and nutrient-rich UCDW [73]. The station is sampled via a small boat ideally twice a week from October through March, and include CTD casts and bottle sampling for nutrients and chlorophyll. The data are available for download on the Palmer-LTER website (pal.lternet.edu). The Palmer cruises used in this study, and the dates in which they were conducted are on Appendix A.

The biogeochemical data available for the Palmer cruises are available as a table in either excel or csv format, and contain information on cruise, date, latitude, longitude, depth, position of the station at the grid and concentration of the variable. The position of the station on the grid is set, in the Palmer-LTER project, to reflect the distance from an initial point (000.000) on a grid tilted relative to latitude and longitude, so that increasing distance in the x and y axes of the Palmer grid reflect either going parallel or perpendicular to the coast. Therefore, the lines (e.g., 200.XXX, 400.XXX) are roughly perpendicular to the coast (considering that the coast is not a straight line), while the stations are separated every 20 km along the lines increasing

toward the offshore (e.g., 200.000, 200.020, etc).

The data available was separated by cruise and station, and the data provided was filtered so that the maximum distance between the data collected and the position of the station it represents in the grid was not larger than 5 km. Since some stations are sampled deeper than others, and in order to make the most of the data available, different datasets were built for each variable and for each cruise: one containing only surface data, one containing the data for all the stations that were sampled to at least 50 m and a third containing the stations that were sampled to at least 150 m. The data were then vertically interpolated to constant depth levels and saved in netCDF (Network Common Data Format) files containing the information about concentration, depth, latitude, longitude, and position (line and station on the LTER grid).

3.4 Results

3.4.1 Non-linearity in photosynthesis-irradiance (P-I) in the presence of subgrid-scale sea-ice variations

Experiments CTRL and PAR_NONL were compared to assess the changes due to the introduction of non-linearities of P-I curve under sub-grid scale sea ice thickness variations previously described. As a first assessment, the climatological monthly means were calculated for both experiments, and the surface chlorophyll concentrations are shown in Figure 3-1 for November to January, which should encompass the phytoplankton growth season. What is observed from the climatological monthly means is that in the CTRL run the phytoplankton bloom happens earlier, with high chlorophyll concentrations near the coast in November and throughout the shelf in December. In PAR_NONL, the bloom peaks in the northern part of the Palmer-LTER grid in December and in the southern part in January.

To assess how well each experiment compares to the Palmer-LTER cruises, cruise data were compared to the monthly geometric mean of the point closest to the sta-

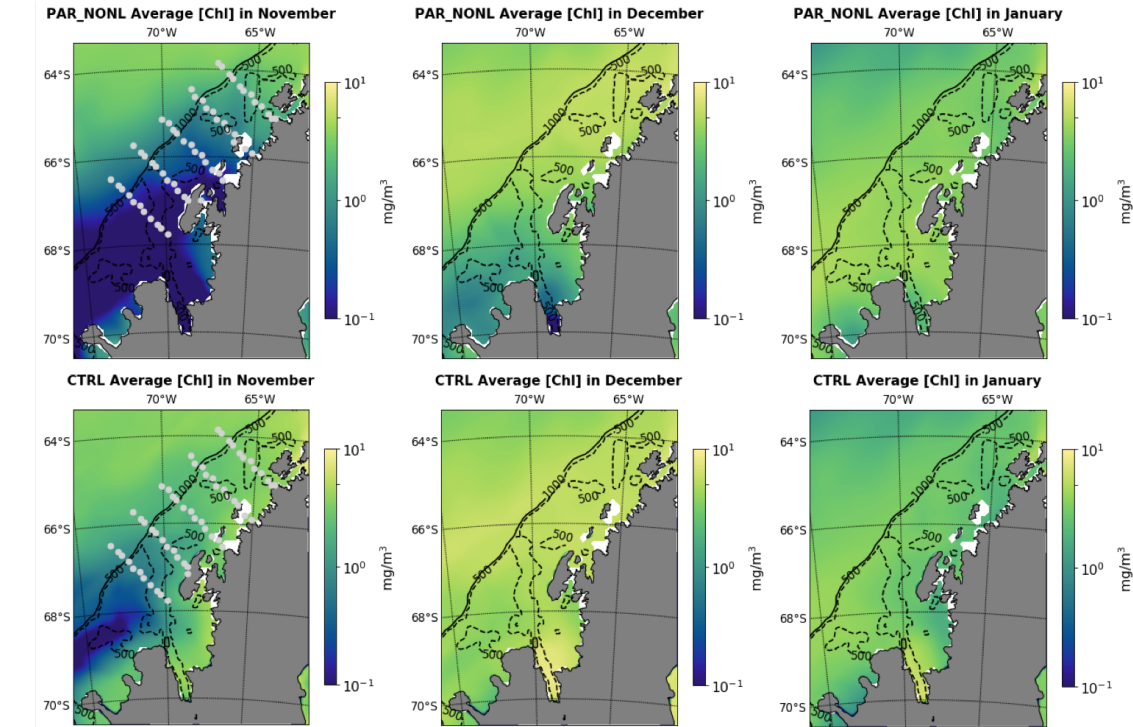


Figure 3-1: Climatological monthly mean surface chlorophyll for experiments PAR_NONL (top) and CTRL (bottom), for the months of November (left), December (middle) and January (right). Note the log-scale used in the color bar.

tions sampled in the MITgcm model grid, for the month in which the cruise occurred. Geometric mean is defined as the n th root of the product of n numbers and it provides a better representation of the mean state of a set of numbers with exponential distribution. For chlorophyll concentrations, therefore, geometric mean is used throughout this study rather than arithmetic mean. To check for changes in the interannual variability, the geometric mean maximum water column chlorophyll value of every station in the Palmer grid was calculated for both model results and Palmer-LTER data, and the deviations from this mean are plotted for the cruises in which each station was sampled, along with the maximum chlorophyll concentration, in figures 3-2 and 3-3 (for Palmer-LTER grid lines 200 and 600, respectively).

Although the surface chlorophyll maxima appear to be higher in the CTRL run during the month of December, the maximum water column chlorophyll concentrations during January show overall slightly higher values for PAR_NONL when com-

pared to CTRL, even though both experiments overestimate chlorophyll from mid-shelf to offshore relative to observations. On line 200, in some years with particularly intense blooms such as 2005 and 2006, PAR_NONL showed increased chlorophyll concentrations in the stations closer to shore, with a more evident onshore-offshore bloom compared to CTRL. However, in some years of low chlorophyll concentration in the observations such as 2003 and 2004, both model experiments show increased chlorophyll concentration relative to the mean, with higher positive anomalies in experiment PAR_NONL. The range of concentrations observed in the Palmer-LTER data is much larger than that found in the model results for both CTRL and PAR_NONL, which indicates that the model was not able to capture the variance exhibited by the observations. Although the onshore-offshore gradients are observed in some of the years in the model results, the magnitude of this gradient is much larger in the cruise data.

In the northern part of the grid (line 600, Figure 3-3), the difference between the CTRL and PAR_NONL results was less pronounced than in the southern part, which is to be expected given the higher influence of sea ice in the southernmost latitudes of the grid. On line 600, both experiments fail to capture large observed phytoplankton concentrations in 1996, 2006 and 2008. Also, both experiments overestimate maximum chlorophyll in the shelf break/offshore region. The Palmer-LTER data exhibits much higher chlorophyll close to shore in most years, while in both model experiments this gradient, if present, is barely noticeable.

To quantify if PAR_NONL was an improvement relative to the CTRL experiment, the spatial correlation coefficient was calculated for each year between the log transformed maximum chlorophyll measured at each station on all the lines during the Palmer-LTER cruises and the log transformed model output corresponding to the same stations and months of the cruises, with results shown in Figure 3-4. Although many of the years/cruises did not present statistically significant correlations, the CTRL run exhibited significant negative correlation with the Palmer-LTER data in 4 cruises (years 1993, 2004, 2012 and 2013, while negative correlation with the PAR_NONL results were only seen in cruise LMG04-01. Variance was also calculated for the chlorophyll data, and is shown in Figure 3-5. It is seen from this figure

that both CTRL and PAR_NONL experiments present much lower variance than in the observations, which was already observed in Figures 3-2 and 3-3 and is linked to the high chlorophyll concentrations simulated in the mid-shelf to offshore areas. Further tests indicate that the excessive chlorophyll concentration observed offshore in the simulations is attributed to excessive iron in the model forcing files.

Progression of the phytoplankton bloom throughout the growth season is measured at Palmer Station. In order to assess whether the experiments analyzed were able to capture the month of bloom initialization and bloom duration throughout the period analyzed, the monthly surface geometric averages for chlorophyll were calculated for experiments CTRL and PAR_NONL, for the period between October and April. Comparing model results with Palmer Station data is challenging, given that the stations are close to the coast and highly influenced by local phenomena that will not be captured in the model. Also, the horizontal resolution of the model makes it difficult to properly simulate coastal bathymetry and circulation. However, the main features of the interannual variability, which depend on larger scale phenomena, should be represented in the model.

Figure 3-6, then, shows the monthly geometric mean of surface chlorophyll concentration for the grid point closest to Palmer Station E, from October through April of each year and for experiments CTRL and PAR_NONL. Both experiments show blooms of similar magnitudes, but in some years the bloom starts a month later in the PAR_NONL experiment close to Palmer Station E. Some of the years described in [39] as having long blooms lasting from December through March (DJFM), such as 1995 and 2009 exhibited blooms starting in November in the CTRL run, while the blooms peaked in December in PAR_NONL. Years described as having November-December (ND) blooms such as 2010 and 2012 in the observations exhibited blooms starting in November on both runs. Although the timing of the bloom seems to be improved in the PAR_NONL experiment, year 2000, described as a ND year, shows a late bloom starting in December in PAR_NONL.

The simulated concentration of diatom and small phytoplankton chlorophyll was also analyzed for Palmer Station E, and Figure 3-7 shows the fraction of the surface

chlorophyll represented by small phytoplankton. In both CTRL and PAR_NONL experiments, the early bloom is dominated by diatoms while small phytoplankton increases towards the end of the season, consistent with the observations from the Palmer Station. Although results for CTRL indicate an earlier onset of the bloom in some years, both experiments presented similar phytoplankton succession.

Although the model experiments analyzed presented significant discrepancies from the data observed during the Palmer-LTER cruises, there is evidence to conclude that PAR_NONL represents an improvement over the CTRL run. Satellite analysis of net community production (NCP) on the WAP indicates that the phytoplankton bloom peaks at the shelf in December/January [47]. The high chlorophyll concentrations found near the coast in November in the CTRL run, therefore, indicates that the phytoplankton bloom happens too early in this experiment. It has also been observed that the phytoplankton bloom follows the sea ice retreat ([47],[94]), so that the bloom would peak first in the northern part of the grid as seen in the PAR_NONL results. Although in some years the spatial correlation with the Palmer-LTER cruise was significant and lower in the PAR_NONL experiment (compared to the correlations from CTRL), like in 2002 (LMG02-01) and 2004 (LMG04-01), in most years it was either similar or higher.

The parameterization of the effects on sea ice on PAR are thought to be more accurate in the PAR_NONL experiment, and that alone is an important argument to choose this experiment over CTRL for the next part of the thesis. Both experiments, however, present much lower spatial variance in the chlorophyll values compared to the Palmer-LTER cruise data and overestimate chlorophyll concentration offshore.

3.4.2 Assessing the timing of the bloom and possible limitations to phytoplankton growth for PAR_NONL experiment

The horizontal resolution of the model grid varies with latitude and longitude, but even the highest horizontal resolutions (near 6 km) still represent a larger area than

the decorrelation length scale found by [21] for biological processes, of around 4.5 km. The relatively large grid cells also lower the capacity of the model to fully capture mesoscale variability and to represent coastal features of circulation. These limitations, associated with the lack of interannual variability in the freshwater runoff inputs (and therefore in dFe inputs), make the point-to-point comparison between model and data challenging. Also, the cruise takes place over several weeks and can sample different stages of the bloom in different stations, which means that there is a temporal progression in the cruise data while the model monthly means represent the same period for every station. Some features of the cruise data are observed in the different years, however, such as the onshore-offshore gradient in chlorophyll concentration. The fact that the model results fail to represent these features in some of the years indicates that changes are necessary to better simulate the phytoplankton dynamics in the region.

To assess the skill of the model to represent the spatial distribution of chlorophyll in each year, the spatial correlation coefficient was calculated for each year between the maximum water-column chlorophyll concentrations observed at each station from the Palmer-LTER cruise observations and the maximum water-column chlorophyll of the corresponding model grid point (for the corresponding geometric monthly mean) of the PAR_NONL output, similar to the analysis done in Figure 3-4. The spatial correlation was calculated for all the points of the grid sampled at each cruise and also separately for the points of the southern part of the cruise (lines 200 and 300) and the northern part (lines 400, 500 and 600), defined as in [26]. The spatial correlations between the cruise data and the model output for December, January and February, for the southern and northern part of the grid are shown in Figure 3-8. Although most of the cruise data were collected during January, the correlations with model output from December and February is shown to assess whether discrepancies between model and data could be due to differences in the timing of the bloom.

While some years showed positive spatial correlations between the observed and January simulated data, like 1994 and 2006, in other years the spatial correlation was negative, like 2004 and 2011. Figures 3-9 and 3-10 show the spatial distribution of

maximum water column chlorophyll anomaly in the PAR_NONL experiment and in the Palmer-LTER cruise for a subset of years. For the calculation of the anomalies, the maximum water column chlorophyll concentration at each station during a particular cruise (or on the points corresponding to the stations sampled, in the model output) was obtained, the geometric mean of these maximums were calculated, and the anomaly is calculated as the water column maximum at each station for that cruise minus the geometric mean of the cruise maxima. The color bar, therefore, displays the spatial distribution of chlorophyll maxima at each cruise and in the simulation output for the month of the cruise being analyzed. It is seen that years with statistically significant, positive January model-data correlations (1994 and 2006, Figure 3-9) are also years in which the model successfully reproduces the onshore-offshore gradient in the chlorophyll concentrations. Another feature observed in 1994 and 2006, in which the correlation is statistically significant for the north and south regions individually and for the whole grid, is that the highest chlorophyll correlations in the PAR_NONL results are found in the southern region.

In 2004 and 2011 (Figure 3-10), PAR_NONL chlorophyll concentrations are higher in the offshore region during January. 2004 and 2011 are also the only year in which the spatial correlation between cruise data and model output is higher during the month of December. In most years the spatial correlation between cruise data and December model output is low, which is a reflection of the phytoplankton bloom first peaking in the offshore region in the beginning of the summer, following the retreat of sea ice. During 2003-2004, however, although sea ice had a late retreat offshore the retreat happened earlier in the shelf region, leading to higher chlorophyll concentrations closer to the coast during December. In the offshore region during this season chlorophyll only peaked offshore during the month of January, which also explaining the positive anomalies observed during these years in Figures 3-2 and 3-3.

It is also notable that the January model data performs better in years when the concentration of sea ice was high during the previous winter, like 1994, 2000, 2005 and 2006, both in the northern and southern regions of the Palmer-LTER grid. Years when sea ice concentration was low during the previous winter, however, such as 1999

and 2011, showed low correlation between the simulated and observed chlorophyll data. During years of low sea ice concentration, the mixed layer tends to be deeper due to less buoyancy gain from sea ice meltwater and more exposure of the surface layer to winds. Although observations suggest that a deeper mixed layer would lower PP due to light limitation, one possibility for the higher chlorophyll concentrations offshore in January during years of low sea ice is that a deeper ML decreases iron limitation in the offshore areas through mixing with subsurface iron-rich waters.

Figure 3-11 shows the climatological surface monthly mean dFe for the PAR_NONL experiment, for the months of December and January, and the anomalies from climatology for the December 2005, January 2006, December 2010 and January 2011. Although the dFe concentration tends to decrease towards offshore, it is relatively constant throughout the shelf on the northern part of the Palmer-LTER grid. It is also seen that dFe is higher in the southern part of the Palmer-LTER grid. During the summer of 2005-2006 a negative dFe anomaly is observed offshore, while during the summer of 2010-2011 a large positive dFe anomaly is observed in December and persists, although with less intensity, during January.

The surface dFe during January is indicative of how limiting this micronutrient will be during this month. However, dFe concentration is also affected by the timing and intensity of the phytoplankton bloom, so that lower dFe in December could also indicate an earlier bloom and a persistent positive dFe anomaly could indicate a less intense bloom. Although poor representation of dFe cycle or of the phytoplankton dependency on this micronutrient could be reasons for the decreased performance of the model in years of low sea ice, it is still important to consider whether the model is properly simulating the timing of bloom initiation.

Since the cruise data only provide one time point per station every year, one way to assess whether the model is missing the timing of the bloom is to look at the data collected at the Palmer and Rothera Stations, representing the near-shore northern and southern areas of the grid, respectively. Although station data provide temporal resolution, the stations are located close to the coast and influenced by local events, such as the presence of icebergs, calving and localized freshwater

discharges that will not be captured by the model. However, a consistent pattern in the differences between the model and the data, as well as differences in how the simulated phytoplankton responds to a specific change in the physical environment, could indicate whether changes are necessary in the model. What is observed from the time-series of PAR_NONL surface chlorophyll and the surface chlorophyll collected at Palmer Station E and Rothera Station (Figure 3-12) is that at both stations the model exhibits less interannual variability than in the station data, leading to low correlation between the observed data and the model results (<0.2), and that the bloom happens consistently later in the model compared to the data from Rothera Station. The next section of this chapter, therefore, is focused on sensitivity analysis for model parameters related to phytoplankton growth and losses, in order to improve the spatial representation of the bloom in the model as well as to correct for the late bloom observed in the southern part of the grid relative to the data from Rothera Station.

3.4.3 Sensitivity analysis of the biogeochemical model

The version of REcoMv2 used for this study utilized the same biogeochemical model parameters in [28], which integrates a lower-resolution simulation on a global grid without the Arctic region. It is expected, therefore, that adjustments will be needed in the phytoplankton growth and loss term parameters in order to better simulate WAP species and conditions. The iron cycle is another part of the model which may require adjusted parameters. Using a single iron-binding ligand and uniform iron concentration in the glacial input (which does not include interannual variability) is most likely an overly simplistic representation of the iron cycle in the region, but considering the lack of data available to develop a more detailed approach, adding complexity to the model may introduce further errors and make the interpretation of results more difficult. A set of 20 sensitivity experiments were carried out with adjustments to maximum photosynthesis rate for small phytoplankton and diatoms, Fe:N intracellular ratio for phytoplankton, half-saturation constant for iron uptake, initial slope of the P-I curve for both phytoplankton types, Fe scavenging rate and

grazing rate. Details of the adjustments made are shown in Tables 2 and 3 of Appendix A.

Changes to parameters related to the iron cycle were focused at increasing iron limitation offshore, given that there is evidence that increased iron supports offshore blooms in the model results while observations from the Palmer-LTER data suggest that this micronutrient is limiting far from the coast. Parameters related to phytoplankton growth and losses were aimed at adjusting the timing of the bloom, which was observed to be late compared to station data particularly in the comparison with the Rothera Station data in the south of the grid. The results from chapter 2 indicate that sea ice variability was well reproduced in the southern part of the Palmer-LTER grid, so it is likely that the delayed blooms are not a consequence of poorly represented sea ice in the model.

For the experiments described in Appendix A, surface small phytoplankton and diatom chlorophyll concentration from years 3-7 of the integration were compared to the results of the PAR_NONL experiment during the month of January, for the grid points corresponding to the Palmer-LTER stations. Some of the tests were discontinued after 7 years (period of the spin-up) due to one of the following reasons: they either showed no growth of small phytoplankton, presented higher chlorophyll concentrations in the shelf break and offshore stations compared to PAR_NONL, or presented no visible difference in chlorophyll concentration and timing of the bloom. The option to stop the sensitivity analysis experiments after spin-up was made to avoid spending computer time unnecessarily. Experiments 1, 7, 14 and 19, however, were run for the same 31 years as PAR_NONL. The spatial correlations between maximum water column chlorophyll in these experiments (exp1, exp7, exp14 and exp19) and the Palmer-LTER cruise data were calculated, similar to the analysis shown in Figures 3-4 and 3-8, and the results for the tests that represented significantly improved correlations, exp1 and exp19, are shown in Figure 3-13. To assess whether the timing of the bloom was changed significantly in exp1 and exp19, the spatial correlation between chlorophyll cruise data and monthly mean model outputs for December, January and February is shown in figure 3-14. For exp1, the initial slope of the P-I

curve, the the maximum photosynthesis rate and the iron to nitrogen ratio were increased for both small phytoplankton and diatoms (values shown on Appendix A), and the half-saturation constant for iron uptake was lowered. In exp19, maximum preference for grazing on diatoms was increased, as well as iron to nitrogen ratio and maximum rate of photosynthesis for both small phytoplankton and diatoms.

The sensitivity analyses indicate that changing the initial slope of the P-I curve and the maximum photosynthesis rate mostly changed the timing of the bloom, and a balance between the sets of parameters chosen for small phytoplankton and diatoms was necessary in order to prevent small phytoplankton from either taking over throughout the whole growth season or from not growing at all. Increasing the preference for grazing on diatoms also helped to promote succession from diatoms to small phytoplankton later in the growth season. The parameter that seemed to have the largest influence on the onshore-offshore gradient of chlorophyll was the iron to nitrogen ratio, although altering the iron half-saturation constant and the scavenging rate had only minor effects on the results.

In general, the sensitivity experiments improved the skill of the model to reproduce the chlorophyll concentrations observed in the cruises when compared to PAR_NONL, especially between 2011 and 2014. In the Northern region of the WAP (lines 400-600), the sensitivity experiments for years 1996 and 1997 had large positive spatial correlations with the Palmer cruises (PD96-01 and PD97-01), while PAR_NONL had negative correlation. PAR_NONL, however, had higher correlations during 2006, 2007 and 2009 (LMG06-01, LMG07-01 and LMG09-01). In the southern region (lines 200 and 300), Januaries of 2009, 2011, 2012 and 2013 had positive correlations between the sensitivity test experiments and the Palmer-LTER cruise data, while PAR_NONL had negative correlations with the cruise data, although in 2009 and 2013 the correlation was not significant at 0.05 level. In all experiments, the spatial correlations were similar when using the January and February data, and in general better than the spatial correlation with cruise data using December data, indicating that the model correctly represents the phytoplankton bloom first peaking offshore.

To understand the mechanisms that improved the model performance, the years in which the spatial correlation of the skill assessment experiments with the Palmer-LTER chlorophyll data showed the largest improvements relative to the correlations of the PAR_NONL experiment were analyzed in more detail. The years chosen for this analysis were 2011 and 2012. 2011 was preceded by a winter with low sea ice concentration and PAR_NONL showed negative chlorophyll spatial correlation with the Palmer-LTER data for the whole grid and for the southern and northern region, presenting particularly low and statistically significant correlation in the southern part of the grid. Both exp1 and exp19 showed positive spatial correlations during this season, although it was only significant at 95% confidence interval for exp1 in the southern area. 2012, on the other hand, was preceded by a winter of high sea ice concentration with an early retreat. While PAR_NONL showed positive (although not significant at 95% confidence) correlations with the Palmer-LTER data for the whole grid and for the northern part, the correlation was negative in the southern region.

In all of the stations analyzed and for all the experiments, DIN and DSi limitation terms had higher values than the dFe limitation term, indicating that dFe is the limiting nutrient for phytoplankton growth. Figures 3-15 and 3-16 show the average dissolved nitrogen and dissolved silicate measured during the cruises for lines 200 and 600, and the climatological mean DIN and DSi for the corresponding points in PAR_NONL. The Palmer-LTER DIN climatology was built using nitrate data and, when available, nitrate and ammonium. It is seen that although the average DIN and DSi concentrations in the model output are lower than observed during the cruises, macronutrients are not depleted, which is further indication that iron is acting as the limiting nutrient in the simulations. The data shown are for experiment PAR_NONL, but the similar ranges of concentrations are observed for exp1 and exp19.

For the comparisons, Taylor diagrams were plotted to get a full assessment of the statistics [84]. Taylor diagrams combine correlation, standard deviation and RMSE (root mean squared error) in a single two-dimensional plot. Since correlation is widely used to indicate pattern similarity but does not provide information on amplitude of

variation of a dataset, using this statistic in combination with standard deviation makes it easier to determine how much of the overall RMS difference is due to difference in variance compared to the error due to poor pattern correlation. The statistics are plotted on a polar style graph, where the radial distances from the origin to the point is proportional to the standard deviation. The azimuthal positions give the correlation coefficient between two fields, while the dashed line indicates the RMS error.

Year 2011 The summer of 2011 is preceded by a winter marked by low sea ice concentration, especially in the southern part of the LTER grid. The correlations between the MITgcm experiments and the LTER cruise data shows that exp1 and exp19 performed better in both the northern and southern regions and in the whole grid, while PAR_NONL has negative correlation with the cruise data. An analysis of the spatial distribution of maximum chlorophyll in the experiments and in the LTER cruise data shows that PAR_NONL presents higher chlorophyll concentrations from mid-shelf to offshore in all the lines, in sharp contrast with the other experiments and the cruise data, in which the bloom is observed in the stations close to shore (Figure 3-10). In the Taylor diagrams for the northern and southern regions (figure 3-17) it can be observed that all of the simulations analyzed present similar standard deviations for both regions and similar RMSE for the southern region. The high RMSE observed in the southern region for all experiments (PAR_NONL, exp1 and exp19) despite the positive correlations observed for exp1 and exp19 indicate that the model fails to represent the amplitude of variation observed in the chlorophyll data. Also, the southern region during 2011 is one of the only years in which the model data present negative bias in the chlorophyll data. On the northern region, on the other hand, the chlorophyll bias is positive but less than 1 mg/m^3 for exp1 and exp19, and higher than 2 mg/m^3 for PAR_NONL.

Although the phytoplankton bloom starts about one month later in line 200 compared to line 600, the temporal progression of the bloom and differences between exp19 and PAR_NONL are the same for both lines, and shown in figure 3-18 for

stations 40 and 160 of line 600. The low sea ice concentration decreases light limitation (increasing L_{limDia} and L_{limPhy}), leading to a very early onset of the phytoplankton bloom. The bloom starts earlier in exp19 due to the increased maximum photosynthesis rate and initial slope of the P-I curve. By January, the chlorophyll concentration is lower and continuously decreasing due to iron limitation. Iron is more limiting on exp19, however, so that both stations present chlorophyll concentrations below the climatological value in this experiment, while concentrations remain higher than climatology offshore in PAR_NONL given iron is less limiting compared to exp19. The climatological chlorophyll concentrations in exp19 are also lower than in PAR_NONL.

The chlorophyll concentrations observed during cruise LMG11-01 were really high in the southern part of the Palmer-LTER grid, presenting concentrations higher than 15 mg/m³ in station 200.040. During the summer of 2011, [3] observed, based on oxygen isotope data, that line 200 presented more meteoric water than the following years in line 200. The authors also noticed that this year also presented high dFe concentrations, with the largest enrichment observed in the southern edge of Marguerite Bay. Although coastal iron enrichment was observed throughout the coast, line 200 presented high iron concentrations across the whole line. The anomalously high chlorophyll concentrations observed, therefore, are likely to be due to increased glacial iron input during this year. Due to the lack of data, the model forcing presents seasonal variation in glacial inputs, but not interannual. Therefore, some of the variations observed in the cruise data, especially close to the coast, are not likely to be reproduced in the model.

Year 2012 During 2012, exp1 and exp19 presented higher correlation with the chlorophyll from Palmer-LTER cruise LMG12-02 than PAR_NONL for the whole grid and individually for the northern and southern parts of the Palmer-LTER grid. On the southern part of the grid, however, the correlations were high and positive for both exp1 and exp19, and close to -0.7 for PAR_NONL. On the Taylor diagram for the southern region during this cruise (Figure 3-19) it is seen that all experiments

overestimate chlorophyll concentration and present higher standard deviation than the observations, although both exp1 and exp19 present correlations above 0.9. In the southern region, 2012 is a year of high sea ice concentration, but with a fast retreat, as seen in figure 3-20, which shows sea ice concentration in stations 200.040 and 200.160 during October 2011 and April 2012.

Figure 3-21 shows the evolution of water column chlorophyll maximum and iron and light limitations for stations 200.040 (close to the coast) and 200.160 (close to shelf break) during October 2011 and April 2012, as well as the climatological maximum water column chlorophyll between October and April. It is seen that close to the coast in the southern region exp19 chlorophyll climatology shows an earlier bloom compared to PAR_NONL, while offshore the difference in the timing of the bloom is not observed. The earlier bloom is attributed to the differences in the growth parameters between experiments exp19 and PAR_NONL, which lead to less light limitation in exp19. Onshore, both experiments present a strong and early bloom, and show decreasing chlorophyll concentration during the month of January. In exp19, however, the January chlorophyll values are closer to the climatological values, while PAR_NONL shows lower values compared to climatology throughout the whole month, sustained by higher growth rates. Offshore, however, both experiments show an earlier and pronounced bloom, with decreasing concentrations by January. PAR_NONL, however, shows less iron limitation, so that the decrease of the bloom is less sharp between January and March. It is observed, therefore, that both the increases in growth parameters and in iron limitation play a role in increasing the onshore chlorophyll concentrations relative to offshore values, similar to what was observed in the northern part of the region in 2011.

3.5 Discussion and Conclusions

A biogeochemical model was implemented on the circulation and sea ice version of the MITgcm for the WAP region described in chapter 2. The results were compared to data collected at Palmer Station E, to the RaTS dataset and at the Palmer-LTER

cruises. While data collected at Station E and Rothera Station present higher temporal resolution, these stations are coastal and highly influenced by local phenomena, which make the simulation of the values observed very difficult. The cruise data, in contrast, present higher spatial resolution but only a sample per cruise at each station collected. Performing a skill assessment of the model using these sets of data, therefore, provides some insight on the mechanisms that lead to the interannual variations observed in the phytoplankton blooms.

Traditionally in biogeochemical models, light limitation in sea ice covered areas is calculated using the sum of the PAR that reaches the surface ocean at different sea-ice categories in the model. An approach described in [48], however, suggests that using PAR that passes through sea ice leads to an overestimation of PP due to sub-grid scale variability in light transmission through different sea-ice categories. The solution described in the study of [48], which consists of calculating the light limitation under each sea-ice category and using the sum of the limitations to calculate primary production, was used in this study. Using this approach lead to higher interannual variability and improved the comparisons with observations, with phytoplankton blooms happening during December and January at the Palmer-LTER grid.

Other adjustments to the model, however, were necessary given that the initial setup of the biogeochemistry was adjusted to a much larger grid with lower horizontal resolution described in [28]. A set of experiments was run with different values for iron uptake and limitation, growth parameters and grazing. An initial skill assessment consisted of using Taylor diagrams to compare the cruise data to the monthly mean chlorophyll concentration from the month in which the cruise occurred. The experiments that performed better were then further analyzed to identify which changes improved the performance of the model.

While DIN and dSi presented a lower bias in the model results, they did not limit PP, which was assessed by looking at the limitation terms. The availability of iron, however, proved to be important for proper representation of the values observed in the cruises. While validating the iron concentration throughout the grid and time

series is impossible at the moment due to the low amount of data collected in the region, some of the differences observed in the results concur with hypotheses that had been previously formulated for the sources of dFe and how it affects PP in the region. It is thought, for example, that iron limitation is key for the observed onshore-offshore gradient in chlorophyll concentrations in the WAP. Indeed, increasing the amount of iron needed for phytoplankton growth limited PP in the offshore stations more than in the coastal and shelf stations.

Years of high sea ice concentration presented the best correlations with the cruise data. In these years, the bloom is delayed and has faster growth, which leads to a faster iron depletion. This depletion is more marked offshore, where the blooms happens earlier and supply of iron through glacial sources is not available. In years of low sea ice concentration, however, the model had lower correlation with the cruise data. This happens at least partially because iron limitation is decreased in offshore regions due to mixing once the ML deepens. While nutrient replenishing due to ML deepening is to be expected, the increase in phytoplankton, which is not observed in the data, suggests that the inputs used for dFe are overestimated. It is important to notice, however, that the role of zooplankton in controlling the phytoplankton bloom is yet to be fully analyzed.

Although the iron concentrations in the model were highest at around 1 nM, which is lower than the highest concentrations previously observed in the coastal areas by [2][3], the chlorophyll concentrations had a positive bias compared to the cruise data, suggesting that the iron cycle in the region needs to be better understood to be properly simulated. In some years, like 2006 and 2011, the model correctly predicted a bloom in January but with negative bias in the chlorophyll concentration. In 2011, which is one of the only years for which dissolved iron data are available, both meteoric water and dissolved iron were observed to be higher than in 2010 and 2012, especially close to Marguerite Bay. In the model results during 2011, chlorophyll concentrations had negative bias throughout the LTER grid, but the difference was larger in line 200 (which is the closest to Marguerite Bay), suggesting that the high variance observed in the Palmer-LTER chlorophyll data could be influenced by uneven and highly variable

sources of iron. Data on freshwater sources are also scarce in this region, however, especially at the temporal resolution required to provide interannual variability.

While further sensitivity analysis could improve the model performance, the model capacity to properly reproduce the data variability observed in the Palmer-LTER data is hindered by the lack of data on glacial inputs and in the dFe endmembers of the different water masses in the WAP. The experiments that showed increased spatial correlation with the Palmer-LTER data also showed higher correlation with the coastal stations compared (Rothera Station and Palmer E). However, given that coastal stations are highly influenced by sub-grid scale phenomena that are not captured in the model, the correlation between maximum water column chlorophyll concentration from the RaTS dataset and exp19 was still close to 0.4.

The model, however, succeeds at reproducing the evolution of the phytoplankton bloom in the WAP and the spatial distribution of chlorophyll in January during most of the years analyzed. Although there are limitations in the skill assessment of the model due to lack of observations in this area, this is precisely the reason why this model is a useful tool to test some of the hypotheses related to phytoplankton bloom and fate of organic matter in the WAP generated by the Palmer-LTER project.

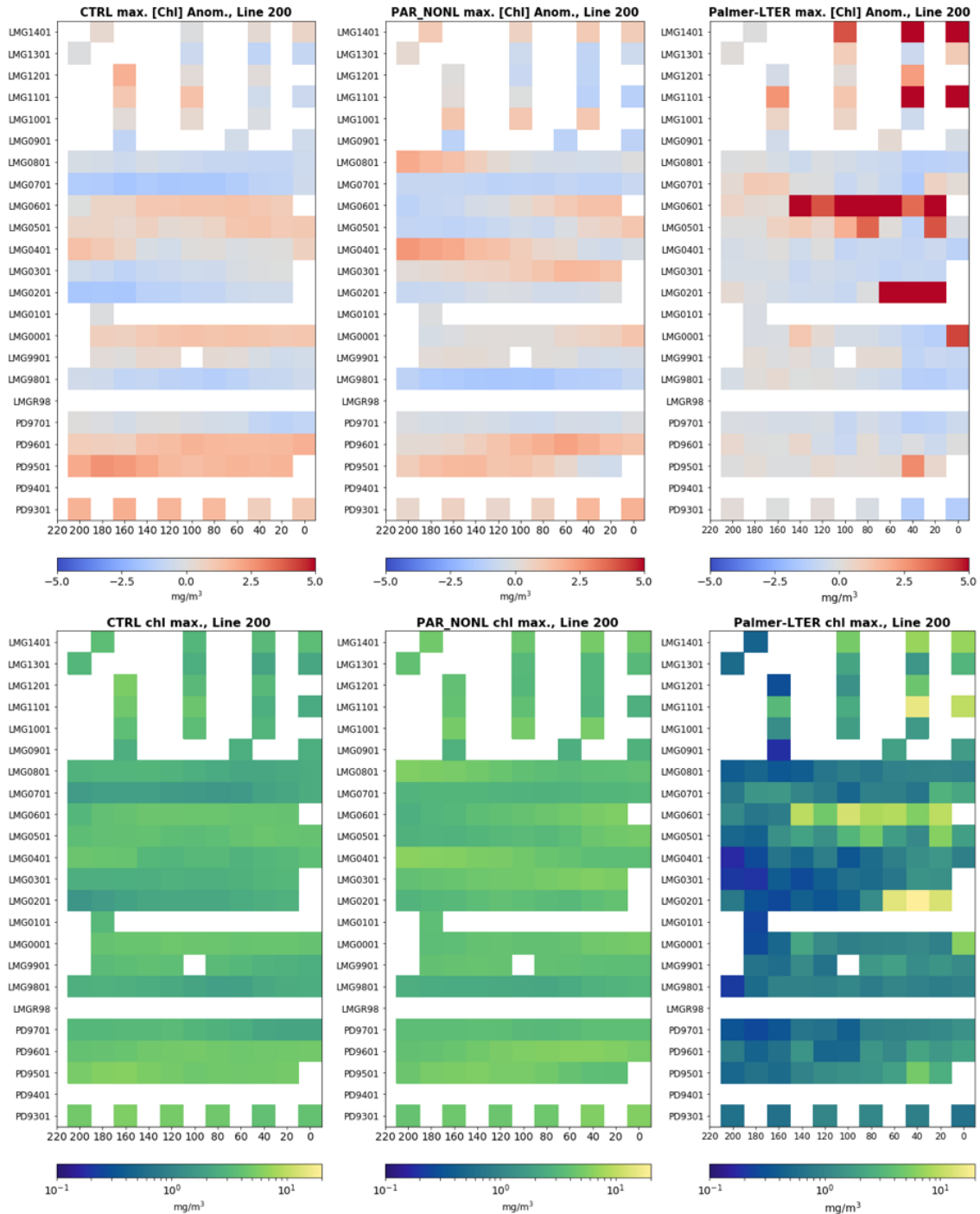


Figure 3-2: Year-distance plot of water-column maximum chlorophyll concentration (bottom row) at each location along the line 200 during the Palmer-LTER cruises for CTRL run (left), PAR_NONL (center) and Palmer data, and the anomaly relative to the geometric mean model or observed station data (top row). X-axis shows the station number, and Y-axis shows the cruise name (cruise period described in Appendix A). Note that a log-scale color bar is used for the chlorophyll concentrations (bottom row) while a linear-scale color bar is used for anomalies (top row).

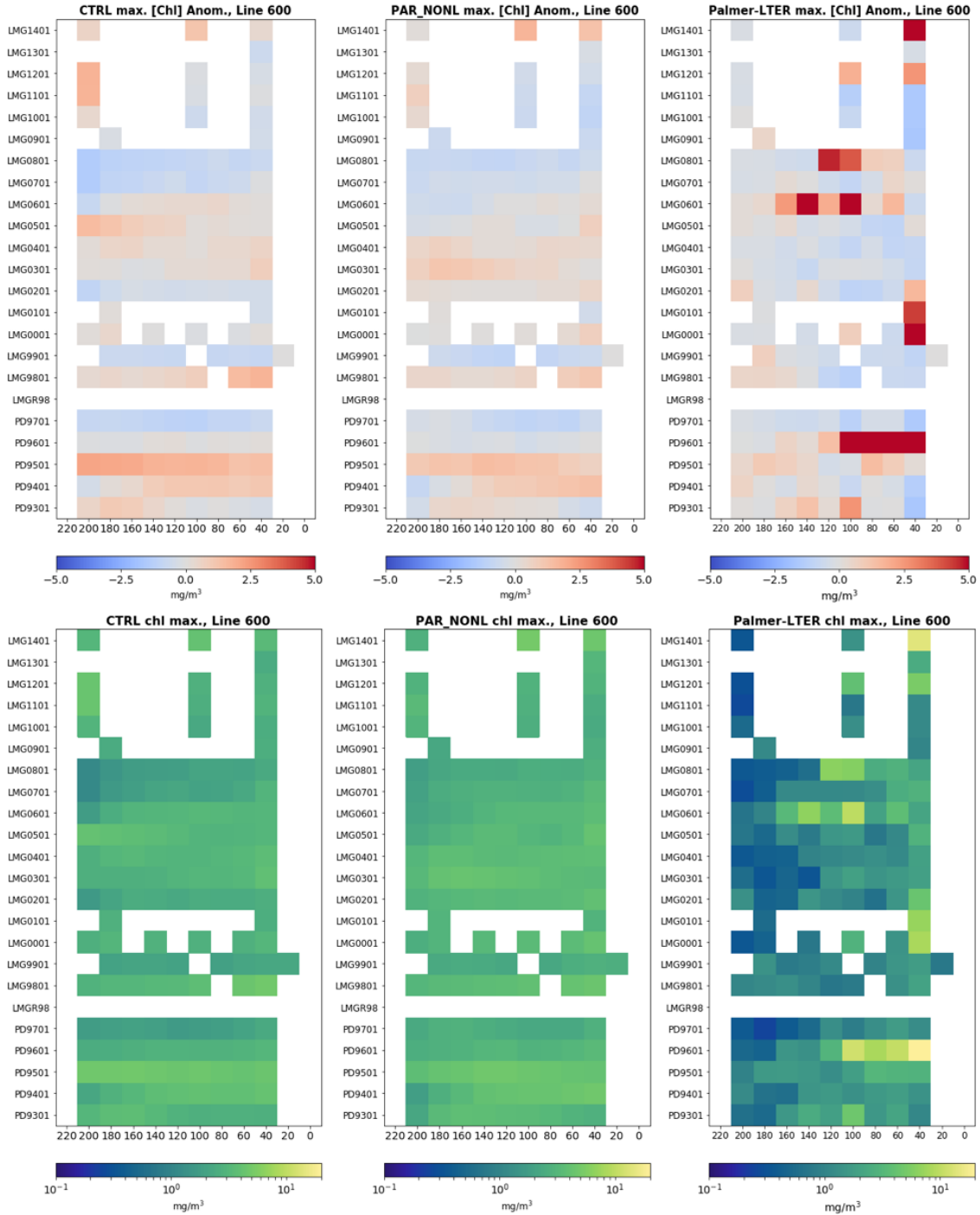


Figure 3-3: Year-distance plot of water-column maximum chlorophyll concentration (bottom row) at each location along the line 600 during the Palmer-LTER cruises for CTRL run (left), PAR_NONL (center) and Palmer data, and the anomaly relative to the geometric mean model or observed station data (top row). X-axis shows the station number, and Y-axis shows the cruise name (cruise period described in Appendix A). Note that a log-scale color bar is used for the chlorophyll concentrations (bottom row) while a linear-scale color bar is used for anomalies (top row).

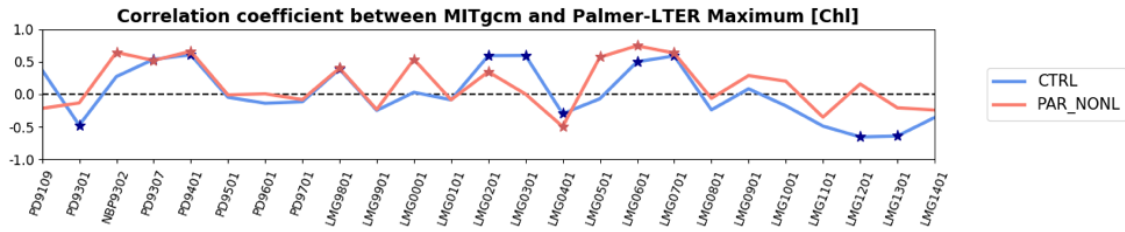


Figure 3-4: Spatial correlation between model experiments CTRL and PAR_NONL and the Palmer-LTER cruise chlorophyll data, calculated for the water-column maximum chlorophyll concentration at each cruise station and for the corresponding monthly mean in the model data. Cruises marked by a star indicate cruises where correlation was statistically significant at the 0.05 level.

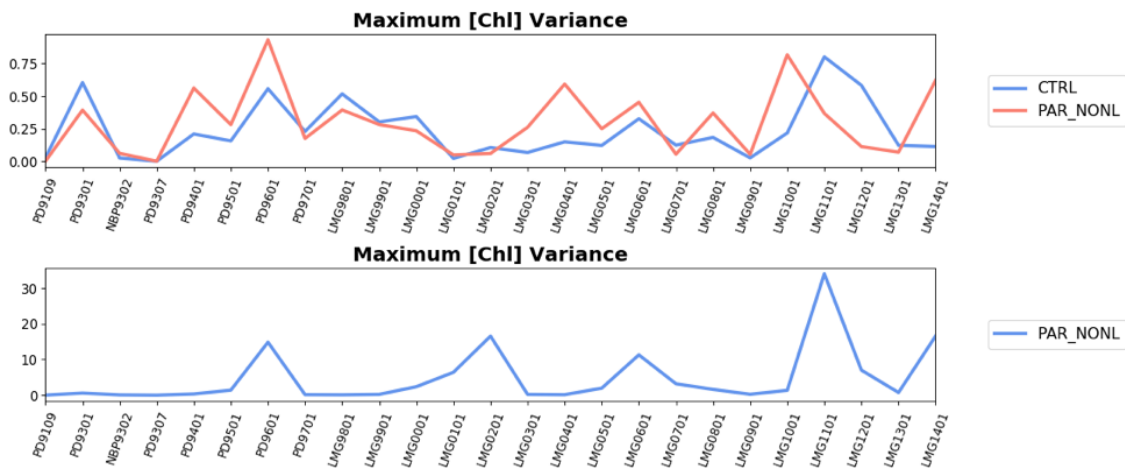


Figure 3-5: Spatial variance between model experiments CTRL and PAR_NONL and the Palmer-LTER cruise chlorophyll data, calculated for the water-column maximum chlorophyll concentration at each cruise station and for the corresponding monthly mean in the model data.

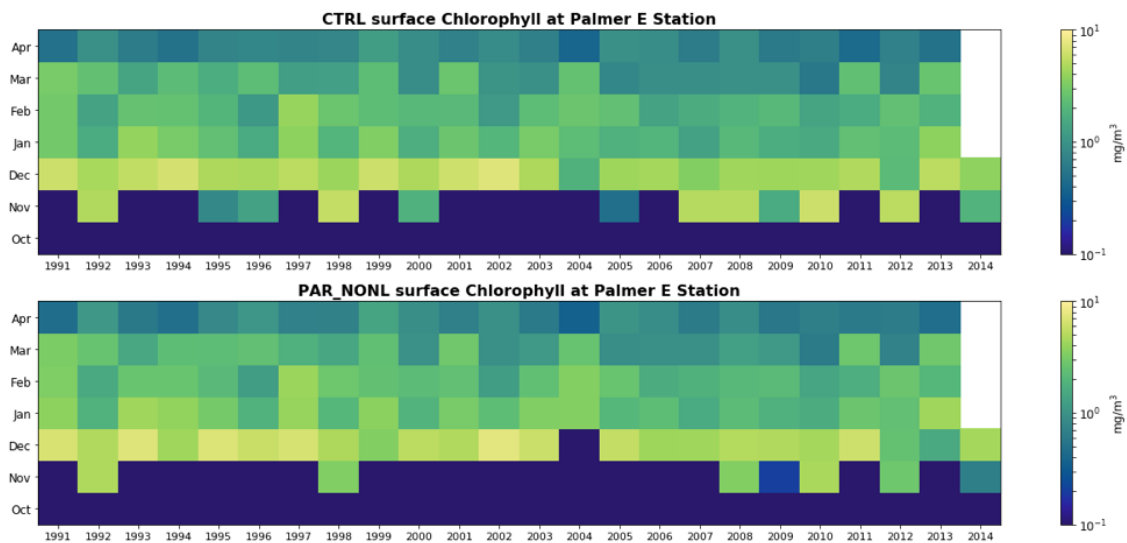


Figure 3-6: Monthly mean surface chlorophyll at the grid station closest to Palmer Station E from October through April each season versus year, for CTRL (top) and PAR_NONL (bottom) runs. Note the log-scale color bar.

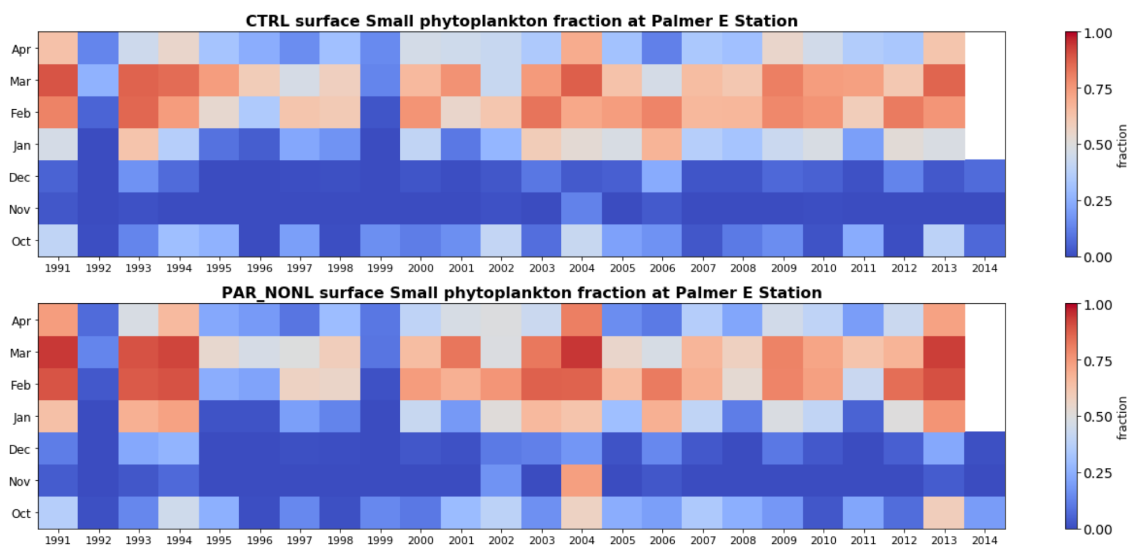


Figure 3-7: Fraction of monthly geometric mean surface chlorophyll composed of small phytoplankton chlorophyll at the grid point closest to Palmer Station E, from October through April every season versus year, for CTRL (top) and PAR_NONL (bottom).

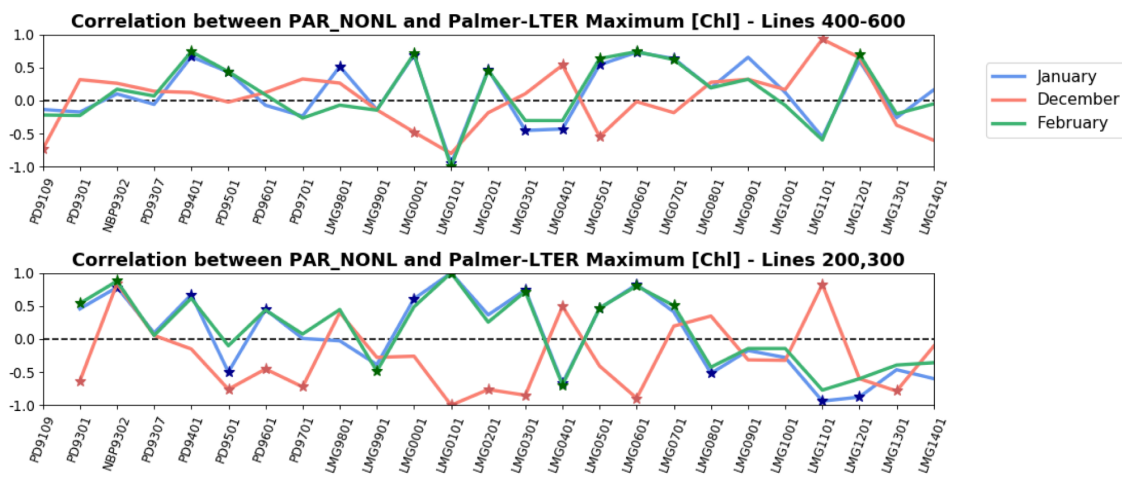


Figure 3-8: Spatial correlation between model experiment PAR_NONL and the Palmer-LTER cruise chlorophyll data, calculated for the maximum chlorophyll concentration at each cruise station and for the corresponding monthly mean for December, January and February in the model data, for lines 400-600 (top) and lines 200-300 (bottom). Cruises marked by a star indicate cruises where correlation was statistically significant at the 0.05 level. Period of each cruise is described in Appendix A.

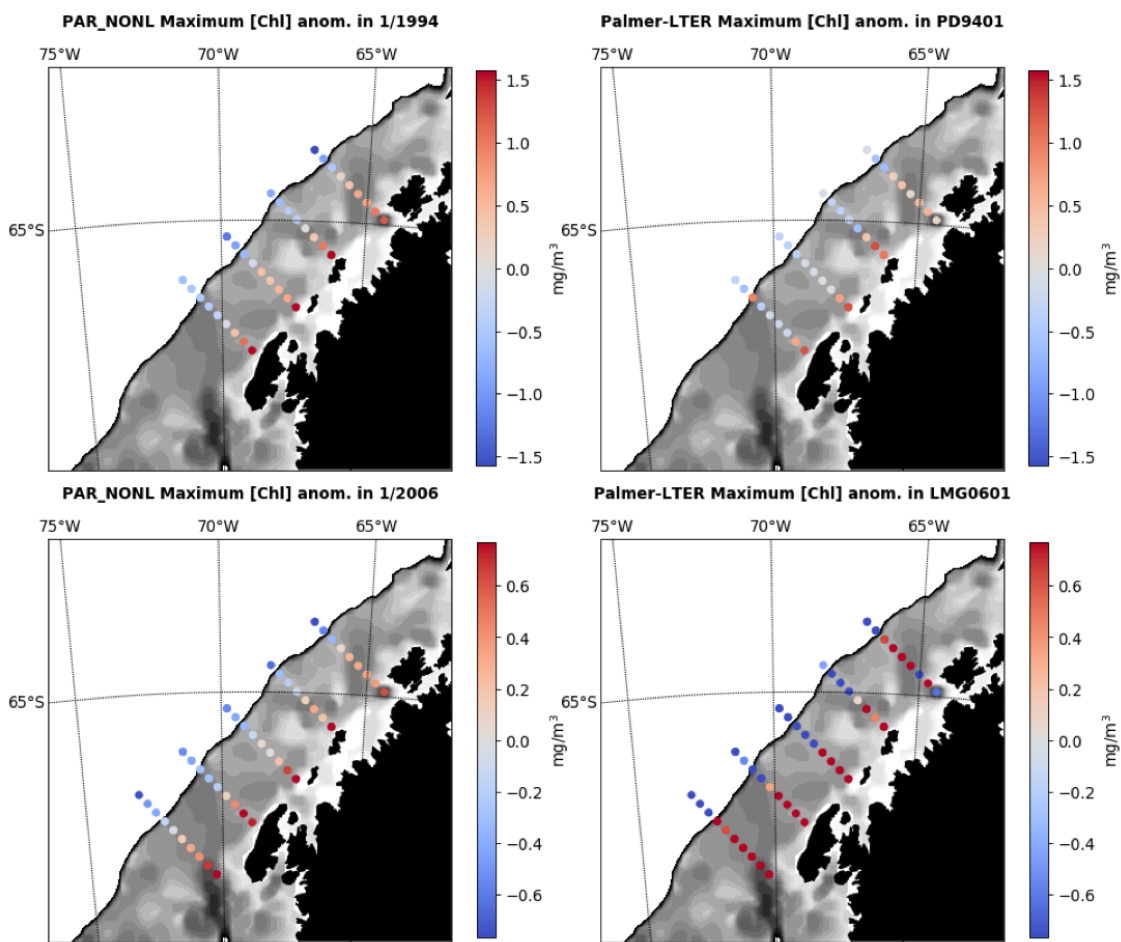


Figure 3-9: Deviation from the geometric mean station water-column maximum chlorophyll concentration for January 1994 (top) and January 2006 (bottom), for the PAR_NONL experiment (left) and Palmer-LTER cruise (right).

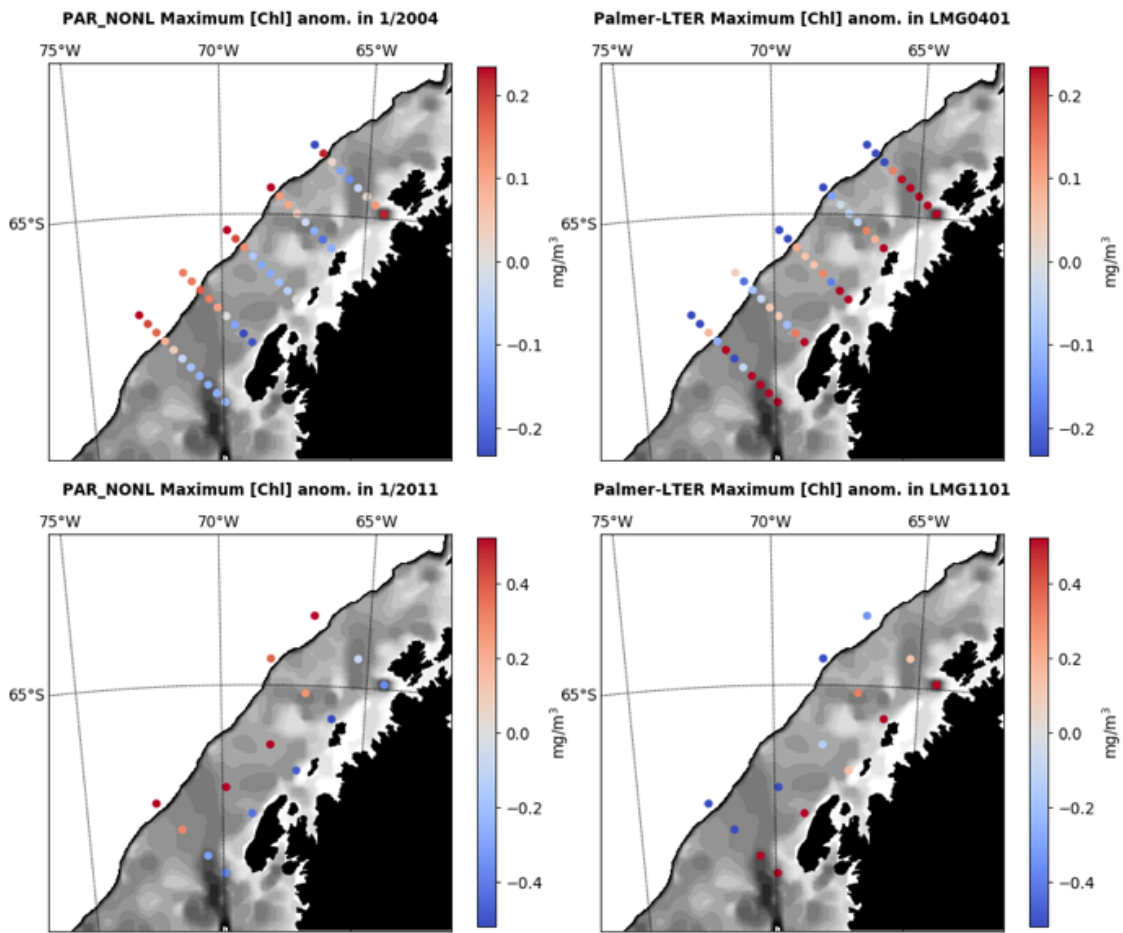


Figure 3-10: Deviation from the geometric mean station water-column maximum chlorophyll concentration for January 2004 (top) and 2011 (bottom), for the PAR_NONL experiment (left) and Palmer-LTER cruise (right).

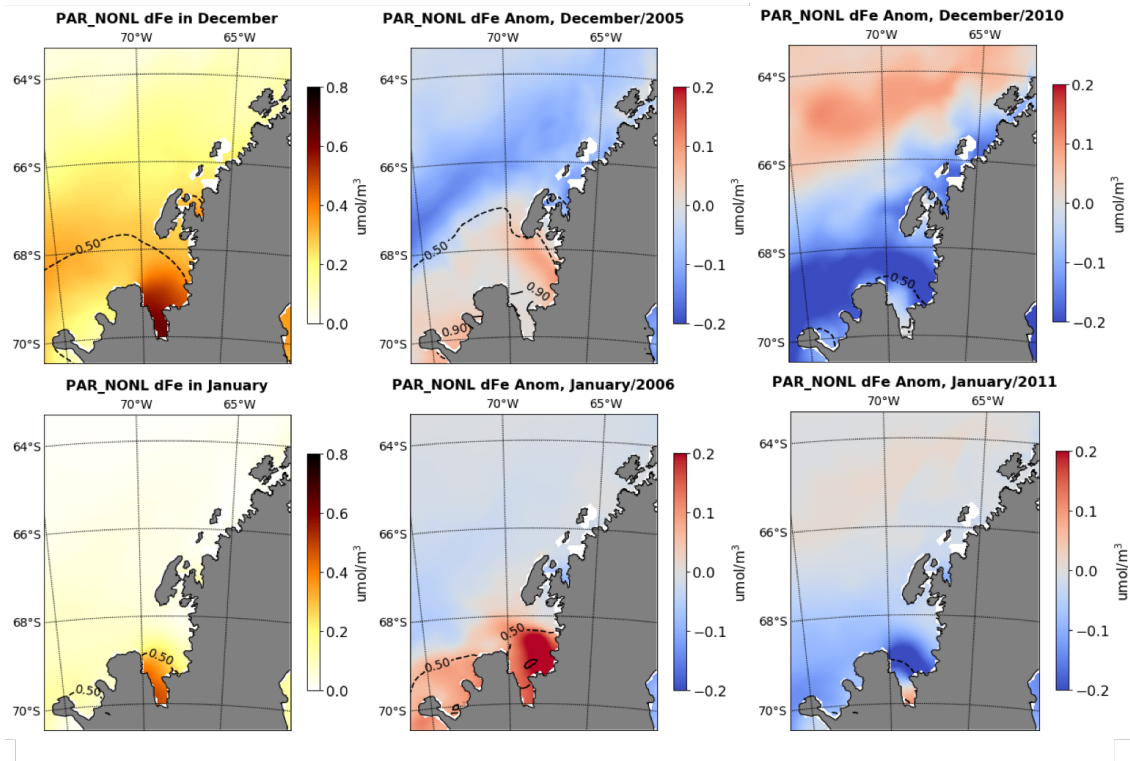


Figure 3-11: PAR_NONL climatological monthly mean surface dissolved iron concentration dFe (left) for the months of December (top) and January (bottom), and surface dFe anomalies from the climatological monthly mean, for December 2005 (top middle), December 2010 (top right), January 2006 (bottom middle) and January 2011 (bottom right).

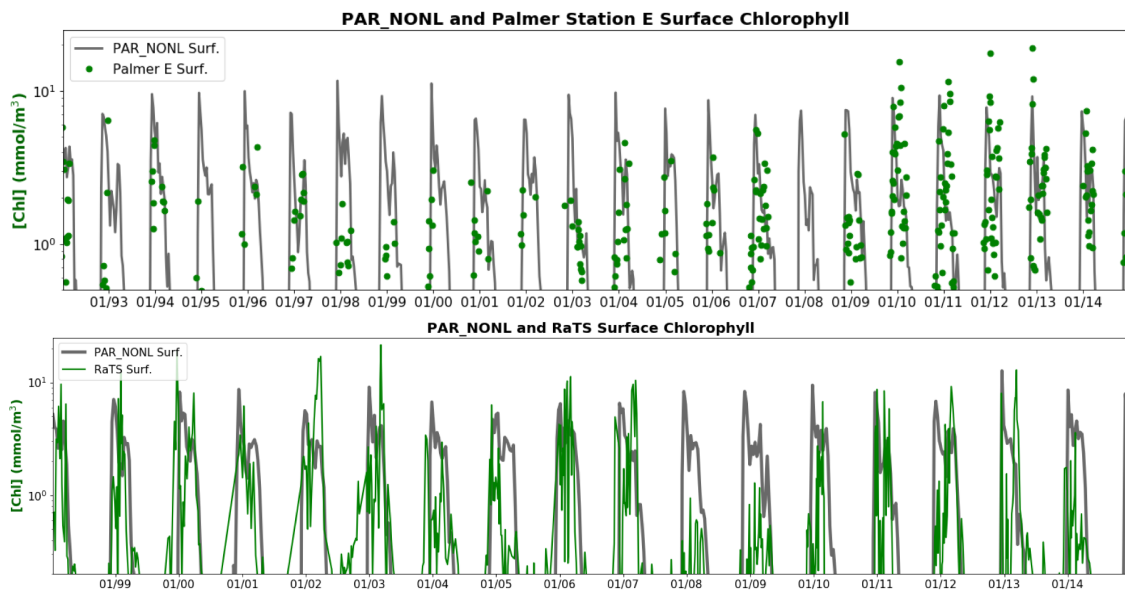


Figure 3-12: PAR_NONL surface chlorophyll concentration versus time for grid point near Palmer Station E (top) and Rothera Station (bottom), in grey, and observed surface chlorophyll collected at these stations (green). Note the log-scale used on the y-axis.

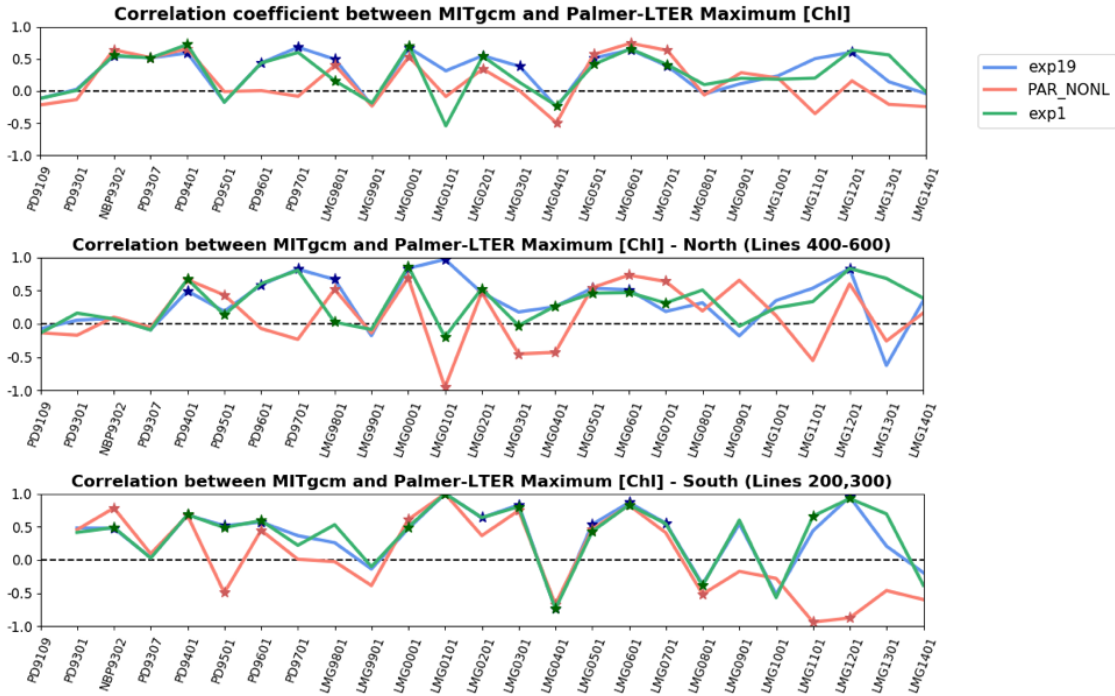


Figure 3-13: Spatial correlation versus year between model experiments PAR_NONL, exp1, exp19 and the Palmer-LTER cruise chlorophyll data, calculated for the water-column maximum chlorophyll concentration at each cruise station and for the corresponding monthly mean in the model data, for lines 200-600 (top), lines 400-600 (middle) and lines 200-300 (bottom). Cruises marked by a star indicate cruises where correlation was statistically significant at the 0.05 level.

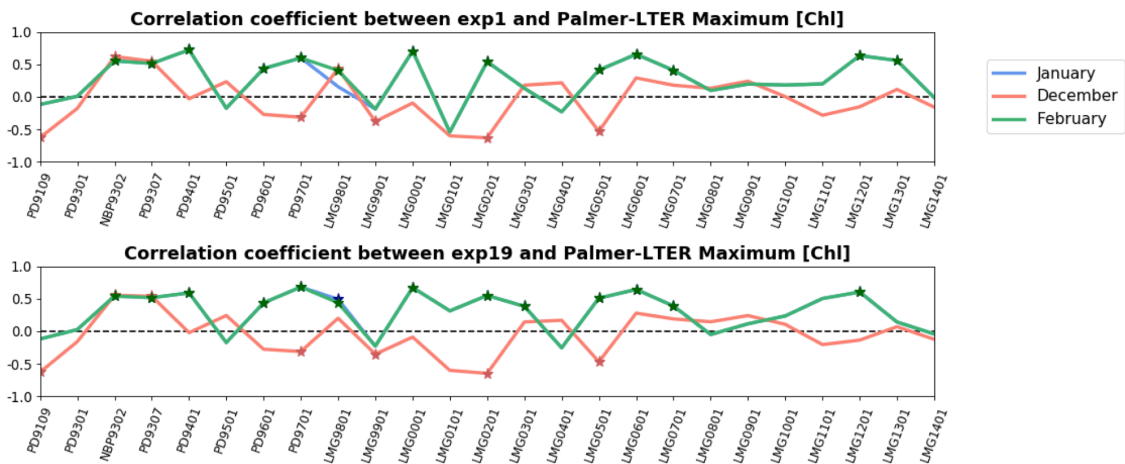


Figure 3-14: Spatial correlation versus year between model experiments and the Palmer-LTER cruise chlorophyll data, calculated for the water-column maximum chlorophyll concentration at each cruise station and for the corresponding monthly mean in the model data, for lines 200-600. Data is shown for exp1 (top) and exp19 (bottom). Cruises marked by a star indicate cruises where correlation was statistically significant at the 0.05 level.

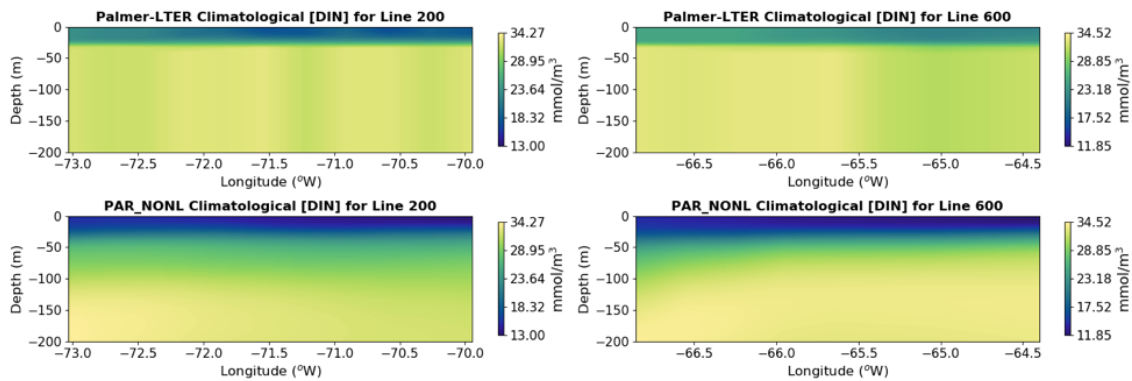


Figure 3-15: Climatological January monthly mean dissolved inorganic nitrogen (DIN) contoured as a function of depth and longitude for PAR_NONL experiment (bottom) and average DIN concentration during the January Palmer-LTER cruises (top), for lines 200 (left) and 600 (right) of the Palmer-LTER grid.

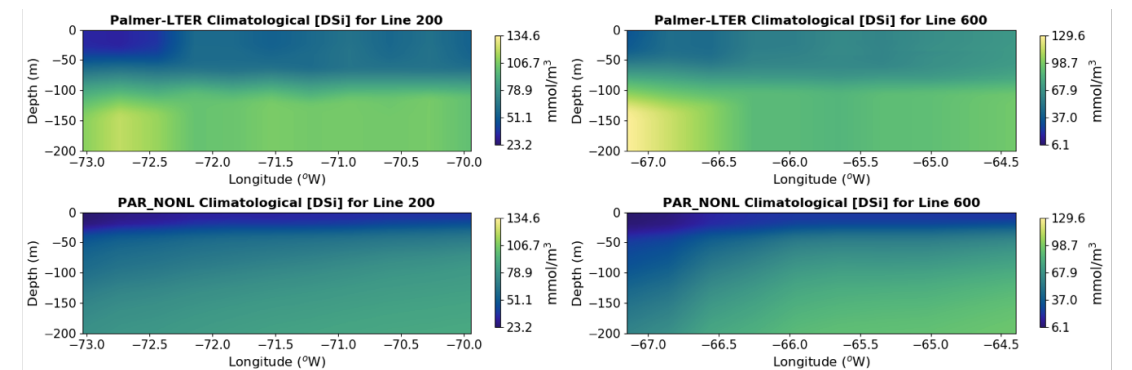


Figure 3-16: Climatological January monthly mean dissolved inorganic silicate (DSi) contoured as a function of depth and longitude for PAR_NONL experiment (bottom) and average DSi concentration during the January Palmer-LTER cruises (top), for lines 200 (left) and 600 (right) of the Palmer-LTER grid.

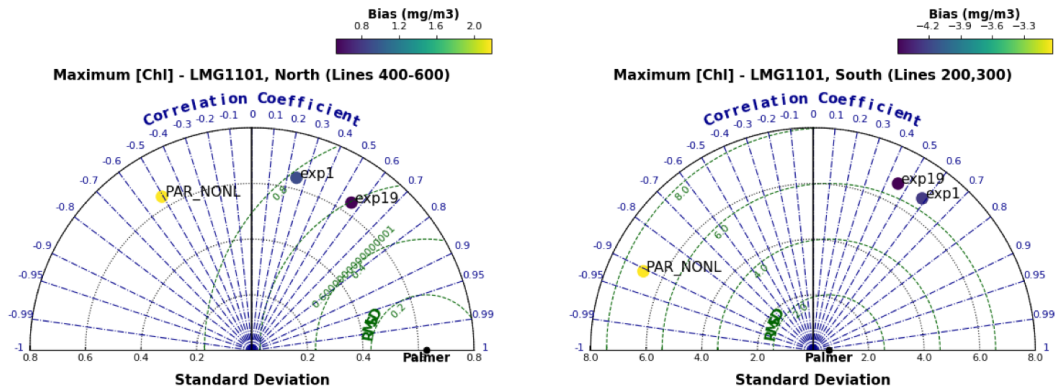


Figure 3-17: Taylor diagram comparing maximum chlorophyll at each station sampled during cruise LMG11-01 and the corresponding MITgcm grid points during January 2011 of experiments PAR_NONL exp1 and exp19 for Palmer-LTER grid lines 400-600 (left) and 200-300 (right).

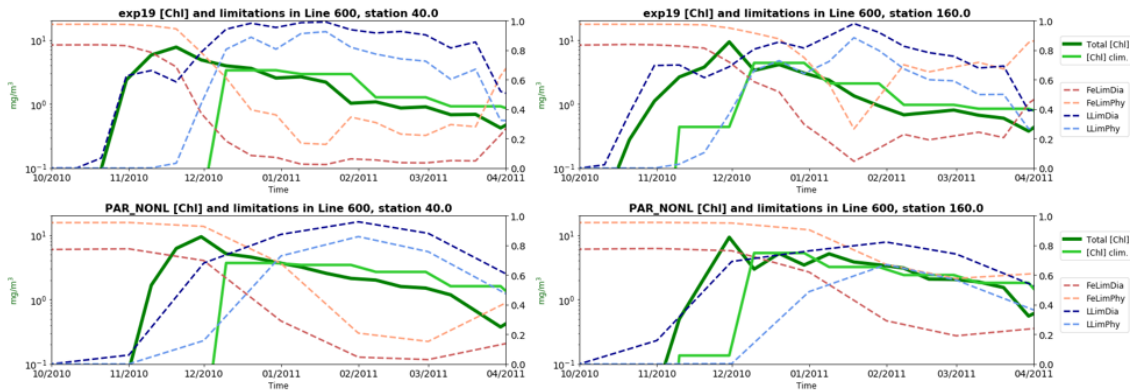


Figure 3-18: Maximum water-column chlorophyll, climatological maximum water-column chlorophyll, surface diatom iron limitation (FeLimDia), surface small phytoplankton iron limitation (FeLimPhy), surface diatom light limitation (LLimDia) and surface small phytoplankton light limitation (LLimPhy) versus time for stations 600.040 (left) and 600.160 (right) for the exp19 experiment (top) and PAR_NONL (bottom), for the period between October 2010 and April 2011. Note that the log-scale y-axis on the left applies to the chlorophyll concentrations while the y-axis on the right applies to the limitation factors.



Figure 3-19: Taylor diagram comparing maximum chlorophyll at each station sampled during cruise LMG12-01 and the corresponding MITgcm grid points during January 2012 of experiments PAR_NONL, exp1 and exp19 for Palmer-LTER grid lines 200-300.

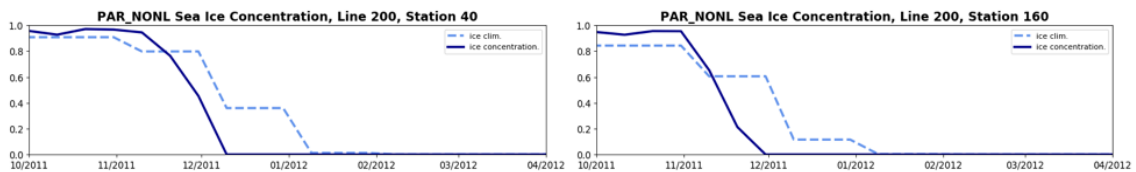


Figure 3-20: PAR_NONL simulated sea ice fraction versus time for the period between October 2011 and April 2012 and simulated climatological sea ice fraction between October and April, for MITgcm grid points corresponding to the location of Palmer-LTER grid points 200.040 (left) and 200.160 (right).

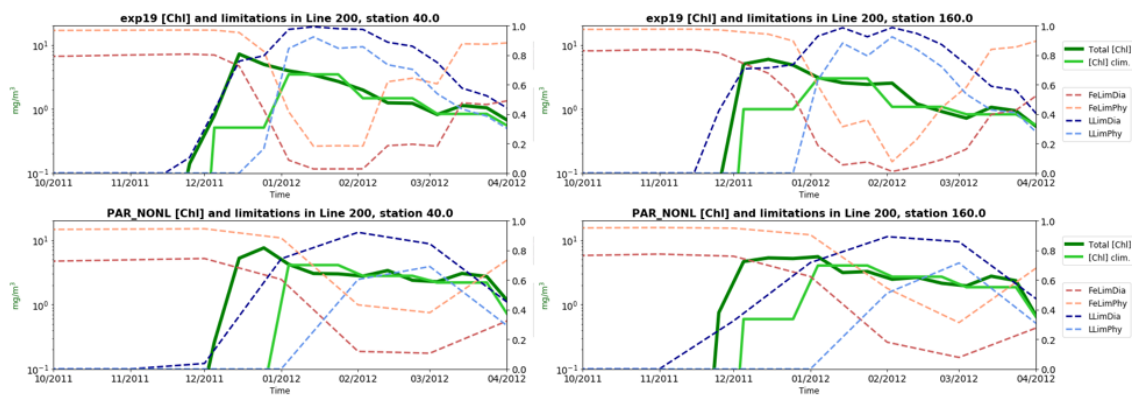


Figure 3-21: Maximum water-column chlorophyll, climatological maximum water-column chlorophyll, surface diatom iron limitation (FeLimDia), surface small phytoplankton iron limitation (FeLimPhy), surface diatom light limitation (LLimDia) and surface small phytoplankton light limitation (LLimPhy) versus time for stations 200.040 (left) and 200.160 (right) for the exp19 experiment (top) and PAR_NONL (bottom), for the period between October 2011 and April 2012. Note that the log-scale y-axis on the left applies to the chlorophyll concentrations while the y-axis on the right applies to the limitation factors.

Chapter 4

Simulation of net primary production (NPP) and air-sea CO₂ fluxes

4.1 Introduction

The Southern Ocean (south of 44°S) is thought to be responsible for 25-30% of the global uptake of atmospheric CO₂ [44]. Although the high-latitude portion of the Southern Ocean has been previously estimated to be a small sink of carbon [82], large-scale estimation of air-sea CO₂ fluxes do not adequately resolve the coastal regions of Antarctica where the intensity of anthropogenic CO₂ is higher [4]. To better assess the impact of high latitudes on the global carbon cycle, therefore, the strength of the Antarctic coastal areas as a sink of atmospheric carbon, as well as the fate of the excess carbon once in the ocean, need to be better understood.

Along the west Antarctic Peninsula (WAP), inorganic carbon at the surface ocean is controlled by a wide variety of physical and biological factors including primary production (PP), respiration, freshwater inputs, brine rejection and mixing with dissolved inorganic carbon (DIC)-rich subsurface waters [9][21]. The distribution of these fluxes is highly variable throughout the shelf regions, leading to spatial and temporal variations in DIC, the partial pressure of CO₂ and air-sea CO₂ exchange. Due to the nature of the WAP ecosystem, characterized by high nitrate concentration, large diatom blooms and an important contribution of krill and salps, the WAP is tipi-

cally expected to have an efficient biological pump. However, a large and persistent imbalance between estimated net community production (NCP) and sinking of particulate organic matter from the surface ocean has been observed [79][19]. Although this imbalance is not unexpected given there are other fates and export pathways available for assimilated organic matter, such as remineralization and lateral transport, the magnitude of this imbalance at the WAP suggests that other pathways besides sinking could significantly affect the fate of the assimilated organic matter. [80] estimate that nearly half of the organic matter (OM) exported from the surface ocean at the WAP may be transported downward by mixing of suspended particles. The role of mixing is important given that it could reduce the depth at which OM is remineralized, leading to shorter carbon sequestration time [79].

There is a growing body of research aimed at quantifying the potential of the WAP for carbon sequestration and storage, which include data on inorganic carbon as well as primary production (PP) and export at daily and seasonal time-scales. The high spatial and temporal variability of biological processes at the WAP, as well sampling constraints and limitations inherent to the different sampling methods, however, make the quantification of the carbon pathways for the whole region extremely difficult. The use of a circulation, sea ice and biogeochemistry model in this region, therefore, can provide estimates of broader seasonal and spatial distribution of PP, particle export and air-sea fluxes, helping to inform future research in areas of particulate interest for sampling.

In this chapter, the model described in chapters 2 and 3 of this thesis is compared to the existing Palmer-LTER data and literature to assess its potential to properly simulate the carbon cycle in the WAP. The goals of this chapter, therefore, are:

- Assessing general patterns of net primary production (NPP) and export flux in the WAP and possible mechanisms that influence the spatial and temporal distribution of export
- Identifying processes that affect the air-sea flux of carbon in the WAP
- Identifying improvements that are necessary to the model in order to accurately

simulate the carbon fluxes in the region

4.2 Literature Review

4.2.1 Quantifying Primary Production and Export – concepts and methods

Total carbon fixed by photosynthesis is the gross primary production (GPP). Part of the GPP is respired by phytoplankton, with the remaining fraction (net primary production, NPP) becoming available for higher trophic levels, the microbial community and export. The metabolic balance of the whole ecosystem, however, is determined by the net community production (NCP), defined by GPP minus the ecosystem respiration, or NPP minus all heterotrophic respiration. NCP governs the potential for biomass accumulation and carbon storage in the system, and at long enough spatial and time scales, assuming steady state, should be balanced by export of organic matter from the system. Another distinction can be made to primary production based on the source of nutrients. New production consists of the primary production generated with exogenous sources of nutrients, and in high latitudes is fueled by nitrate advected or upwelled to the mixed layer. Regenerated production, on the other hand, depends on remineralization within the ecosystem and is given by the respired fraction of NPP. New production and NCP are closely related but are, however, mechanistically different [19].

While NCP and export production are expected to match at long time and spatial scales, the assumption that export is dominated by particle sinking at any given location or time is not necessarily observed. The mismatch between observed NCP and export production could be due to temporal or spatial decoupling of PP and export, or due to methodological bias in the data used to make the different estimates. While there are a number of methods to measure primary and export productions, the limitations and time scales of each method should be considered for proper interpretation of results.

Drawdown of nitrate and DIC over the growth season measure the seasonal new production and NCP, respectively [81]. However, horizontal and vertical transport, as well as errors with the assumption of the wintertime values can lead to biases in the new production and NCP estimates. DIC drawdown is also subject to errors due to the reconstruction of DIC from partial pressure of CO_2 (p_{CO_2}), assumptions on the calculation of gas exchange and dissolution and precipitation of CaCO_3 [81]. Another method used to measure NCP is the imbalance between dissolved O_2 and Ar in the mixed layer (ML). Given both gases have similar solubilities, oversaturation or undersaturation of O_2 relative to Ar indicates biological activity, with oxygen oversaturation driven by photosynthesis and undersaturation driven by respiration. This method, however, has a memory of production over the relatively short O_2 residence time in the surface ocean (of about 10 days) and is subject to errors due to vertical mixing, Ar supersaturation, non-steady-state conditions (which can be observed at the beginning of intense blooms), variability in the piston velocity of CO_2 and varying $\text{O}_2:\text{C}$ stoichiometries [21]. [47] presents a satellite-NCP algorithm specifically calibrated using observations from the Palmer-TER O_2/Ar -NCP. The algorithm developed by [47] gives estimates of NCP at larger spatial and temporal scales, but is based on surface chlorophyll (not accounting for production below the surface layer) and assumes that NCP depends solely on chlorophyll concentration and that this dependence does not vary in time, when in fact NCP also depends on temperature, phytoplankton physiological status and community structure.

The Palmer-LTER project has also used bottle incubation methods to estimate NPP at Palmer Station and during the cruises. NPP data are obtained from 24-hour deck incubations spiked with $\text{NaH}^{14}\text{CO}_3$, and are available through the Palmer-LTER website. Although this dataset, which started in 1995, contains valuable information about NPP at the WAP, this type of measurement is subject to shorter term forcing and cannot be extrapolated for time periods longer than the incubation. Particle export has been measured in the WAP by deploying sediment traps or by calculating the imbalance between ^{238}U and ^{234}Th activity [8] [79]. The daughter isotope (^{234}Th) adheres to sinking particles, so that the deficit in ^{234}Th activity relative to uranium

is related to export production. Accounting for advection and mixing is a limitation for both methods, and certain types of sediment traps are thought to underestimate particle flux [8]. It is likely, then, that export production is underestimated to some level at the WAP.

4.2.2 Primary Production and Export in the WAP

Chlorophyll and NCP along the WAP first peaks offshore, and the bloom follows the sea ice retreat towards the coast [47] [76]. The day of sea ice retreat influences PP, with years of later sea ice retreat leading to higher chlorophyll concentrations in the shelf in January [71][93]. Although the most direct impact of sea ice on PP would be through light control, [47] found that the effect of timing of sea ice retreat persisted throughout the season, suggesting additional controls. The Palmer-LTER cruise data during austral summer reveals a strong onshore-offshore gradient, with the coastal areas being up to eight times more productive than offshore and the largest gradient observed off of Marguerite Bay [94]. The authors estimate the shelf production shoreward of the continental slope ranging from 500-750 mgC/m²d, while slope production was around 250-400 mgC/m²d. Although a north-south gradient is observed in the cruise data, with higher PP in the southern area of the Palmer-LTER grid, annually integrated NCP from satellite imagery [47] shows a weaker latitudinal gradient than monthly data. The weaker gradient in the annually integrated data could be attributed to different phenology of the bloom in different areas or due to longer growth season in the northern part of the LTER grid.

Interannual variability in NPP varied by a factor of seven, with maximum rates on a time-series of cruise data from 1995 to 2006 shows maximum regional average rates in 2006 (1788 mgC/m²d) and minimum in 1999 (248 mgC/m²d, [94]). Most of the variability was observed in the shelf and coastal areas, with daily NPP varying by an order of magnitude, ranging from 250 to 1100 mgC/m²d. In a study using an inverse model based on Palmer-LTER data, [18] find that both small and large phytoplankton are more abundant in years of high chlorophyll concentration and that although NCP differed significantly between years, it accounted for a similar proportion of GPP. The

long-term trend in chlorophyll indicates a decrease in production over the past 30 years, with magnitude of the bloom decreasing by 12% and associated with persistent winds, cloudy days and reduction in marginal ice zone [72].

Using cruise data from 2012-2014, [19] find that particle export, new production and NCP varied greatly at individual stations, and with cruise averages ranging from 0.3 to 1.8 mmolN/m²d for particle export, 3.7 to 8 mmolN/m²d for new production and 1.9 to 8.9 for mmolN/m²d for NCP. At any station, however, either export, NCP or new production could have higher values than the other two rates. On average, however, export calculated from ²³⁸U-²³⁴Th disequilibrium represented 20% to 50% of NCP and new production, and the geometric mean e-ratio, which is the fraction of NPP exported (export flux over NPP), was about 0.18. At Palmer station, where the development of the bloom has been sampled at higher temporal resolution, [87] observes net heterotrophy of about -7 mmolC/m²d in the pre-bloom period for the 2012-2013 season. For the same season, new production during the bloom was 5.3 times higher than vertical export, presenting a higher disequilibrium between production and export than the cruise data, where new production was 2.4 times higher than particle export [79]. For the Palmer station data, particle export from sediment trap and ²³⁸U-²³⁴Th disequilibrium agreed reasonably well, with values ranging from 10.5±1.2 mgN/m²d and 14.9±5.9 mgN/m²d, respectively. Although the ²³⁴Th data showed more variability than the sediment trap data, particle export had less variability than the measured new production [79]. [19] also find that most of the variation in e-ratio for cruise data was due to variation in NPP, with less variability observed in the export data.

Given the large imbalance between particle export and primary production at the Palmer station and in cruise data, [80] suggest that nearly half of the organic matter exported from the WAP surface by the biological pump could be transported by vertical mixing of suspended particles, which would not be captured by ²³⁴Th data. [35] presents data pointing the same direction, finding higher f-ratio and export when stratification was intensified by meltwater. While vertical mixing has been proposed as an important mechanism for particle export, quantifying the influence of different

mechanisms in export production remains a challenge in the WAP.

4.2.3 Inorganic carbon in the surface ocean and air-sea fluxes

Measurements of air-sea CO_2 fluxes suggest that the coastal area of the WAP is a strong sink of atmospheric carbon. In a study by [37] at Ryder Bay, the authors found that in the summertime the surface waters were undersaturated with respect to atmospheric CO_2 throughout the whole season, and that there was a strong negative correlation between DIC and salinity that deviated from the dilution line, indicating carbon removal through NCP. The authors estimate that PP is expected to remove 50-200 $\mu\text{mol/kg}$ of DIC in the meltwater surface during the summer. [43], using summer inorganic carbon data from Ryder Bay during three different years (2011-2013), found strong variation in the strength of the region as a carbon sink. 2013 was estimated to uptake 0.22 $\text{molC/m}^2\text{year}$, while 2011 presented much stronger fluxes and an uptake of 1.03 $\text{molC/m}^2\text{year}$, with an average annual value for the region calculated between 0.59 and 0.94 $\text{molC/m}^2\text{year}$.

On studies that included data from the Palmer-LTER cruises, large spatial gradients in the carbon cycle variables were found. [21] found strong control by biological processes and substantial mesoscale variability in surface p_{CO_2} and O_2 in the WAP, and [31] found an onshore-offshore gradient in surface p_{CO_2} , pH, CaCO_3 saturation state, total alkalinity and DIC. A north-south gradient was also observed in most of the variables, with the exception of DIC. The latitudinal gradient in DIC was not observed, but different processes controlled its concentration in different parts of the grid: dilution in the north of the LTER grid and strong biological production in the southern part. [37], however, found that at Ryder Bay, close to the southern part of the LTER grid, the lowest concentrations of DIC, total alkalinity (TA) and p_{CO_2} were related to melting sea-ice, indicating that different processes could be important during different times of the year. The study by [37] also found that Circumpolar Deep Water (CDW) at Marguerite Bay had higher DIC concentration than toffshore CDW, indicating that the concentrations of the carbonate cycle related variables change in the water masses at the WAP as they make their way across the shelf due

to remineralization of organic matter.

In contrast to the summer data, observations during the winter by [43] at Ryder Bay indicate that during this season the WAP is a source of atmospheric carbon. The authors estimated a flux of about $-15 \text{ molC/m}^2\text{year}$ (with negative sign meaning towards the ocean) during the summer and $+10 \text{ molC/m}^2\text{year}$ during the winter, and an amplitude of $200 \mu\text{mol/kg}$ in the annual cycle of DIC. The lowest DIC concentration was reached in December due to strong PP, and a maximum of about $2200 \mu\text{mol/kg}$ was observed in September due to net heterotrophy and mixing with CDW. Throughout the Palmer-LTER grid, [65] found that although the summer surface DIC presented was highly variable, the mid-summer DIC did not relate to the surface DIC in the previous summer, suggesting an annual replenishment of surface DIC during the fall and winter and a relatively stable deep DIC pool in the WAP.

4.3 Methods

The model used in this chapter uses the same physics and similar biogeochemistry setup used in chapters 2 and 3, with same length of simulation and frequency of output. The changes made to the biogeochemistry, extra diagnostics analyzed that had not been previously described and changes to initial conditions are described below.

4.3.1 Changes in initial and boundary conditions

One of the problems identified with the biogeochemical model in chapter 3 was the high chlorophyll concentration in the offshore areas of the model, attributed to excess of dissolved iron (dFe) in the initial condition. For this chapter, therefore, the dissolved iron initial and boundary conditions were altered so that that simulated dFe offshore would exhibit lower concentrations. Unfortunately, there is not enough dFe data available so that a bias could be calculated robustly and subtracted from the forcing files. In the initial condition used in chapter 3, surface concentrations of dFe are relatively low, with values around 0.2 nmol/m^3 at the WAP shelf. At

depth, dFe increases to values around 0.8 nmol/m³. The approach chosen, therefore, was to lower the dFe concentration in the top 50 m by 0.1 nmol/m³, and lower the concentration by 0.3 nmol/m³ below that depth. These values were subtracted from the initial condition throughout the whole grid for initial conditions, and also in the boundary files. Although the new approach chosen is somewhat arbitrary, the values previously used, derived from a global (minus Arctic) model data, were also not validated against in situ data and there is no evidence that they would consist of a more realistic representation.

4.3.2 WAP_BGC Experiment

The experiment analyzed in the Results section below with the modified dFe initial and boundary conditions is referred to as WAP_BGC and is largely similar to exp19 described in chapter 3. In addition to the dFe changes, the only additional change made to the code was lowering the small phytoplankton initial slope of the P-I (Photosynthesis-irradiation curve) from 0.17 to 0.14 W/mmolC m²d. This alteration was made to bring the small phytoplankton and diatom proportions in the model similar to the proportion found in exp19 (described in chapter 3). This adjustment was needed given that the lower iron concentrations found in the initial and boundary condition strongly favored small phytoplankton growth.

4.3.3 Diagnostics Files

Gross Primary Production (GPP) and Net Primary Production (NPP)

In the model, GPP is calculated as:

$$GPP_{phy} = C_{phot} \times Phy_C \quad (4.1)$$

Where C_{phot} is the carbon specific rate of photosynthesis, and Phy_C is the phytoplankton carbon pool. The photosynthesis rate is different for small phytoplankton and diatoms, and GPP is calculated separately for each phytoplankton component. So, although the main currency throughout the model is nitrogen, GPP is given in

units of mmolC/m³d. Another diagnostic of the model is phytoplankton respiration. The calculation of NPP is done separately using the outputs for GPP and phytoplankton respiration:

$$NPP = GPP_{phy} + GPP_{dia} - resp_{phy} - resp_{dia} \quad (4.2)$$

where GPP_{phy} and GPP_{dia} are the outputs for GPP by small phytoplankton and diatoms, respectively, and $resp_{phy}$ and $resp_{dia}$ are the respiration terms. Respiration terms represent the sum of maintenance metabolic losses and the costs of biosynthesis, which are proportional to nutrient assimilation. The units of NPP are the same as GPP.

Zooplankton respiration, in the model, is a closure term designed to bring zooplankton concentrations back to Redfield ratio, given C:N ratio is variable in the phytoplankton and might lead to a different ratio in the zooplankton as well. When the intracellular heterotrophic C:N ratio is lower than Redfield, heterotrophic respiration is assumed to drive the ratio back to Redfield with a time scale K_{het} so that:

$$r_{het} = f_T \times \frac{q_{het}^{C:N} - q_{Redfield}^{C:N}}{K_{het}} \quad (4.3)$$

if $q_{het}^{C:N} > q_{Redfield}^{C:N}$ and zero if $q_{het}^{C:N} < q_{Redfield}^{C:N}$, r_{het} is the heterotrophic respiration, $q_{het}^{C:N}$ is the zooplankton C:N and $q_{Redfield}^{C:N}$ is the Redfield ratio and f_T is the Arrhenius function, given by:

$$f_T = -4500 \times \left(\frac{1}{T} - \frac{1}{T_{ref}} \right) \quad (4.4)$$

where T is the temperature and T_{ref} is the reference temperature, 288.15 K. Although zooplankton respiration is provided as a diagnostic output, it is not formulated to directly represent the physiology of respiration and transfer of mass to the dissolved inorganic carbon and nitrogen components. NCP, therefore, needs a different parameterization of zooplankton respiration in order to be compared to the particle export. Therefore, the closest flux to particle export is NPP, which was used in the analyses

done in this study. Although GPP is also provided as a diagnostics output it was not included in the analyses, in part due to the fact that there is more in situ NPP data compared to GPP samples, so that the skill assessment of the model is more reliable when using NPP. NCP, GPP and respiration terms , therefore, require additional investigation.

Export Production The export production in the model is derived from the sinking of diatoms, small phytoplankton and detritus. Diatoms and small phytoplankton sink with a constant predefined velocity, while detritus velocity increases linearly with depth, starting at 10 m/d. Sinking is calculated individually for diatoms, small phytoplankton and detritus at every depth and time step, and the export flux is saved as the sum of their carbon components that sink through a predefined depth, considered to be 100 m in this study. The sinking flux, therefore is given by:

$$C_{sink} = Phy_C \times ws_{phy} + Dia_C \times ws_{dia} + Det_C \times ws_{det} \quad (4.5)$$

where Phy_C , Dia_C and Det_C are the carbon pools of small phytoplankton, diatoms and detritus, and ws is their sinking velocity.

In the current setup of the model, the sinking velocity for phytoplankton is set to zero, and the sinking of both diatoms and small phytoplankton is made via their transfer to the detritus pool, determined by an aggregation rate. The aggregation rate is calculated by multiplying a constant by the carbon component of each phytoplankton type. The aggregation rate is 0.165 d^{-1} for diatoms and 0.015 d^{-1} for small phytoplankton.

Detritus degradation to the dissolved organic carbon component (DOC) is temperature dependent, calculated using a constant rate and the Arrhenius function:

$$DOC = remin_C \times f_T \times Det_C \quad (4.6)$$

where $remin_C$ is the degradation constant (set to 0.15 d^{-1}). The remineralization of DOC into DIC is done in a similar way, by multiplying the DOC component by a

constant rate (0.1 d^{-1}) and f_T . The remineralization of the detritus nitrogen pool to DIN is dealt with in a similar way as the remineralization of detritus carbon to DIC.

4.4 Results

4.4.1 Comparing exp19 and WAP_BGC

The chlorophyll concentrations from WAP_BGC simulation were compared to the results from exp19 by calculating the correlation between cruise and model chlorophyll data. For the model data, the monthly means for the month of each cruise were used. The correlations were calculated between the maximum chlorophyll concentration of each station of each cruise and the maximum chlorophyll concentration of the model grid point closest to the corresponding station. It is seen in figure 4-1 that lowering the iron concentrations in the input and boundary files improved the representation of chlorophyll in the whole grid and individually in the northern (lines 400 to 600) and southern (lines 200 and 300) regions of the Palmer-LTER grid. The improvement was particularly noticeable in the southern part of the grid, where correlations increased significantly in years of low sea ice concentration (1999, 2008, 2011), consistent with the hypothesis raised in chapter 3 that excess iron in the offshore area was responsible for the high chlorophyll concentrations observed in the model result.

WAP_BGC, however, presented lower correlation with the LTER data in 2005 (LMG-0501) and 2006 (LMG-0601), which was a year of extremely high chlorophyll concentration. Figure 4-2 shows the spatial distribution of the maximum chlorophyll concentration at each station. The maximum chlorophyll is obtained at each station and the geometric mean is calculated for the cruise, with the anomalies in 2006 from this mean shown in the figure. The main difference between the experiments was the distribution of the bloom in the southern part of the grid, with the bloom in line 200 being constrained to the stations closest to shore in WAP_BGC. The higher correlation with exp19 raises the question of whether years with anomalously high chlorophyll concentrations are related to increased iron input, but there is not enough

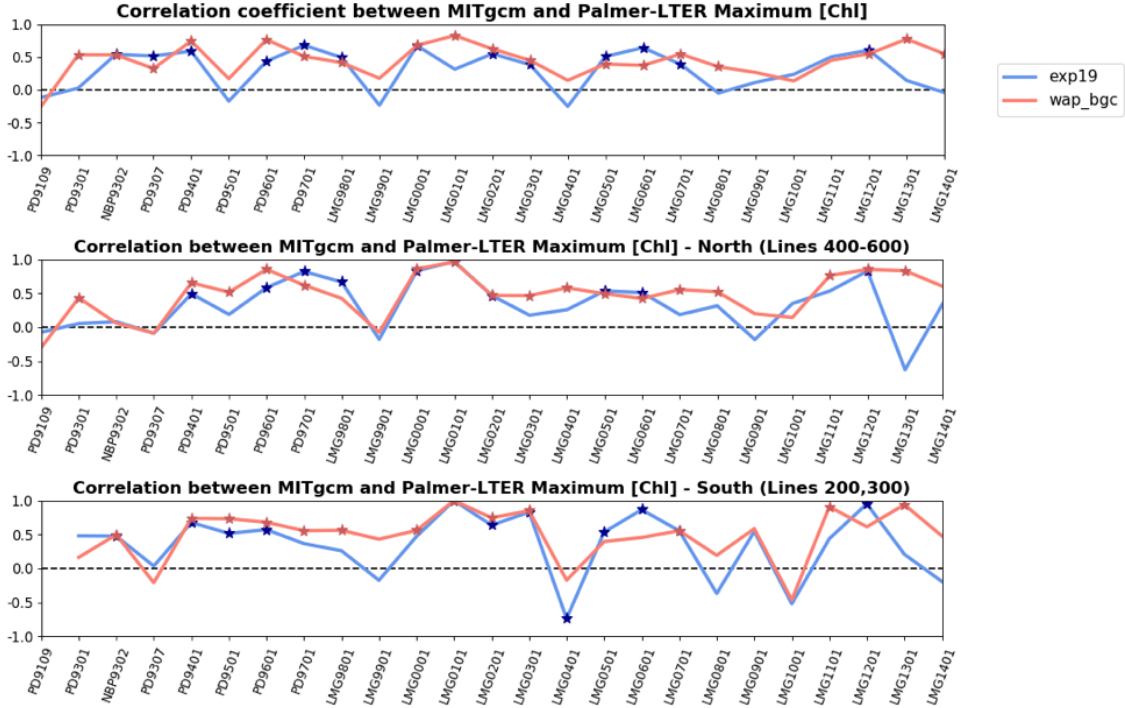


Figure 4-1: Spatial correlation between model experiments WAP_BGC and exp19 and the Palmer-LTER cruise chlorophyll data, calculated for the water-column maximum chlorophyll concentration at each cruise station and the corresponding monthly mean in the model data (top), for the stations sampled in lines 400-600 (middle) and lines 200-300 (bottom). Points marked with a star indicate where correlation was significant at a 0.05 level.

data to validate this hypothesis.

The monthly climatologies for WAP_BGC surface chlorophyll concentration is shown in figure 4-2. It is seen that the phytoplankton bloom first peaks offshore during November, and that on the shelf the bloom is stronger during December in the northern part of the Palmer-LTER grid and during January in the southern part. Chlorophyll production persists until April, and during the period between May and October chlorophyll concentrations are equal or lower than 10^{-1} mg/m³. Given that overall WAP_BGC presented better correlations with the Palmer-LTER data, WAP_BGC was analyzed to assess its skill in reproducing NPP and air-sea CO₂ fluxes in the WAP.

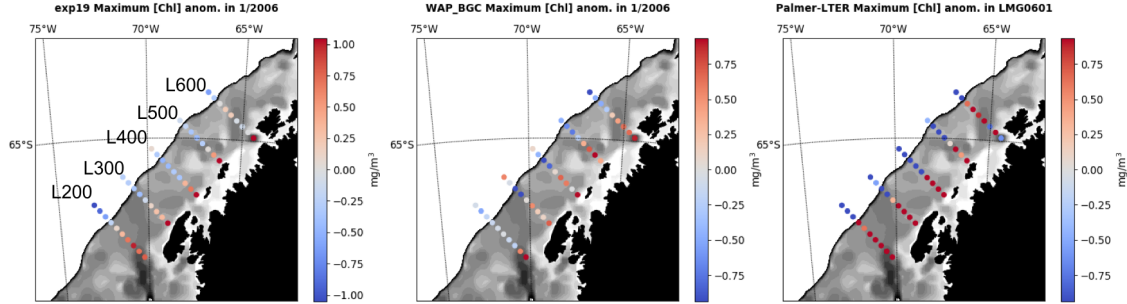


Figure 4-2: Distribution of anomaly of water-column maximum chlorophyll concentration at each station, where the anomaly is computed as the difference from the geometric mean calculated individually for model and observation, for model exp19 (left), model WAP_BGC (middle) and for observed Palmer-LTER cruise data (right).

4.4.2 General patterns of NPP, GPP, Export and e-ratios

As a first step to assess the skill of the model in reproducing the rates observed in the Palmer-LTER project, the climatological monthly mean NPP, GPP, carbon export and e-ratio were calculated for the WAP_BGC results for the duration of the experiment (years 1991 to 2014). The results are presented in figure 4-4 for the months of November, December and January. The results of [47] show that NCP first peaks offshore and is high at the Southern Antarctic Circumpolar Current (ACC) Frontal Zone between October and December, being low in this region thereafter, and peaks at the Shelf Zone in December and January. Although we cannot compare simulated NPP with the rates from [47], which are given in NCP, the temporal progression of NCP and NPP should be comparable. The model results indeed show peak primary production rates around the shelf break (where ACC flows) in December and higher production near the coast in December and January, peaking at the northern part of the grid in December and at the southern part of the grid in January. Primary production, however, remains relatively high in offshore areas off Marguerite Bay in January, reaching values over $20 \text{ mmolC/m}^2\text{d}$, which suggests that the offshore dFe concentrations might still be overestimated despite the changes made to the forcing files.

The carbon export monthly means show highest values in the same areas as the highest NPP values at each month, but a lag in export is evident in the e-ratios,

which present relatively high values where NPP was high in the previous month. The areas where e-ratio in the model is equal or approaching 1 in November and December correspond to areas of high sea ice concentrations during these months. At the same place, carbon export and NPP are similar and close to the value set on the model as minimum concentration for biogeochemical tracers, of 10^{-8} units. The highest e-ratios in the northern part of the grid are reached in February (when e-ratio is about 0.7), and in March in the southern part of the grid (e-ratio is about 0.6), indicating a two-month lag with the NPP maximums. From May to October the e-ratios are higher than one but both carbon export and NPP approach zero. Particle export measured during the Palmer-LTER cruise ranged from 0.2 to 3.9 mmolN/m²d, with most values close to 1 mmolN/m²d [19]. Using a Redfield C:N ratio of 106:16, these measurements would be equivalent to a range between 1.35 and 26 mmolC/m²d. The carbon export in the model is on the higher end of the observed values through much of the shelf, and the January e-ratios are about twice as high as the geometric mean e-ratio calculated for the cruise data between 2012-2014 of 0.18 ± 0.67 [19].

Palmer-LTER cruise NPP was estimated by [94] to be around 500 to 750 mgC/m²d at the shelf (41.6 to 62.4 mmolC/m²d) and 250 to 400 mgC/m²d at the slope (20.8 to 33.3 mmolC/m²d). In the northern part of the shelf modeled NPP reached values around 60 mmolC/m²d in December and 40 mmolC/m²d in January, NPP peaking with values around 40 mmolC/m²d in the southern part of the shelf, and maximum NPP around 60 mmolC/m²d in the slope area. Thus, the WAP_BGC experiment results presents NPP comparable to the values described in [94] in the northern part of the shelf, underestimates NPP in the southern part of the shelf and overestimates NPP at the slope.

Figures 4-5 and 4-6 show WAP_BGC experiment results for the vertical distribution of the climatological monthly mean NPP, climatological carbon export and climatological mixed layer depth (MLD) for lines 200 and 600 of the Palmer-LTER cruise, for the months of December and January. The climatological monthly means were calculated for the period analyzed in the experiments, between 1991 and 2014. It is observed that on Line 600, in the northern part of the LTER grid, NPP is higher

in December, where it peaks at near the surface with the highest values of around 3.2 mmolC/m³d observed around stations 120 to 180, which include the mid-shelf to shelf break region. Particle export is higher at the stations where NPP is higher, close to the shelf break. Also in December, however, although NPP is higher close to the coast relative to the offshore area, export is higher offshore than in the coastal stations, with the higher export likely reflecting sinking of particles formed during the month of November. In January, most of the NPP is noticed in close to the MLD, likely indicating nutrient limitation.

On Line 200, NPP peaks offshore in December, with values close to 3 mmolC/m³d, and the bloom extends to the coast in January, although with lower maximums, around 1.5 mmolC/m³d. In the southern region, the bloom close to shore extends from the surface to the MLD, indicating less iron stress towards the surface in the southern part of the LTER grid. While particle export was higher offshore in December, it was relatively constant throughout the whole line in January.

The Palmer-LTER NPP data is based on 24 hour on-deck incubations spiked with ¹⁴C and represent short time-scale rates that are not expected to match the model monthly means for NPP on a point to point comparison. The Palmer-LTER dataset, however, encompasses multiple years and can provide valuable information on the broader spatial and temporal distribution of NPP. Similar to the analysis done for chlorophyll, therefore, the model vertically integrated data was compared to the Palmer-LTER cruise by comparing rates and spatial distribution of cruise NPP with monthly means from the model output.

Figures 4-7 and 4-8, therefore, compare vertically integrated NPP from the Palmer-LTER cruises with the monthly mean WAP_BGC vertically integrated NPP from the corresponding month of the cruise. The depth of sampling for the Palmer-LTER data is based on light levels, with every station sampled as deep as the euphotic zone, determined at 1% of the surface PAR. So, although the vertical integration for the cruise data is done for different depths, it represents the vertically integrated NPP for the whole water column. The years compared are 2002 and 2003, identified in Vernet et al (2008) as years of high and low chlorophyll, respectively, and for which the model

chlorophyll concentration presented good spatial correlation with the Palmer-LTER data. It is observed that although the NPP values were comparable in 2002, the NPP maxima were lower in the model than in the Palmer-LTER data. In 2003, however, the NPP maxima were comparable. The spatial variability of NPP in the LTER data and the range of values measured for both years, however, is much higher in the cruise data than in the model results.

To investigate the interannual variability of NPP and export along the Palmer-LTER grid and to identify areas in which particle export could be higher, the annual total NPP and carbon export were calculated for each station of the Palmer-LTER grid, for the period of one year starting every August. Total NPP and carbon export for 1992, for example, would reflect the total quantities from August 1991 to July 1992. The Palmer-LTER grid stations were then separated in coastal (stations 0-60 for lines 200-600) and shelf break/offshore (stations 160-220, lines 200-600), and north (lines 400-600, all stations) and south (lines 200-300, all stations), shown in Figure 4-9.

Comparing the coastal and shelf break/offshore stations it is seen that, when integrated over one year, coastal stations have lower NPP, which is inconsistent with the observations, and that NPP offshore is particularly high in years of negative sea ice anomaly the preceding winter (1999, 2009, 2011). Although observations suggest higher NPP close to shore and lower NPP in years of low sea ice, WAP_BGC represented an improvement over exp19, which presented annually integrated NPP of about 8 molC/m^2 at the shelf break and 6 molC/m^2 in the coastal stations. The results indicate, however, that dFe concentrations offshore could still be too high in the initial condition, with stronger blooms being produced in the low sea ice years due to mixing of subsurface dFe. Carbon export exhibits similar interannual variability to NPP in both the coastal and shelf break areas, with e-ratios being lower in the coastal area most years. Offshore, e-ratios were more variable and presented a larger range of values compared to onshore. The lower e-ratios in the coastal area could be due to higher remineralization rates, advection of particulate matter offshore or due to differences in vertical mixing between coastal and offshore stations.

Comparing the north and south regions of the Palmer-LTER grid, it is noticed that the northern area has higher annually integrated NPP. Although the NPP data available from the Palmer cruises represent in-situ short-term rates and cannot be extrapolated to infer longer time-scale production, annually integrated NCP from [47], derived from chlorophyll concentration, indicates that primary production is higher in the southern area of the grid. The high NPP observed in the north region in the model is likely driven by the anomalous high production observed in the shelf break and offshore areas. Export ratios are similar between the northern and southern areas, although maxima reaching 0.5 are observed in the southern region during 2003 and 2010.

To evaluate the reasons for the variability in the e-ratios, the average yearly vertically integrated NPP and export, and the anomalies from the averages for the 2005-2006 and 2007-2008 periods, are shown in Figure 4-10. These years were chosen to represent years of high and low e-ratios. 2005-2006 had relatively low e-ratios throughout the whole grid, while 2008 had relatively high e-ratios. While in the offshore regions other years presented higher e-ratios than 2008, during this year e-ratio was relatively high in both onshore and offshore regions, and in the northern and southern regions of the LTER grid. It is seen that in 2005-2006 the NPP anomalies are positive in the coastal areas and in areas around the shelf break between lines 200 and 600, and while particle export anomalies are positive in the coastal areas, they are either small or negative around the shelf break. In 2007-2008, however, NPP and particle export anomalies are positive throughout the shelf and in Marguerite Bay.

Figure 4-11 shows WAP_BGC NPP anomaly from the monthly climatology calculated for the duration of the integration, and climatological and monthly MLD and particle export during December 2007 and January 2008 for line 200 of the Palmer-LTER grid. On this line, the vertically integrated NPP is positive in all stations, while export anomalies are negative offshore (Figure 4-10). In December NPP anomalies shown in Figure 4-11 were positive throughout the whole line, while export was anomalously high across the shelf but lower than the climatology in the shelf break and offshore regions. In January, NPP remained anomalously high offshore,

with positive anomalies restricted to depths around the ML in the shelf. Export during this month was high in the shelf break and offshore, and close to climatological values in the coastal areas.

To better understand the influence of mixing and advection in the particle export patterns, a broader investigation relating particle concentration, vertical mixing and currents throughout the whole grid and time period of the analysis would be necessary. It is possible, however, that the lower export observed offshore in the simulation during December 2007 could be due to advection of particles to a different location. The Antarctic Circumpolar Current (ACC), which flows along the shelf break, is a dominant circulation feature in the WAP, and the currents are stronger around the shelf break region compared to coastal areas. The influence of advection would also explain why, in the shelf break area, the highest NPP yearly anomaly is observed between lines 200 and 300, while the largest export is seen further northeast around the offshore stations of line 300.

On line 600 of the Palmer-LTER grid, vertically integrated NPP shown in Figure 4-10 was higher than in the climatology along the shelf break and offshore areas in 2005-2006, while 2007-2008 showed a high positive anomaly in the export data and a modest increase in NPP. Figures 4-12 and 4-13 show the vertical profile of NPP, along with MLD and particle export, for November and December of 2005 and 2007. In 2005, although NPP anomaly was positive in November around the shelf break and offshore areas, export remained close to the climatological values in November and were lower than the climatological values in December. In 2007, although the NPP anomalies were positive in the shelf break and offshore area, the NPP increase was more modest than observed in 2005. Particle export, however, showed positive anomalies, which persisted in December despite negative NPP anomalies during that month. These patterns would be consistent with advection playing a larger role in the offshore area of line 600, where increased NPP during 2005-2006 would lead to excess export further north, while increased export in the same region during 2007-2008 would be due to increased NPP further south. In the coastal areas, the patterns in the NPP and export anomalies show a more similar spatial distribution.

4.4.3 Inorganic carbon cycle and air-sea CO₂ fluxes

In order to properly simulate the air-sea CO₂ exchange in the model, it is necessary to properly reproduce the inorganic carbon cycle in the surface ocean. As a first assessment of the skill of the model in reproducing DIC and total alkalinity (TA), the climatological monthly means of these tracers were calculated for WAP_BGC results, for the duration of the experiment (1991-2014). The surface values for November, December and January are shown in Figure 4-14. As is observed in [31], there is more variability in the shelf and coastal areas compared to offshore for both DIC and TA, due to the influence of freshwater fluxes and PP. [31] also observe an onshore-offshore gradient in DIC and TA, which is seen in the DIC data throughout the summer and more apparent in the TA values during December and January. The authors also observe a north-south gradient in TA during the cruises, although this gradient was not seen in the DIC data due to the influence of dilution in the northern part and PP in the southern part. In the WAP_BGC results, while a north-south gradient in DIC is not immediately obvious in the locations of the Palmer-LTER stations, DIC is much lower in Marguerite Bay, where concentrations reach values close to 1900 mmol/m³. In the TA January data, mid to outer shelf have lower concentrations in the locations of line 200, consistent with lower concentrations found in the southern region during the Palmer-LTER cruises.

The range of observed surface DIC concentrations from the cruise data ranged from 1850 to 2173 $\mu\text{mol}/\text{kg}$ on the shelf and onshore areas, with higher offshore concentrations ranging from 2072 to 2255 $\mu\text{mol}/\text{kg}$. The model DIC climatological means exhibited summer maximums near 2150 mmol/m³ in December, and minimums close to 1900 mmol/m³, consistent with the observed values given that extremes of concentration ranges are not expected to be observed in climatologies. The observed TA concentrations ranged from 2265 to 2355 $\mu\text{mol}/\text{kg}$ offshore and 2087 to 2396 $\mu\text{mol}/\text{kg}$ on the shelf and coastal areas in the study of [31]. In January, the model concentrations are on the lower end of the observed values offshore, with TA around 2250 mmol/m³, and show values around 2280 mmol/m³ through most of the shelf, with

minimums around 2000 near the coast and in Marguerite Bay. Although measurements of air-sea CO₂ flux are scarce in the Palmer-LTER grid, the region is expected to be a sink of atmospheric carbon. The model results suggest that, during the summer, the shelf is a relatively strong sink, with flux minimums around -7 molC/m²y in the northern part of the shelf in December and around lines 200 and 300 in January.

To evaluate the skill of the model in reproducing the interannual variability of the inorganic carbon cycle, the monthly means of WAP_BGC DIC and TA were compared with the available cruise data. Figure 4-15 shows the correlation and bias between surface DIC and TA from the Palmer-LTER cruise data and the corresponding monthly mean points from the WAP_BGC output. The correlations were calculated for the whole grid and individually for the southern (lines 200, 300) and the northern (lines 400 to 600) parts of the grid. Both DIC and TA had better correlation with the cruise data in the northern part of the grid, where correlations were predominantly positive. In the south region correlation was more variable and negative for DIC in 1995 (PD-9501), 2000 (LMG-0001) and 2010 (LMG-1001). During the years of negative spatial correlation in the DIC data, however, the correlation was not significant. The biases in the results show that the model underestimated DIC and TA, with differences no larger than 40 mmol/m³ in most of the years in the grid.

Figures 4-16 and 4-17 show the surface DIC concentrations from the cruise data and the corresponding monthly means for the model results and anomalies from the mean surface DIC calculated for each station, using the data collected at the cruise and the monthly mean model results from the years sampled. Figure 4-16 shows the results for line 200 of the Palmer-LTER grid, and Figure 4-17 shows the results for line 600. Unlike chlorophyll and NPP cruise data, which represents short term rates and concentrations, surface DIC drawdown represents the cumulative effects of seasonal processes including NCP. Comparing the model monthly means to cruise data, therefore, is telling of whether the model was able to reproduce the observed phenomena throughout the season. It is observed that, overall, the interannual variability and onshore-offshore gradient of surface DIC is well represented in the model in both lines 200 and 600.

In 1996 (PD96-01), when a large phytoplankton bloom is observed in the northern part of the Palmer-LTER grid (but not in the south), DIC anomalies are negative in both cruise data and model results in line 600, and positive in line 200. 2006, identified as a high chlorophyll year throughout the grid ([94]), shows negative DIC anomalies in both lines 200 and 600. In year 2011, in which a large phytoplankton bloom is observed in the Palmer data, the model does not accurately show the observed strong negative anomalies. During this year, however, [3] observed high dFe concentration specially towards the southern part of the LTER grid, indicating that local processes that are not expected to be reproduced in the model might be responsible for the large bloom.

Figures 4-18 and 4-19 show a similar analysis for surface TA. It observed that while the onshore-offshore gradient is present in the model results, the differences between modeled and observed TA are higher on line 600, indicating that the north-south TA gradient in the model is underestimated. Similar to the DIC results, however, years of high negative and positive TA anomalies are well represented in the model, indicating good simulation of the interannual variability.

Figure 4-20 show the vertical profiles of DIC of the Palmer data for cruise LMG-0101 and the monthly mean WAP_BGC DIC for January 2001, for lines 200 and 600 of the Palmer-LTER grid. During the 2001 cruise, DIC was sampled at depth at stations close to shore, mid-shelf and at the shelf break, which is the reason why this year is shown. It is seen that although the simulated and observed surface DIC are similar, subsurface DIC is underestimated in the model. This could be an artifact of the initial and boundary conditions chosen, given that large scale datasets such as GLODAPv2 (Global Ocean Data Analysis Project for Carbon, version 2) could present biases towards the open-ocean values. [37] observed that DIC concentrations in the modified Upper Circumpolar Deep Water (UCDW) measured in the north of Marguerite Bay were higher than the DIC concentrations from the ACC-derived UCDW due to the influence of remineralization as UCDW flows through the shelf. Also, [65] observed that during the winter vertical mixing replenishes DIC at the surface layer, so that mid-summer DIC concentrations at the surface are not related

to DIC concentrations from the previous summer and are related to the DIC pool in the deep regions. Low subsurface DIC concentration in the initial and boundary conditions, therefore, would also partially explain the negative surface biases observed in the model.

Climatological monthly mean air-sea CO₂ fluxes were calculated for the WAP_BGC results for the duration of the integration, and the results for January and August are shown in Figure 4-21. Negative values indicate fluxes towards the ocean, while positive fluxes indicate degassing. Although degassing is expected during the winter months, the model shows fluxes close to zero due to the presence of sea ice. The sea ice free areas during the winter, however, still present slightly negative fluxes, indicating that the ocean is a weak sink of carbon given the simulated DIC concentrations associated with increased CO₂ solubility in cold waters, can still lead to lower p_{CO2} in the ocean relative to atmospheric values. During the summer, coastal areas in the southern part of the LTER grid present fluxes around -7 molC/m²y, while offshore the region is a weaker sink of carbon. An observational study at Ryder Bay, on the northern part of Marguerite Bay, by [43] indicates that that region is a strong sink of carbon during the summer, with fluxes as low as -15 molC/m²y, while winter fluxes are positive and close to 10 molC/m²y. Although it is not possible to extrapolate the values from Ryder Bay to the WAP, the ranges of values found for air-sea CO₂ fluxes in the integration is much smaller, with winter fluxes are either close to zero due to sea ice coverage or slightly negative, indicating a weak sink of carbon in the model.

To properly assess the potential of the model to simulate carbon fluxes along the WAP, simulated p_{CO2} still needs to be compared to the Palmer-LTER underway p_{CO2} data. Figure 4-22, which shows the average annual air-sea CO₂ flux, therefore, constitutes an initial assessment of the model results which needs to be investigated further. North of Marguerite Bay the model exhibits a stronger sink than predicted by [43], of about 0.59 to 0.94 molC/m²y. Although there is not enough data to validate the air-sea fluxes throughout the grid, the comparison with the data collected at Ryder Bay indicates that although the summer fluxes are weaker in the model, the potential of the region to act as a sink is overestimated given the model does not

predict degassing during the winter months.

Figure 4-22 also shows the annual air-sea CO₂ flux anomalies, as well as anomalies of annually integrated NPP and average surface salinity, for the periods between August 2001 and July 2002, and August 2005 and July 2006. These periods were chosen for representing years of positive and negative DIC anomalies, respectively, observed throughout the whole Palmer-LTER grid. By comparing the air-sea CO₂ flux anomalies with anomalies of NPP and surface salinity, it is possible to infer the processes that are more likely to influence the gas flux anomalies. Positive NPP would be expected to lower gas fluxes, making the region a stronger sink, while salinity provides information about the effects of dilution of DIC and can also indicate anomalies in vertical mixing, given lower surface salinity would indicate a more stable ML.

During the 2001-2002 period, negative NPP anomaly at Marguerite Bay seems to be responsible for the positive flux anomalies (which indicate a weaker sink of carbon), since negative salinity anomaly suggests dilution by sea ice and glacial sources, which would lead to a more stable ML with lower DIC concentrations. At the locations of the Palmer-LTER stations, however, air-sea fluxes seem to be influenced by physics, given that regions of positive NPP anomalies still present positive air-sea CO₂ anomalies. Except for the coastal areas, where CO₂ fluxes are close to zero, salinity anomalies are predominantly positive throughout the shelf and shelf break area, indicating that the fluxes could be affected by mixing with DIC-rich subsurface waters.

During 2005-2006, both biological and physical effects seem to be complementary, with negative salinity anomalies, while NPP anomalies are predominantly positive throughout the shelf. Mid-shelf around lines 500 and 600, however, present negative NPP anomalies and slightly positive CO₂ flux anomalies, indicating a large role of primary production in controlling the CO₂ flux in the shelf. Offshore, however, positive flux anomalies seem to be related to positive surface salinity anomalies, despite higher NPP in some areas. To properly calculate the influence of PP in the drawdown of DIC and therefore on the air-sea fluxes, DIC values would have to be compared to the DIC-salinity dilution line. However, the dilution line is calculated based on

freshwater and UCDW DIC concentrations, and improper representation of UCDW DIC would lead the errors in the calculation. In order to properly calculate the slope of the dilution curve, however, it is necessary to identify a DIC concentration that is representative of the shelf-UCDW values on the model, taking into account that UCDW temperatures present a negative bias with the observed values, also due to the bias of the boundary and initial conditions. Further work in this regard is warranted.

4.5 Discussion and Conclusions

In this chapter, the ocean circulation, sea ice and biogeochemistry model previously described in chapters 2 and 3 of this thesis was slightly modified, and the results were analyzed to assess the skill of the model to predict NPP and surface inorganic carbon cycles in the WAP. The modifications done to the model relative to the experiments described in chapter 3 include changing the initial condition for dFe, which was lowered to curb the phytoplankton bloom previously observed at the shelf break and offshore, and adjusting the initial slope of the phytoplankton growth curve. The simulation used in this chapter (WAP_BGC) represented higher correlations with the Palmer-LTER cruise chlorophyll data, agreeing with the hypothesis of chapter 3 that dFe was overestimated in the initial and boundary conditions.

Even with this modification, simulated NPP in the phytoplankton bloom along the shelf break region is overestimated compared to the Palmer-LTER grid observation, although the magnitude of this overestimation is lower than in previous simulations. The temporal and spatial progression of the bloom throughout the summer at the WAP, however, is well represented in the model, with the bloom first peaking offshore in November/December and following the retreat of sea ice towards the coast. The spatial variability of NPP in the model is lower than observed during the Palmer-LTER cruises, which is not surprising given that the cruise data represent daily rates, which are presumably smoothed in the monthly means analyzed in the model, and given that the model does not include interannual variability of glacial discharges (and consequently dFe inputs).

Maximum e-ratios in the model results present a lag of two months compared to the maximum NPP rates, and are more variable and generally higher in the shelf break/offshore stations compared to the stations near the coast. Although a more comprehensive analysis is needed to quantify the effects of mixing and circulation on particle export, an initial assessment of the model results indicates that advection had a larger influence on the distribution of export in the offshore area. Quantifying the influence of vertical mixing in particle export with in situ data is a challenging endeavor, given that vertical mixing introduces errors to the O_2/Ar NCP estimates, and mixing of suspended particles is not captured in the ^{238}U - ^{234}Th disequilibrium export estimates. Model results with good representation of the surface mixed layer physics, therefore, provide a useful tool to quantify the effect of physics in sinking particles. Before the influence of mixing and advection can be quantified in the model, the next step in this research is to conduct an assessment of top-down controls on the phytoplankton and of the portion of NPP that is remineralized. To conduct this analysis however, improved model diagnostics are needed, with a physiological representation of zooplankton respiration. It is possible that the lower e-ratios calculated for the northern part of the LTER grid are due to higher remineralization rates during the longer growth season.

Interannual variability of DIC and TA in the model was consistent with the observed in the Palmer-LTER cruises, and indicate that the model is able to reproduce the variability of physical and biological phenomena in the WAP. The seasonal drawdown and spatial patterns of DIC concentrations are a better indicator of the skill of the model than cruise data for chlorophyll and NPP, which are influenced by higher variability phenomena such as storms and eddies that are not reproduced by the model. Both modeled DIC and TA, however, present lower values than observed in the Palmer-LTER cruises. The bias towards lower surface DIC and TA in the model extends at least down to 150 m, and is possibly caused by lower concentrations in the initial and boundary conditions at depth.

The model results show that the WAP could be a regional location of net CO_2 drawdown, with larger uptake in the shelf area. While during the summer, the ob-

served fluxes are lower than the fluxes observed by [43] at Ryder Bay, with model results around $-7 \text{ molC/m}^2\text{y}$ and in situ data as low as $-15 \text{ molC/m}^2\text{y}$, it is still possible that the model overestimates the potential of the WAP as a carbon sink due to the lower surface DIC in the fall and winter. The effect of sea ice in the air-sea gas fluxes also needs to be investigated. In the model, air-sea fluxes are calculated for the grid cell and multiplied by the open-water fraction assuming linearity in gas exchange. It is possible, though, that the effect of sea ice in modulating the wind and surface turbulence at sub-grid scales would impact gas transfer.

Overall, the model is able to reproduce the seasonal and interannual variability in physical, biological and chemical processes in the WAP, and constitutes a powerful tool to test hypotheses raised by the Palmer-LTER project. The analyses conducted thus far indicate that part of the biases of the model results when compared to cruise data are due to improper representation of inorganic carbon and nutrients in the initial and boundary conditions. Building better forcing files, however, is a great challenge given the lack of data in the region. The analyses done in this thesis support the hypotheses that anomalously large phytoplankton blooms are fueled by glacial dFe inputs, and that mixing plays an important role in exporting organic matter to the deep.

Next steps to better understand the dynamics of the biogeochemistry in the WAP include better parameterizations of the iron cycle and of the influence of sea ice in the air-sea gas transfers. To quantify the influence of PP in the inorganic carbon cycle, it is important to identify an average DIC concentration for UCDW in the model data, so that DIC can be plotted against an appropriate dilution line. Since the formulation of zooplankton respiration is not based on zooplankton physiology, it is worth developing an equation that can properly simulate this quantity so that the amount of carbon respired by zooplankton can be calculated offline using temperature and zooplankton biomass outputs. This would allow export to be compared to an estimated NCP to assess the temporal and spatial scales at which these two quantities are expected to be similar.

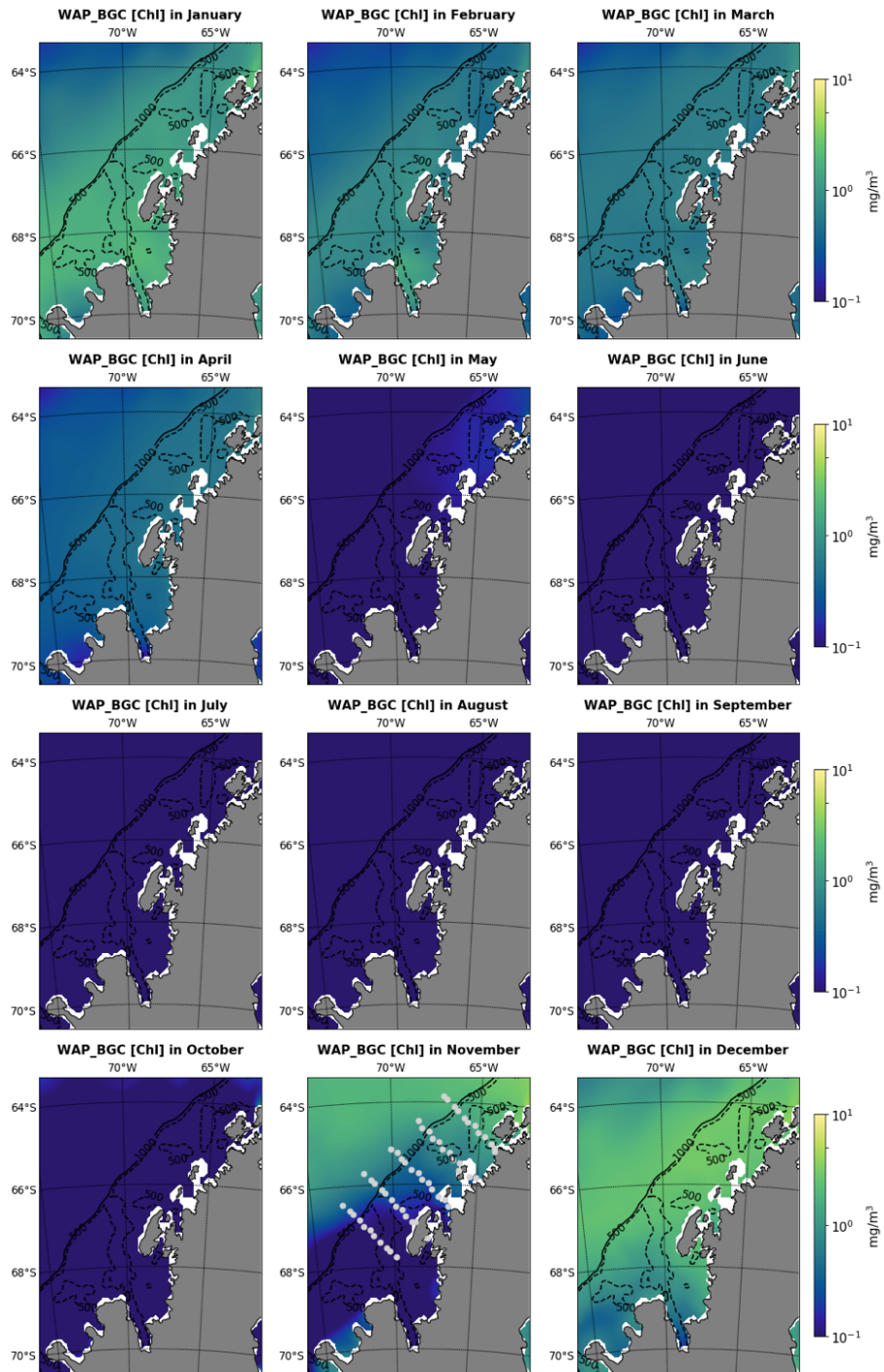


Figure 4-3: Monthly climatology of surface chlorophyll concentration for WAP_BGC experiment, calculated using model output from 1991 to 2014.

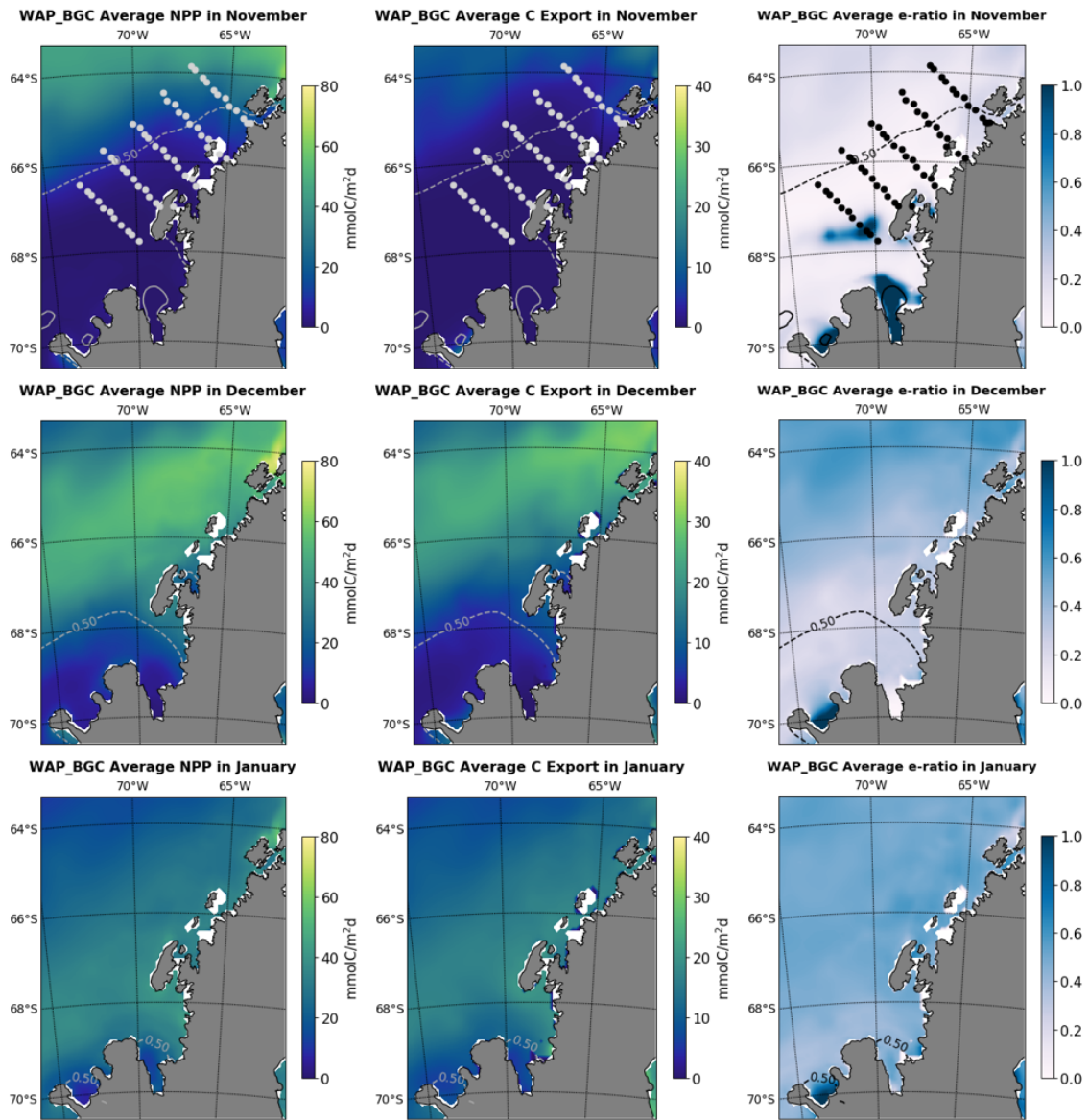


Figure 4-4: Model WAP_BGC climatological (from 1991-2014) showing monthly means for NPP (left), carbon export below 100 m (middle) and e-ratio (right) for November (top), December (middle) and January (bottom). Dashed line represents sea ice concentration and dots plotted in November represent the location of the Palmer-LTER grid stations.

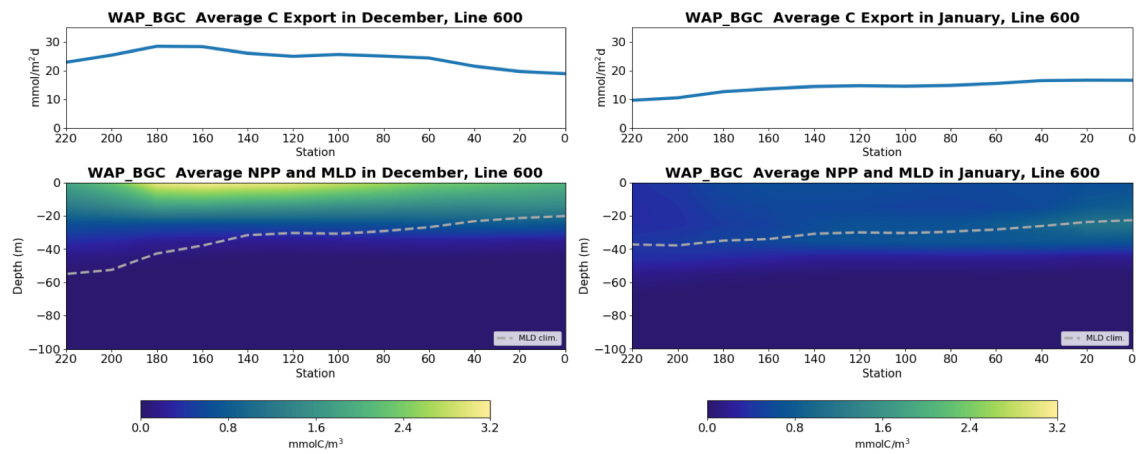


Figure 4-5: Climatological monthly mean C export (top) and NPP (bottom) calculated for 1991 to 2014 for WAP_BGC results, for December (left) and January (right), for stations of Line 600 of the Palmer-LTER grid.

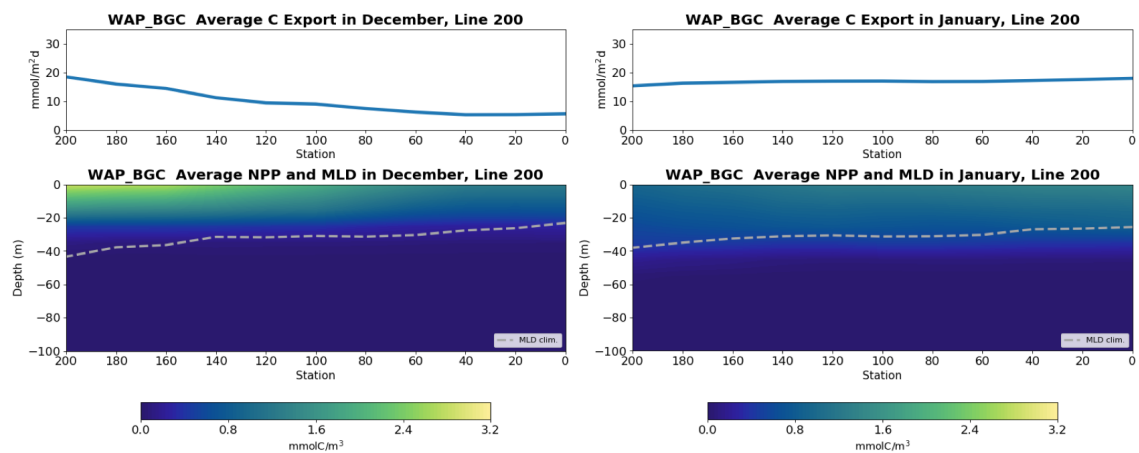


Figure 4-6: Climatological monthly mean C export (top) and NPP (bottom) calculated for 1991 to 2014 for WAP_BGC results, for December (left) and January (right), for stations of Line 200 of the Palmer-LTER grid.

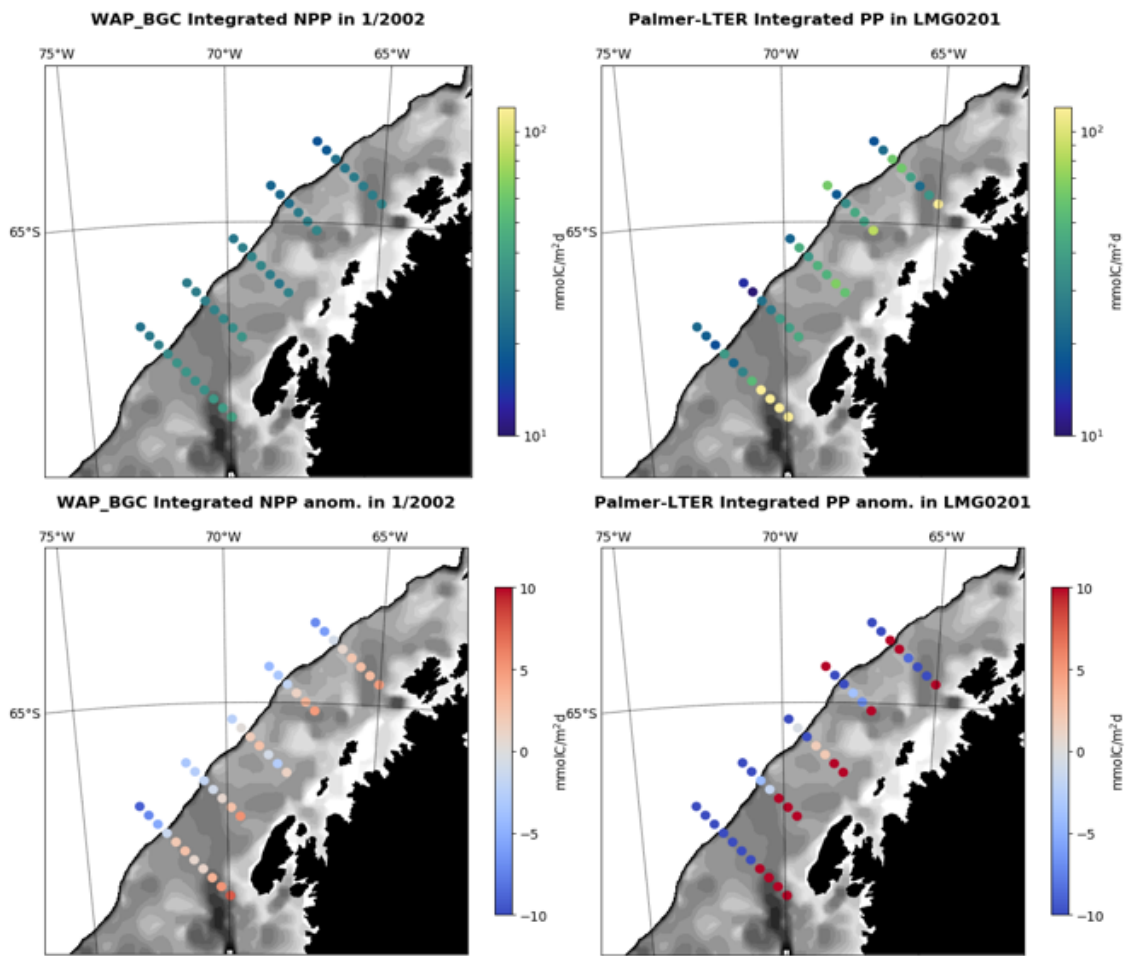


Figure 4-7: Vertically integrated NPP (top) and deviations from the mean integrated NPP calculated for all the stations (bottom) for WAP_BGC monthly means of January 2002 (high chlorophyll year, left) and Palmer-LTER cruise LMG02-01.

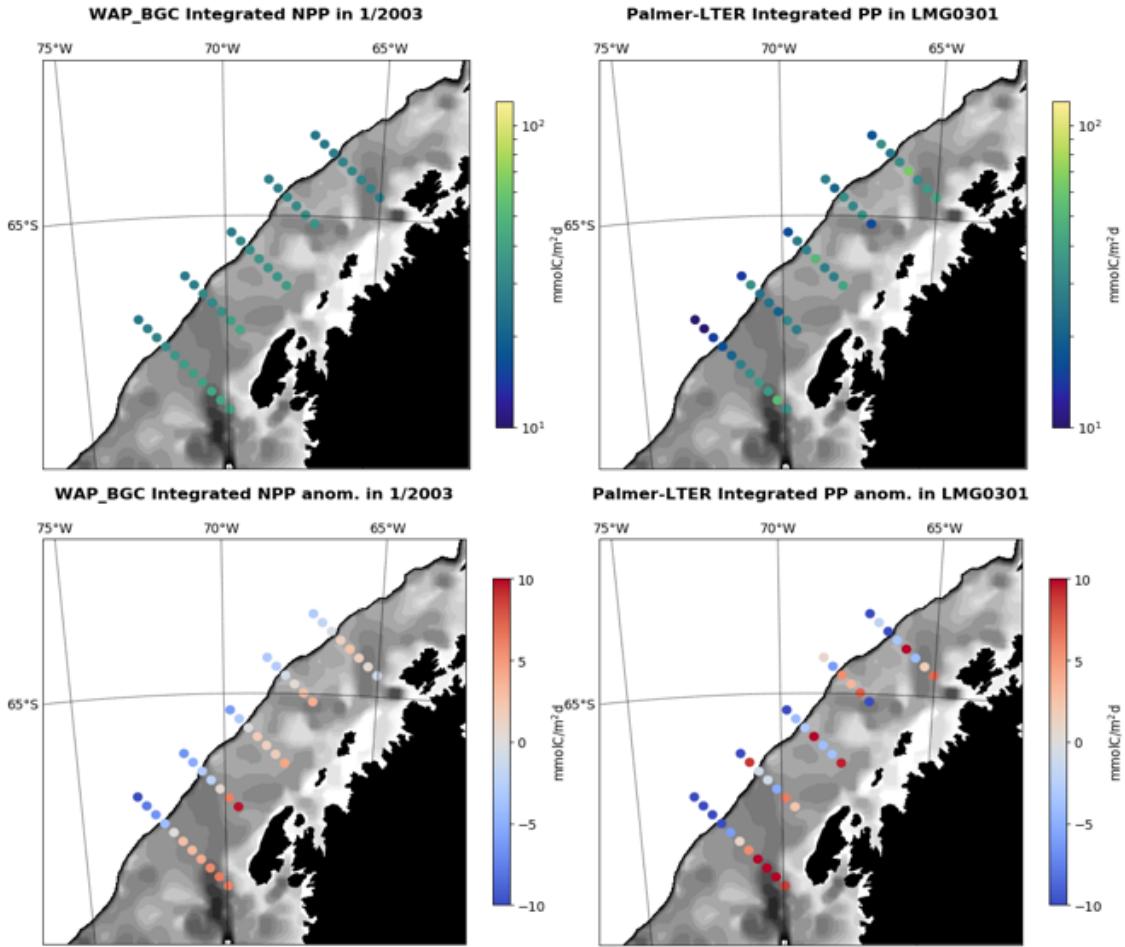


Figure 4-8: Vertically integrated NPP (top) and deviations from the mean integrated NPP calculated for the stations (bottom) for WAP_BGC monthly means of January 2003 (left) and Palmer-LTER cruise LMG03-01.

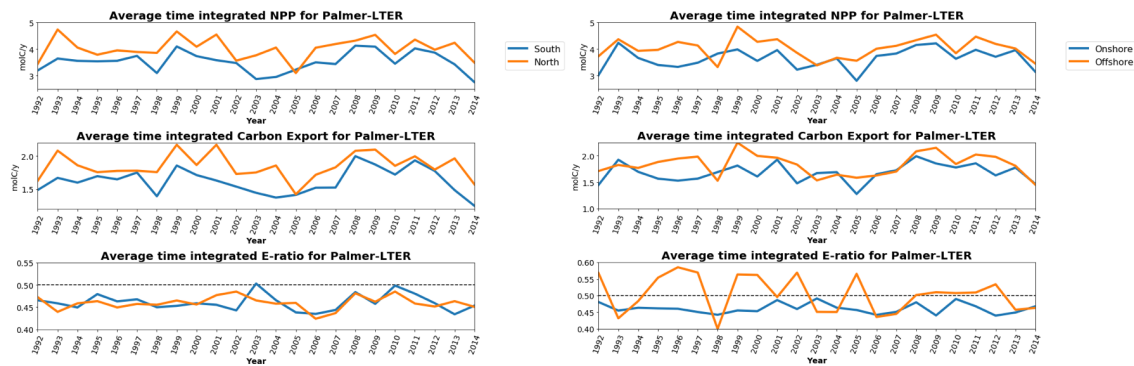


Figure 4-9: WAP_BGC yearly and vertically integrated simulated NPP (top), carbon export (middle) and e-ratio (bottom) for Palmer-LTER grid North (Lines400-600, orange) and South (Lines 200 and 300, blue) areas (left), and onshore (stations 0-60, blue) and shelf break/offshore (stations 160-220, orange) areas (right).

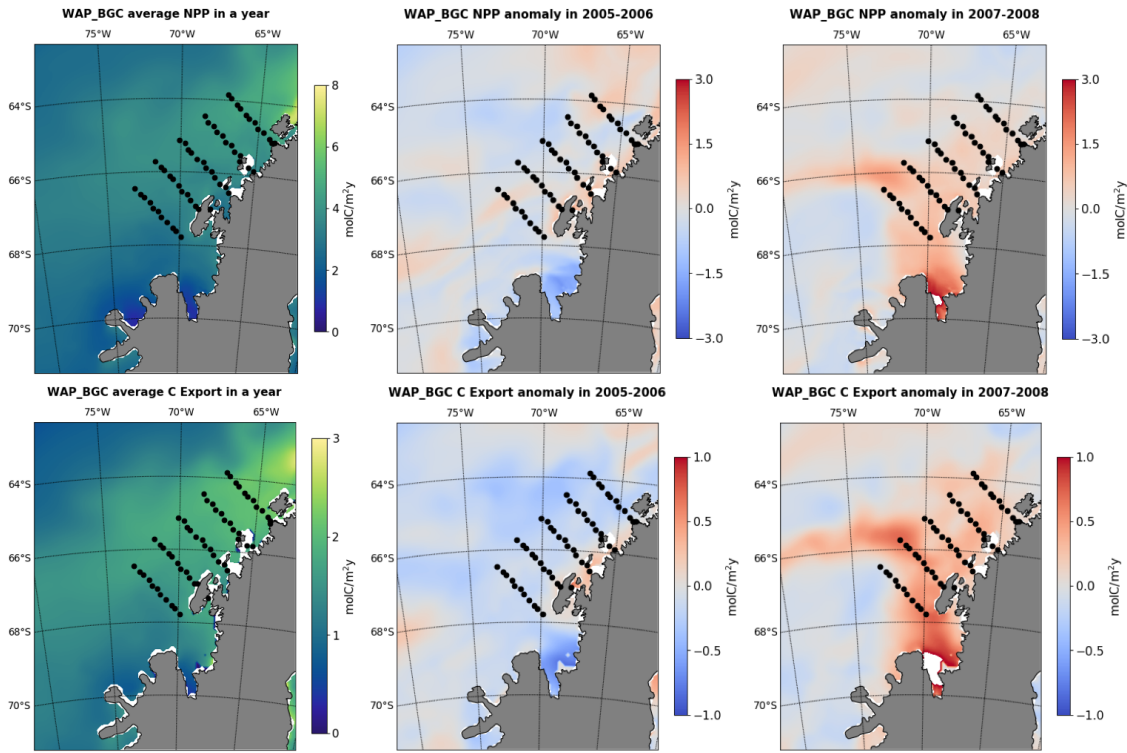


Figure 4-10: WAP_BGC yearly (August to July) simulated NPP (top) and carbon export (bottom) for the model climatology (left), and anomalies for August 2005-July 2006 (middle) and August 2007-July 2008 (right).

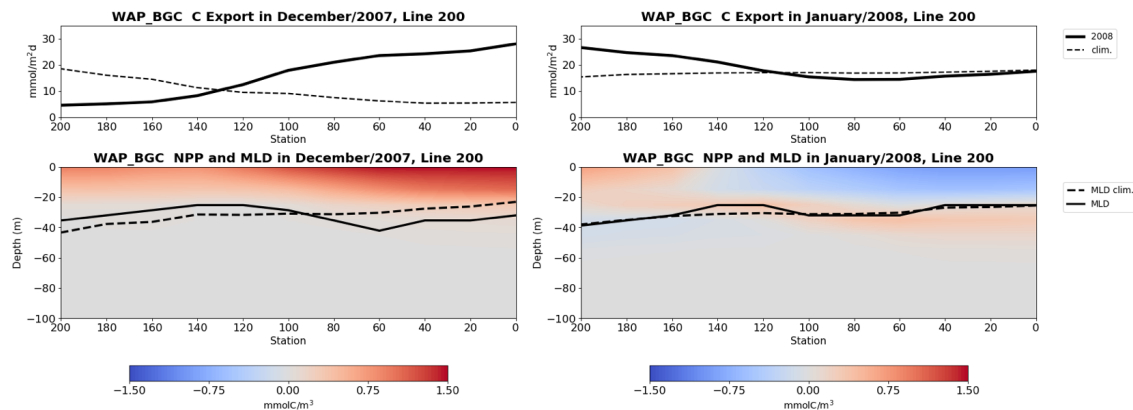


Figure 4-11: Vertical profile of experiment WAP_BGC simulated NPP anomaly from the climatology, MLD and particle export across line 200 of the Palmer-LTER grid for the monthly mean of December 2007 (left) and January 2008 (right).

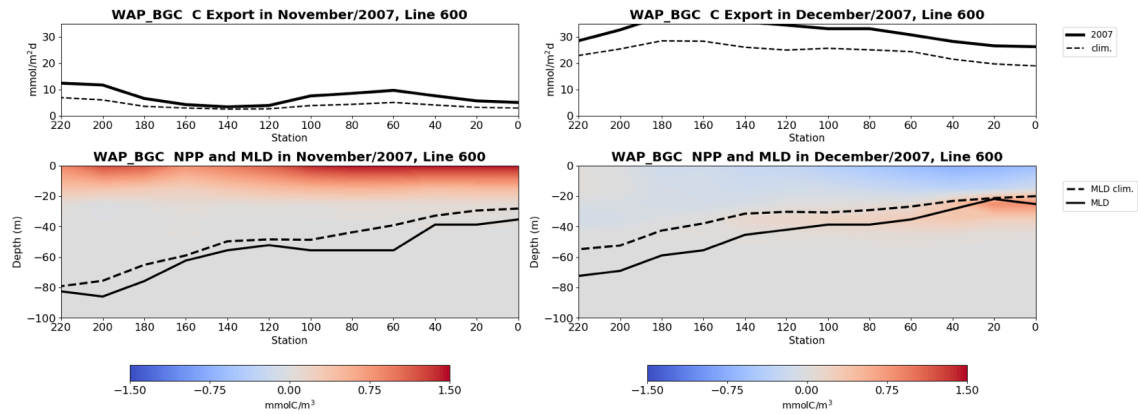


Figure 4-12: Vertical profile of experiment WAP_BGC simulated NPP anomaly from the climatology, MLD and particle export across line 600 of the Palmer-LTER grid for the monthly mean of December 2007 (left) and January 2008 (right).

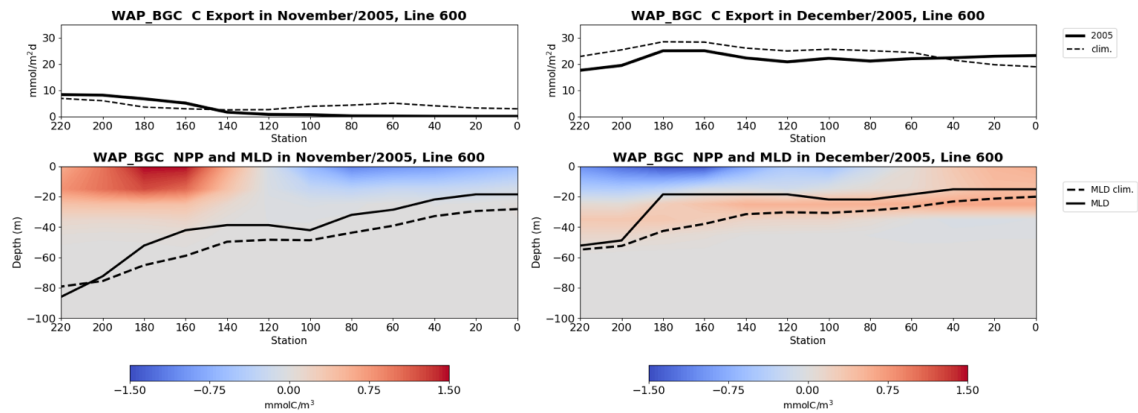


Figure 4-13: Vertical profile of experiment WAP_BGC simulated NPP anomaly from the climatology, MLD and particle export across line 600 of the Palmer-LTER grid for the monthly mean of November 2005 (left) and December 2005 (right).

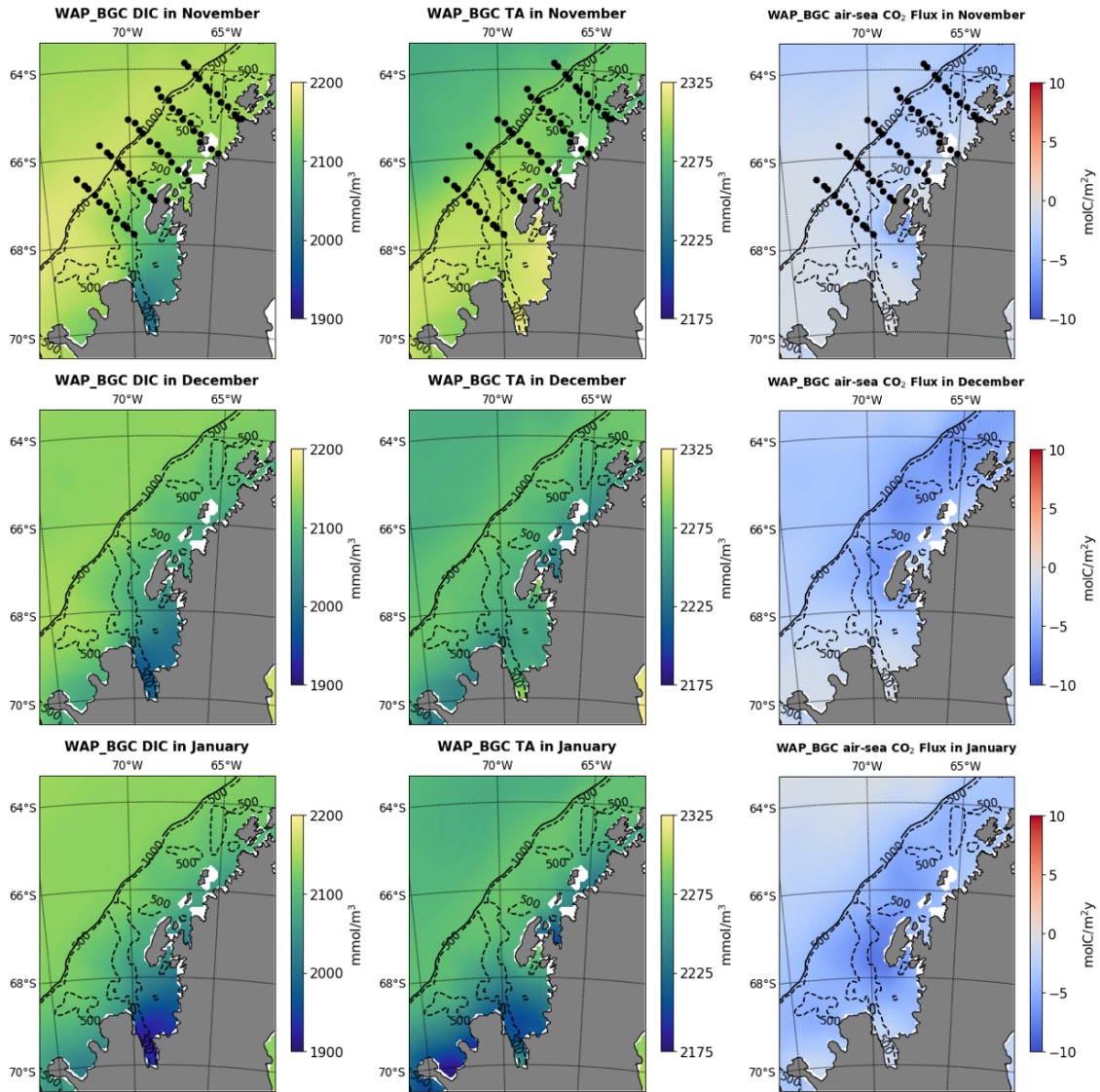


Figure 4-14: Climatological surface DIC (left), Alkalinity (middle) and air-sea CO_2 flux (right) calculated for WAP_BGC results from 1991 to 2014 for November (top), December (middle) and January (bottom).

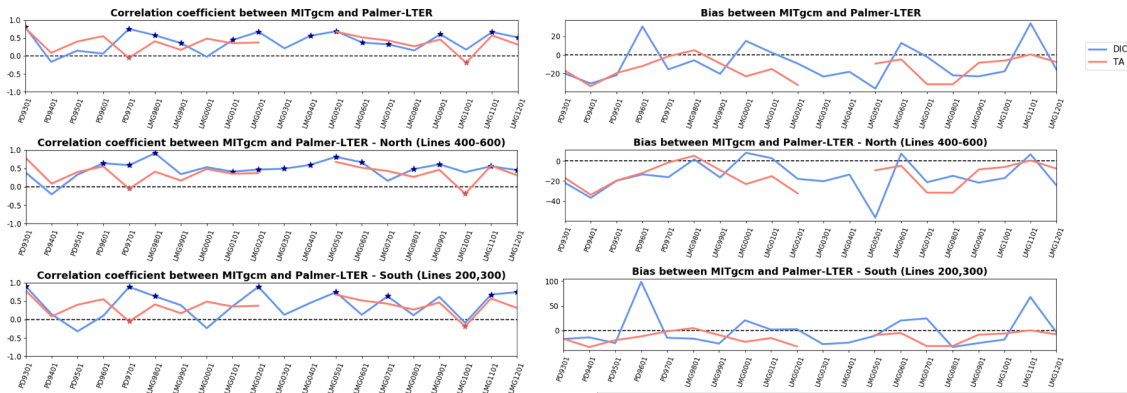


Figure 4-15: Correlation coefficient (left) and bias (right) between experiment WAP_BGC results and Palmer-LTER cruise data for surface DIC and surface alkalinity, for all stations of the Palmer-LTER grid (top), Lines 400-600 (middle) and Lines 200 and 300 (bottom). Points marked with a star indicate where correlation was significant at a 0.05 level.

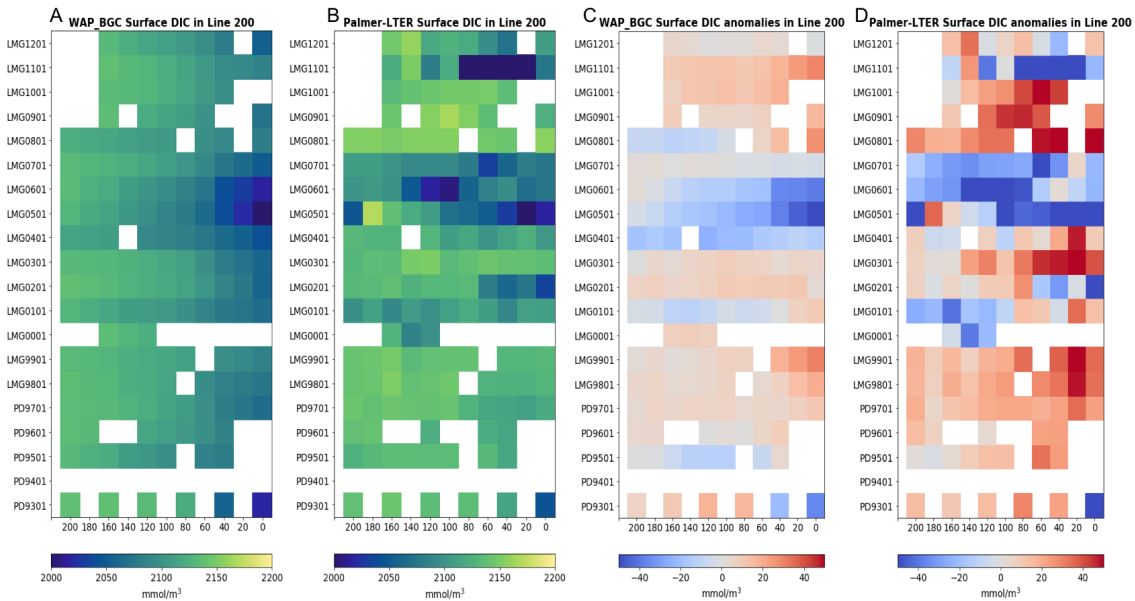


Figure 4-16: Data for Line 200 of the LTER grid; A – Surface DIC from experiment WAP_BGC at the points sampled during Palmer-LTER cruises; B – Surface DIC from Palmer-LTER cruises; C – Anomalies from the average surface DIC during the months of Palmer-LTER cruises, calculated for each station from experiment WAP_BGC output; D – Anomalies from the average surface DIC during Palmer-LTER cruises, calculated for each station from Palmer-LTER cruise data.

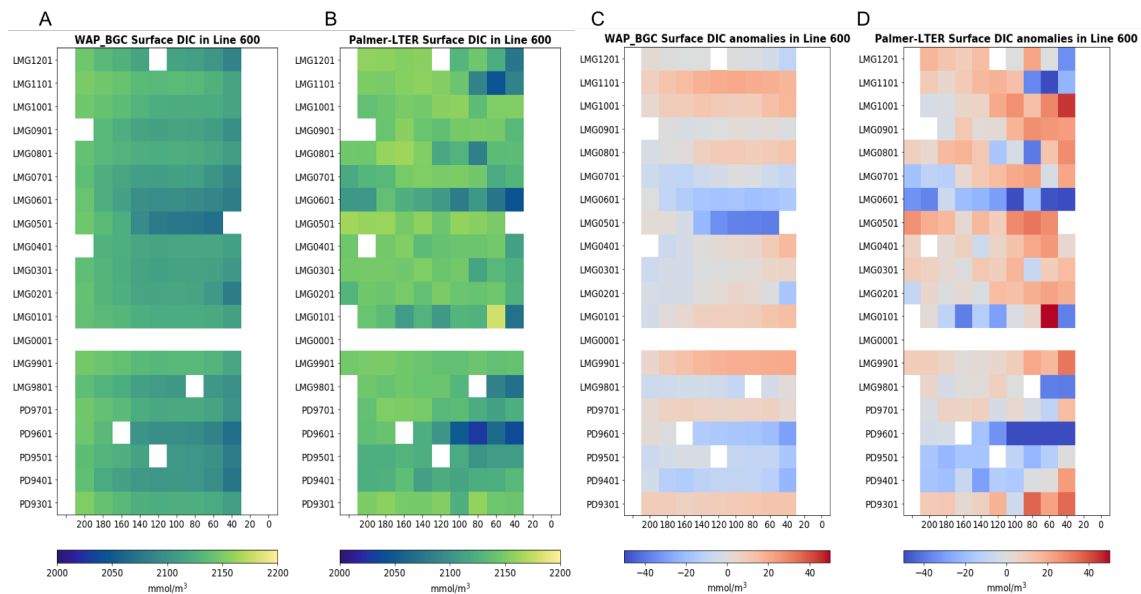


Figure 4-17: Data for Line 600 of the LTER grid; A – Surface DIC from experiment WAP_BGC at the points sampled during Palmer-LTER cruises; B – Surface DIC from Palmer-LTER cruises; C – Anomalies from the average surface DIC during the months of Palmer-LTER cruises, calculated for each station from experiment WAP_BGC output; D – Anomalies from the average surface DIC during Palmer-LTER cruises, calculated for each station from Palmer-LTER cruise data.

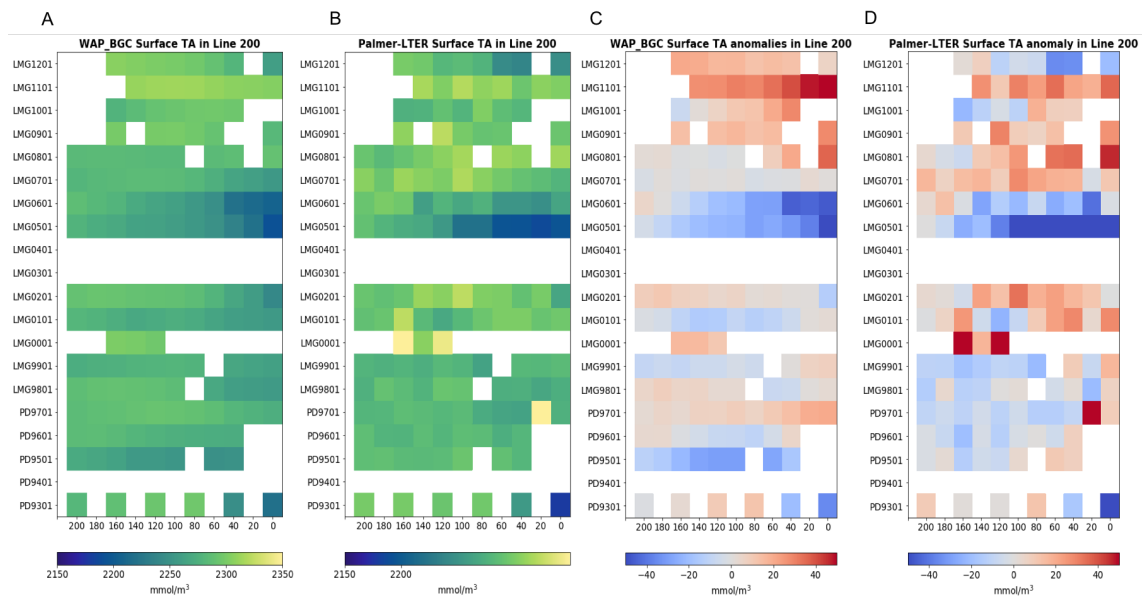


Figure 4-18: Data for Line 200 of the LTER grid; A – Surface Alkalinity from experiment WAP_BGC at the points sampled during Palmer-LTER cruises; B – Surface Alkalinity from Palmer-LTER cruises; C – Anomalies from the average surface Alkalinity during the months of Palmer-LTER cruises, calculated for each station from experiment WAP_BGC output; D – Anomalies from the average surface Alkalinity during Palmer-LTER cruises, calculated for each station from Palmer-LTER cruise data.

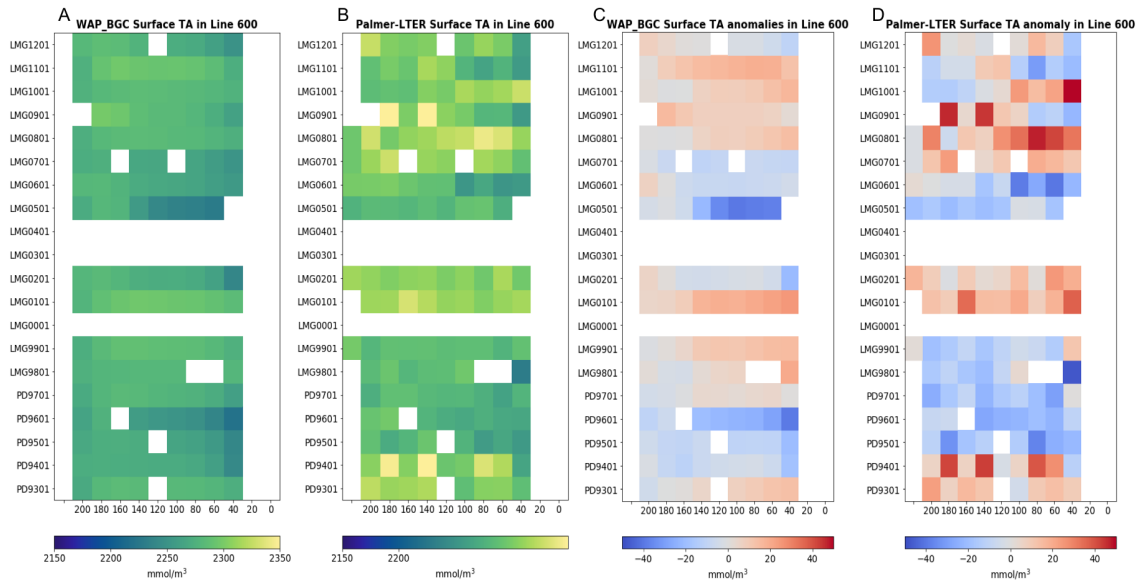


Figure 4-19: Data for Line 600 of the LTER grid; A – Surface Alkalinity from experiment WAP_BGC at the points sampled during Palmer-LTER cruises; B – Surface Alkalinity from Palmer-LTER cruises; C – Anomalies from the average surface Alkalinity during the months of Palmer-LTER cruises, calculated for each station from experiment WAP_BGC output; D – Anomalies from the average surface Alkalinity during Palmer-LTER cruises, calculated for each station from Palmer-LTER cruise data.

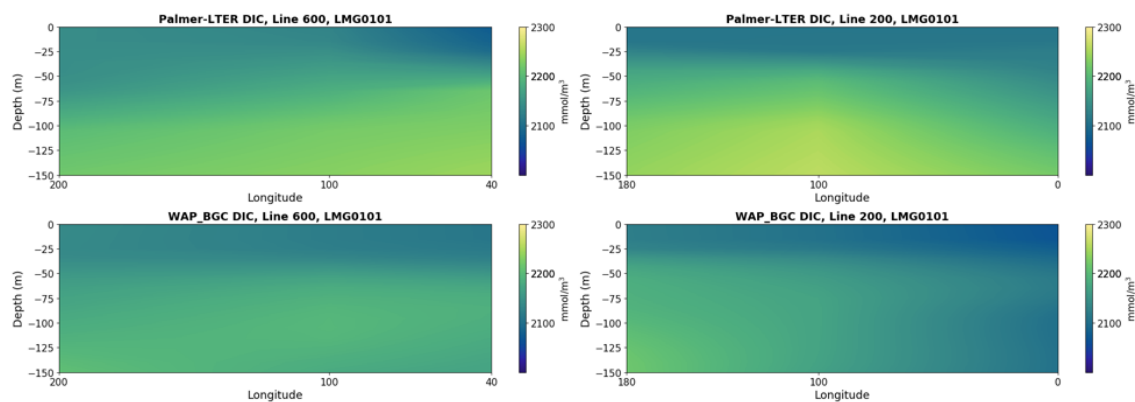


Figure 4-20: Vertical profile of DIC sampled at Palmer-LTER cruise LMG-0101 (top) and experiment WAP_BGC monthly mean for January 2001 (bottom), for line 600 (left) and line 200 (right) of the Palmer-LTER cruise.

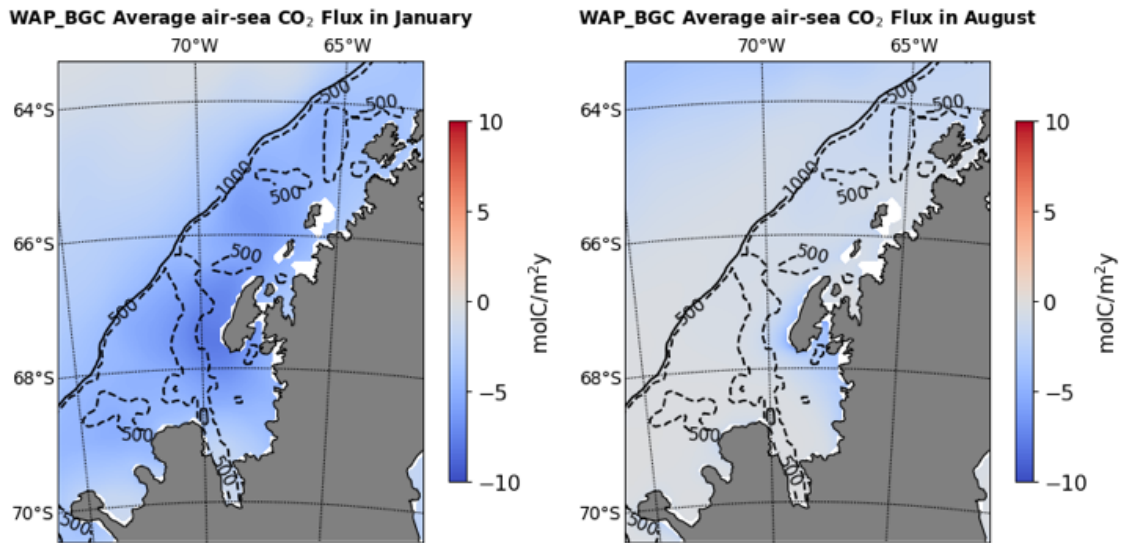


Figure 4-21: Climatological monthly mean air-sea CO_2 flux from WAP_BGC experiment output, for January (left) and August (right).

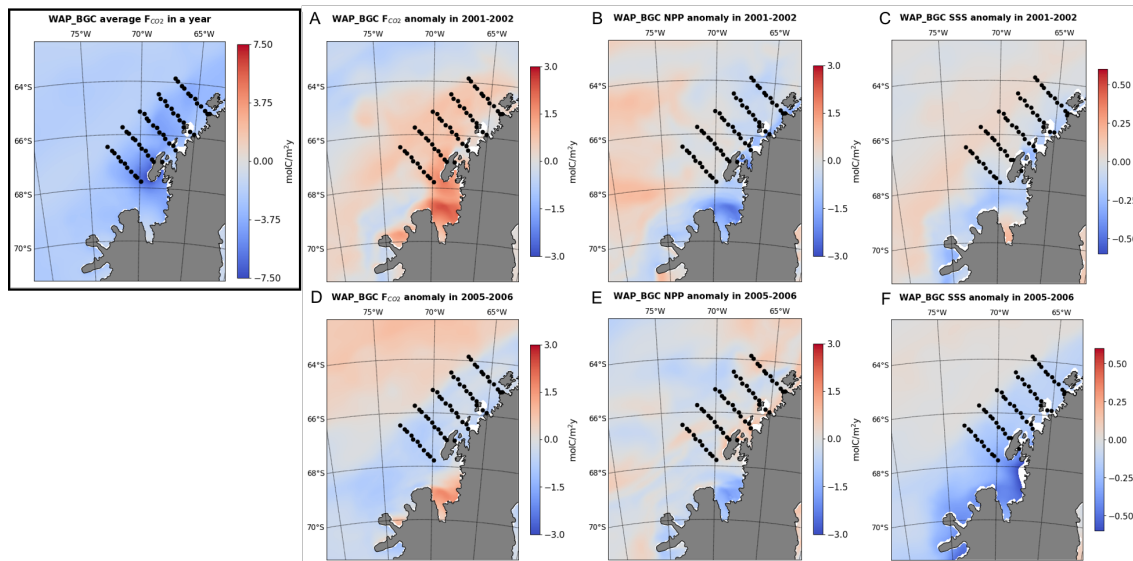


Figure 4-22: All data from WAP_BGC results. On black box: total annual air-sea flux of CO_2 from 1991 to 2014. Anomaly from the climatological yearly air-sea CO_2 flux calculated for the period between August 2001 and July 2002 (A) and August 2005 to July 2006 (D); anomaly from climatological yearly NPP (calculated from 1991 to 2014) for the 2001-2002 period (B) and the 2005-2006 period (E); Anomaly from yearly mean surface salinity (calculated between 1991-2014) for the 2001-2002 period (C) and for the 2005-2006 period (F).

Chapter 5

Conclusions

An ocean circulation, sea ice and biogeochemistry model was constructed for the WAP and tested for its skill to reproduce the seasonal cycles and interannual variabilities of the regional ocean circulation, sea ice, chlorophyll, primary production (PP), and inorganic carbon cycle. To better simulate the phenomena observed at the WAP, modifications were made to both the physics and the biogeochemistry of the model, and the simulations were compared to data collected by the Palmer-LTER project during regional survey cruises that take place during the austral summer since 1991, as well as data from Palmer Station and from the Rothera Time Series (RaTS).

The circulation and sea ice model is based on the regional MIT-Ocean GCM simulation implemented by [69], and uses the same grid and forcing files. However, their study was focused on large scale freshwater balance and did not evaluate the skill of the model in simulating the mixed layer depth (MLD) and interannual variability of sea ice at the region of the Palmer-LTER grid. Properly simulating these physical parameters, however, is extremely important for this study given the influence of MLD and sea ice on the biogeochemistry of the region. Therefore, modifications were done to the model in order to better reproduce the characteristics of the MLD observed in the data collected during the Palmer-LTER project and sea ice extent and concentration obtained from satellite data (SSM/I).

A bias towards shallow MLD in the model when compared to the observations was identified, and a few approaches were tested in an attempt to deepen the mixed

layer: lowering the prescribed volume of surface freshwater runoff, increasing the critical Richardson number to increase vertical mixing, and changing the wind-sea ice drag coefficient. The wind-sea ice drag coefficient had been previously decreased in the study of [69] so that the model results would match the observed freshwater fluxes in the George VI Ice Shelf. While changing the freshwater inputs and critical Richardson number had very small effects on the model MLD, increasing the wind-sea ice drag coefficient significantly improved the model results, leading to a higher temporal correlation between the simulated and observed (satellite) sea ice data and deepening of the model ML. The improvements happened given sea ice transport is increased when using a higher drag coefficient, which led to a faster sea ice retreat and less melt in the region of the Palmer-LTER grid.

Despite the increase in model MLD, a shallow bias persisted when comparing monthly mean MLD in the model results to the synoptic MLD in the Palmer-LTER data. Previous modeling studies have also identified a bias towards shallow MLD in the Southern Ocean ([6][12]), and it has been hypothesized that this bias is due to the absence of a parameterization representing Langmuir circulation in the vertical mixing schemes. Two different approaches to incorporate the mixing effects of Langmuir circulation parameterization, then, were tested in this model. The first approach represents Langmuir circulation effects as an enhancement factor applied to the turbulent velocity scale in the vertical mixing (L17), and the second approach introduces a new formulation for the velocity scale (LF17). A correction term was also applied to the wind speed to account for the influence of sea ice in modulating wind, based on the study of [1]. The closest match to the Palmer-LTER MLD was obtained by the second approach, adopting a new formulation for the velocity scale, in simulation KPP_Ut.

Although the changes introduced to the model physics significantly improved the simulated MLD, a smaller bias towards shallow ML still persisted. The model, however, properly represents sea ice seasonal and interannual variability, and the distribution of the water masses present in the WAP during the different seasons. The physical configuration of simulation KPP_Ut described in chapter 2, therefore, was

used in chapter 3 to test the performance of the biogeochemical model in simulating the seasonal and interannual variations in the phytoplankton bloom.

To assess the skill of the model to reproduce the phytoplankton blooms in the WAP, model results were compared to chlorophyll data collected during the Palmer-LTER regional survey cruises and from the seasonal/annual time-series at Palmer Station E and Rothera Station. The regional survey cruise data only represent a single time point per station for each season and do not provide information on the seasonal evolution of the bloom; near-shore time-series station data are highly influenced by local sub-grid scale phenomena that are not captured by the model. Therefore, comparing the model to either dataset has to be done with caution. The regional survey data, however, provide valuable information on the spatial distribution and magnitude of the phytoplankton bloom, while station time-series data provide information on the timing and evolution of the bloom.

The biogeochemical model implemented for the WAP during this study was the Regulated Ecosystem Model version 2 (REcoMv2), described in [30]. One modification that was made to the model was the introduction of a parameterization for sub-grid scale effects in light transmission through different sea ice categories described in [48]. The new parameterization introduced is based on the idea that calculating light limitation for phytoplankton growth by using the grid-average photosynthetically available radiation (PAR) when there is sub-grid scale variability in ice thickness leads to overestimation of the bloom. With the new approach, therefore, light limitation terms are calculated under each sea ice category, and the grid-average of the limitation terms is used to calculate phytoplankton growth. Introducing the effect of non-linearity in light transmission through different sea ice thicknesses delayed the phytoplankton bloom, increased variance and spatial correlation between simulated and observed chlorophyll concentrations during most of the years simulated.

The model, underestimated the magnitude of the observed onshore-offshore gradient in chlorophyll concentration that is observed during the regional survey cruises, that show a much stronger bloom near coastal areas. It was also noticed that the spatial correlation between simulated chlorophyll during January and chlorophyll data

from the Palmer-LTER cruises was higher during years preceded by a high sea ice winter, while years preceded by low sea ice winters showed lower model-data correlations and higher chlorophyll concentrations from mid shelf to offshore in the model results. An analysis of the model biological limitation terms showed that iron, which is thought to be limiting in the offshore areas, was less limiting during years of low sea ice when the ML tends to be deeper, leading to the mixing of iron-rich subsurface waters and relieving iron limitation. While properly validating the iron sources in the model is not a possibility given that iron data in the WAP are scarce, decreasing the iron concentration in the initial and boundary conditions of the biogeochemical model improved the spatial representation of the phytoplankton blooms, suggesting that the model forcings overestimate the concentration of this micronutrient and indicating that iron is, indeed, important for the observed onshore-offshore gradients in phytoplankton.

In years preceded by a high sea ice winter, the bloom is delayed and has faster growth in the model, which leads to a faster iron depletion. The iron depletion is more marked offshore, where the bloom happens earlier and where the supply of iron through glacial sources is not available. In years of low sea ice concentration, however, the model had lower correlation with the cruise data. This happens at least partially because iron limitation is decreased offshore due to mixing with dissolved iron-rich subsurface waters once the ML deepens. Dissolved iron concentration (dFe), therefore, needs to be adjusted in the model initial and boundary conditions not only to better represent the concentrations of the different water masses in the WAP, but also to better represent glacial sources, which are thought to be an important source of dFe. From the years in which dFe data is available, [3] observes that 2011 has much higher dFe concentrations than found in data from 2012 and 2013, coinciding with a more intense phytoplankton bloom. This was also a year in which the model presented negative bias in chlorophyll compared to the survey cruise data, while in most years the model chlorophyll bias was positive.

Overall, the temporal and spatial progression of the bloom throughout the spring-summer at the WAP is well represented in the model, with the bloom first peak-

ing offshore in November/December and following the retreat of sea ice towards the coast. The simulated NPP is consistent with values observed during the Palmer-LTER cruises, although the model results exhibit lower spatial and temporal variability. One of the reasons for the lower variability in the model results is that interannual variability is not represented in the model forcings, and the cruise data are compared to monthly mean outputs, which presumably smooth the most extreme values.

The peak carbon export in the model results, marked by maximum e-ratios, exhibit a lag of two months compared to the maximum NPP rates, and e-ratios are more variable and generally higher in the shelf break/offshore stations compared to the stations near the coast. Although a more comprehensive analysis is needed to quantify the effects of mixing and circulation on particle export, an initial assessment of the model results indicates that advection had a larger influence on the distribution of export in the offshore area where currents are stronger. Before the influence of advection in simulated export can be quantified, however, a better assessment of the top-down controls on phytoplankton needs to be performed, and a better diagnostic for zooplankton respiration, more suited to represent zooplankton physiology, needs to be implemented.

In an analysis of the inorganic carbon cycle in the model, it is found that the simulated surface dissolved inorganic carbon (DIC) and total alkalinity (TA) have lower concentrations than observed in the Palmer-LTER cruises. This bias could be at least partially caused by lower concentrations in the initial and boundary conditions at depth. The model shows that the WAP could be a regional location of net CO₂ drawdown, although the potential of the region to act as a sink of atmospheric carbon might be overestimated in the model due to the lower DIC concentrations.

While some further adjustments are still needed to improve the model simulation of the phytoplankton bloom, the results with the present best case from the suite of sensitivity experiments indicate that the model is able to represent the seasonal and interannual variations observed in the circulation, water mass distribution and sea ice observed in the WAP, and has identified gaps in the observations that could guide improvement of the simulation of the regional biogeochemistry. Despite adjustments

needed, the seasonal progression of the phytoplankton bloom is well represented in the model, and pattern of net primary production (NPP) rates in the simulations is largely consistent with observations.

The next steps moving forward with this research in terms of model development and assessment involve improving the initial and boundary conditions for the biogeochemical tracers and performing an assessment of the top-down controls for phytoplankton in the model. Changes to the model code are also needed, including adding a zooplankton respiration term based on physiology, instead of the closure term currently implemented, so that particle export can be compared to net community production (NCP). For a better assessment of the skill of the model to represent air-sea CO₂ fluxes, it is still necessary to compare the simulated pCO₂ to the underway pCO₂ collected during the Palmer-LTER cruises.

Appendix A

Tables

Table A.1: Tracers included in the biogeochemical model REcoMv2

Tracer	Tracer Name	Units
DIN	Dissolved inorganic nitrogen	mmol/m ³
DIC	Dissolved inorganic carbon	mmol/m ³
Alk	Total Alkalinity	mmol/m ³
PhyN	Small phytoplankton nitrogen	mmol/m ³
PhyC	small phytoplankton carbon	mmol/m ³
PChl	small phytoplankton chlorophyll-a	mmol/m ³
detN	Detritus nitrogen	mmol/m ³
detC	Detritus carbon	mmol/m ³
HetN	heterotrophic zooplankton nitrogen	mmol/m ³
HetC	Heterotrophic zooplankton carbon	mmol/m ³
DON	Dissolved organic nitrogen	mmol/m ³
EOC	Extra-cellular organic carbon	mmol/m ³
DiaN	Diatom nitrogen	mmol/m ³
DiaC	Diatom carbon	mmol/m ³
DChl	Diatom chlorophyll-a	mmol/m ³
DiaSi	Diatom silicate	mmol/m ³
detSi	Detritus silicate	mmol/m ³
DSi	Dissolved silicate	mmol/m ³
dFe	Dissolved iron	μ mol/m ³
PCalc	Small phytoplankton CaCO ₃	mmol/m ³
detCalc	Detritus CaCO ₃	mmol/m ³

Table A.2: Parameters changed during sensitivity analysis experiments

Parameter	Parameter Name
p _{zdia}	Maximum preference for grazing on diatoms
p _{phy} ^{max}	Phytoplankton maximum C-specific rate of photosynthesis (d ⁻¹)
p _{dia} ^{max}	Diatom maximum C-specific rate of photosynthesis (d ⁻¹)
Fe2N	Iron to nitrogen ratio
K _{phy} ^{Fe}	Small phytoplankton half-saturation constant for iron uptake (μmolFe/m ³)
K _{dia} ^{Fe}	Diatom half-saturation constant for iron uptake (μmolFe/m ³)
α _{phy}	Small phytoplankton initial slope of the P-I curve (W/mmolCm ² d)
α _{dia}	Diatom initial slope of the P-I curve (W/mmolCm ² d)
K _{scav} ^{Fe}	Scavenging rate
graz	Maximum grazing loss parameter (mmolN/m ³ d)

Table A.3: Parameters changed during sensitivity analysis experiments

Experiment	pzdia	p_{phy}^{max}	p_{dia}^{max}	Fe2N	K_{phy}^{Fe}	K_{dia}^{Fe}	α_{phy}	α_{dia}	K_{scav}^{Fe}	graz
CTRL	0.65	3.0	3.5	0.033	0.02	0.12	0.14	0.19	0.0156	3.0
exp1	0.65	3.5	4.0	0.04	0.01	0.08	0.17	0.23	0.0156	3.0
exp2	0.65	3.5	4.0	0.045	0.01	0.08	0.17	0.23	0.0156	3.0
exp3	0.65	3.5	4.0	0.04	0.015	0.10	0.17	0.23	0.0156	3.0
exp4	0.65	3.5	4.0	0.045	0.015	0.10	0.17	0.23	0.0156	3.0
exp5	0.65	3.5	4.0	0.045	0.015	0.10	0.14	0.19	0.0156	3.0
exp6	0.65	4.0	4.5	0.045	0.015	0.10	0.17	0.23	0.0156	3.0
exp7	0.65	4.0	4.5	0.04	0.01	0.08	0.17	0.23	0.0156	3.0
exp8	0.65	4.0	4.5	0.04	0.01	0.08	0.17	0.23	0.025	3.0
exp9	0.65	4.0	4.5	0.04	0.01	0.08	0.17	0.23	0.007	3.0
exp10	0.65	4.5	5	0.04	0.01	0.08	0.17	0.23	0.0156	3.0
exp11	0.65	4.0	5	0.04	0.01	0.08	0.14	0.18	0.0156	3.0
exp12	0.65	4.0	4.5	0.04	0.01	0.08	0.17	0.23	0.0156	3.0
exp13	0.65	3.8	4.5	0.04	0.01	0.08	0.16	0.23	0.0156	3.0
exp14	0.65	3.8	4.5	0.04	0.01	0.08	0.16	0.23	0.0156	3.5
exp15	0.65	3.5	4.0	0.04	0.01	0.08	0.17	0.23	0.0156	3.0
exp16	0.65	3.5	4.0	0.04	0.02	0.12	0.17	0.23	0.0156	3.0
exp17	0.65	3.0	3.5	0.04	0.02	0.12	0.17	0.23	0.0156	3.0
exp18	0.65	3.5	4.0	0.04	0.02	0.12	0.14	0.19	0.0156	3.0
exp19	0.7	3.5	4.0	0.04	0.02	0.12	0.17	0.23	0.0156	3.0
exp20	0.55	3.5	4.0	0.04	0.02	0.12	0.17	0.23	0.0156	3.0

Table A.4: Cruises sampled by the Palmer-LTER Project

Cruise Name	Date
PD91-09	November 1991
PD93-01	January, February 1993
NBP93-02	March 1993
PD93-07	August, September 1993
PD94-01	January, February 1994
PD95-01	January, February 1995
PD96-01	January, February 1996
PD97-01	January, February 1997
LMG98-01	January, February 1998
LMG99-01	January, February 1999
LMG00-01	January, February 2000
LMG01-01	January, February 2001
LMG02-01	January, February 2002
LMG03-01	January, February 2003
LMG04-01	January, February 2004
LMG05-01	January, February 2005
LMG06-01	January, February 2006
LMG07-01	January, February 2007
LMG08-01	January, February 2008
LMG09-01	January, February 2009
LMG10-01	January, February 2010
LMG11-01	January, February 2011
LMG12-01	January, February 2012
LMG13-01	January, February 2013
LMG14-01	January, February 2014

Appendix B

Including effects of different sea ice categories in PAR transmittance - Implementation

The number of categories of the sea ice model can be altered and is defined by the parameter MULTDIM (defined in this study as 7), declared in the routine SEAICE.h, which contains most of the sea ice field declarations. The different ice categories are variable and defined by thickness, and the thickness distributions are equally distributed between two times the actual thickness of sea ice and an imposed minimum of 5 cm.

A SEAICE package variable was created called QSWM to store the sea ice short-wave radiation that passes through each sea ice category and the open ocean, also defined in SEAICE.h. Calculations pertinent to the implementation of the subgrid-scale PAR calculations are performed on a script called seaice_growth.F, which is responsible for all the updates on sea ice thickness, snow depth and sea ice concentration at every time step. On seaice_growth.F, a local variable called SHW_cov was created to store the short-wave that passed through each sea ice category (calculated in a script called seaice_budget_ocean.F). QSWM, then, is filled with SHW_cov and with the short-wave that reaches open ocean.

Two different routines were modified in the RECOM package: recom_forcing.F,

which calls the biogeochemical model, and `recom_sms.F`, which contains the phytoplankton growth equations. On `recom_forcing.F`, the only modifications necessary were the inclusion of a local variable named `PARadiationM`, with the same dimensions as `QSWM` so that the short-wave fluxes under sea ice can be considered and then averaged after the PAR and phytoplankton routines have been called.

`QSWM` is read by `recom_sms.F`, and multiplied by half, which is the percentage of short-wave assumed to be PAR at the WAP. On this script, an extra dimension had to be added to the variable `surf_light`, which reads the calculated PAR, so that it could accommodate the values calculated for the different sea ice categories and for open ocean. Local variables also had to be created to store PAR during the calculations before averaging of the PAR and light limitation variables. The variables created are: `Limphy_mult` (small phytoplankton light limitation for the multiple sea ice categories), `Limdia_mult` (similar variable for diatoms), `PARtemp` (temporary PAR values to be used during calculations) and `PARavem`, which stores the average PAR already divided by the area covered by each sea ice category. `PARavem` is then summed and passed as a diagnostic.

Upper and lower limits of light are calculated for each category at each cell taking into account the attenuation coefficients of water and chlorophyll, and the average light available for the cell (for each category) is stored in `PARavem`. This value is then used to calculate the light limitation for phytoplankton and diatoms according to:

$$Limphy_mult_i = (1 - \exp(-\alpha_{phy} \times q_{phy}^{Chl} \times \frac{PARavem_i}{P_{phy}^{max}})) \times \frac{SIC}{7} \quad (B.1)$$

For each sea ice category i , and as:

$$Limphy_mult_{i+1} = (1 - \exp(-\alpha_{phy} \times q_{phy}^{Chl} \times \frac{PARavem_i}{P_{phy}^{max}})) \times (1 - SIC) \quad (B.2)$$

For open ocean. The values of `Limphy_mult`, and the similarly calculated `Lim-`

dia_mult, are added and used in the phytoplankton growth equations called later in the model.

Bibliography

- [1] Andreas, E.L., Horst, T.W., Grachev, A.A., Persson, P.O., Fairall, C.W., Guet, P.S., Jordan, R.E., *Parametrizing turbulent exchange over summer sea ice and the marginal ice zone*, Quarterly Journal of the Royal Meteorological Society, 136, 927-943, 2010.
- [2] Annett, A.L., Skiba, M., Henley, S.F., Venables, H.J., Meredith, M.P., Statham, P.J., Ganeshram, R.S., *Comparative roles of upwelling and glacial iron sources in Ryder Bay, coastal west Antarctic Peninsula*, Marine Chemistry, 176, 21-33, 2015.
- [3] Annett, A.L., Fitzsimmons, J.N., Séguret, M.J.M., Lagerström, M., Meredith, M.P., Schofield, O., Sherrell, R.M., *Controls on dissolved and particulate iron distributions in surface waters of the Western Antarctic Peninsula shelf*, Marine Chemistry, 196, 81-97, 2017.
- [4] Arrigo, K.R., van Dijken, G., Long, M., *Coastal Southern Ocean: A strong anthropogenic CO₂ sink*, Geophysical Research Letters, 35, L21602, 2008.
- [5] Beardsley, R.C., Limeburner, R., Owens, W.B., *Drifter measurements of surface currents near Marguerite Bay on the western Antarctic Peninsula shelf during austral summer and fall, 2001 and 2002*, Deep Sea Research Part II: Topical Studies in Oceanography, V. 51, issues 17-19, 1947-1964, 2004.
- [6] Belcher, S.E., Grant, A.L.M., Hanley, K.E., Fox-Kemper, B., Van Roekel, L., Sullivan, P.P., Large, W.G., Brown, A., Hines, A., Calvert, D., Rutgersson, A.,

- Pettersson, H., Bidlot, J., Janssen, P.A.E.M., Polton, J.A., *A global perspective on Langmuir turbulence in the ocean surface boundary layer*, Geophysical Research Letters, 39, L18605, 2012.
- [7] Boyer, T. P., Antonov, J. I., Baranova, O. K., Garcia, H. E., Johnson, D. R., Locarnini, R. A., Mishonov, A. V., O'Brien, T. D., Seidov, D., Smolyar, I. V. and Zweng, M. M., *World Ocean Database 2009, Chapter 1: Introduction*, in S. Levitus (ed.), NOAA Atlas NESDIS 66, World Ocean Database 2009, U.S. Gov. Printing Office, Wash. D.C., p. 216, 2009.
- [8] Buessler, K.O., McDonnell, A.M.P., Schofield, O.M.E., Steinberg, D.K., Ducklow, H.W., *High particle export over the continental shelf of the west Antarctic Peninsula*, Geophysical Research Letters, 37, L22606, 2010.
- [9] Carrillo, C.J., Smith, R.C., Karl, D.M., *Processes regulating oxygen and carbon dioxide in surface waters west of the Antarctic Peninsula*, Marine Chemistry, 84, 161-179, 2004.
- [10] Clarke, A., Meredith, M.P., Wallace, M.I., Brandon, M.A., Thomas, D.N., *Seasonal and interannual variability in temperature, chlorophyll and macronutrients in the northern Marguerite Bay, Antarctica*, Deep-Sea Research Part II, 55, 1988-2006, 2008.
- [11] Cook, A.J., Fox, A.J., Vaughan, D.G. and Ferrigno, J.G., *Retreating glacier fronts on the Antarctic Peninsula over the past half-century*. Science, 308, 541-544, 2005.
- [12] D'Asaro, E.A., *Turbulence in the upper-ocean mixed layer*, Annual Reviews in Marine Sciences, 6, 101-115, 2014.
- [13] Dee, D. P., Uppala, S. M., Simmons, A. J., Berrisford, P., Poli, P., Kobayashi, S., Andrae, U., Balmaseda, M. A., Balsamo, G., Bauer, P., Bechtold, P., Beljaars, A. C. M., van de Berg, L., Bidlot, J., Bormann, N., Delsol, C., Dragani, R., Fuentes, M., Geer, A. J., Haimberger, L., Healy, S. B., Hersbach, H., Holm,

- E. V., Isaksen, L., Kallberg, P., Kohler, M., Matricardi, M., McNally, A. P., Monge-Sanz, B. M., Morcrette, J.-J., Park, B.-K., Peubey, C., de Rosnay, P., Tavolato, C., Thepaut, J.-N. and Vitart, F., *The ERA-Interim reanalysis: configuration and performance of the data assimilation system*, Quarterly Journal of the Royal Meteorological Society 137(656): 553–597, 2011.
- [14] Dickson, A.G., and Goyet, C., *Handbook of Methods for the Analysis of the Various Parameters of the Carbon Dioxide System in sea water. Version 2*, Oak Ridge National Laboratory, Oak Ridge, 1994.
- [15] Dierssen, H.M., Smith, R.C., Vernet, M., *Glacial meltwater dynamics in coastal waters west of the Antarctic Peninsula*, Proceedings of the National Academy of Science USA, 99, 1790-1795, 2002.
- [16] Doney, S.C., Lindsay, K., Caldeira, K., Campin, J.M., Drange, H., Dutay, J.C., Follows, M., Gao, Y., Gnanadesikan, A., Gruber, N., Ishida, A., Joos, F., Madec, G., Maier-Reimer, E., Marshall, J.C., Matear, R.J., Monfray, P., Mouchet, A., Najjar, R., Orr, J.C., Plattner, G.K., Sarmiento, J., Schlitzer, R., Slater, R., Totterdell, I.J., Weirig, M.F., Yamanaka, Y. and Yool, A., *Evaluating global ocean carbon models: the importance of realistic physics*, Global Biogeochemical Cycles, 18, GB3017, 2004.
- [17] Ducklow, H. W., K. Baker, D. G. Martinson, L. B. Quetin, R. M. Ross, R. C. Smith, S. E. Stammerjohn, M. Vernet, and W. Fraser, *Marine pelagic ecosystems: The West Antarctic Peninsula*, Philos. Trans. R. Soc. London, Ser. B, 362, 67–94, 2007.
- [18] Ducklow, H.W., Doney, S.C., Sailley, S.F., *Ecological controls on biogeochemical fluxes in the western Antarctic Peninsula studied with an inverse foodweb model*, Advances in Polar Science, Vol.26, N.2, 122-139, 2015.
- [19] Ducklow, H.W., Stukel, M.R., Eveleth, R., Doney, S.C., Jickells, T., Schofield, O., Baker, A.R., Brindle, J., Chance, R., Cassar, N., *Spring-summer net community production, new production, particle export and related water column*

- biogeochemical processes in the marginal sea ice zone of the West Antarctic Peninsula 2012-2014*, Philosophical Transactions of the Royal Society A, 20170177, 2018.
- [20] Eveleth, R., Cassar, N., Sherrell, R.M., Ducklow, H., Meredith, M.P., Venables, H.J., Lin, Y., and Li, Z., *Ice melt influence on summertime net community production along the Western Antarctic Peninsula*, Deep Sea Research Part II: Topical Studies in Oceanography, 139, 89-102, 2017.
- [21] Eveleth, R., Cassar, N., Doney, S. C., Munro, D. R., and Sweeney, C., *Biological and physical controls on O_2/Ar , Ar and pCO_2 variability at the Western Antarctic Peninsula and in the Drake Passage*, Deep Sea Research Part II: Topical Studies in Oceanography, 139, 77-88, 2017.
- [22] Fogt, R.L., Bromwich, D.H., Hines, K.M., *Understanding the SAM influence on the South Pacific ENSO teleconnection*, Climate Dynamics, 36, 1555-1576, 2011.
- [23] Fretwell, P., Pritchard, H.D., Vaughan, D.G., Bamber, J.L., Barrand, N.E., Bell, R., Bianchi, C., Bingham, R.G., Blankenship, D.D., Casassa, G., Catania, G., Callens, D., Conway, H., Cook, A.J., Corr, H.F.J., Damaske, D., Damm, V., Ferraccioli, F., Forsberg, R., Fujita, S., Gim, Y., Gogineni, P., Griggs, J.A., Hindmarsh, R.C.A., Holmlund, P., Holt, J.W., Jacobel, R.W., Jenkins, A., Jokat, W., Jordan, T., King, E.C., Kohler, J., Krabill, W., Riger-Kusk, M., Langley, K.A., Leitchenkov, G., Leuschen, C., Luyendyk, B.P., Matsuoka, K., Mouginot, J., Nitsche, F.O., Nogi, Y., Nost, O.A., Popov, S.V., Rignot, E., Ripplin, D.M., Rivera, A., Roberts, J., Ross, N., Siegert, M.J., Smith, A.M., Steinhage, D., Studinger, M., Sun, B., Tinto, B.K., Welch, B.C., Wilson, D., Young, D.A., Xiangbin, C., Zirizzotti, A., *Bedmap2: improved ice bed, surface and thickness datasets for Antarctica* Cryosphere 7, 375–393, 2013.

- [24] Garibotti, I.A., Vernet, M., Ferrario, M.E., *Annually recurrent planktonic assemblages during summer in the seasonal ice zone west of the Antarctic Peninsula (Southern Ocean)*, Deep-Sea Research I, 52, 1823-1841, 2005.
- [25] Geider, R.J., MacIntyre, H.L., Kana, T.M., *A dynamic regulatory model of phytoplankton acclimation to light, nutrients, and temperature*, Limnology and Oceanography, 43, 679-694, 1998.
- [26] Gleiber, M.R., Steinberg, D.K., and Schofield, O.M.E., *Copepod summer grazing and fecal pellet production along the Western Antarctic Peninsula*, Journal of Plankton Research, Vol 38, Issue 3, 732-750, 2015.
- [27] Hauck, J., Volker, C., Wang, T., Hoppema, M., Losch, M., Wolf-Gladrow, D.A., *Seasonally different carbon flux changes in the Southern Ocean in response to the Southern Annular Mode*, Global Biogeochemical Cycles, 27, 1236-1245, 2013.
- [28] Hauck, J., Völker, C., Wolf-Gladrow, D.A., Laufkötter, C., Vogt, M., Aumont, O., Bopp, L., Buitenhuis, E.T., Doney, S.C., Dunne, J., Gruber, N., Hashioka, T., John, J., Le Quéré, C., Lima, I.D., Nakano, H., Séréfian, R., Totterdell, I., *On the Southern Ocean CO₂ uptake and the role of the biological carbon pump in the 21st century*, Global Biogeochemical Cycles, 29, 1451-1470, 2015.
- [29] Hauck, J., Volker, C., *Rising atmospheric CO₂ leads to large impact of biology on the Southern Ocean CO₂ uptake via changes of the Revelle factor*, Geophysical Research Letters, 42, 1459-1464, 2015.
- [30] Hauck, J., Kohler, P., WolfGladrow, D., Volker, C., *Iron fertilization and century-scale effects of open ocean dissolution of olivine in a simulated CO₂ removal experiment*, Environmental Research Letters, 11, 024007, 2016.
- [31] Hauri, C., Doney, S.C., Takahashi, T., Erickson, M., Jiang, G. and Ducklow, H.W., *Two decades of inorganic carbon dynamics along the Western Antarctic Peninsula*, Biogeosciences, 12, 6761-6779, 2015.

- [32] Hofmann, E.E., Klinck, J.M., *Hydrography and circulation of Antarctic Continental Shelf: 150°E eastward to the Greenwich Meridian*. In: Brink, K.H., Robinson, A.R. (Eds.), *The Sea, The Global Coastal Ocean, Regional Studies and Synthesis*. 11. John Wiley & Sons, New York, pp. 997–1042, 1998.
- [33] Hohn, S., *Coupling and decoupling of biogeochemical cycles in marine ecosystems*, PhD Thesis, Universitat Bremen, 2009.
- [34] Holland, P.R., Bruneau, N., Enright, C., Losch, M., Kurtz, N.T. and Kwok, R., *Modeled Trends in Antarctic Sea Ice thickness*, *Journal of Climate*, 27, 3784–3801, 2014.
- [35] Huang, K., Ducklow, H.W., Vernet, M., Cassar, N., Bender, M.L., *Export production and its regulating factors in the West Antarctic Peninsula region of the Southern Ocean*, *Global Biogeochemical Cycles*, 26, GB2005, 2012.
- [36] Hunke, E.C. and Dukowicz, J.K., *An elastic-viscous-plastic model for sea ice dynamics*, *Journal of Physical Oceanography*, 27:1849–1868, 1997.
- [37] Jones, E.M., Fenton, M., Meredith, M.P., Clargo, N.M., Ossebaar, S., Ducklow, H.W., Venables, H.J., and de Baar, H.J.W., *Ocean acidification and calcium carbonate saturation states in the coastal zone of the West Antarctic Peninsula*, *Deep-Sea Research II*, 139, 181-194, 2017.
- [38] Key, R.M., Olsen, A., van Heuven, S., Lauvset, S.K., Velo, S., Lin, X., Schirnick, C., Kozyr, A., Tanhua, T., Hoppema, M., Jutterstrom, S., Steinfeldt, R., Jeansson, E., Ishi, M., Perez, F.F., Suzuki, T., *Global Ocean Data Analysis Project, Version 2 (GLODAPv2)*, ORNL/CDIAC-162, NDP-P093. Carbon Dioxide Information Analysis Center, Oak Ridge National Laboratory, US Department of Energy, Oak Ridge, Tennessee, 2015.
- [39] Kim, H., Doney, S.C., Ianuzzi, R.A., Meredith, M.P., Martinson, D.G., Ducklow, H.W., *Analysis for Dynamics of Heterotrophic Bacteria in an Antarc-*

- tic Coastal Ecosystem: Variability and Physical and Biogeochemical Forcings*, Frontiers in Marine Science, 3 (214), 2016.
- [40] Klinck, J.M., Hofmann, E.E., Beardsley, R.C., Salihoglu, B., Howard, S., *Water-mass properties and circulation on the west Antarctic Peninsula continental shelf in austral fall and winter 2001*, Deep Sea Research Part II: Topical Studies in Oceanography, V 51, issues 17-19, 1925-1946, 2004.
- [41] Large, W.G., McWilliams, J.C., Doney, S.C., *Oceanic vertical mixing: A review and a model with a nonlocal boundary layer parameterization*, Reviews of Geophysics, 32, 363-403, 1993.
- [42] Large, W.G. and Yeager, S.G., *The global climatology of an interannually varying air-sea flux data set*, Climate Dynamics, 33:341–364, 2009.
- [43] Legge, O.J., Bakker, D.C.E., Johnson, M.T., Meredith, M.P., Venables, H.J., Brown, P.J., Lee, G.A., *The seasonal cycle of ocean-atmosphere CO₂ flux in Ryder Bay, west Antarctic Peninsula*, Geophysical Research Letters, 42, 2934-2942, 2015.
- [44] Lenton, A., Tilbrook, B., Law, R.M., Bakker, D., Doney, S.C., Gruber, N., Ishii, M., Hoppema, M., Lovenduski, N.S., Matear, R.J., McNeil, B.I., Metzl, N., Mikaloff Fletcher, S.E., Monteiro, P.M.S., Rodenbeck, C., Sweeney, C., Takahashi, T., *Sea-air CO₂ fluxes in the Southern Ocean for the period 1990-2009*, Biogeosciences, 10, 4037-4054.
- [45] Li, Q., and Fox-Kemper, B., *Assessing the Effects of Langmuir Turbulence on the Entrainment Buoyancy Flux in the Ocean Surface Boundary layer*, Journal of Physical Oceanography, v 47, 2863-2886, 2017.
- [46] Li, Q., Fox-Kemper, B., Breivik, O, Webb, A., *Statistical models of global Langmuir mixing*, Ocean Modelling, 113, 95-114, 2017.

- [47] Li, Z., Cassar, N., Huang, K., Ducklow, H.W., Schofield, O., *Interannual variability in net community production at the Western Antarctic Peninsula region (1997-2014)*, Journal of Geophysical Research: Oceans, 121, 4748-4762, 2016.
- [48] Long, M.C., Lindsay, K., Holland, M.M., *Modeling photosynthesis in sea ice-covered waters*, Journal of Advances in Modeling Earth Systems, 07, 2015.
- [49] Losch, M., Menemenlis, D., Campin, J.M., Heimbach, P., Hill, C., *On the formulation of sea-ice models. Part 1: Effects of different solver implementations and parameterizations*, Ocean Modelling, 33, 129-144, 2010.
- [50] Luo, C., Mahowald, N., Bond, T., Chuang, P.Y., Artaxo, P., Siefert, R., Chen, Y., Schauer, J., *Combustion iron distribution and deposition*, Global Biogeochemical Cycles, 22, GB1012, 2008.
- [51] Marshall, J., Adcroft, A., Hill, C., Perelman, L., Heisey, C., *A finite-volume, incompressible Navier-Stokes model for studies of the ocean on parallel computers*, Journal of Geophysical Research, 102, 5753-5766, 1997.
- [52] Martinson, D.G., Stammerjohn, S.E., Ianuzzi, R.A., Smith, R.C., Vernet, M., *Western Antarctic Peninsula physical oceanography and spatio-temporal variability*, Deep-Sea Research II, 55, 1964-1987, 2008.
- [53] McDougall, T.J., Barker, P.M., *Getting started with TEOS-10 and the Gibbs Seawater (GSW) Oceanographic Toolbox*, SCOR/IAPSO WG127. 978-0-646-55621-5, 2011.
- [54] McWilliams, J.C., and Sullivan, P.P., *Vertical mixing by Langmuir circulations*, Spill Science & Technology Bulletin, v 6, issues 3-4, 225-237, 2000.
- [55] Mellor, G.L. and Kantha, L., *An Ice-Ocean Coupled Model*, Journal of Geophysical Research, 94, 10,937-10,954, 1989.
- [56] Meredith, M.P., King, J.C., *Rapid climate change in the ocean west of the Antarctic Peninsula during the second half of the 20th century*, Geophysical Research letters, 32, 1-5, 2005.

- [57] Meredith, M.P., Brandon, M.A., Wallace, M.I., Clarke, A., Leng, M.J., Renfrew, I.A., van Lipzig, N.P.M., King, J.C., *Variability in the freshwater balance of northern Marguerite Bay, Antarctic Peninsula: results from $\Delta^{18}O$* , Deep. Res. Part II Top. Stud. Oceanogr. 55, 309–322, 2008.
- [58] Meredith, M.P., Wallace, S.I., Stammerjohn, S.E., Renfrew, I.A., Clarke, A., Venables, H.J., Shoosmith, D.R., Souster, T., Leng, M.J., *Changes in the freshwater composition of the upper ocean west of the Antarctic Peninsula during the first decade of the 21st century*, Progress in Oceanography, 87, 127–143, 2010.
- [59] Meredith, M.P., Venables, H.J., Clarke, A., Ducklow, H.W., Erickson, M., Leng, M.J., Lenaerts, J.T.M., Van den Broeke, M.R., *The Freshwater System West of the Antarctic Peninsula: Spatial and Temporal Changes*, Journal of Climate, 26, 1669-1684, 2013.
- [60] Meredith, M.P., Stammerjohn, S.E., Venables, H.J., Ducklow, H.W., Martinson, D.G., Ianuzzi, R.A., Leng, M.J., van Wessem, J.M., Reijmer, C.H., Barrand, N.E., *Changing distributions of sea ice melt and meteoric water west of the Antarctic Peninsula*, Deep Sea Research Part II: Topical Studies in Oceanography. V. 129, 40-57, 2017.
- [61] Miller, P.A., Laxon, S.W., Feltham, D.L., Cresswell, D.J., *Optimization of a Sea Ice Model Using Basinwide Observations of Arctic Sea Ice Thickness, Extent, and Velocity*, Journal of Climate, 19, 1089-1108, 2006.
- [62] Mitchell, B.G., Holm-Hansen, O., *Observations of modeling of the Antarctic phytoplankton crop in relation to mixing depth*, Deep Sea Research Part A. Oceanographic Research Papers, v 38, issues 8-9, 981-1007, 1991.
- [63] Moffat, C., Beardsley, R.C., Owens, B., van Lipzig, N., *A first description of the Antarctic Peninsula Coastal Current*, Deep-Sea Research Part II, Topical Studies in Oceanography, 55, 277-293, 2008.

- [64] Moffat, C., Meredith, M., *Shelf-ocean exchange and hydrography west of the Antarctic Peninsula: a review*, Philosophical Transactions of the Royal Society A, 376: 20170164, 2018.
- [65] Montes-Hugo, M., Doney, S., Ducklow, H., Fraser, W., Martinson, D., Stammerjohn, S., Schofield, O., *Recent Changes in Phytoplankton Communities Associated with Rapid Regional Climate Change Along the Western Antarctic Peninsula*, Science, 323, 1470-1473, 2009.
- [66] Montes-Hugo, M., Sweeney, C., Doney, S.C., Ducklow, H., Fouin, R., Martinson, D.G., Stammerjohn, S. and Schofield, O., *Seasonal forcing of summer dissolved inorganic carbon and chlorophyll a on the western shelf of the Antarctic Peninsula*, Journal of Geophysical Research, 115, C03024, 2010.
- [67] Phillips, O.M., *Spectral and statistical properties of the equilibrium range in wind-generated gravity waves*, Journal of Fluid Mechanics, 156, 505-531, 1985.
- [68] Raiswell, R., Benning, L.G., Tranter, M., Tulaczyk, S., *Bioavailable iron in the Southern Ocean: the significance of the iceberg conveyor belt*, Geochemical Transactions, 9:7, 2008.
- [69] Regan, H.C., Holland, P.R., Meredith, M.P., Pike, J., *Sources, variability and fate of freshwater in the Bellingshausen Sea, Antarctica*, Deep-Sea Research Part I, 133, 59-71, 2018.
- [70] Rozema, P.D., Venables, H.J., van de Poll, W.H., Clarke, A., Meredith, M.P., Buma, A.G.J., *Interannual variability in phytoplankton biomass and species composition in northern Marguerite Bay (West Antarctic Peninsula) is governed by both winter sea ice cover and summer stratification*, Limnology and Oceanography, 62, 235-252, 2017.
- [71] Saba, G.K., Fraser, W.R., Saba, V.S., Iannuzzi, R.A., Coleman, K.E., Doney, S.C., Ducklow, H.W., Martinson, D.G., Miles, T.N., Patterson-Fraser, D.L., Stammerjohn, S.E., Steinberg, D.K., and Schofield, O.M., *Winter and spring*

- controls on the summer food web of the coastal West Antarctic Peninsula*, Nature Communications, 5, 2014.
- [72] Schofield, O., Ducklow, H.W., Martinson, D.G., Meredith, M.P., Moline, M.A., Fraser, W.R., *How do polar marine ecosystems respond to rapid climate change?*, Science, 328 (5985), 1520-1523, 2010.
- [73] Schofield, O.M., Ducklow, H., Bernard, K.S., Doney, S. C., Patterson-Fraser, D., Gorman, K., Martinson, D., Meredith, M.P., Saba, G.K., Stammerjohn, S., Steinberg, D.K., and Fraser, W., *Penguin biogeography along the West Antarctic Peninsula: Testing the canyon hypothesis with Palmer LTER observations*, Oceanography, 26 (3), 204-206, 2013.
- [74] Schofield, O., Brown, M., Kohut, J., Nardelli, S., Saba, G., Waite, N., Ducklow, H., *Changes in the upper ocean mixed layer and phytoplankton productivity along the West Antarctic Peninsula*, Philosophical Transactions of the Royal Society A, 376:20170173, 2018.
- [75] Shartau, M., Engel, A., Schroter, J., Thoms, S., Volker, C., Wolf-Gladrow, D., *Modelling carbon overconsumption and the formation of extracellular particulate organic carbon*, Biogeosciences, 4, 433-454, 2007.
- [76] Smith Jr., W.O., Comiso, J.C., *Influence of sea ice on primary production in the Southern Ocean: a satellite perspective*, Journal of Geophysical Research, 113, C05S93, 2008.
- [77] Stammerjohn, S.E., Martinson, D.G., Smith, R.C., Ianuzzi, R.A., *Sea ice in the western Antarctic Peninsula region: Spatio-temporal variability from ecological and climate change perspectives*, Deep-Sea Research II, 55, 2041-2058, 2008.
- [78] Steinberg, D.K., Ruck, K.E., Gleiber, M.R., Garzio, L.M., Cope, J.S., Bernard, K.S., Stammerjohn, S.E., Schofield, O.M.E., Quetin, L.B., Ross, R.M., *Long-term (1993-2013) changes in macrozooplankton off the Western Antarctic Peninsula*, Deep-Sea Research I, 101, 54-70, 2015.

- [79] Stukel, M.R., Asher, E., Couto, N., Schofield, O., Strebel, S., Tortell, P., Ducklow, H.D., *The imbalance of new and export production in the western Antarctic Peninsula, a potentially "leaky" ecosystem*, Global Biogeochemical Cycles, 29, 1400-1420, 2015.
- [80] Stukel, M.R., Ducklow, H.W., *Stirring up the biological pump: vertical mixing and carbon export in the Southern Ocean*, Global Biogeochemical Cycles, 31, 1420-1434, 2017.
- [81] Sweeney, C., Hansell, D.A., Carlson, C.A., Codispoti, L.A., Gordon, L.I., Marra, J., Millero, F.J., Smith, W.O., Takahashi, T., *Biogeochemical regimes, net community production and carbon export in the Ross Sea, Antarctica*, Deep Sea Research Part II, 47, 3369-3394, 2000.
- [82] Takahashi, T., Sutherland, S.C., Chipman, D.W., Goddard, J.G., Ho, C., Newberger, T., Sweeney, C., Munro, D.R., *Climatological distributions of pH, pCO₂, total CO₂, alkalinity, and CaCO₃ saturation in the global surface ocean, and temporal changes at selected locations*, Marine Chemistry, 164, 95-125, 2014.
- [83] Talley, L.D., Pickard, G.L., Emery, W.J., Swift, J.H., *Descriptive Physical Oceanography: An Introduction (sixth edition)*, Elsevier, Boston, 560 pp, 2011.
- [84] Taylor, K.E., *Summarizing multiple aspects of model performance in a single diagram*, Journal of Geophysical Research, v 106, 7183-7192, 2001.
- [85] Taylor, M.H., Losch, M., Bracher, A., *On the drivers of phytoplankton blooms in the Antarctic marginal ice zone: a modeling approach*, Journal of Geophysical Research: Oceans, 118, 63-75, 2013.
- [86] Thompson, D.W.J., Wallace, J.M., *Annular Modes in the Extratropical Circulation. Part I: Month-to-Month Variability*, Journal of Climate, V.13, 1000-1016, 2000.
- [87] Tortell, P.D., Asher, E.C., Ducklow, H.W., Goldman, J.A.L., Dacey, J.W.H., Grzyski, J.J., Young, J.M., Kranz, S.A., Bernard, K.S., Morel, F.M.M.,

Metabolic balance of coastal Antarctic waters revealed by autonomous p_{CO_2} and Delta O_2/Ar measurements, Geophysical Research Letters, 41, 6803-6810, 2014.

- [88] Turner, J., Volwell, S.R., Marshall, G.J., Lachlan-Cope, T.A., Carleton, A.M., Jones, P.D., Lagun, V., Reid, P.A., Iagovkina, S., *Antarctic Climate Change during the last 50 years*, International Journal of Climatology, 25, 279-294, 2005.
- [89] Turner, J., Comiso, J. C., Marshall, G. J., Lachlan-Cope, T. A, Bracegirdle, T. J., Maksym, T., Meredith, M. P., Wang, Z., and Orr, A., *Non-annular atmospheric circulation change induced by stratospheric ozone depletion and its role in the recent increase of Antarctic sea ice extent*, Geophysical Research Letter, 36, L08502, 2009.
- [90] Turner, J., Lu, H., White, I., King, J.C., Phillips, T., Hosking, J.S., Bracegirdle, T.J., Marshall, G.J., Mulvaney, R., Deb, P., 2016. *Absence of 21st century warming on Antarctic Peninsula consistent with natural variability*. Nature 535, 411-415.
- [91] Van Wessem, J.M., Meredith, M.P., Reijmer, C.H., van den Broeke, M.R., Cook, A.J., *Characteristics of the modelled meteoric freshwater budget of the western Antarctic Peninsula*, Deep Sea Research Part II: Topical Studies in Oceanography, 139, 31-39, 2016.
- [92] Vaughan, D.G., Marshall, G.J., Connolley, W.M., Parkinson, C., Mulvaney, R., Hodgson, D.A., King, J.C., Pudsey, C.J. and Turner, J., *Recent Rapid Regional Climate Warming on the Antarctic Peninsula*, Climatic Change, 60, 243-274, 2003.
- [93] Venables, H.J., Clarke, A., Meredith, M.P., *Wintertime controls on summer stratification and productivity at the western Antarctic Peninsula*, Limnology and Oceanography, 58, 1035-1047, 2013.

- [94] Vernet, M., Martinson, D., Ianuzzi, R., Stammerjohn, S., Kozlowski, W., Sines, K., Smith, R., Garibotti, I., *Primary production within the sea-ice zone west of the Antarctic Peninsula: I – Sea ice, summer mixed layer, and irradiance*, Deep-Sea Research II, 55, 2068-2085, 2008.
- [95] Wanninkhok, R., *Relationship between wind-speed and gas exchange over the ocean*, Journal of Geophysical Research – Ocean, 97, 7373-7382, 1992.
- [96] Webb, A., and Fox-Kemper, B., *Impacts of wave spreading and multidirectional waves on estimating stokes drift*, Ocean Modelling, 96, 49-64, 2015.
- [97] Yamamoto-Kawai, M., McLaughlin, F.A., Carmack, E.C., Nishino, S., Shimada, K., *Aragonite undersaturation in the Arctic Ocean: effects of ocean acidification and sea ice melt*, Science, 326, 1098-1100, 2009.
- [98] Zender, C., Bian, H., Newman, D., *Mineral dust entrainment and deposition (DEAD) model: description and 1990s dust climatology*, Journal of Geophysical Research, 108:4416, 2003.